Influence of high temperature mechanisms on microstructural evolution of Dual Phase steels

Bharath Bandi

Submitted in part fulfilment of the requirements for the degree of Doctor of Philosophy at University of Warwick

Warwick Manufacture Group

University of Warwick

Table of Contents

Acknowledgement

This PhD work would not have been possible without the help I received from various people throughout the journey. Firstly, I want to express my sincere gratitude towards my supervisor, Dr Prakash Srirangam, for his continuous support and guidance. I am eternally grateful to him for sharing his wealth of knowledge to the betterment of my PhD thesis. I would like to convey my sincere gratitude towards my industrial supervisor, Dr Joost van Krevel, who has shared his immense knowledge about steel processing both in academic and industrial perspective. I am extremely grateful to him for providing all the material required for the completion of this thesis work. Most importantly, the corrections and comments which he has given to the work played a key role in improving the quality of the PhD. Every meeting I had with him helped me to understand and progress my work towards the achievement of the objectives of this work. I would also like to extend my gratitude towards my co-supervisor, Professor Mark. A. Williams for helping me completing my thesis work.

I am extremely grateful to all my colleagues and staff from WMG for helping me in various stages of my work. Special thanks to Dr. Geoff West, Dr. Sabrina Yan, Tom Moore, Numan Aslam, Mick Green, Zulfiqar Husain, Zac Parkinson and Fengzai Tang for training me on the various equipment used to complete the work. I am extremely grateful to Prof. Claire Davis for supporting me and helping me in overcoming tough obstacles in this journey. I take this opportunity to thank my friend and colleague, Dr. Carl Slater, for being a constant support and for helping me at various stages of this journey.

I am extremely grateful to Prof. Surya Prakash for constantly encouraging me from the very beginning of my career. I am extremely lucky to have his unconditional support and guidance in all aspects of my life. I take this opportunity to thank Dr. Venkat Rao and Maruthi Rao for their unconditional support throughout this journey. I am forever indebted to these three people for helping me overcome various obstacles I faced in this journey.

I also thank all my friends for supporting me and encouraging me during my ups and lows of my PhD journey. I am extremely grateful to all my friends during my PhD time, especially Sharhid Jabar, Mir Hamza, Anubhav Singh, Dr. Jiaqi Duan, Dr. James

Declaration

I, Bharath Bandi, confirm that the work presented in this thesis is my own. It has been written and compiled by myself and has not been submitted anywhere else. The work in this thesis has been undertaken by me except where otherwise stated.

Bharath Bandi

September 2021.

Research Contributions

Peer reviewed publications:

1. Bandi, B., Van Krevel, J., Aslam, N., & Srirangam, P. (2019). A Model and Experimental Validation to Predict Heating Rates for Overlap Between Ferrite Recrystallization and Austenite Transformation in Dual Phase Steel Manufacture. JOM, 71(4), 1386-1395. https://doi.org/10.1007/s11837-019-03358-2 **(Chapter 6)**

2. Bandi, B., van Krevel, J., Nandi, S., Husain, Z., & Srirangam, P. (2020). Effect of manganese bands on austenite formation of low carbon steels in dual phase steel manufacture. Materials Today: Proceedings. https://doi.org/10.1016/j.matpr.2020.06.384 **(Chapter 8)**

International conferences:

1. Bharath Bandi, Joost van Krevel, Prakash Srirangam, "Effect of High Temperature Processes on Dual Phase Steel Manufacture." TMS 2020, San Diego, California, USA, 23-27 Feb 2020. **(Oral presentation) (Chapter 7)**

2. Bharath Bandi, Joost van Krevel, Sukalpan Nandi, Prakash Srirangam, "Effect of manganese bands on austenite formation of low carbon steels in dual phase steel manufacture." ICAM5, NIT Warangal, India, 25-27th Sep 2019. **(Oral presentation) (Chapter 8)**

Manuscripts submitted:

1. Bharath Bandi, Joost Van Krevel, Prakash Srirangam. "Interaction between ferrite recrystallization and austenite formation in dual phase steel manufacture." **(Chapter 7) – Accepted in MMTA journal.**

Abstract

Dual phase steels are one of the prominent advanced high strength steels used as structural and safety components in the present day automotive industries. The microstructure of these steels is significantly affected by various processing steps involved in the manufacturing process. During the heating, and soaking steps of the continuous annealing process, the microstructure of the initial cold rolled material undergoes various mechanisms such as ferrite recovery and recrystallization, cementite spheroidization and dissolution, and austenite formation. These processes generally occur consecutively, and the final microstructural features are highly sensitive to the progress of these processes. However, to fulfil the ever rising demand for higher strength materials, increasing the amount of alloying content in order to induce precipitate hardening and solid solution strengthening is becoming a common practice. The higher percentage of alloying content can potentially retard the high temperature processes, especially ferrite recrystallization process, and thereby shift their progress into the austenite formation region. This research work was done to understand the effect of simultaneous happening of these high temperature processes on the microstructural evolution of DP steels by application of high heating rates during the heating step of annealing process.

In this research work, Boron-Vanadium micro-alloyed steels with manganese segregation were used to evaluate the effect of overlap of ferrite recrystallization, cementite spheroidization and austenite formation processes on the microstructural evolution of DP steels. The activation energy for recrystallization of 50% cold reduced steel was calculated using the Johnson-Mehl-Avrami- Kolmogorov equation and was found to be 339 kJ/mole. This is much higher than the self-diffusion activation energy for bcc iron (251 kJ/mole) which indicates the retarding effect of alloying elements on the progress of recrystallization process. The experimentally obtained recrystallization fraction values prove that increase in the cold reduction increases the kinetics of the recrystallization process. This was evidenced by the increase in the Avrami exponent from 0.87 for 50% cold reduced steel to 0.98 for 75 % cold reduced steel. It was found from the dilatometric measurements that increase in heating rate increased both the recrystallization start temperature and the austenite start temperature. A continuous heating rate model was developed using the Johnson-Mehl-Avrami- Kolmogorov

constants and process starting temperatures to predict the heating rates required to obtain a specific amount of overlap between ferrite recrystallization and austenite formation processes. It was found that with increase in cold reduction the amount of overlap possible for a given heating rate decreases. The model predicted that heating rates of 0.2 ^{0}C/s, 0.9 ^{0}C/s, 1.8 ^{0}C/s, 7 ^{0}C/s, 50.5 ^{0}C/s, and 511 ^{0}C/s are required for a predefined overlap of 1%, 15%, 34%, 67%, 88% and 99% respectively.

Using the heating rates obtained from the model, heat treatments were conducted on 50% cold reduced steels at increasing inter-critical temperatures and soaking times. It was found that with the increase in overlap of high temperature processes the amount of martensite formed decreased for the samples directly quenched without soaking time (0 sec). However, for higher soaking times, increase in overlap increased the austenite kinetics and thereby increased the final martensite fraction. For instance, sample annealed at 0.2 ^{0}C/s at 750 ^{0}C for 900 sec produced 51% of martensite, whereas sample at 50.5 ^{0}C/s at 750 ^{0}C for 900 sec produced 57% of martensite in the final microstructure. Moreover, increase in heating rates transformed martensite with necklace morphology to banded morphology. Using SEM microstructural images, hardness measurements, EDX scans, and EBSD results different austenite formation mechanisms were proposed for different percentages of overlaps, inter-critical temperatures and soaking times. SEM microstructural images and EBSD scans show that the austenite preferentially nucleates and grows on recrystallized ferrite grain boundaries during slow heating rate condition thereby developing necklace martensite morphology. The stability of spheroidized cementite and potentially long distances between grain boundary nucleated austenite was found to be responsible for slower austenite kinetics at slower heating rate condition. For higher heating rate condition, the presence of partially spheroidized cementite and dislocation rich recovered ferrite region enabled faster austenite formation kinetics. Increase in heating rate in hot rolled steels also increased the austenite formation kinetics. Moreover, hot rolled steels developed through thickness martensite morphological anisotropy and texture inhomogeneity. In both hot rolled and cold rolled steels, the manganese segregated region found to have at least 3 times higher manganese concentration. ThermoCalc simulations show that the manganese segregated region has a 70 ^{0}C lower equilibrium austenite formation temperature than the non-segregated region which can potentially lead to martensite bands at the centre of the sheets.

List of Symbols and Abbreviations

Symbol	Definition
Fe	Iron
C	Carbon
Mn	Manganese
Si	Silicon
Al	Aluminium
Cr	Chromium
V	Vanadium
B	Boron
LULUCF	Land Use, Land-Use Change and Forestry
SIMS	Secondary-ion mass spectrometry
CAL	Continuous annealing line
DP	Dual Phase Steel
HSLA	High Strength Low Alloy Steel
CCT	Continuous cooling transformation
TTT	Time Temperature Transformation
A_{e1}	Austenite Equilibrium Start Temperature

A_{e3}	Austenite Equilibrium Finish Temperature
A_{c1}	Austenite Start Temperature
A_{c3}	Austenite Finish Temperature
R.x.T	Recrystallization Start Temperature
X	Recrystallization Fraction
Q	Activation Energy for Recrystallization Process
R	Universal Gas Constant
H.R.	Heating Rate
BVHR	Boron Vanadium Hot Rolled Steel
BVCR 50%	Boron Vanadium % Cold Reduced Steel
SEM	Scanning Electron Microscope
TEM	Transmission Electron Microscope
°C	Degrees Centigrade
EDX	Electron Dispersive X-ray Spectroscopy
EBSD	Electron Back Scattered Diffraction
FIB	Focused Ion Beam
ASTM	American Society for Testing and Materials
BCC	Body Centred Cubic

BCT	Body Centred Tetragonal
FCC	Face Centred Cubic
mm	Millimetre
µm	Micrometre
nm	Nanometre
α	Alpha Fibre
Γ	Gamma Fibre
Ε	Epsilon Fibre
Θ	Theta Fibre
Η	Eta Fibre
Ζ	Zeta Fibre
T	Temperature
t	Time

List of Tables

List of Figures

Chapter 1 - Introduction

1.1. Challenges faced by automotive-steel industry

The development of steel as a structural material is one of the most significant achievements of humankind. Its commercialization and rapid development had enabled numerous scientific advancements in various other fields [1]. Amongst all, the automotive industry is one area where the development of new grades of steels had significant impact on the choice of materials used. This is because of the fact that the steel is being used as a major structural and safety component in the automobile industry since the initial basic vehicle manufacture (1900's) to the present day highly advanced automobile. In the beginning of the 20th century, wood was the major material used for the manufacturing of automobiles [2]. However, by the 1920's, steel became the major choice of material because of its excellent ability to be pressed into intricate shapes. Moreover, steel became increasingly cost-effective with an added advantage of high weldability [3]. However, in the past few decades, the usage of new materials like Aluminium, Magnesium and Carbon-Fibre reinforced polymers is continuously increasing, mainly due to their light weight properties.

After the Second World War, rapid economic growth in developed countries led to a significant improvement in both automotive and transport industry. However, with this development, the world has seen a drastic increase in the number of casualties from road accidents. Due to this there was a significant pressure to increase the safety of automobiles. One of the most historic events was Stop de Kindermoord (stop the child murder) protests held in The Netherlands in the year 1972 [4]. **Figure 1.1** shows the number of casualties caused by road accidents in Netherlands from the year 1950 to 2010 [5]. Similar trends were observed throughout the world. In response, governments of various countries passed legislative acts to ensure automotive industry to produce vehicles which are much safer than the previous ones. World Forum for Harmonization of Vehicle Regulations (Europe) and National Highway and Traffic Safety Administration (USA) are notable agencies which regulate the safety of automobiles [6]. Implementation of safety belts and bumpers are one of the initial requirements imposed by these administrations [7].
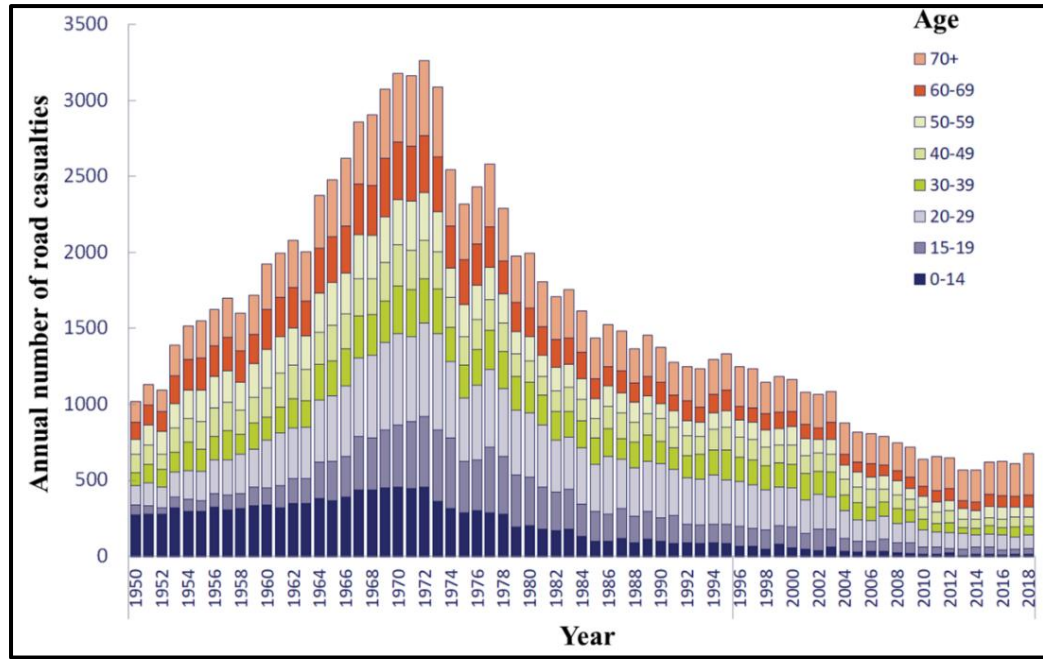
Figure 1. 1: Annual number of road casualties in Netherlands from 1950 to 2018 [5].

At the same time, the amount of greenhouse gases started to increase at an alarming rate, mainly due to the increase in fossil fuel consumption in the various industrial sectors [8]. To add to this, there is an increasing uncertainty in the price of fuel from the oil industry. For instance, in the year 1973, the Organization of Arab Petroleum Exporting Countries imposed an oil embargo on all the countries which were perceived to support Israel in the Yom Kippur war [9]. This resulted in an oil shock which made the oil price increase by 400 % globally by the year 1974 [10]. This embargo is considered as one of the significant historic events which triggered both governments and industries to drive towards a fuel efficient economy. With the continuous changing political situation in the oil rich countries, various oil shocks are continuously creating huge fluctuations in the oil prices, especially in the years 1979, 1990 and 2007 [11,12].

Figure 1.2. a) shows the global increase in the amount of carbon dioxide emissions from the year 1758 to 2018 [8]. This clearly indicates the urgency required to reduce the global warming situation. Most importantly, the majority of greenhouse gases are emitted from the transport industry. This is evident from **Figure 1.2. b),** which shows the amount of greenhouse gases emitted in United Kingdom to be maximum from transport sector in the year 2018 [13]. Consequentially, increased public pressure and strict government regulations are driving automotive industry towards lesser fuel

2

emissions. Moreover, customers' expectations on comfort, reliability, speed and safety are continuously increasing. Therefore, in the past few decades, automotive industry is mainly driven by two conflicting demands: 1) Increasing the passenger safety by using high strength vehicle components, and 2) Decreasing the fuel emissions by reducing the components individual weight and therefore the overall weight of the vehicles [14].
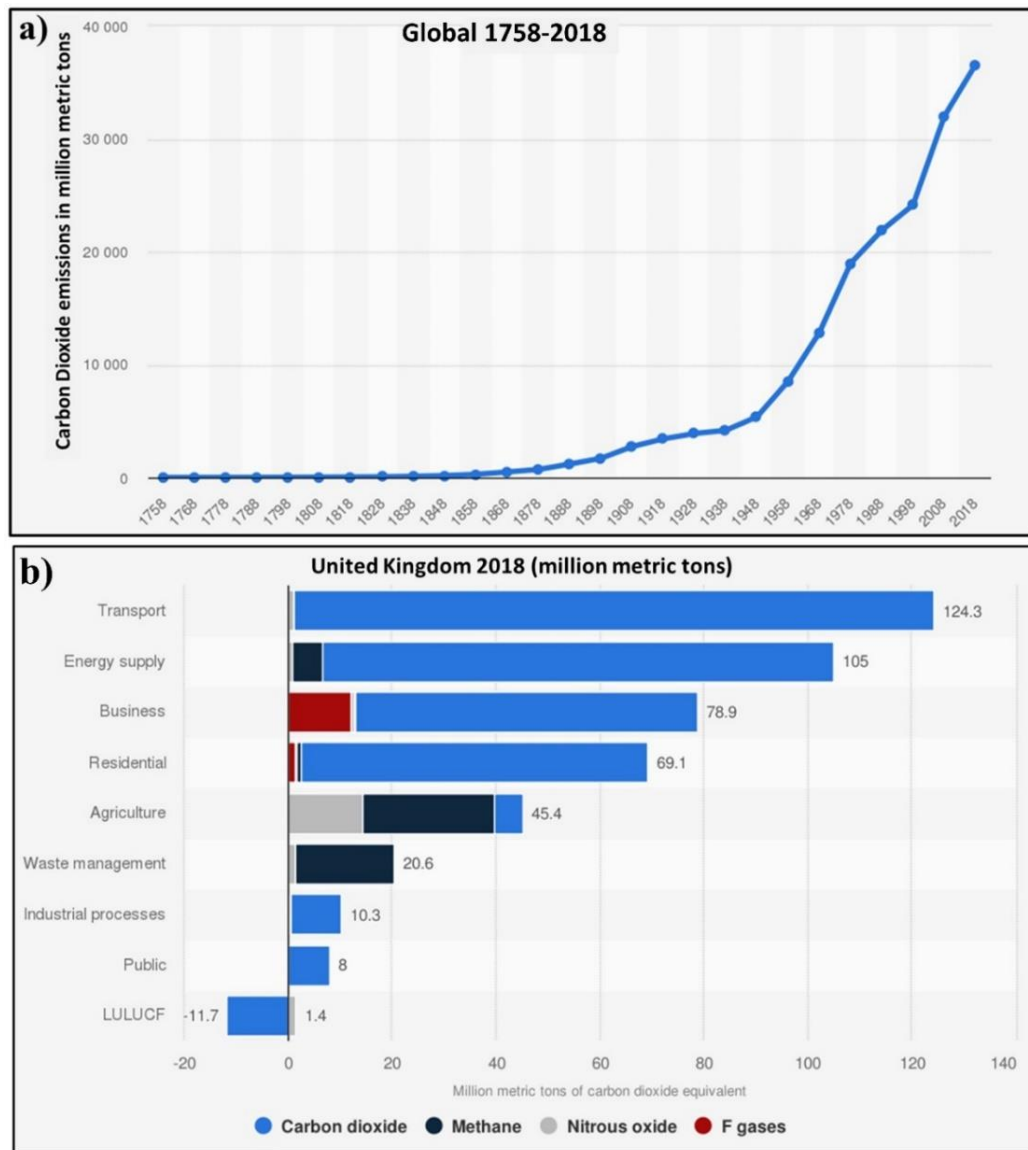
Figure 1. 2: a) Global carbon dioxide emissions from the year 1758 to 2018 (in million metric tons) [8], and b) Amount of greenhouse gas emissions in the United Kingdom (UK) in the year 2018 [13].

In order to achieve a significant decrease in the fuel consumption, the automotive industry employed the approach of decreasing the overall weight of the vehicles. One

of the first steps employed for mass reduction was to manufacture automobiles using body frame integral structure (Uni-body) instead of the heavy body on frame structure (BOF) [15]. This enabled vehicles to be more rigid, light in weight and fuel efficient. Even though the majority of vehicles in the present day employ a Uni-body structure (~80%), some are still made with BOF structure because of the other specific advantages needed in off-road driving [16]. Most importantly, the mass reduction strategy, led to the development of Advanced High Strength Steels (AHSS), which are more sophisticated steels, than the previous steels, with carefully designed alloying content, complex microstructures and enhanced mechanical properties.

1.2. Advanced High Strength Steels

During the initial development of high strength steels, the automotive industry used strain aged steels as the high strength light weight material [17]. However with the advancement of continuous casting technology, these steels were replaced with martensitic and recovery annealed steels [18]. The first commercial success of high strength steel application was demonstrated in the mid 1970's by the introduction of Charger XL model into the market by Chrysler Corporation. The use of high strength steels enabled these manufacturers to reduce the mass of the vehicle by 286 kg [19]. This initial success story displayed the potential of high strength steels. In the meantime, the first generation of AHSS steels like Dual Phase steels were developed. However, to commercialize these steels, more than 20 years of scientific advancements was needed [3]. This was mainly to overcome the welding problems and the lower cooling capabilities of the process lines. Meanwhile, during this period, High Strength Low Alloy Steels (HSLA) were extensively used as structural and safety components [20]. These steels use fine grained microstructure with precipitate hardening to produce yield strengths ranging from 280-550 MPa with a satisfactory ductility levels [21]. However, the ever increasing demand for high strength steels and the continuous advancement in the steel processing technology paved the way to the commercialization of AHSS steels. Replacement of High Strength Low Alloy (HSLA) parts with thinner AHSS counterparts with equivalent or improved functionality not only increased the fuel efficiency due to weight reduction, but also increased the crash safety due to their higher strength [22]. **Figure 1.3** shows the comparison of various

4

commercial steels in terms of their respective mechanical properties. This clearly shows the superior mechanical properties provided by the AHSS steels and justifies its increased usage in automotive industry. According to the World Steel Dynamics report the usage of AHSS steels would reach 23.7 million tons by the year 2025 [23]. In other words the amount of AHSS used per vehicle will be doubled by the year 2025 [24].

AHSS are sophisticated steels designed through a carefully monitored heating and cooling processes. These steels possess precisely selected chemical compositions and have multiple phases like ferrite (α), martensite ($\dot{\alpha}$), bainite, and austenite (γ) in their microstructure [25]. Among these AHSS steels, dual phase (DP) steels are termed as the first generation AHSS steels and are extensively used in automotive industries. Note that other AHSS steels like Transformation Induced Plasticity (TRIP) and Twinning Induced Plasticity (TWIP) steels have higher strengths and better formability compared to DP steels (**Figure 1.3.**). But still DP steels are preferred over these particular AHSS steels. This is because the other AHSS steels like TRIP and TWIP steels pose practical problems like high alloying costs, casting problems, poor weldability and manganese segregation [26]. With the ever increasing demand for reducing fuel emissions and increasing passenger safety regulations, the challenge towards the steel industries to develop new steels and/or enhance the mechanical properties of the existing steel grades is continuously increasing. From a metallurgical perspective, the key to improve the mechanical properties of a given steel lies in understanding and controlling the microstructure evolution during the manufacturing process. This thesis work focuses on understanding the microstructure evolution of DP steels during its manufacturing process.
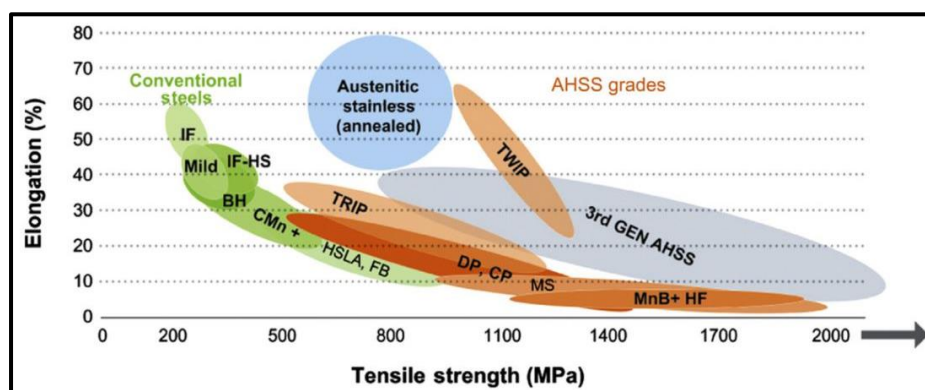
Figure 1. 3: Comparison of mechanical properties of various commercial steels [3].

1.3. DP steels in modern day Automobiles

DP steels are first generation AHSS steels which contain ferrite and martensite phases in the final microstructure. The most important properties of DP steels that attract automobile manufacturers are high strain hardening coefficient with large uniform elongation, no yield point phenomena, low yield strength to tensile strength ratio and good baking hardenability. The materials used for structural and safety components of automobiles are chosen in such a way that the deceleration of passengers would not exceed a certain thresholds during a crash event [27]. Two main principles are followed to increase the survivability of the passenger: 1) Creation of zones where the components present must be able to absorb maximum kinetic energy, and 2) Creation of safety zones where the components must be able to transfer or dissipate the kinetic energy.

The components which need high energy absorption must be made with materials which deform over a large range of strain. In other words, materials which have large area under stress-strain curve are ideal for this application. The high work hardening rate of DP steel grades prove them to be an excellent choice for this purpose. **Figure 1.4** compares the stress-strain curves of a HSLA and a DP grade steel [28]. Even though, the yield strengths of both the grades are similar, DP steel work hardens to higher tensile strength. Therefore, for a given strain, DP steel absorbs more energy. This allows these steels to have high applications as safety components in the automotive industry. For example, recently Ford, a leading motor manufacturing company, used more than 40% of DP steels for the Body in white components (BIW) in its recent Ford edge model [29]. A detailed pie chart of materials used with its corresponding components is shown in **Figure 1.5**.
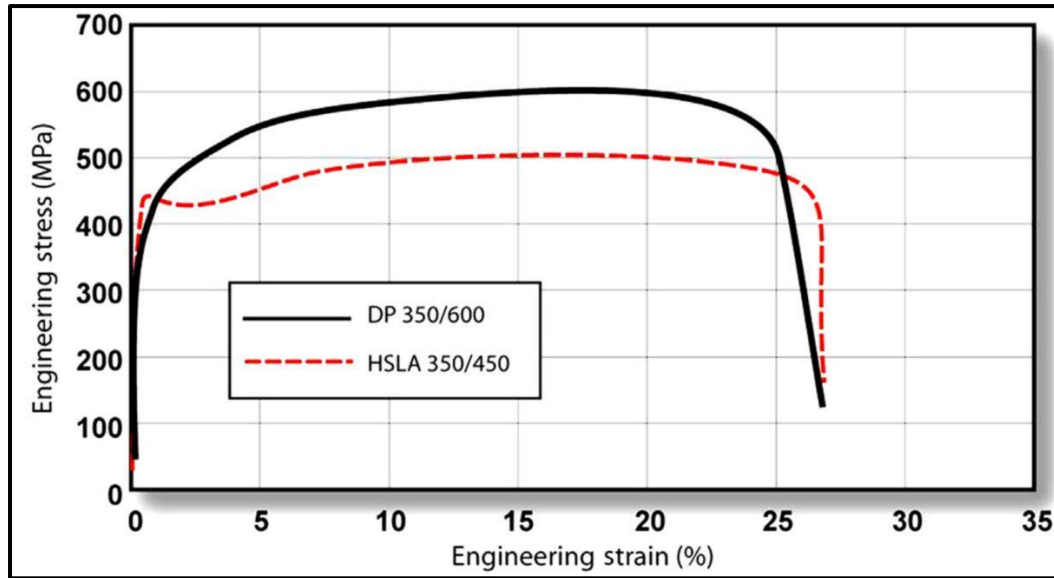
Figure 1. 4: Engineering stress-strain curves of DP and HSLA steels [28].
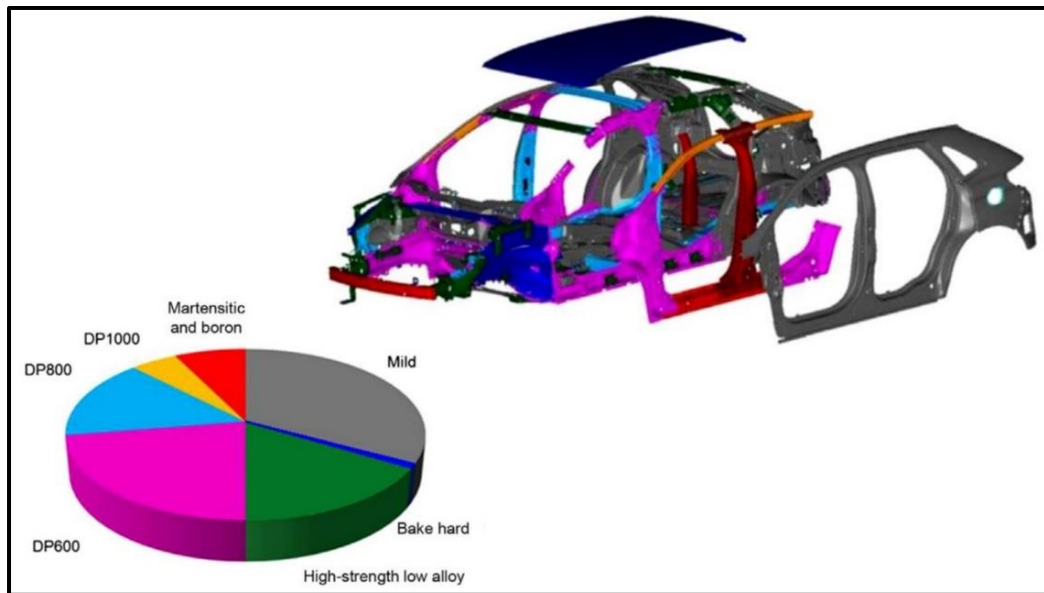
Figure 1. 5: Pie chart of materials used in Ford Edge car [29].

The second principle is to create a safety cell for the passengers. The materials required for the components in this zone must have high resistance to intrusion. Martensitic steels are highly used for this purpose because of their higher tensile strength (2 GPa). However, due to limited ductility (see **Figure 1.3**), these steels are hard to be manufactured into complex shapes which are required for vehicle components. With the increase in tensile strength, from 650 MPa to 1200 MPa [30,31] and its apparent retention of ductility has enabled the automotive industry to gradually increase its

percentage of DP steels usage. Therefore, DP steels with tensile strengths up to 1200 MPa are becoming an economical alternative in these anti-intrusion components as well. For instance, Generals Motors increased the usage of DP steels from almost nothing in its GM 1990 legacy vehicle to >35% usage in its recent 2016 Chevy Malibu Model [32]. This trend is shown in **Figure 1.6**. However, the ductility of high strength DP steel grades is very low when compared to its lower strength grades.
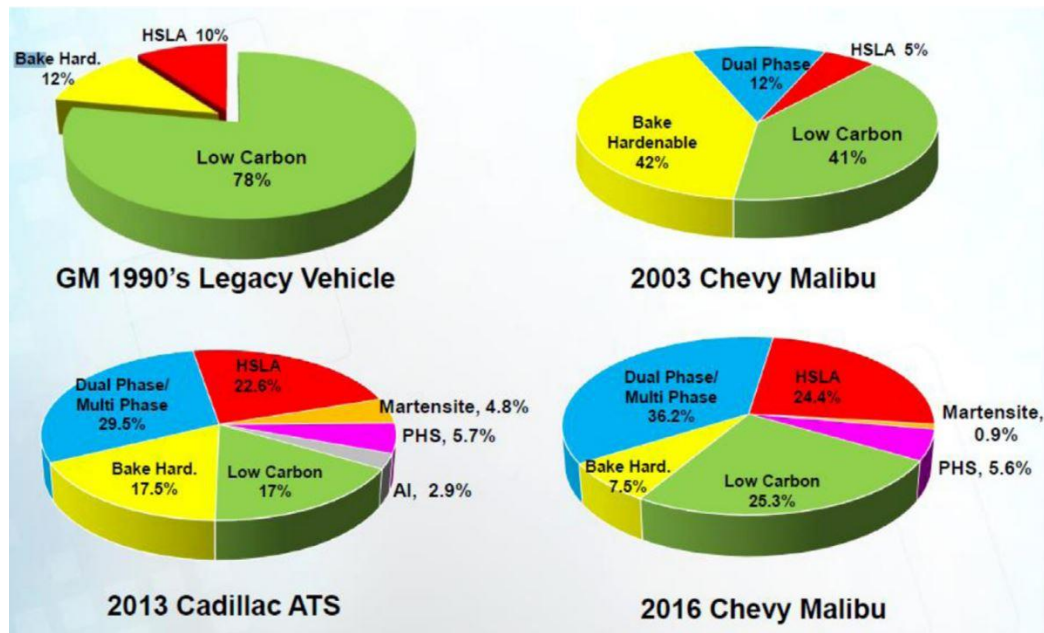
Figure 1. 6: Growth of DP steels usage in General Motors [32].

In a typical automobile, DP steels are primarily being used as safety and structural parts where superior resistance to impact, fatigue, intrusion and denting etc is required. The automobile components which are generally made up of DP steel grades are given in **Table 1**. A schematic representation of DP steel components used in the SAAB automobile is shown in **Figure 1.7**. It can be noticed that the majority of DP steel grades used in the present-day automobiles have strength below 800 MPa. The lower ductility of high strength DP grades can be the reason for their limited usage.

Table 1. 1: DP steel grades (DP Yield Strength/Tensile Strength) with their respective automobile applications [33].

Dual Phase Steel grade	Automobile Component
DP 800/ 1180	B-pillar upper.
DP 700/1000	Roof Rails.
DP 600/980	B-pillar, floor panel tunnel, engine cradle, front sub-frame package tray, shot gun, seat.
DP 500/800	Body side inner, quarter panel inner, rear rails, rear shock reinforcements.
DP 350/600	Floor panel, hood outer, body side outer, cowl, fender, floor reinforcements.
DP 300/500	Roof outer, door outer, body side outer, package tray, floor panel.
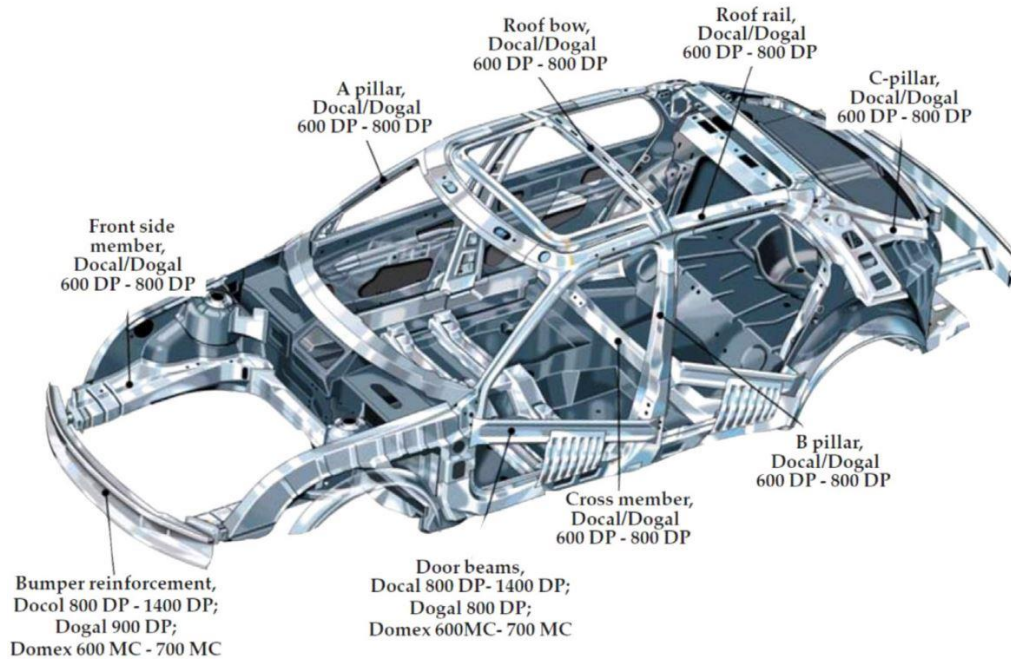
Figure 1. 7: DP steel components used in the SAAB automobile [31].

The increasing demand for DP steels and its indisputable economical/environmental advantage over other AHSS steel grades makes it important for the present-day researchers to develop a deeper knowledge in this field. Especially the unpredictability in the mechanical properties with slight variation in composition and/or processing routes is the biggest limitation of the steels. The key to understand this phenomenon

lies in understanding the variation of final microstructure and the effects of various intermediate processes occurring during the manufacturing steps of these steels. The final microstructure of DP steels is greatly affected by the various intermediate steps and high temperature mechanisms involved during the manufacturing process. The high temperature mechanisms such as ferrite recovery, recrystallization, grain growth, cementite spheroidization and austenite formation have direct influence on the final microstructure. The progress of these high temperature mechanisms is in turn influenced by various process parameters such as alloy content, hot rolling, cold reduction percentage, inter-critical annealing parameters etc. This PhD work is focused on the microstructure evolution in microalloyed DP steels under various process parameters with special emphasis on the various mechanisms occurring during the manufacturing process. The main focus of this study is to understand the effect of progress of high temperature mechanisms, especially ferrite recovery, recrystallization, grain growth, cementite spheroidization and austenite formation, on the final microstructure of DP steels in low-carbon manganese segregated cold rolled and hot rolled ferrite-pearlite steels.

Chapter 2 - Literature Review

DP steels were first developed in the 1960's by British Iron and Steel Research association (UK) and Inland Steel Corporation (US) [34]. Even after 60 years of its initial development, there are still many open scientific questions, especially in the microstructural evolution of these steels. In theory, the microstructure of these steels consists of two major phases: 1) Soft alpha Ferrite phase (α) which provides ductility, and 2) Hard Martensite phase which provides strength. A typical DP steel microstructure with soft ferrite matrix (black) and hard martensite islands (grey) is shown in **Figure 2.1** [35]. The ferrite phase contains iron in the form of body centre cubic (BCC) crystal structure, whereas martensite contains iron in the form of body centre tetragonal (BCT) structure. The ferrite phase has a maximum carbon solubility of 0.02 %. It forms when austenite phase is slowly cooled below ferrite start temperature (A_{r3}) by continuously rejecting carbon through a diffusion driven process. Martensite forms through a diffusion less shear transformation when the austenite is cooled faster than the critical cooling rate. The formed martensite has same carbon content as the parent austenite phase. In these steels, the ferrite matrix is responsible for the majority of its ductility. Moreover, it also contributes to some percentage of the strength depending upon the alloying content in the solution and precipitates form. Martensite gives majority of the strength and its high hardness/strength is due to the supersaturated carbon present in the solid solution and the large dislocation density associated with it.

DP steels generally contain 0.06-0.15 wt% Carbon, 1-3 % Manganese, 0.05-1 % Aluminium, 0.3-1 % Silicon and/or other precipitate forming micro-alloying elements such as Boron, Titanium, Vanadium and Niobium in it [36]. Even though the term DP suggests a simple two phase ferrite and martensite microstructure, there is actually a complexity of microstructural features behind this facade of dual phase steels. During the actual industrial processing routes pearlite, bainite, retained austenite and carbide precipitates can also form with slight change in the processing parameters. Moreover a wide range of microstructural features like martensite volume fraction (VM), martensite carbon content (CM) [37], ferrite grain size (SF), ferrite/martensite morphology, texture, ferrite precipitate distribution and ferrite dislocation density [38]

are very sensitive to compositional variations and also to the slightest variation in the processing routes [39]. These wide range of microstructural features will in turn have a direct influence on the mechanical properties [40,41]. Therefore, the main challenge is to develop industrially relevant processing routes for producing desired microstructural features with acceptable properties with minimum variation. The key to understand the microstructural evolution depends upon the chemical composition and the process parameters employed in the manufacturing process. In this chapter research done relevant to microstructural evolution during the continuous annealing process will be discussed. More specifically, the importance of austenite formation on the final microstructure during the manufacturing process of these steels is critically discussed.
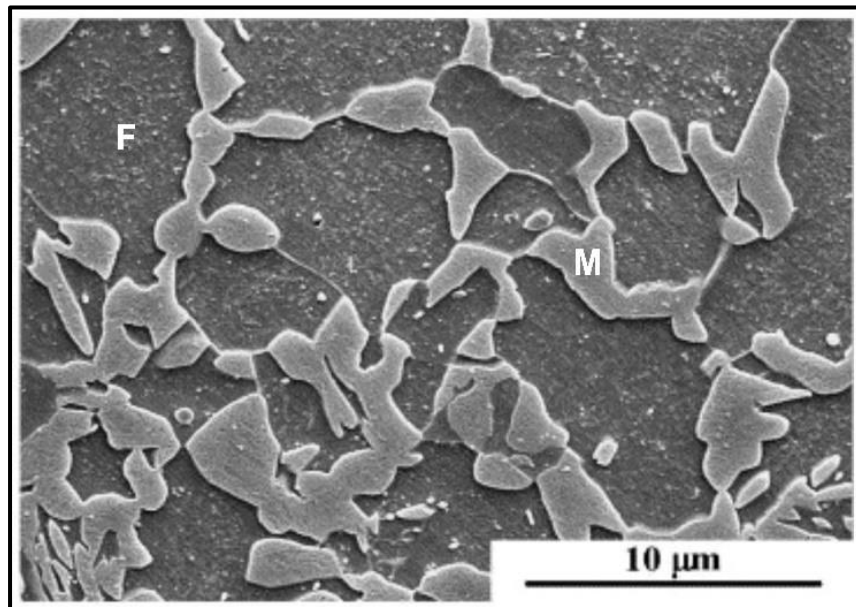
Figure 2. 1: A typical DP steel with ferrite (F) and martensite (M) phases in it [35].

2.1. DP steel manufacturing route

Industrial production of DP steels consists of a series of critical processing steps involving both mechanical and thermal treatments. A general production layout of these steels in SSAB manufacturing plant, Sweden (Borlänge) is shown in **Figure 2.2** [42]**.** The sequential order of the main steps involving in the production by the majority of DP steel manufacturers are as follows: continuous casting, hot rolling, pickling, cold rolling, and continuous annealing involving inter-critical annealing, quenching

and tempering steps. A brief overview of the major steps relevant to the microstructure evolution is discussed below.
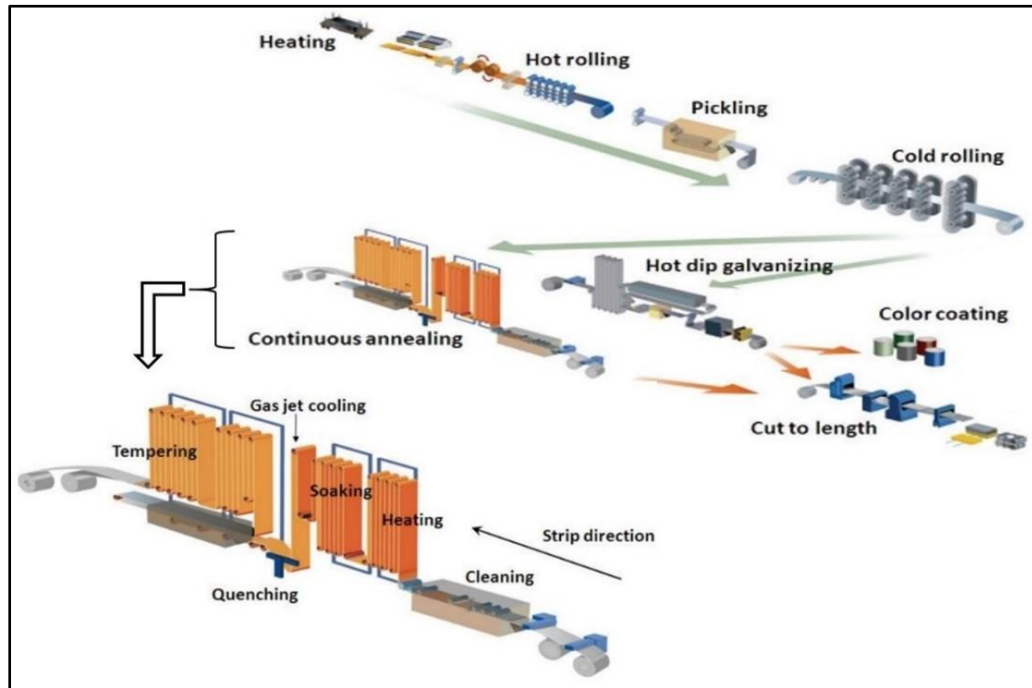
Figure 2. 2: Production layout of DP steels in SSAB, Sweden (Borlänge) [42].

2.1.1. Hot Rolling Step

After slab production in the continuous casting, the slabs are reheated to complete austenitizing temperature (1100-1250 °C) in the reheating furnace such that a fully annealed microstructure exists prior to the hot rolling step. Large thickness reduction is achieved in the subsequent hot rolling step. In general, hot rolling can be categorised into rough rolling and finish rolling. **Figure 2.3** shows the schematic representation of hot rolling in the low carbon steels. In rough rolling stage (reversing mill), the slab is reduced from around 220-260 mm thickness to 10-16 mm thickness. The temperature for all the passes is generally maintained above the non-recrystallizing temperature (TNR). The austenite gets continuously recrystallized through dynamic recrystallization forming equiaxed grains. In the finish rolling stage (tandem mill), the final hot rolling reduction is done to a thickness of 3-6 mm. The final passes of this step is generally done below the TNR temperature to achieve pancaked austenite grains and subsequent fine ferrite grains in the final hot rolled microstructure. The phases present in the hot rolled microstructure depends upon the temperatures

employed during hot rolling and coiling processes, and also on the subsequent cooling cycle during coiling. Industrially a ferrite-pearlite microstructure is produced/preferred. One of the major reasons for this is because the ferrite-pearlite is relatively softer than other microstructures, and therefore the loads required in the subsequent cold rolling step doesn't exceed the capacity of the mill. However, occasionally other microstructures like ferrite-pearlite-bainite, or ferrite-bainite or fully bainite or fully martensite are also produced depending upon the requirements.
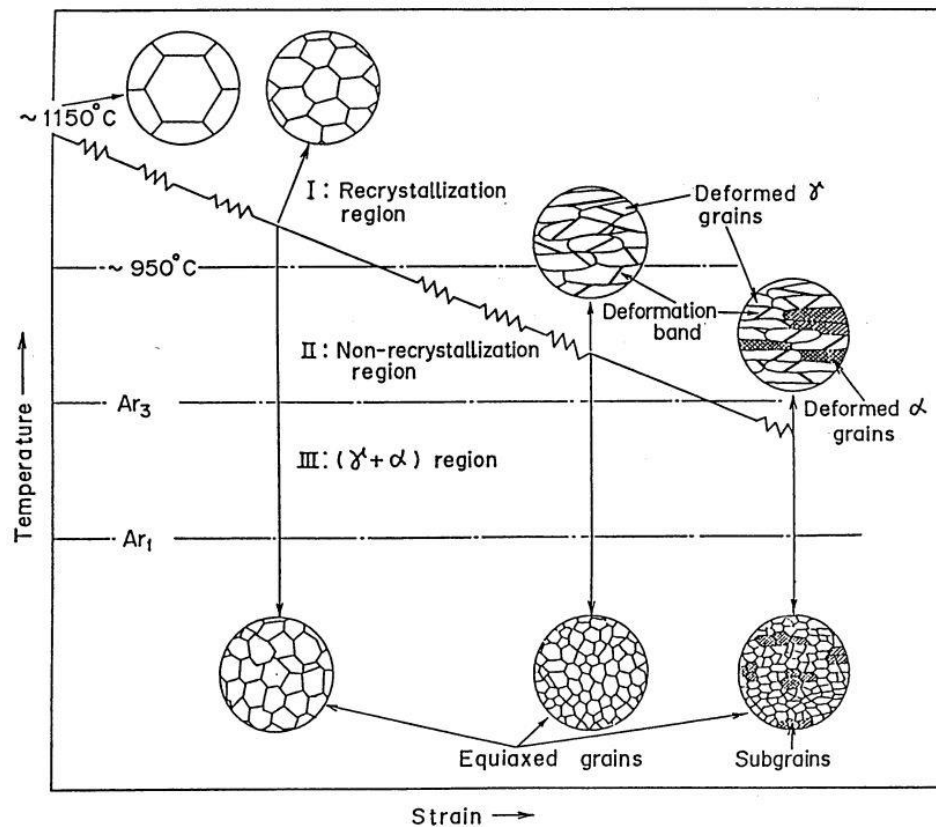
Figure 2. 3: Schematic representation of hot rolling of low carbon steels. [43]

2.1.2. Cold Rolling Step

After hot rolling, during the cooling step, the surface of the strip is prone to severe oxidation. These oxide scales are removed in the pickling line, where dilute hydrochloric acid is used to remove the scales and produce a good surface finish [44]. After pickling process, the strips are subjected to cold rolling in order to further reduce the thickness and induce stored deformation energy into the material. In industry, the final thickness of the cold rolled strip depends upon the targeted DP grade and the consumer requirement and it ranges between ~1 to 3 mm.

14

2.1.3. Continuous Annealing Line

The cold reduced steel is then transferred to the continuous annealing line (CAL) for final heat treatment process in which partial re-austenitization takes place. The first step in CAL consists of heating the initial cold reduced (occasionally hot rolled) sheets into the inter-critical temperature (between A_{c1} and A_{c3}) of ferrite-austenite region [36]. It should be noted that the initial cold reduced material can have various initial microstructures such as ferrite-pearlite, fully bainite, fully martensite or ferrite-pearlite-bainite etc. Irrespective of the initial microstructure, the heating step is compulsory where the initial room temperature microstructure is converted to ferrite-austenite microstructure at high temperature. In industry, the rate at which the strip is heated to this inter-critical region depends upon the strip thickness, furnace length and the line speed. The second step in CAL involves soaking for a given time at a given inter-critical temperature such that a desired amount of ferrite-austenite phase fraction is formed. As the austenite is a diffusion driven process, increase in soaking time increases its volume fraction until the equilibrium value. A specific amount of soaking time is chosen such that a desired amount of austenite is formed for the given DP steel grade. After soaking, the material is water quenched such that all the austenite present at the high temperature is transformed to martensite leading to a ferrite-martensite dual phase microstructure at room temperature. Industrially, instead of direct quenching from the inter-critical region, a slow cooling step followed by fast quenching step can also be employed. The strip is further re-heated in the last step of CAL in order to temper the martensite. This tempering step increases the ductility of these steels, however, slightly decreases their strength. **Figure 2.4** shows the schematic representation of annealing process in DP steel manufacture through CCT, TTT and equilibrium phase diagram. As shown, the steel is heated and soaked in austenite-ferrite regime and then fast quenched below critical cooling rate such that the austenite at high temperature transforms to martensite at room temperature. Thus, a DP steel is manufactured with a soft ferrite and hard martensite in the microstructure. It should be noted that occasionally DP steel is also manufactured by annealing at fully austenitic temperature, followed by quenching such that the undercooled austenite transforms to ferrite and the remaining to martensite. In this case, the initial cold reduction percentage, or the line speed employed during heating has no influence on the final microstructure. This PhD thesis concentrates on the microstructure evolution

during the conventional heating and soaking step (CAL) into the inter-critical region of the manufacturing process.
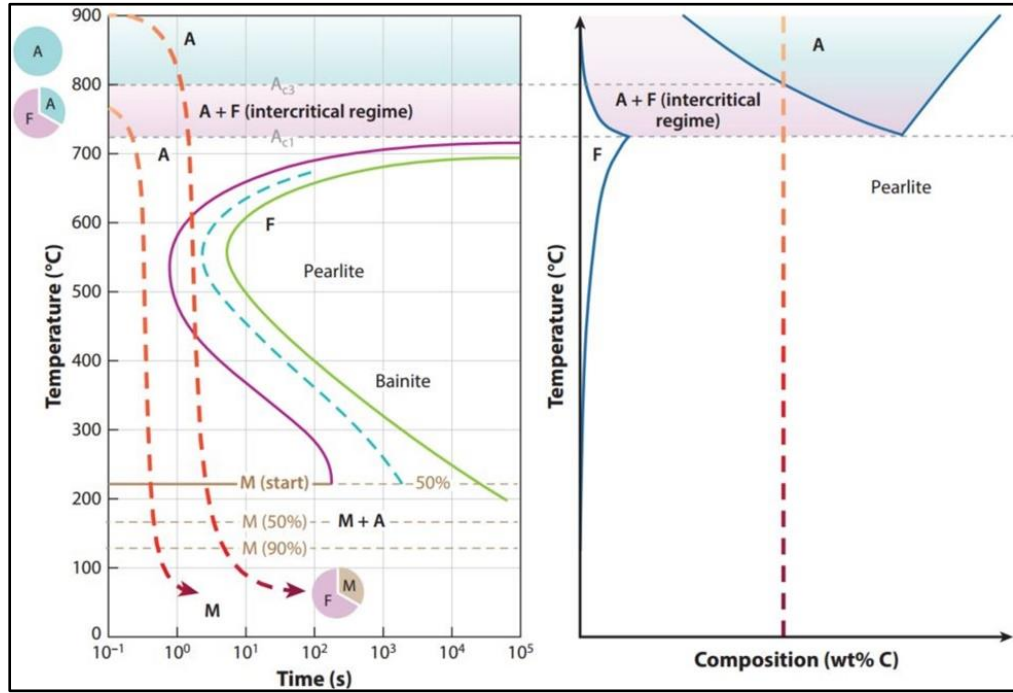
Figure 2. 4: Schematic representation of annealing in DP steel manufacture through CCT, TTT and equilibrium phase diagrams. [36]

2.2. Re-Austenitisation Process

As discussed above, the most crucial step of DP steel manufacturing involves partial austenitization process of initial microstructure by heating and soaking the initial steel into the inter-critical temperature range. The austenite phase consists of iron in the form of face centred cubic (FCC) crystal structure. It is generally stable between 723 °C and 1500 °C and has a maximum carbon solubility of 2.06 %. The final microstructural features such as solute segregation, volume fraction of phases, their morphology and distribution, and grain sizes etc [45] depend on the composition, morphology, volume fractions and distribution of the parent austenite phase present at the inter-critical temperature. In this regard, understanding and controlling the formation of the parent austenite phase is critical for controlling the final microstructure and therefore the mechanical properties. So, it is very important to study and understand the austenite formation mechanism on various

16

thermomechanical heat treatments especially which are relevant to industrial processing routes. Although austenite decomposition has been widely investigated in the last century [46–48], work related to austenite formation has increased only in the last three decades [49]. The reasons for this limited study could be: a) austenite formed at higher temperature is generally overlooked because it is no longer present in the final room temperature microstructure, and b) difficulty in directly characterizing the austenite phase at high temperatures. However, with the rise in DP steel usage coupled with recent advancements in high temperature characterization techniques there is an increased interest in austenite formation mechanism in both industrial and academic research. [50,51]. Moreover, other high temperature mechanisms such as ferrite recovery, recrystallization, grain growth, cementite spheroidization and precipitate dissolution/formation occur during inter-critical annealing process [36]. This PhD thesis focuses on the mechanism of austenite formation with respect to the influence of these high temperature mechanisms at various inter-critical annealing parameters.

The first publication on austenite formation in steels goes way back to the year 1905, which reported a nucleation and growth mechanism [52]. This was confirmed by Roberts and Mehl in the year 1943, by measuring the rate of austenite formation using a microstructure of ferrite-cementite aggregates [53]. Even after these initial findings there has been little research on austenite formation during this period. A majority of the work was dedicated towards the austenite decomposition process. Only after seven decades from the first publication, significant amount of research was done on austenite formation, thanks to the increased interest in DP steels and its potential for usage in automotive applications. In 1981, Speich *et al.* published an excellent work on austenite formation in low carbon DP steels with hot rolled ferrite-pearlite initial microstructure [54]. Compared to previous research studies [55,56] this work led to a very distinct understanding about austenite formation in steels. One of the major conclusions of this work was that the growth of austenite during inter-critical annealing would continue even after the complete dissolution of pearlite. To explain this phenomenon a three-step mechanism for austenite formation was proposed. The schematic representation of the proposed mechanism is shown in **Figure 2.5**.
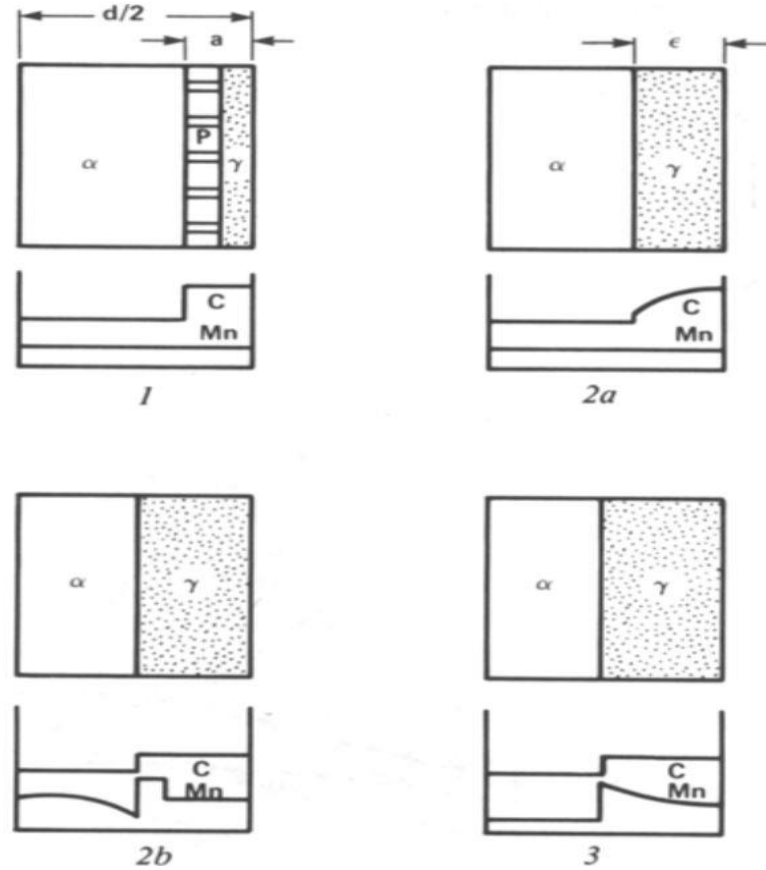
Figure 2. 5: Mechanism of Austenite formation during intercritical annealing: 1. Nucleation and Growth of austenite by Pearlitic dissolution. 2. Growth of austenite into ferrite. 3. Equilibration of austenite and ferrite through manganese diffusion [54].

In the first step, rapid nucleation of austenite takes place at ferrite-pearlite interface and the subsequent growth of this austenite takes place by simultaneous dissolution of adjacent pearlite (carbon rich). In this step a high carbon concentrated austenite is formed. In the second step, the austenite grows from ferrite boundaries into the ferrite grains and is controlled by carbon diffusion in austenite and/or manganese diffusion in ferrite. In the third step, slow equilibration of austenite and ferrite takes place by manganese diffusion in the formed austenite [54]. Because austenite is forming on the grain boundaries, the transformation products also mostly form on the grain boundaries according to this proposed mechanism [57,58]. However, the austenite formation is prone to occur not only at grain boundaries, but also within the grain interiors [59]. Moreover, austenite formation and its martensitic transformation becomes more complicated with increased alloy content and varying processing parameters such as the degree of cold rolling expressed in percentage of reduction,

18

and also with the inter-critical annealing parameters such as heating rate, annealing temperature, holding time and cooling rate[60]. In the following sections, the effect of these parameters on microstructure evolution will be discussed in detail.

2.3. Effect of composition

In this section, effect of alloy additions on microstructure evolution and consequential mechanical properties (relevant to DP steels) will be discussed. The choice of alloying elements depends upon their cost, their effect on casting and welding, and most importantly on their effect on mechanical properties. The formation of ferrite-austenite mixture during the heating step and the subsequent decomposition products during the cooling step are greatly influenced by the alloying elements. The main alloying elements in dual phase steels include carbon, manganese, silicon, aluminium, chromium and optional precipitate forming elements [31]. These alloying elements have a huge influence on the A_{c1} and A_{c3} temperature, $\alpha+\gamma$ temperature range, austenite stability, hardenability, and martensite start temperature etc.

2.3.1. Carbon

Dual phase steel is a low carbon steel which typically contain 0.06 to 0.15 wt% of carbon. Carbon is a very strong austenite stabilizer and increases the hardenability of steels. Moreover, an increase in carbon content increases the strength of the martensite phase. However, with the increase in carbon content, the ductility of the steel decreases [31,61]. For instance, Valeria et al., reported that increase in carbon content increases the strength of DP steels, but simultaneously decreases the ductility [61]. **Figure 2.6 (a, b)** shows that, for 50% martensite volume fraction, an increase in carbon content from 0.08% to 0.2% increases the tensile strength by 500 MPa and decreases % area reduction by 8%.

19
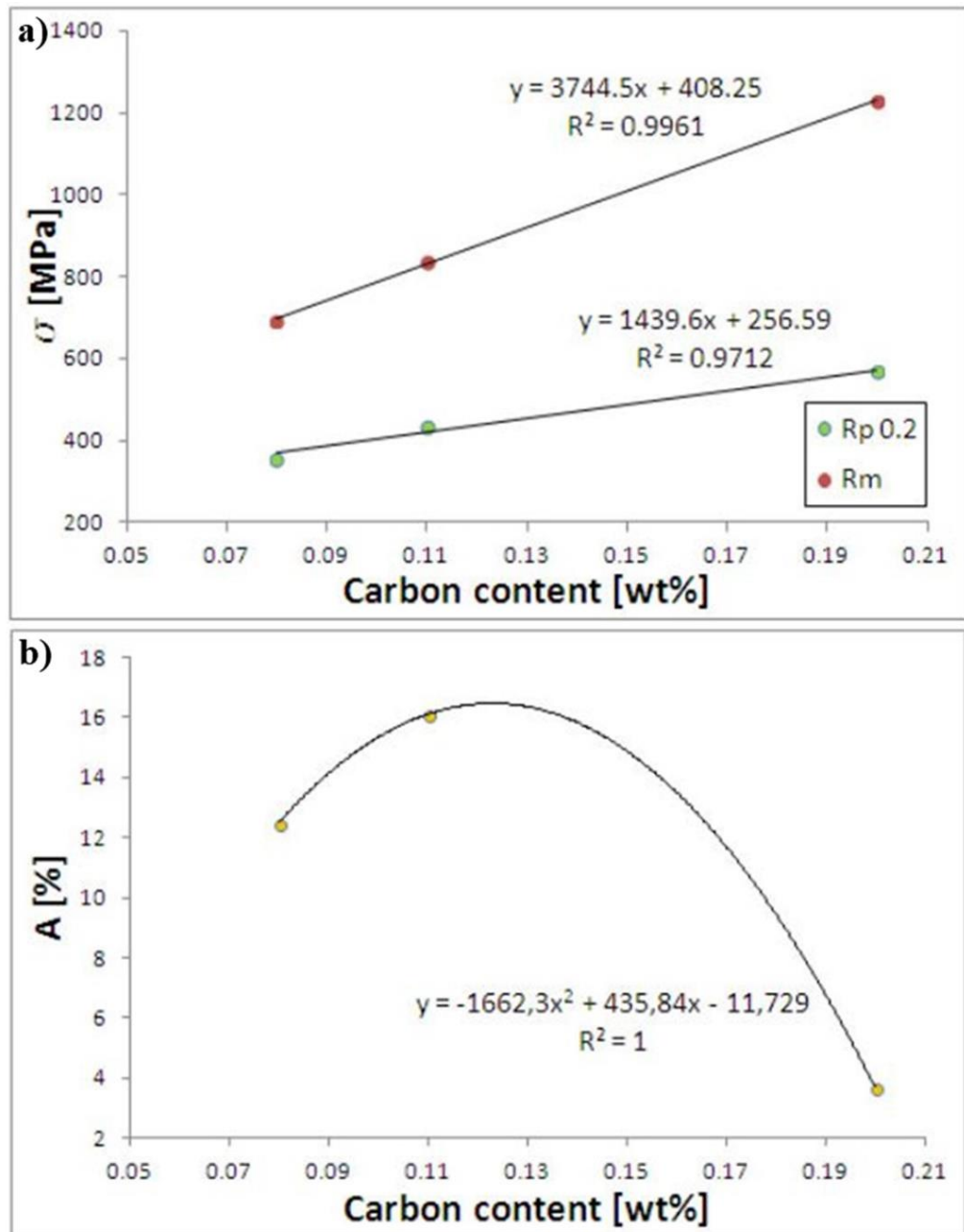
Figure 2. 6: Effect of carbon content on **a)** Tensile strength and **b)** %Area reduction of 50% martensite volume fraction DP steels [61].

2.3.2. Silicon

Silicon addition not only increases the strength of the steels by solid solution strengthening, but also increases the ductility by inducing high work hardening rate through higher dislocation density [62,63]. Silicon and chromium also increases the hardenability of the steel and therefore retards pearlite formation [64]. However, silicon tends to form harmful surface oxides, like Mn_2SiO_4 and SiO_2, which pose sever

problems during hot rolling, coating/galvanizing and welding processes [65]. Due to this silicon is increasingly replaced with aluminium in modern day steel making. Both silicon and chromium are ferrite stabilizers.

2.3.3. Aluminium

Aluminium suppresses cementite formation, and like silicon it also increases A_{c1} to A_{c3} temperature range. This decreases the sensitivity of austenite volume fraction with annealing temperature [66]. However, Al doesn't act as a solid solution strengthener, therefore, replacement of Si with Al decreases the strength of the steel by a substantial amount [67].

2.3.4. Manganese

One way to compensate this loss of solid solution strengthening, is by increasing the amount of manganese content in steel [68]. In DP steels, manganese is generally between 1 to 1.5 wt%, however in recent times up to 3 wt% of Mn is also being used [36]. It is an excellent austenite stabilizer and a good ferrite solid solution strengthener. For every 1 % of Mn an increase in tensile strength of 20-35 MPa occurs [31,69]. Moreover, Mn content in steel increases the amount of austenite present at a given temperature by decreasing the A_{c1} temperature. Therefore, this increases the overall martensite content and thereby increases the overall tensile strength. Additionally, Mn decreases the grain boundary mobility of austenite thereby refining the austenite grains and the subsequent martensite islands [70]. The most important advantage of Mn is in lowering the martensite start temperature. This enables the martensite phase to form at low temperatures, thereby increasing the dislocation density in the surrounding ferrite matrix. This is advantageous because it decreases the yield strength (YS) to tensile strength (TS) ratio [71]. However, with the increase in the solute concentration (especially Mn in DP steels), the chance for solute segregation to occur increases. The effect of this solute segregation on the microstructure evolution of DP steels will be further discussed in section **2.9.3.** In this PhD work, one of the prime focuses is to study the microstructural evolution of DP steels in Mn segregated low carbon steel with respect to process parameters.

2.3.5. Microalloying elements

Along with the above-mentioned elements, DP steels are also alloyed with micro-alloying elements like boron, titanium and vanadium etc. Boron when added in minute quantities (ppm levels) increases the hardenability [72–74] of steels by decreasing the amount of ferrite nucleation on the austenite grain boundaries, thereby, increasing the martensite fraction in the final microstructure [75–77]. There are three main mechanisms which are widely accepted. 1) At high temperatures, solute boron atoms tend to segregate at the austenite grain boundaries and decreases its interfacial energy, thereby decreasing the potential nucleating sites for ferrite grains [78]. 2) The presence of boron decreases the self-diffusion coefficient of iron atoms [79]. So, the consequential decrease in the iron atom jump frequency decreases the diffusion required for ferrite formation, thereby, increasing the hardenability of steels. 3) Boron containing precipitates (Fe_{23} (B, C)$_6$) nucleate coherently at the austenite grain boundaries below 1150 ^{0}C with a parallel cube-cube relation with the adjacent austenite grains [78]. This coherency, between the precipitates and the austenite crystals, drastically decreases the interfacial energy at the grain boundary, therefore, decreasing the ferrite nucleation rate. **Figure 2.7** shows the Secondary-ion mass spectrometry (SIMS) image of austenite grain boundary segregation of boron. In addition to enhancing hardenability of steels, boron is also economically cost-effective [80] and hence is widely used as an alloying element in ultra-high strength steels (UHSS) such as martensitic steels [81], press-hardened boron steels [82], DP steels, and TRIP steels etc.
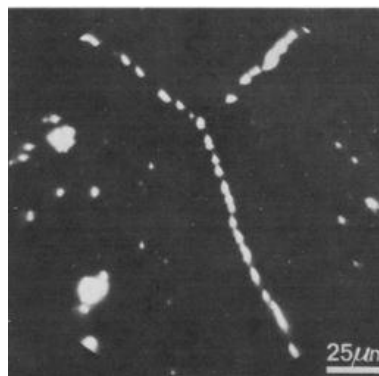
Figure 2. 7: Segregation of boron on prior austenitic grain boundaries, a SIMS image [78].

In DP steels, boron addition decreases the critical cooling rates thereby minimizing the residual stresses in the final microstructure [83]. Moreover, boron is critical in order to achieve a fine dispersion of martensitic islands at practical cooling rates available in the industrial mill equipment [84]. It should also be noted that the addition of boron decreases the percentage of austenite present at a particular inter-critical temperature [85,86]. However, this decrease in austenitic content increases the carbon percentage in it, thereby, increasing its hardenability [87]. Thus, even though the amount of austenite present at a particular inter-critical temperature will be relatively low in boron micro-alloyed steels, more austenite transforms to martensite. Moreover, the influence of cooling rates on the martensite content and its corresponding mechanical properties also decrease with increase in the percentage of boron content [88]. This advantageous effect of boron on hardenability will be effective only if a significant amount of it is still available in the free solute form in the austenitic temperature range [89]. In this regard, other alloying elements like aluminium, titanium and niobium are added to steel to prevent boron reaction with nitrogen to form BN precipitates in steels. Eq.1 shows the stoichometrical relation of these alloying elements required to remove nitrogen from the solid solution [90]. Here unbalance factor represents the chance of reactivity of boron and nitrogen. If unbalance factor is greater than zero than the reaction will not proceed.

$$\text{Unbalance factor} = \frac{14}{48}\,\text{Ti} + \frac{14}{51}\,\text{V} + \frac{14}{93}\,\text{Nb} + \frac{14}{27}\,\text{Al} - \text{N} \geq 0 \dots\dots\dots\dots\dots\text{Eq.1}$$

Vanadium is another element which is extensively added in the AHSS steels for its advantages from precipitates. Vanadium precipitates are known for their ability to act as excellent nucleating agents for intra-granular ferrite which is beneficial for the toughness of the material [91]. The lattice mismatch between $(001)_{VN}$ // $(001)_{\alpha}$ is very small, thereby, enabling the nucleation of ferrite around it [92]. Additionally, the strengthening effect and the toughness improvement induced by the fine dispersion of vanadium carbo-nitrides and grain refinement is the main advantage of this micro-alloy addition [93]. The undissolved precipitates in austenitic temperature range restrict the growth of austenitic grains [94,95], whereas the precipitates which are dissolved at austenitic temperature range, and re-precipitate during cooling are responsible for strengthening of steel [96]. Vanadium carbo-nitrides provide this optimum combination of undissolved and completely dissolved precipitates in the

austenite solid solution. This is because the vanadium carbide (VC) is completely soluble in austenitic temperature range and precipitates only during or after the phase transformation, whereas, the vanadium nitride (VN) is stable even in the austenitic temperature range [97] (also TiN). **Figure 2.8** shows the solubility and the equilibrium stability of various precipitates with respect to their corresponding temperatures. Here it can be seen that VC is soluble and VN is insoluble in the inter-critical region. **Figure 2.9** shows the interphase [98] and random vanadium precipitates [99] extracted on a carbon replica.
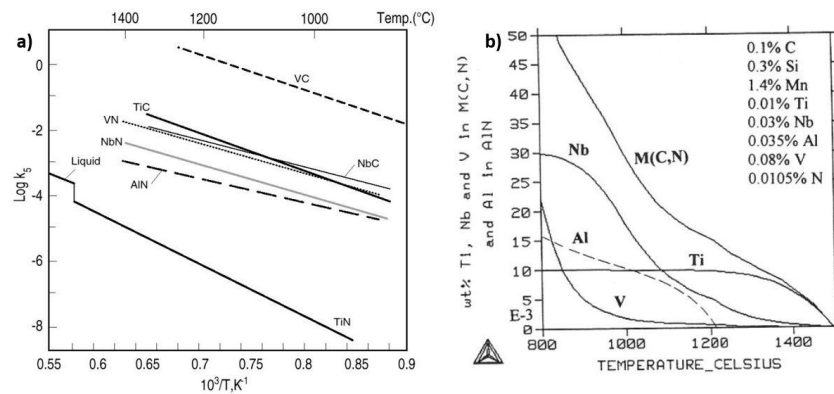
Figure 2. 8: a). Graph representing the solubility of various precipitates corresponding to their respective temperatures b). Precipitation behavior of nitrides and carbo-nitrides of V, Nb, Al, Ti [96].
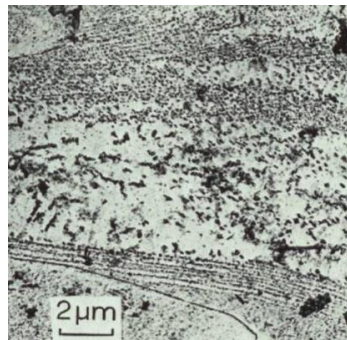
Figure 2. 9: Carbon replica image of interphase and randomly nucleated vanadium carbo-nitrides [99].

During stretch flange forming process, high strength DP steels tend to develop cracks and tears at the sheet edges [100]. These cracks generally initiate between the ferrite and martensite phases due to the large differences in their strengths [101]. One way to decrease this interphase de-cohesion is to minimise the strain incompatibilities between these phases by decreasing their strength differences [102]. In this regard, the

24

selective precipitate strengthening of ferrite induced by fine dispersion of vanadium carbo-nitrides significantly increases the ferrite phase strength, thereby decreasing strain incompatibilities between the phases [103]. The selective precipitation of vanadium carbo-nitrides in ferrite phase is shown in the **Figure 2.10**. In this PhD work vanadium precipitation is briefly studied with respect to the heating rate parameter of the inter-critical annealing step.
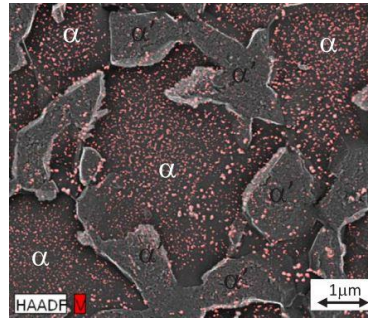
Figure 2. 10: Carbon replica image showing the higher density of vanadium precipitates in the ferrite phase (α) when compared to the martensite phase (ὰ) [103].

During inter-critical annealing, the relative stability of ferrite and austenite is hugely influenced by type and quantity of micro-alloying elements. Ferrite stabilizing elements, increase the A_{e1} temperature by forming a gamma loop in the equilibrium phase diagram. On the contrary, austenite stabilizing elements increase the A_{e1} temperature. **Figure 2.11** shows the influence of alloying elements on the eutectoid temperature. It can be seen that the ferrite stabilizers increased the eutectoid temperature, whereas the austenite stabilizers decreased the eutectoid temperature. **Table 2.1** shows the common alloying elements for ferrite and the austenite stabilizers.
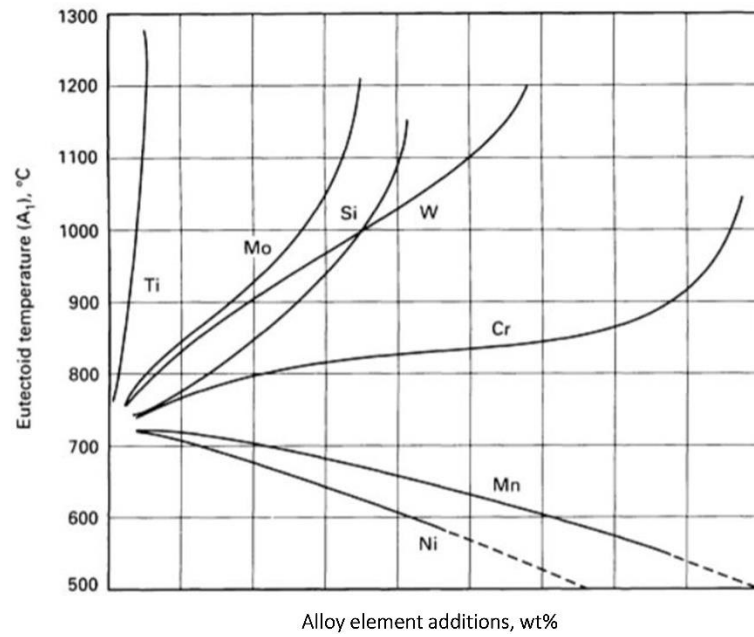
Figure 2. 11: Effect of common alloying elements on the eutectoid temperature.

Table 2. 1: Ferrite and Austenite stabilising elements.

Ferrite stabilizers	Austenite stabilizers
Silicon	Carbon
Aluminium	Manganese
Chromium	Nickel
Vanadium	-
Boron	-

2.4. Effect of inter-critical temperature, soaking time and cooling rate

Annealing in the inter-critical region is a critical step in the manufacturing of not only DP steels but also for other AHSS steels like Quench partitioned steels, TRIP steels, carbide free bainite steels and medium Mn steels [104]. Inter-critical annealing enables the formation of austenite products which are generally not possible with fully austenitic annealing for steels of the same composition. This is because, the carbon concentration in austenite will be substantially higher in the inter-critical temperature range when compared to the austenite above A_{c3} temperature. This higher carbon concentration increases the austenite stability and therefore drastically delays the pearlitic transformation. **Figure 2.12** represents the pseudo-binary equilibrium phase diagram of Fe-C, which schematically shows the enrichment of carbon in the austenite phase with the decrease in the inter-critical temperature [31]. Therefore, the austenite formed at lower inter-critical temperature has higher carbon content and consequentially requires lower cooling rate for martensitic transformation.
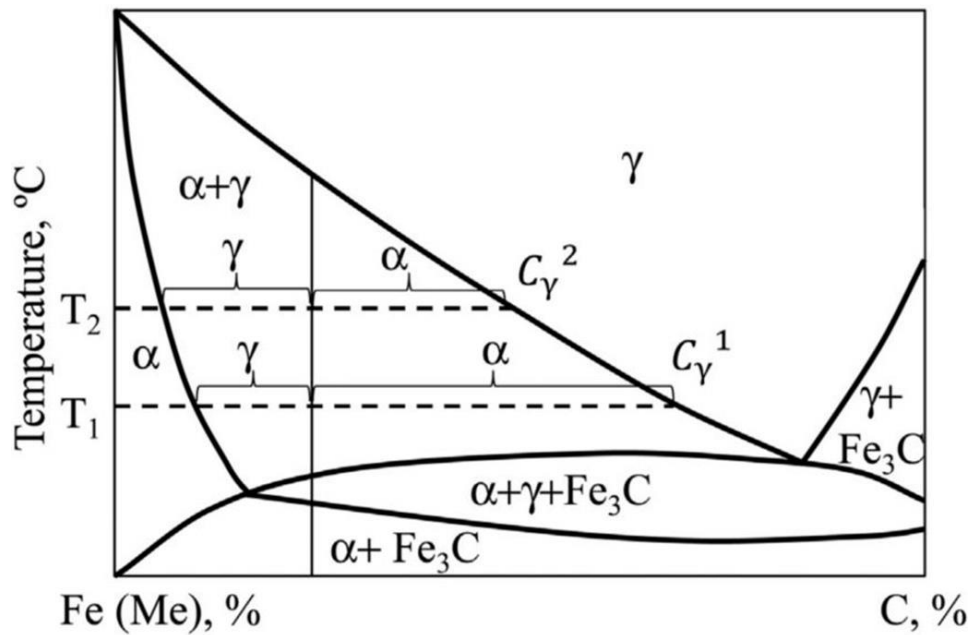
Figure 2. 12: Pseudo-binary Fe-C phase diagram in the inter-critical temperature range [31].

As discussed above, the annealing temperature determines the carbon content of austenite and the critical cooling rate required for martensitic transformation. Additionally with the increase in inter-critical temperature both the austenitic volume

fraction and the formation rate increases. However, the equilibrium austenite formation is generally attained at the lower inter-critical temperatures. **Figure 2.13 a)** shows the increase in austenite volume fraction and formation rate with the temperature for a low carbon steel with 0.12 wt % of carbon [54]. From this figure it can also be seen that the equilibrium austenite fraction is reached for lower inter-critical temperatures for soaking times more than 15 minutes. It should also be noted that the austenite formation rate reached maximum during complete pearlitic dissolution [105]. During cooling, the pre-existing ferrite present in the inter-critical region facilitates epitaxial growth of new ferrite without the nucleation step [106]. The formation of new ferrite also enriches the carbon content in the remaining austenite and therefore promotes martensitic transformation. Therefore, it should be noted that for slower cooling rates the chance of epitaxial ferrite growth increases and consequently the carbon content in the remaining austenite increases. This increases the hardenability of the remaining austenite. This phenomenon slightly decreases the sensitivity of martensite volume fraction with inter-critical annealing temperature. However, at very high cooling rates the chance of epitaxial ferrite growth decreases and therefore the martensite volume fraction will be similar to the volume fraction of austenite at inter-critical temperature [107]. It should be noted that both the increase in inter-critical temperature and the soaking time increases the volume fraction of austenite. If the cooling rate during quenching is above the critical cooling rate, then the increase in austenite fraction also increases the final martensite volume fraction. As martensite being the harder phase, the increase in its volume fraction generally increases the strength and decreases the ductility [108]. However, it is also well reported that the strength of martensite decreases with decrease in the carbon content. During inter-critical annealing, as the volume fraction of austenite increases, the amount of carbon present in it decreases. This in turn decreases the strength of martensite in the final microstructure. This decrease in strength with increase in martensite volume fraction effects the increase in tensile strength. **Figure 2.13 (b, c)** shows the effect of martensite volume fraction on carbon content and tensile strength [109]. It can be clearly seen that even though the increase in martensite volume fraction increases the strength, the simultaneous decrease in the carbon content decreases the strength. It should be noted that the relative strength differences between ferrite and martensite phases effect the final mechanical properties of these steels. As the strength difference between these phases increases, the strain incompatibilities

during deformation increases [36]. This leads to increase in void density at the ferrite-martensite interface which in turn leads to premature fracture. Therefore, it is critical to evaluate the individual strengths of these phases at different intercritical parameters. For this purpose, nano-indentation is generally employed to systematically evaluate the individual strengths of ferrite and martensite phases. For instance Mazaheri et al., evaluated the Nano hardness measurements for ferrite and martensite phase produced at inter-critical temperature of 770 ^{0}C for different soaking times [110]. **Figure 2.14 (a, b)** shows the SEM microstructure images of DP steel annealed for 14 minutes with nano-indents in ferrite and martensite phases respectively. It was found that the nano-hardness values of both ferrite and martensite phase decreased with the increase in the soaking time. Cheng et al., and Hernandez et al, quantitatively showed that the tempering of martensite decreases the strength of both ferrite and martensite phases [111,112]. **Figure 2.14 c)** shows the comparison of nano hardness values of ferrite and martensite phases in tempered and un-tempered state.
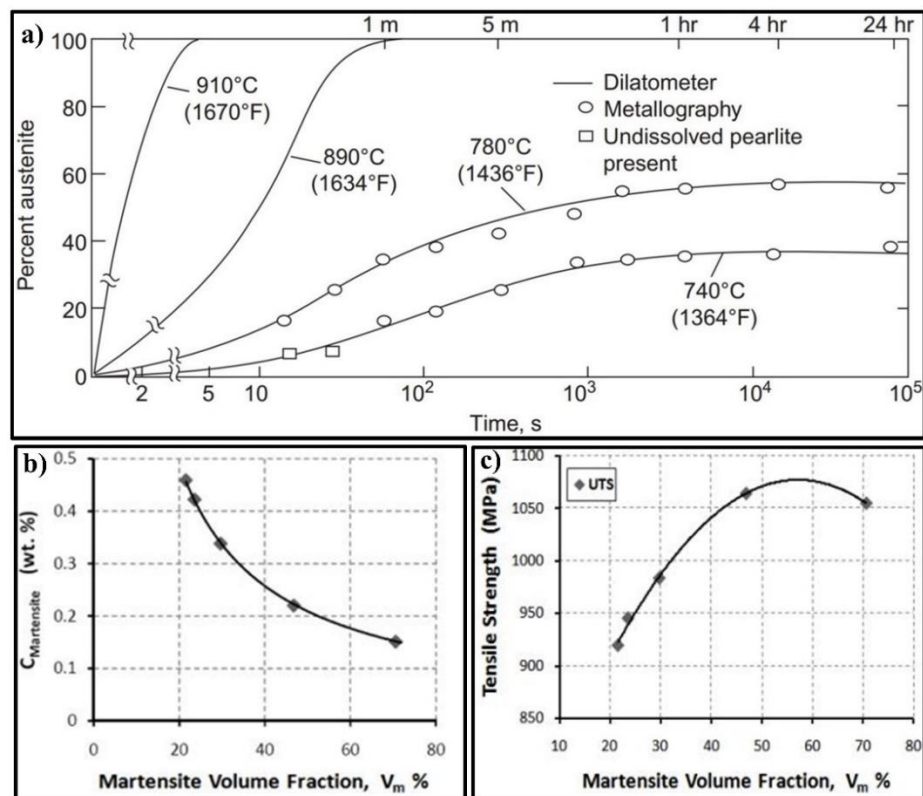
Figure 2. 13: **a)** Austenite volume fraction for different inter-critical temperatures and soaking times for steel with composition of 0.12C-1.5Mn [54], Effect of martensite volume fraction on **b)** carbon content and **c)** ultimate tensile strength [109].
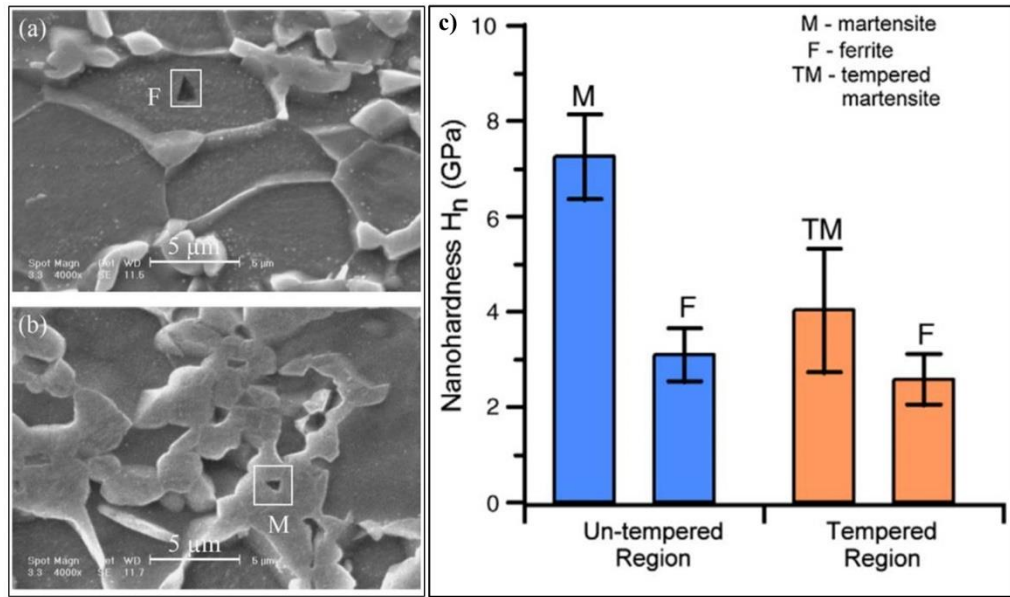
Figure 2. 14 (a, b): SEM microstructural images of DP steel with nano-indents in ferrite and martensite respectively [110]; and **c)**: Comparison of nano-hardness values of ferrite and martensite phases in tempered and un-tempered form [111].

2.5. Effect of rolling on initial microstructure

2.5.1. Effect of hot rolling

Hot rolling is a very important step in the DP steel manufacture, as it reduces the thickness of the slab and also produces the initial microstructure for the annealing process. This is very crucial as the rate of austenite formation is significantly affected by the initial microstructure. It has been reported in the literature that ferrite with a spheroidized carbides microstructure produces the lowest formation rate and martensitic microstructure produces highest formation rate [113,114]. As the austenite phase generally nucleates between ferrite-carbide interfaces the microstructure with larger interfacial area will produce higher kinetics. The coiling temperature and the cooling rate after the last pass in the finishing mill are the key parameters which determine the microstructure after hot rolling. For instance, a high coiling temperature and slow cooling rate of hot rolled strip produces a coarse-lamellar pearlite, whereas, low coiling temperature and fast cooling rate produces martensitic microstructure [113]. It's reported that even after the cold rolling and annealing process, the hot rolled microstructure is inherited by the final DP steel microstructure [115]. As discussed in

30

Section 2.1, the microstructure of DP steel obtained from the hot rolled condition generally contains coarse ferrite grains with martensite islands present at the grain boundaries. **Figure 2.15** shows the microstructure of DP steel obtained from a hot rolled ferrite-pearlite microstructure annealed at 740 ^{0}C with varying soaking times [54]. It can be clearly seen that the austenite is both nucleated and grown along the grain boundaries. However, in the majority of commercial production, the hot rolled material is further cold reduced to lesser thickness and then used as raw material for the CAL process. The microstructure evolution becomes more complicated in the cold rolled steels as other processes like ferrite recovery and recrystallization, and rapid cementite spheroidization will have a profound influence on the austenite formation mechanism and its kinetics. In the next section this will be discussed in more detail.
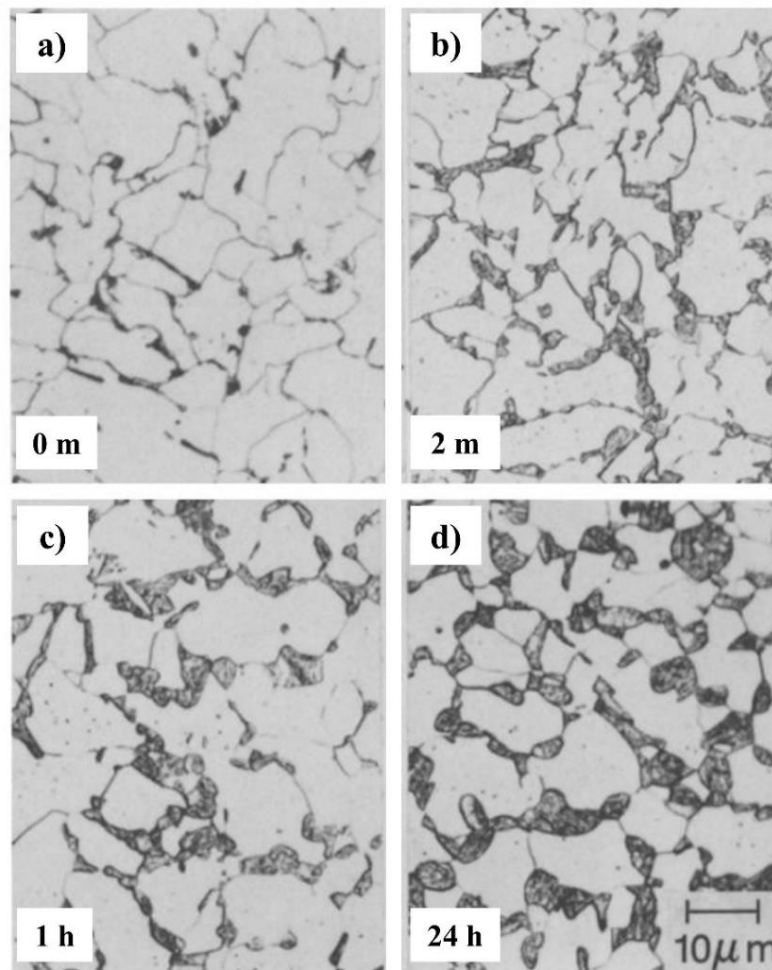
Figure 2. 15: DP steel microstructures obtained from hot rolled ferrite-pearlite microstructure annealed at 740 ^{0}C and different soaking times of a) 0 min, b) 2 min, c) 1 hour, and d) 24 hour respectively [54].

31

2.5.2. Effect of cold rolling

The cold rolling step is employed to further reduce the thickness of the hot-rolled strip. Most importantly this step introduces considerable amount of stored deformation energy into the material. In order to incorporate the overall macroscopic reduction from deformation, the grains at the microscopic level must change their shape. This leads to a huge increase in the grain boundary area. This occurs by continuous entrapment of new mobile dislocations by the existing dislocations [116]. As shown in **Figure 2.16**, the surface area (grain boundary area) of a cubic grain increases by 16.6% for a cold reduction of 50%, 270% for a cold reduction of 90% and so on. Dislocation structures not only form at the grain boundaries but also in the grain interiors. Additionally, new vacancies and interstitial defects are also generated in the grain interiors. The sum of energies of newly created defects such as dislocations, vacancies and interstitials correspond to the stored deformation energy generated during the cold reduction step [42,116]. With the increase in cold reduction, there will be an increase in the defect accumulation and therefore an increase in cold deformed energy. It should be noted that only 1% of the total work done on the material is stored as the deformation energy, and the remaining 99% is dissipated as heat [116]. Along with dislocation accumulation, the cold reduction step also fragments the cementite particles and distribute them along the grain boundaries [117]. Additionally, during deformation the change in the shape of individual grains occurs in such a way that the crystallographic planes rotate along preferred orientations relative to the crystal structure and the applied stress [118]. In summary, the cold rolling step has three main effects on the material:

1. It increases the stored strain energy (increase in dislocation density and residual stresses [119]) in the material which in turn increases the driving force for the recovery and recrystallization process [120].

2. It increases the ferrite grain boundary area by elongating the grains. Along with this, the grain boundaries and grain interiors are clustered with fragmented cementite particles [59,117].

3. Increase in preferential orientation or texture with the increase in cold reduction ratio [118].

$Volume = 1000\,\mu m^3$
$Surface\ Area = 600\,\mu m^2$
$10\,\mu m \ \times \ 10\,\mu m \ \times \ 10\,\mu m$

50 % Reduction

$Volume = 1000\,\mu m^3$
$Surface\ Area = 700\,\mu m^2$ **Surface area increase=16.6%**

$5\,\mu m \ \times \ 20\,\mu m \times \ 10\,\mu m$

90 % Reduction

$Volume = 1000\,\mu m^3$ **Surface area increase=270%**
$Surface\ Area = 2220\,\mu m^2$

$1\,\mu m \ \times \ 100\,\mu m \ \times \ 10\,\mu m$
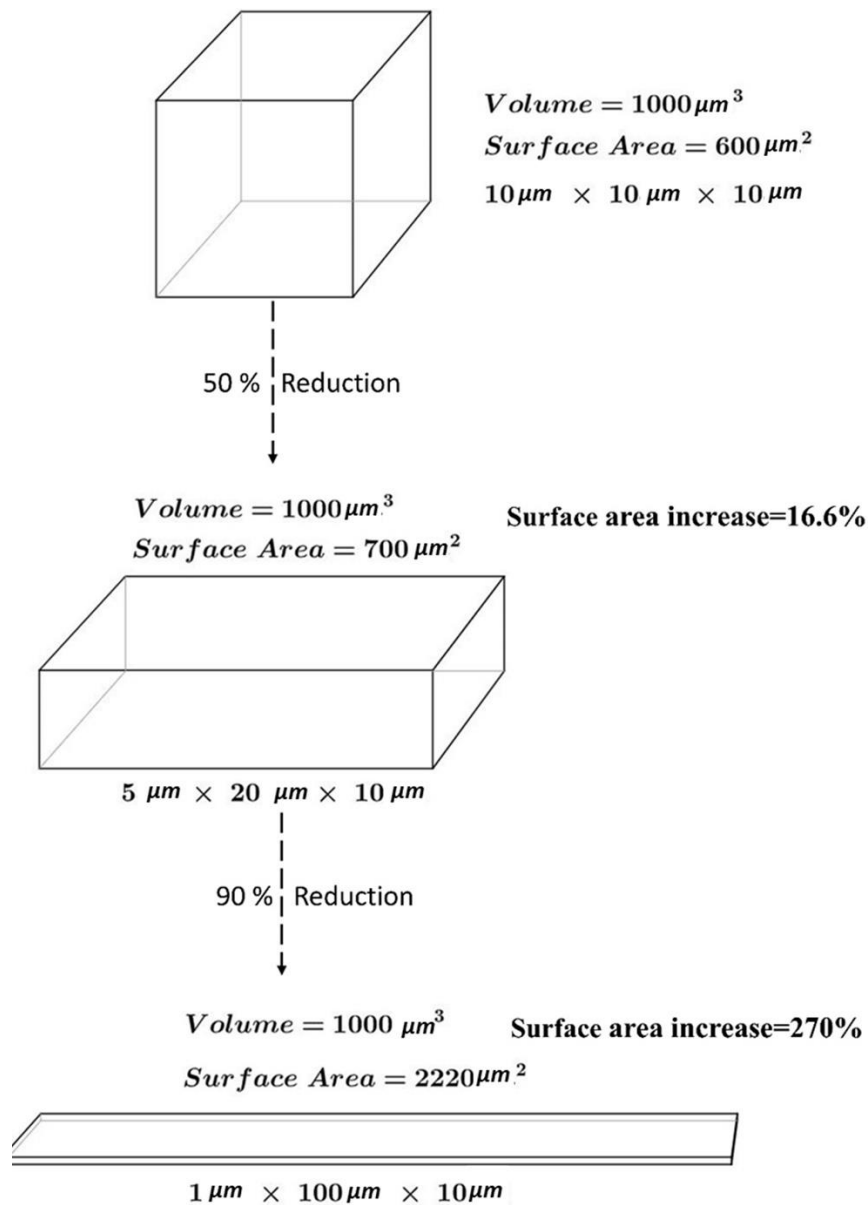
Figure 2. 16: Schematic representation of increase in surface area with plane strain deformation of a cubic grain as observed during cold rolling.

2.6. Texture evolution

Polycrystalline materials having a preferred crystallographic orientation are said to be having texture [121]. Depending upon the number of grains/crystals oriented in a non-random preferred orientation, the sample is categorised as weak, moderate and strong texture. A single crystal material by definition is an extreme example of a complete

texture. However, in polycrystalline materials, the preferred orientation of grain/crystals is generally achieved during the deformation process. During deformation process such as rolling, the preferred slip systems with maximum resolved stress/Schmid factor glide and also rotate because of the force direction constraint causing the grains to align in a preferred orientation thereby producing texture [122,123]. **Figure 2.17 (a, b, and c)** shows the mechanism of texture formation during a typical uniaxial loading condition. When compared to no force constraint condition (**Figure 2.17 b**), the gliding slip systems rotate to compensate the force constraint in **Figure 2.17 c,** generating texture in a polycrystalline material [122].
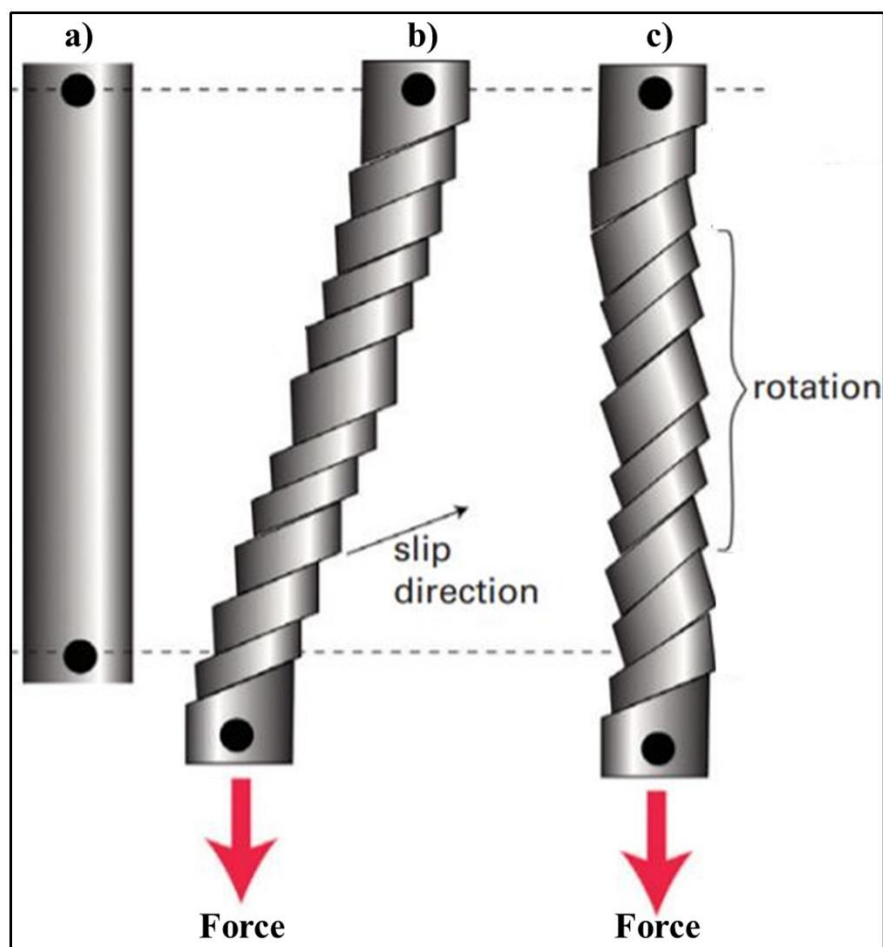
Figure 2. 17 : Comparison of slip plane glide and rotation: a) before loading, (b, c) during loading b) without lateral force constraint and c) with lateral force constraint [122].

Both hot rolling and cold rolling processes induce texture into the microstructure of the strip products. The texture of a given microstructure can be best described using

the orientation distribution functions (ODF). **Figure 2.18** shows the representation of ODF maps for BCC materials with the corresponding texture fibers. In hot rolling the texture evolution is affected by temperature during rolling, recrystallization of austenite, and decomposition of austenite during cooling. During cold rolling the texture evolution is completely dependent on the final thickness of the product. When compared to cold rolled material, the texture in hot rolled steels have through thickness inhomogeneity [43,124–129]. **Figure 2.19** shows the texture inhomogeneities between surface and centre of low carbon hot rolled steel using the α, γ, and ε fibres in the reduced Euler space [126]. Perlovich et al., reported that in Fe-0.5C-1Cr-2Ni-1Mo hot rolled steels, the surface showed texture components of {112}<111>, {110}<112>, whereas centre showed components of {100}<110>, {112}<110>, and {554}<225>. Similarly, Park et al., reported texture inhomogeneity in Ti/Nb bearing interstitial free steel with centre having {001}<110> as main component and surface having {225}<554> as main component. Raabe et al., reported that in hot rolled austenitic stainless steels, the centre contained cold rolled type of texture with β-fibre accompanied by a cubic orientation and the surface contained shear texture with {001}<110> and {112}<110> components.
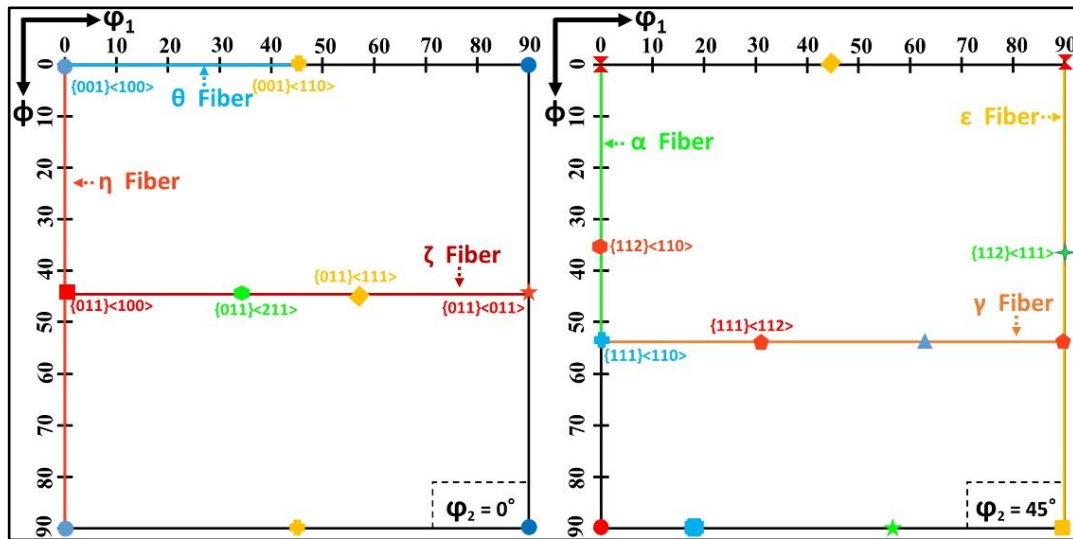
Figure 2. 18: Schematic representation of ODF maps at $\varphi_2 = 0°$ and $\varphi_2 = 45°$ with the main BCC texture fibers.
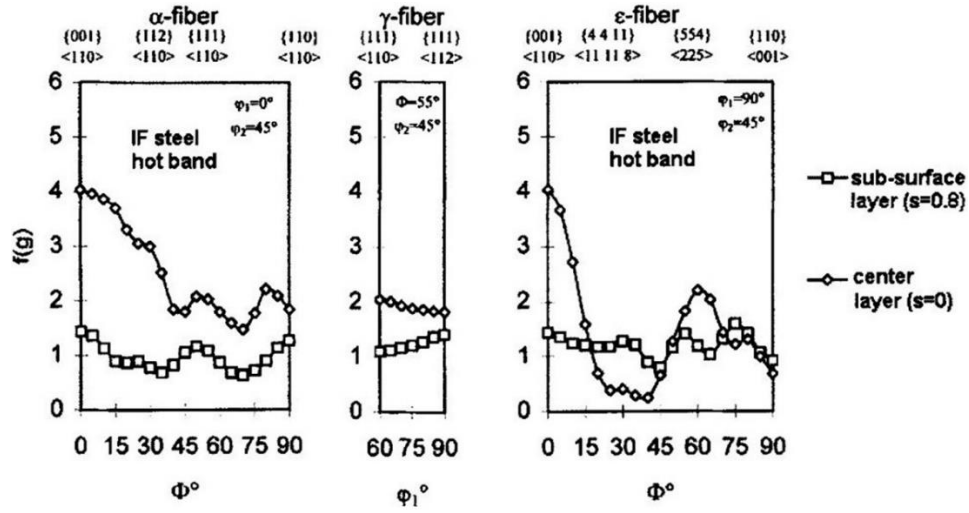
Figure 2. 19: Through thickness texture inhomogeneity in hot rolled steels. [126]

The difference between the surface and centre texture in the hot rolled steels has mainly been attributed to the rapid cooling happening at the surface during rolling deformation and the inhomogeneity of the strains developed across the thickness [127]. This can potentially change the phases present at the surface and centre during the deformation process leading to texture inhomogeneity. The friction between the rolls and the surface of the sheet produce large shear strains at the surface [124,126]. Perlovich et al., also proposed that the deformation mechanism at the surface follows collective dislocation climb under the condition of increased interstitial content [130]. These thermal and mechanical differences between surface and centre of the sheet thickness during hot rolling cause texture inhomogeneity in hot rolled strips. **Figure 2.20 (a, b)** shows the simulated through-thickness (s=1 is surface, s=0 is centre) distribution of temperature and shear strain tensor (ε_{xy}) respectively in hot rolled ferritic steels [124]. It can be seen that there is a huge difference in temperature between the surface and the centre. Moreover, the shear strain is found to be maximum at the surface. It should be noted that the final ferrite texture is inherited from the austenite texture developed during high temperature deformation. Therefore, the texture inhomogeneity developed in austenite during hot rolling is also seen in the ferrite in the final microstructure. The main orientation relations proposed for steels are Bain ($\{001\}_\gamma \| \{001\}_\alpha$), Kurdjumov-Sachs ($\{111\}_\gamma \| \{011\}_\alpha$), Nishiyama-Wassermann ($\{112\}_\gamma \| \{011\}_\alpha$) [43]. In cold rolling, as there is no role of temperature and the plain strain condition is generally achieved throughout the thickness. Raabe et

al., and Peranio et al., reported a through thickness texture inhomogeneity and differences in ferrite-pearlite spatial distribution in both hot rolled and cold rolled ferrite pearlite steels [126,131]. A banded ferrite-pearlite morphology with strong α fibre texture ({001} <1$\bar{1}$0> and {112} <1$\bar{1}$0>) at the centre of the thickness and a heterogeneous ferrite-pearlite distribution with week texture at the surface of the sheet was observed in rolled ferrite-pearlite sheets [118]. Moreover, when compared to the centre of the sheet, surface was reported to have a larger dislocation density due to additional shear stresses involved during deformation. It was also observed that the ferrite-pearlite banded structure at centre will restrict the grain growth to two dimensions only. Due to the existence of texture inhomogeneity and differences in the ferrite pearlite morphology along the rolled sheet, the final DP steel microstructure can inherit a through thickness anisotropy. This microstructural anisotropy in terms of distribution, and morphology between surface and centre of the DP steel sheet is shown in **Figure 2.21** [118]**.**

Figure 2. 20: (a) Temperature, and **b) Shear strain tensor distribution in hot rolled ferritic steels** [124]**.**
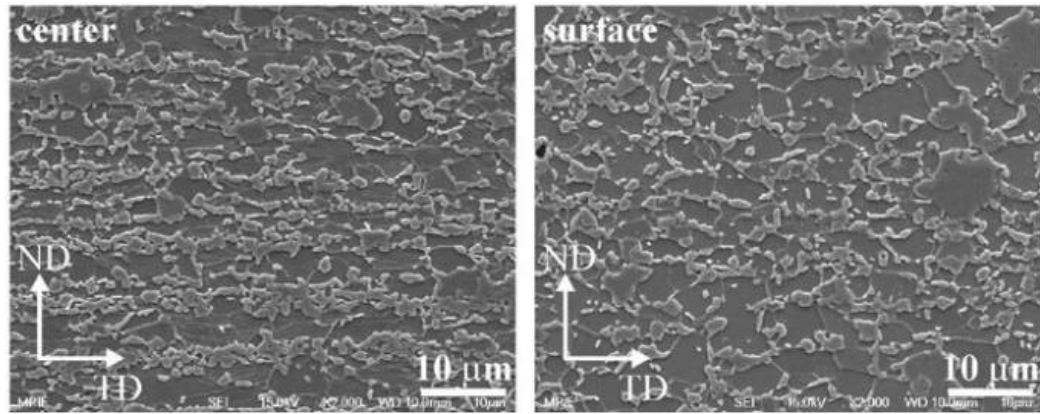
Figure 2. 21: Microstructural differences at centre and surface of the sheet annealed in IA range [118].

2.7. Recovery and Recrystallization

During the heating step in CAL, the cold rolled material generally undergoes three main processes before austenite start temperature (A_{c1}): 1) Recovery, 2) Recrystallization and 3) Cementite spheroidization [132]. The release of stored deformation energy is the driving force for both recovery and recrystallization processes [133]. Recovery occurs by the annihilation of vacancies and interstitials, and rearrangement of dislocations [134].The rearrangements of dislocations occur due to the tensile and compressive stress fields associated with bottom and top of the dislocation line. Due to this the opposite sign dislocations attract and the same sign dislocations repel leading to the formation of low angle boundaries or sub grains. It should be noted that the annihilation of point defects during recovery process will not cause significant decrease in hardness. With the increase in temperature and time, growth of sub grains occur through coalescence. This whole process decreases the individual energies of dislocations and hence the overall stored deformation energy. **Figure 2.22** shows the schematic representation of various stages in recovery process [133].

(a) Dislocation tangles

(b) Cell formation

(c) Annihilation of dislocations within cells

(d) Subgrain formation

(e) Subgrain growth
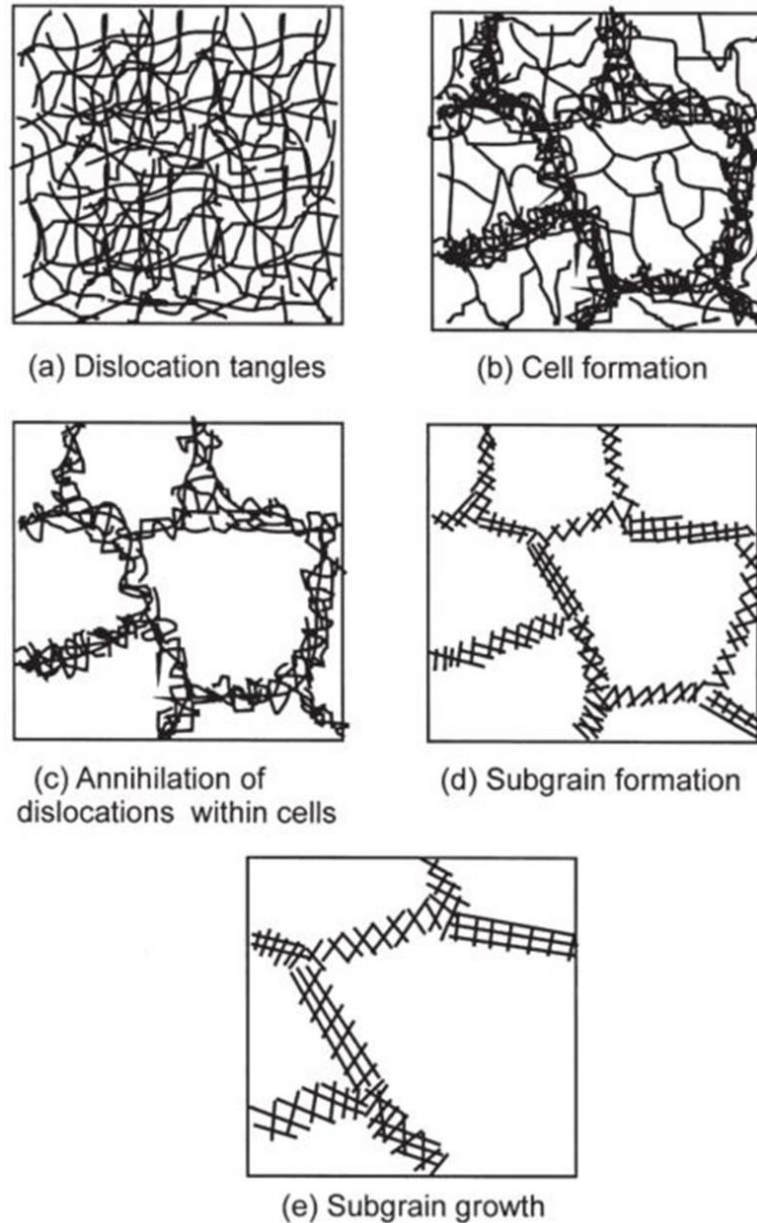
Figure 2. 22: Schematic representation of various stages in recovery process [133].

Recrystallization process is a thermally activated process where new strain free grains of same phase are nucleated and grown in the cold deformed material. The newly formed grains decrease the stored deformation energy by consuming the deformed matrix [135,136]. Therefore, the recrystallization kinetics increases with the increase in cold reduction percentage. Moreover, with the increase in temperature the time required to get fully recrystallized microstructure decreases. **Figure 2.23** shows an increase in recrystallization kinetics with increase in temperature in a 50% cold reduced Fe-C-Mn steel [137]. It should also be noted that the progress of recovery process decreases the stored deformation energy and thereby decreases the driving

force for the progress of recrystallization process. The kinetics of recrystallization process generally follows the sigmoidal curve which is typical to the transformation following nucleation and growth phenomenon. Here the rate of transformation is slow during the initial and final periods, but rapid during the intermediate period [138]. The slow kinetics at the initial period can be attributed to the time required for the new nuclei to form and grow. During the end of the transformation the slower rate can be attributed to the impingement of the growing grains and the diminishing parent phase.

The recrystallization kinetics is best described by Johnson–Mehl–Avrami–Kolmogorov (JMAK) model. The JMAK model assumes that the nucleation occurs randomly and the growth rate is uniform in all directions and is unaffected by the extent of transformation. This is shown below in **equation 2.1** and **2.2**. Here X represents the recrystallization fraction, t represents time, Q represents activation energy and T represents absolute temperature. This model explains the isothermal phase transformation in the solids. It was first developed by Kolmogorov in the year 1937 [139] and was further studied by Avrami [140] and Johnson–Mehl [141] in the year 1939. This model assumes that the nucleation occurs randomly throughout the material. Moreover, it also assumes that the growth rate is uniform in all directions and is unaffected by the extent of transformation. The linearized forms of **Eq 2.1** are used to calculate the JMAK constants. It is also critical to calculate the activation energy (Q) required for the progress of the reaction. This can indicate the retardation effect on the recrystallization process induced by the addition of solute atoms [132]. As shown in **Eq 2.3**, activation energy (Q) can be calculated by applying logarithm on both sides of the **Eq 2.2**. Further rearrangement gives the equation to calculate the Q value as shown in **Eq 2.4**.

$$X = 1 - exp^{-bt^n}$$ ....**Eq. 2.1**

$$b = b_0 exp^{-Q/RT}$$ ....**Eq. 2.2**

$$\ln b = \ln b_0 - \frac{Q}{RT}$$ ....**Eq. 2.3**

$$\text{Activation energy } Q = \left[\frac{(\ln b_1 - \ln b_2)}{\left(\frac{1}{RT_2} - \frac{1}{RT_1}\right)} \right]$$ ....**Eq. 2.4**

Here T_1 and T_2 represents the isothermal temperatures used to calculate the recrystallization kinetics, and ln b_1 and ln b_2 represents the corresponding values from the **Eq. 2.1**
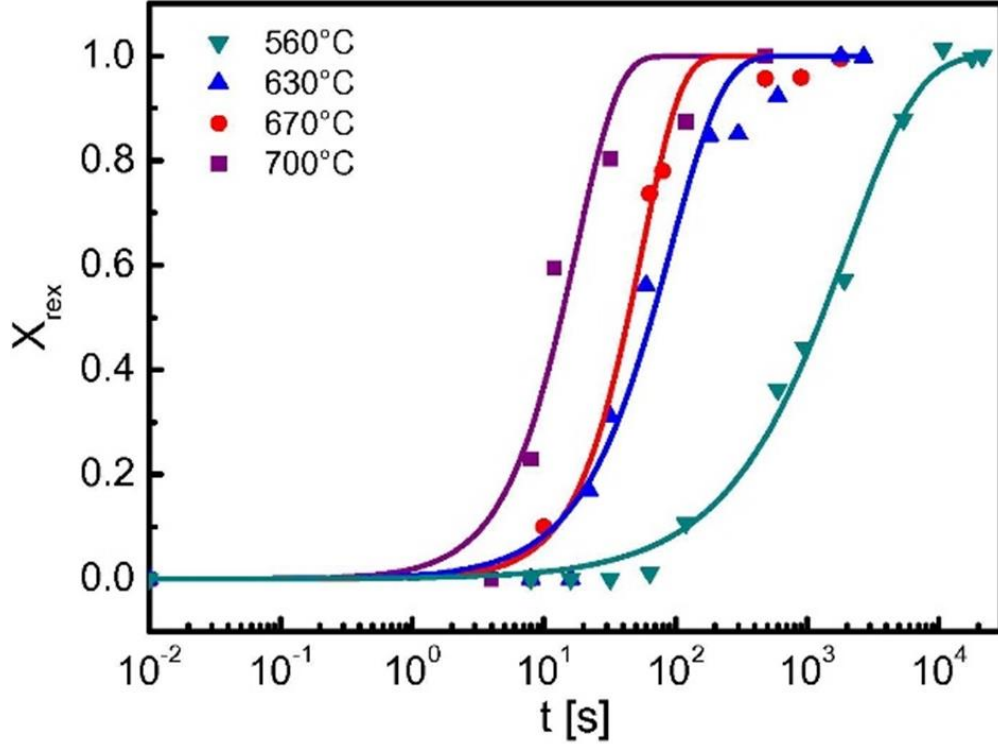
Figure 2. 23: Recrystallization kinetics of 50% cold reduced Fe-C-Mn steel at four different temperatures (560 ^{0}C, 630 ^{0}C, 670 ^{0}C and 700 ^{0}C) [137].

2.8. Cementite Spheroidization

Along with recrystallization process, cementite spheroidization is the other high temperature mechanism which occurs during the heating step of cold deformed material. Cementite spheroidization also occurs in hot rolled material, but, takes hundreds of hours to complete [142]. This process takes place very rapidly in cold rolled material, for instance within 30 minutes in a 50% cold reduced 0.08C-1.45Mn steel [117]. This is attributed to the decrease in interfacial energy of fragmented cementite particles and enhanced carbon diffusion through dislocations in cold deformed material. Many studies have reported that in a fully recrystallized and spheroidized microstructure, austenite nucleates and grows along the ferrite-ferrite boundaries [60,117]. Granbom et al., proposed that the spheroidized cementite

particles at the grain boundaries will be more susceptible for austenite nucleation than the cementite particles in the grain interiors [42]. The cementite particles inside the grains dissolve through a rapid carbon diffusion towards the grain boundaries thereby enhancing the growth of austenite. A step-wise schematic representation of this mechanism proposed by Granbom et al., is shown in **Figure 2.24** [42]**.** Here austenite nucleates first at the grain boundaries where cementite particles are present. Later the growth of this austenite nuclei happens by simultaneous dissolution of cementite particles present in the grain interiors and the carbon diffusion towards the austenite nuclei.
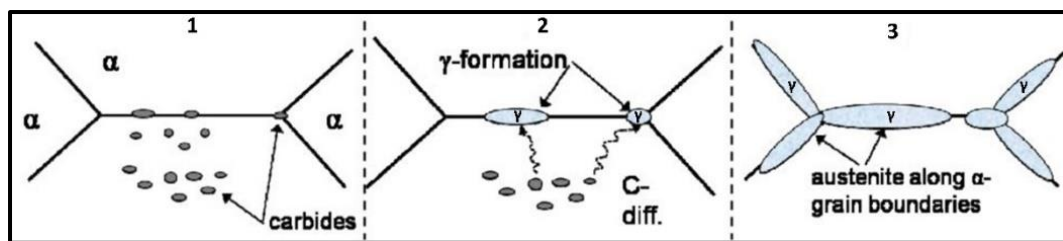
Figure 2. 24: A stepwise austenite formation mechanism in a fully recrystallized and cementite spheroidized microstructure [42].

Teixeira et al., also studied the effect of cementite particles, both isolated cementite and pearlite cementite, on the austenite formation and the subsequent DP steel microstructure [143]. In this study, the microstructure contained 36 % of carbon in isolated cementite particles and the remaining in the pearlite lamella. **Figure 2.24 (a)** shows the 60 % cold rolled microstructure with isolated cementite particles and pearlite lamella. Unlike, Granbom et al., study the majority of isolated cementite particles are aligned along the rolling direction and are very close to the ferrite grain boundaries. **Figure 2.25 (b)** shows the corresponding inter-critically annealed DP steel microstructure. It can be seen that the austenite nucleated initially at the isolated cementite particles (yellow arrow). It has been concluded that the austenite preferentially nucleates at the isolated cementite particles near the grain boundaries followed by the pearlite colonies.

Conventionally during the heating step of DP steel manufacture, ferrite recovery, recrystallization and cementite spheroidization processes are completed or near to completion before the onset of austenite formation. However, due to the increase in alloy content and with the increase in heating rate during the heating step, these high

temperature mechanisms shift to austenite formation region [36]. In the following section, the effect of this shift on austenite formation will be discussed.
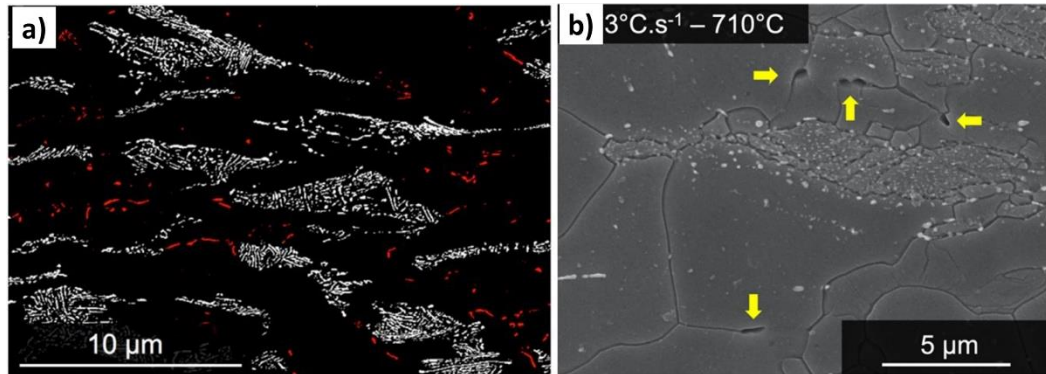
Figure 2. 25: (a) SEM image of 60 % cold rolled low carbon steel with isolated cementite particles (red) and fragmented pearlite colonies (white), and (b) SEM image of inter-critically annealed (3 ^{0}C/s, and 710 ^{0}C) DP steel microstructure with austenite nuclei (yellow arrow).

2.9. Austenite formation

2.9.1. Heating rates employed

As discussed in **Section 2.1**, austenite formation during the heating stage of CAL is the most crucial step in the DP steel manufacture. This is because both the microstructural features and the mechanical properties of DP steels are highly influenced by the composition, distribution, morphology and volume fraction of the parent austenite phase. Other high temperature mechanisms such as ferrite recovery, ferrite recrystallization, grain growth and cementite spheroidization also have profound effect on the microstructural evolution and generally these processes precede austenite formation step [117,144]. However, with the continuous increase in demand to produce high strength light-weight materials, the addition of high amounts of precipitate forming elements (Ti, V and Nb etc.) and substitutional alloying elements (Mn, Cr, and Al etc.) is becoming a common practice in the modern day industries [103,145–148]. However, with the increase in solute concentration, the kinetics of ferrite recrystallization and grain growth becomes sluggish. This is because of the decrease in grain boundary mobility due to solute drag effect and/or precipitate

pinning action [132,145]. This sluggish kinetics is mostly evident in the recrystallization process and can be experimentally identified by an increase in the recrystallization start temperature and/or by the increase in the activation energy (Q). For instance, Vitesh et al., found that an increase in Mn concentration by 2 wt% increased the recrystallization start temperature by 50 ^{0}C [149]. Similarly, Granbom et al., reported that the addition of 0.015 wt% Nb increases the recrystallization start temperature by 20 ^{0}C [150]. Therefore, with the increase in solute concentration, ferrite recrystallization become sluggish and its completion could be delayed until the onset of austenite formation. Moreover, recrystallization being a diffusion driven process, its kinetics is not only dependent on the temperature, but also on the time given at that particular temperature [151]. Therefore, with a slight increase in the heating rate employed, the recrystallization percentage at a given temperature will be decreased. On the other hand, significant research is being done to introduce ultrafast annealing into the conventional annealing lines [152–154]. This increased interest in employing high heating rates is due to its potential in increasing the energy efficiency of the manufacturing process by decreasing the furnace length of the CAL [152]. One of the major consequences of employing high heating rates is the availability of limited time for the progress of ferrite recrystallization and cementite spheroidization processes [37,153]. Due to this, these processes will not be completed before the start of austenite formation. Therefore, the synergetic effect of increasing alloying content and heating rate allow high temperature processes to happen simultaneously above A_{c1} temperature [36].

In the last decade, the effect of this simultaneous happening of ferrite recrystallization and austenite formation processes on the microstructural evolution of DP steels was extensively studied [49,132,145,155–161]. More specifically, with the introduction of the complex interplay between the high-temperature processes, the prime focus was to understand the change in austenite formation mechanism. The researchers have achieved the overlap of these processes, by retarding the recrystallization process by employing very high heating rates during the heating step of CAL. **Table 2.2** shows the wide range of heating rates employed in the literature with corresponding alloy content, initial microstructures and cold reductions. For instance, Huang et al., employed a heating rate of 100 ^{0}C/s on a 50% cold reduced ferrite-pearlite steel with a composition of Fe-0.06C-1.86Mn-0.155Mo [132]. Similarly, Azizi-Alizamini et al.,

conducted heat treatment experiments on 80% cold-rolled ferrite pearlite steel with a heating rate of 900 ^{0}C/s [49]. In their subsequent study, Azizi-Alizamini et al., employed 50 ^{0}C/s and 300 ^{0}C/s on two different steels with martensite and ferrite-carbide aggregate microstructures [155]. Massardier et al., used a very high rate of 1000 ^{0}C/s on 75% cold reduced low carbon aluminium killed steel [156,157]. Kulakov et al., employed a heating rate of 100 ^{0}C/s on three different steels having ferrite–pearlite, ferrite–bainite–pearlite and martensite microstructures [158]. Similarly, Chbihi et al., used a heating rate of 100 ^{0}C/s on Fe-0.15C-1.48Mn steel with a banded ferrite-pearlite microstructure [159]. De Knijf et al., used very high heating rates of 500 and 1000 ^{0}C/s on hot rolled and 80% cold rolled reduced pearlitic steels [160]. Similarly, Philippot et al., and Bellavoine et al., employed 10 ^{0}C/s for 50% cold reduced micro-alloyed steels with ferrite-martensite microstructure [145,161].

Table 2. 2: Typical heating rates employed in literature with corresponding alloy content, initial microstructure and cold reduction.

S.No.	Reference	Alloy content	Initial microstructure	Cold reduction % (Thickness)	Heating rate employed
1	Huang et al.,	Fe - 0.06C - 1.86Mn - 0.155Mo	Ferrite-Pearlite microstructure	50% (1.5 mm)	100 ^{0}C/s
2	Azizi-Alizamini et al.,	Fe - 0.17C - 0.74Mn	Ferrite-Pearlite microstructure	80% (1.8 mm)	900 ^{0}C/s
3	Massardier et al.,	Fe - 0.06C - 0.3Mn - 0.05Al - 0.005N	Ferrite-coarse intragranular	75% (0.6 mm)	1000 ^{0}C/s

			Pearlite microstructure		
4	Kulakov et al.,	Fe - 0.105C - 1.85Mn - 0.15Si - 0.34 Cr	Ferrite–Pearlite, Ferrite–Bainite–Pearlite and Martensite microstructures	50% (1.8 mm)	100 ^{0}C/s
5	Chbihi et al.,	Fe - 0.15C - 1.48Mn	Banded Ferrite-Pearlite microstructure	75% (0.7 mm)	100 ^{0}C/s
6	Azizi-Alizamini et al.,	Fe - 0.17C - 0.74Mn - 0.012Si - 0.04 Al	Martensite and Ferrite-Carbide aggregate microstructures	80% (1.8 mm)	50 ^{0}C/s and 300 ^{0}C/s
7	Bellavoine et al.,	Fe - 0.075C - 2.5Mn - 0.6(Cr + Si) - 0.025to0.047Nb - 0.026to0.04Ti	Ferrite-Martensite microstructure	50% (1.25 mm)	10 ^{0}C/s
8	De Knijf et al.,	Fe - 0.25C – 1.5Si – 3Mn	Pearlitic microstructure	80% (0.5 mm)	500 and 1000 ^{0}C/s

9	Philippot et al.,	Fe - 0.08C - 2.5Mn - 0.7(Cr + Si + Mo) - 0.05 (Ti + Nb)	Ferrite-Martensite microstructure	50% (1.4 mm)	10 ^{0}C/s
10	Petrov et al.,	Fe - 0.11C - 1.26Si - 2.07Mn - 0.015P	Ferrite-Pearlite microstructure	75% (1 mm)	140 to 1500 ^{0}C/s

These research works used a wide range of high heating rates and produced very interesting results by allowing the complex interplay between ferrite recrystallization and austenite formation. However, in these studies, the heating rates employed are inconsistent and mostly seem arbitrary (10, 50, 100, 300, 500, 900 and 1000 ^{0}C/s). The reason behind this could be because that the sole aim of the researchers was to achieve a maximum amount of overlap by choosing heating rates as high as possible in the available heat treatment furnaces. However, it should be noted that the progress of recrystallization will be different for different heating rates [159]. In other words, the amount of recrystallization to be completed after the onset of austenite formation will be different for different heating rates. Therefore, the wide range of heating rates makes it difficult to systematically compare the microstructural evolution in all these studies. Along with the heating rate, the extent of overlap will also be dependent on the composition, initial microstructure, and the percentage of cold reduction [36]. For instance, with the increase in solute concentration the recrystallization kinetics decreases and therefore its overlap with austenite formation increases [162]. On the other hand, recrystallization kinetics increases with the increase in cold reduction percentage and therefore, can decrease the percentage of overlap [135]. Therefore, it is critical to achieve similar percentages of overlap in these wide ranges of materials to facilitate a systematic comparison of microstructural evolution for various initial microstructures, cold reductions and alloying content. To achieve the same percentage of overlap, different materials will require different heating rates. Therefore, instead of randomly choosing high heating rates, it is critical to systematically select the heating rates according to the desired amount of overlap to be achieved. Therefore,

one of the major aims of this study is to develop a method to generate heating rates to produce a predefined amount of overlap for a given steel.

2.9.2. Effect of Overlap on austenite formation

The study of employing high heating rates for understanding the influence of concurrent high temperature mechanisms on microstructural evolution gave many conflicting results. Some research studies reported that with the increase in the coupling of ferrite recrystallization and austenite formation a higher amount of finely distributed austenite is produced during the inter-critical annealing step [155,160,163]. There is also considerable amount of literature showing that with the increase in overlap, the final microstructure transforms more into a banded martensite microstructure [132,164–166]. For instance, Petrov et al., conducted high heating rate inter-critical annealing experiments on 75 % cold reduced Fe-0.11C-1.26Si-2.07Mn-0.015P steel with ferrite-pearlite initial microstructure [163]. It was found that with the increase in heating rate from 140 ^{0}C/s to 1500 ^{0}C/s, the grain size of both ferrite and martensite have significantly refined (5 μm to 1 μm). Similarly, De Knijf et al., reported that increase in the heating rate from 10 ^{0}C/s to 1000 ^{0}C/s decreased the prior austenitic grain size from 3.8 μm to 1.7 μm [160]. Azizi-Alizamini et al., also achieved ultra-fine dual phase steel microstructure by annealing ferrite-carbide initial microstructure at a heating rates of 1 ^{0}C/s, 50 ^{0}C/s, and 300 ^{0}C/s [155]. **Figure 2.26 (a, b, and c)** shows the SEM micrographs of dual phase steels produced by inter-critical annealing at 750 ^{0}C/ for 10 s at heating rates of 1 ^{0}C/s, 50 ^{0}C/s, and 300 ^{0}C/s. It can be seen that with increase in heating rate the morphology of both ferrite and austenite (now martensite) transformed more into equiaxed morphology. Moreover, it can be seen that the ferrite grain size has significantly refined with increase in heating rate. The ferrite grain size was reported to decrease from 8 μm at 1 ^{0}C/s to 1.2 μm at 300 ^{0}C/s. This grain refinement phenomenon is attributed to reduction in grain growth kinetics and increase in the austenite nucleation density (1.5 x 10^{10} m^{-2} to 1.4x10^{11} m^{-2}) at higher heating rates. Azizi-Alizamini et al., proposed that at higher heating rates, the increase in nucleation density is achieved due to higher driving force, caused by increased superheat [49]. Similarly, Li et al., and Andrade-Carozzo et al., proposed that at higher heating rates, austenite will have higher potential nucleating sites. [152,167]. However, it was postulated that increase in the nucleating sites is due to the

presence of higher fraction of recovered ferrite in the microstructure during the soaking step of inter-critical annealing process. On the contrary, Mohanty et al., proposed that an increase in heating rate will cause a decrease in nucleation density [168]. According to this study, the growth of austenite is dominating mechanism at higher heating rates, whereas the nucleation of austenite is dominating mechanism at lower heating rates.
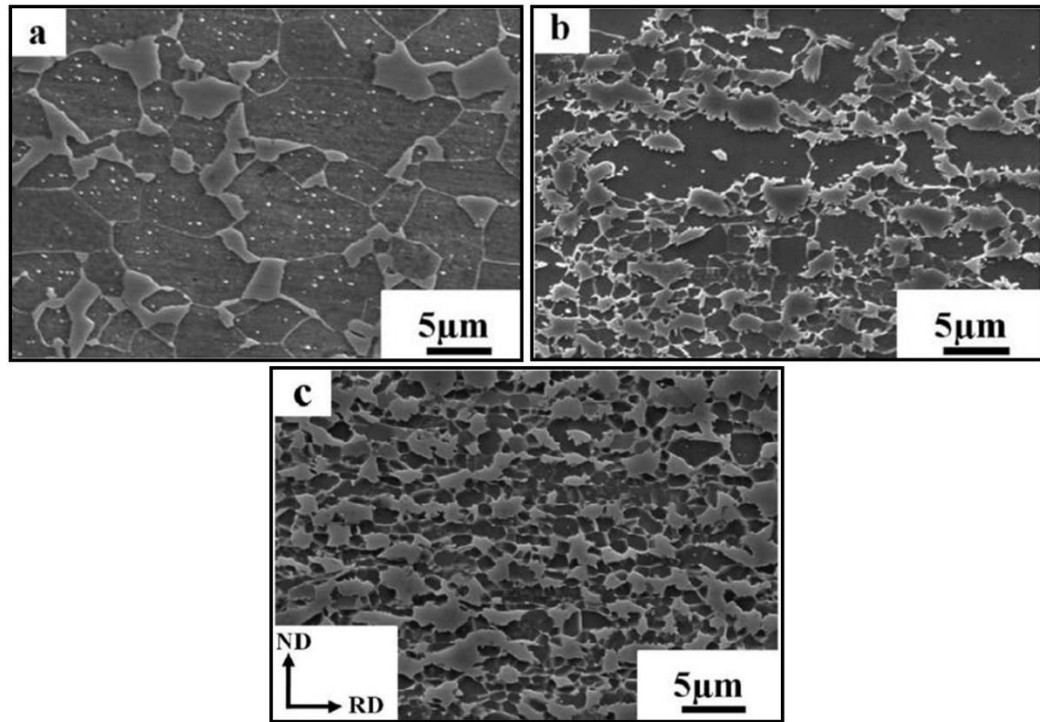
Figure 2. 26: SEM images DP steel microstructures obtained from 80% cold reduced steel through inter-critical annealing at 750 ^{0}C and 10 s at heating rates of a) 1 ^{0}C/s, b) 50 ^{0}C/s and c) 300 ^{0}C/s.

In contrast to the above results, a martensite with banded morphology was also reported by various publications [132,158,164–166,168]. Huang et al*.,* systematically studied the effect of heating rate, annealing temperature and soaking time on ferrite recrystallization and austenite formation kinetics in both cold rolled and hot rolled ferrite-pearlite steels [132]. As expected, the amount of ferrite recrystallization at a particular temperature decreased with the increase in heating rate from 1 to 100 ^{0}C/s. Thus, for 100 ^{0}C/s condition, recrystallization was found to be sluggish at lower temperatures and progressed into higher temperatures where austenite formation also occurred simultaneously. This is represented in **Figure 2.27 (a)**, where it can be

observed that the progress of recrystallization is significantly shifted into the austenite formation region for high heating rates. Very interestingly, for a given holding time and annealing temperature, increase in heating rate increased the austenite volume fraction. This is schematically shown in **Figure 2.27 (b)**. Therefore, with the increase in heating rate, the amount of martensite increases in the overall microstructure. This therefore increases the overall strength of the material. However, it should be noted that the increase in strength with increase in heating rate will not be true for slow cooling rates. Because higher austenite content will have lower carbon content, thereby decreasing its hardenability. So, at slow cooling rates this austenite might transform to ferrite or pearlite leading to a lower tensile strength [168].
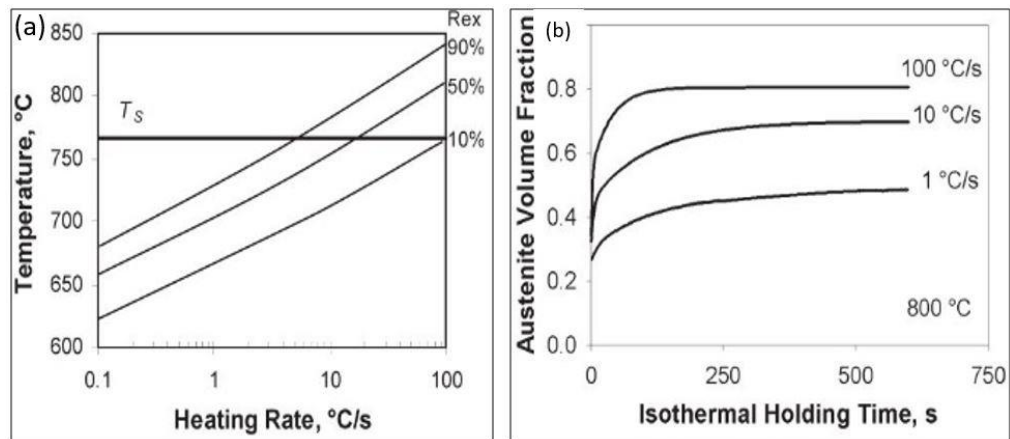
Figure 2. 27: Effect of heating rate on (a). ferrite recrystallization and, (b) Austenite formation kinetics [132].

It was also reported that the increase in heating rate for cold rolled material changed the austenite distribution from ferrite grain boundary and pearlite colony nucleated morphology to strictly pearlite colony nucleated morphology. This change in martensite morphology and increase in austenite kinetics was explained by comparing the nucleation sites and growth mechanism at slow and high heating rates. Since, ferrite recrystallization completes before the start of austenite formation at slow heating rates (1 ^{0}C/s), austenite nucleates both at ferrite grain boundaries and pearlitic bands. It was proposed that for lower heating rates, the rate of austenite formation depends on the growth of austenite nucleated at both ferrite grain boundaries and pearlite colonies. At ferrite grain boundaries, the carbon has to diffuse along longer distances, whereas the carbon in pearlitic colonies will have to move along shorter

diffusion paths. It was proposed that the competition of growth between austenite nucleated at different locations leads to slower transformation rates in slow heating rate condition. It was also proposed in this study that during faster heating rates the moving ferrite grain boundaries due to recrystallization will not provide suitable nucleating sites for austenite. This will allow the pearlite nucleated austenite grains grow without any apparent competition. This lack of growth competition enhances the rapid nucleation and growth of austenite at the directionally elongated pearlitic sites leading to a banded martensite distribution. This is schematically represented in **Figure 2.28**. This study also revealed that the rate of austenite formation increases with increase in heating rate even in the hot rolled samples. It was proposed that the faster heating rates enable rapid nucleation of austenite both at ferrite grain boundaries and pearlite colonies. This creates a continuous network of austenite grains in the steel sample as shown in **Figure 2.29**. Due to this all the grains grow without any apparent competition leading to high formation rates of austenite at high heating rates. This distributional variation also led to significant differences in mechanical properties [37]. Das et al., also reported the effect of martensite morphology on the mechanical properties of dual phase steels [169]. This study systematically compared the tensile properties of fine and fibrous, blocky and banded, and island type martensite morphologies, shown in **Figure 2.30**. Fine and fibrous martensite morphology was produced by fully austenitic annealing followed by quenching followed by inter-critical annealing, blocky and banded was produced by fully austenitic annealing followed by inter-critical annealing and quenching, whereas island type morphology was produced by purely inter-critical annealing. It was found that DP steel with fine and fibrous martensite morphology produced lowest yield strength ratio (0.61) and highest work hardening (351 MPa) and ductility (total elongation 19.7 %).
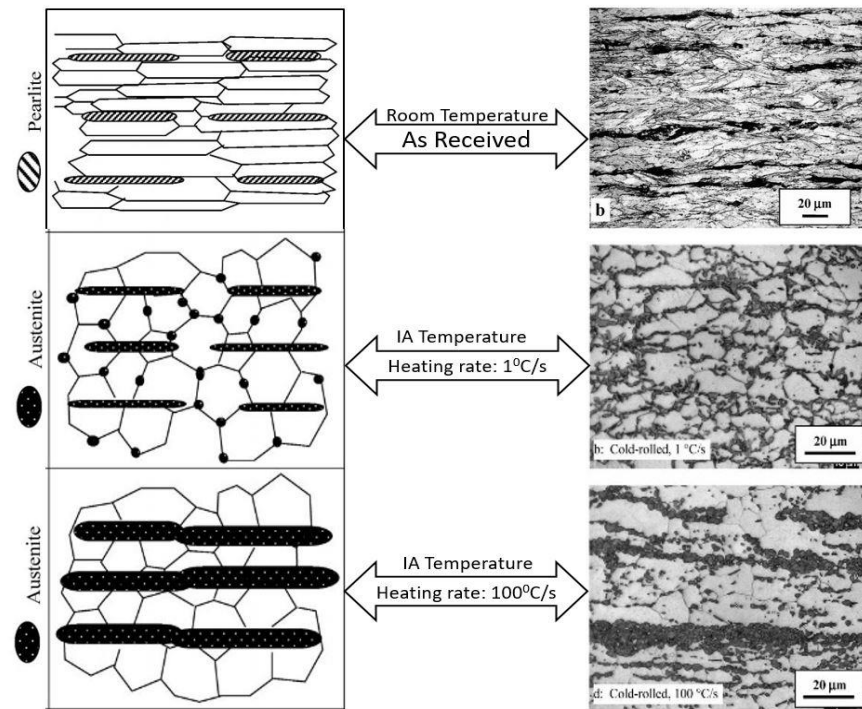
Figure 2. 28: Effect of heating rate on austenite morphology in 50% cold reduced ferrite-pearlite microstructure [132].
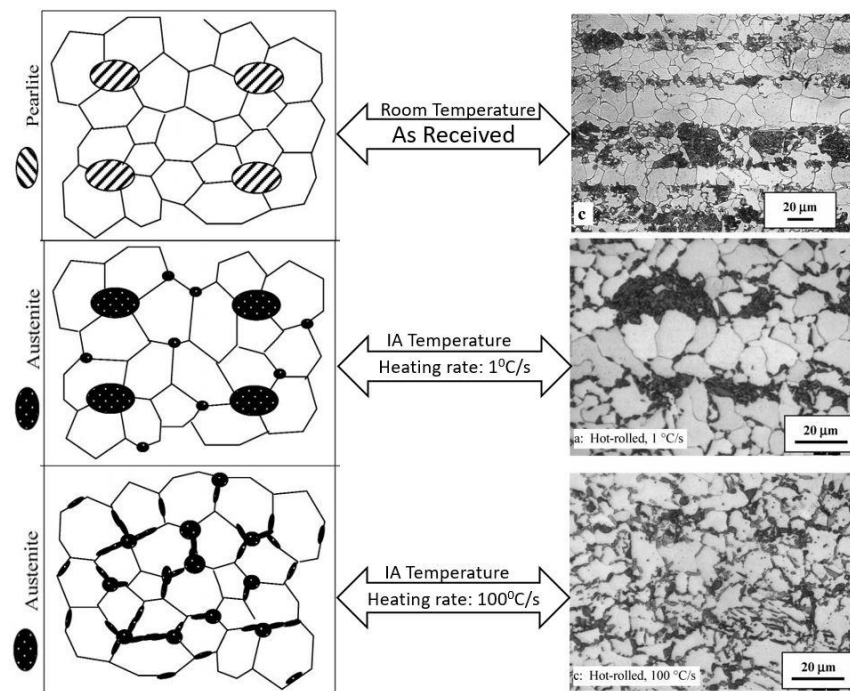
Figure 2. 29: Effect of heating rate on austenite morphology in hot rolled ferrite-pearlite microstructure [132].
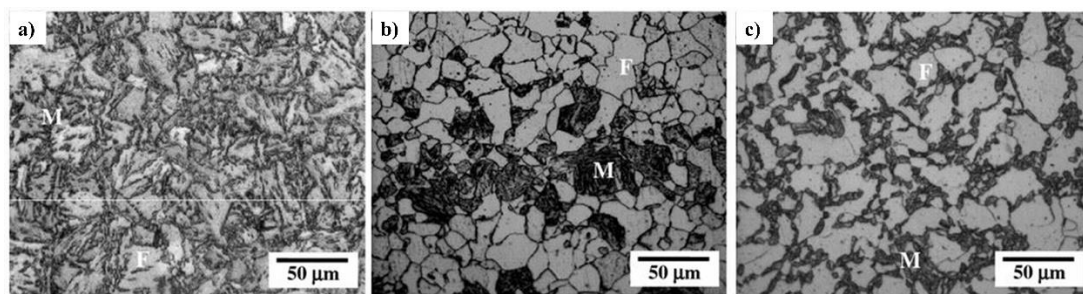
Figure 2. 30(a, b, and c): Optical micrographs of DP steels with martensite morphologies of fine and fibrous, blocky and banded, and island type respectively [169].

In the above study, Huang et al., pointed out that at higher rates the preferential nucleating sites will be carbon rich pearlitic regions and the moving ferrite grain boundaries would not be ideal sites for nucleation. Phase field modelling and cellular automaton modelling with this principle achieved banded martensite which was similar to the experimentally obtained microstructures [164,165]. However, with the increase in heating rate different studies have pointed out at different additional nucleating sites [158,167,170–172]. For instance, it was reported that with the increase in heating rate austenite not only nucleates at ferrite-pearlite boundaries but also at ferrite-ferrite boundaries [170,171]. This was attributed to the presence of cementite particles at ferrite grain boundaries [170]. Moreover, several studies have reported that the increase in heating rate allows the austenite phase to preferentially nucleate in the deformed ferrite matrix [158,159,167,172]. Additionally, Andrade-Carozzo et al., reported that the preferential nucleation of austenite in the deformed matrix will retard the progress of recrystallization process [167]. It was proposed that the consumption of un-recrystallized ferrite by the newly formed austenite grains hinders the progress of recrystallization process. However, along with Huang et al., several studies proposed an opposite phenomenon [132]. It was pointed out that the progress in ferrite recrystallization hinders austenite formation and therefore with the increase in heating rate pearlite colonies will become potential nucleating sites [132,152,164,165]. In contrary to this, Kulakov et al., observed preferential austenite nucleation in the deformed matrix and proposed that the decrease in the stored deformation energy decreases the activation energy for austenite formation [158]. Moreover, it was stated that a heterogeneous nucleation is promoted in the un-recrystallized ferrite due to the presence of defect structure.

53

In addition to this, different researchers postulated different reasons for the increase in austenite kinetics with heating rates [132,158,168,173]. Mohanty et al., proposed that increase in growth kinetics and decrease in nucleation kinetics is the reason for this [168], whereas, Huang et al., attributed it to the lack of growth competition for pearlite nucleated austenite [132]. The formation of martensite bands is generally attributed to the nucleation of austenite in pearlitic colonies. For instance , Zheng et al., and Mohanty et al., pointed out that the reason behind banding is due to slower diffusion rate of carbon in grain boundary nucleated austenite when compared to that of the austenite nucleated in the pearlite colony [164,168]. On the other hand, Kulakov et al., Chbihi et al., and Mumford et al., supported the rapid growth phenomenon in deformed matrix as the reason behind the martensite banding at high heating rates [158,159,173].

The formation of banded martensite morphology at high heating rates did not occur in the cold reduced steels with initial microstructures containing mixture of bainite and martensite or fully martensite microstructure[143,158]. **Figure 2.31 (a - f)** shows the effect of increase in heating rate (1 ^{0}C/s to 100 ^{0}C/s) on the martensite morphologies of the 50% cold reduced steels with initial microstructures of ferrite - pearlite, ferrite – bainite - pearlite, and fully martensite [158]. It can be seen that with increase in heating rate ferrite – pearlite microstructure produced more banded martensite morphology. However, in both ferrite – bainite - pearlite, and fully martensite initial microstructure steels, increase in heating rate did not cause martensite banding. The more uniform distribution of alloying elements (carbon) in these initial microstructures can be responsible for the non-banded microstructures. Moreover, the strain partitioning in these microstructures during cold rolling can decrease the overlap percentage and therefore banded martensite in the final microstructure. However, it should be noted that initial microstructures with bainite and/or martensite phases in it are not preferred in the industrial manufacturing process due to the requirement of additional steps during coiling. Moreover, the presence of bainite and/or martensite phases drastically increase the loads required for completing cold rolling process.
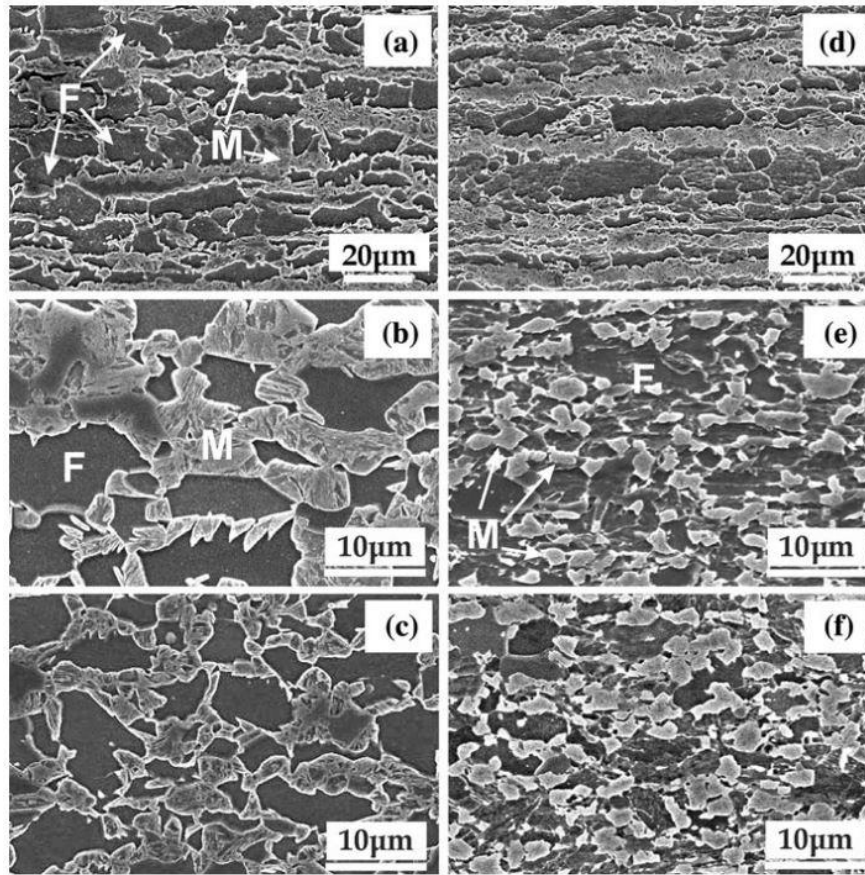
Figure 2. 31: SEM micrographs of DP steel microstructures obtained from 50% cold reduced steels with initial microstructures of (a, d) Ferrite - Pearlite, (b, e) Ferrite – Bainite - Pearlite, and (c, f) Martensite inter-critical annealed at 760 ^{0}C at heating rates of (a, b, and c) 1 ^{0}C/s, and (d, e, and f) 100 ^{0}C/s [158].

2.9.3. Manganese segregation bands

In addition to the process parameters, the formation of second phase banded morphology (in this case martensite) is greatly influenced by the alloying elements and the amount of segregation associated with it. In order to increase strength and/or ductility, increasing the amount of alloying elements in steel composition is a common practice in industrial manufacturing process. The advantages of the typical alloying elements (C, Mn, Si, Cr, Al etc.,) in DP steels is discussed in section 2.3. However, with the increase in the solute concentration (especially Mn in DP steels), the chance for solute segregation to occur increases [174,175]. This is due to the fact that the solubility of solute atoms in solid is many orders less than that of the solubility in liquid [176]. This therefore leads to solute atom segregation, mainly micro and macro

55

segregation. Due to this, the solute elements are continuously partitioned between solid and liquid in the inter-dendritic regions. This enrichment or depletion of solute atoms in inter-dendritic regions is generally in the order of micro-meters and therefore defined as micro segregation. Moreover, the continuous rejection of solute atoms also happens on a large scale, leading to a very high concentrated liquid to solidify at last in the centre of the cast. This is referred as macro-segregation and is generally seen in the order of large length scales relative to the ingot dimensions. The amount of segregation of a given solute mainly depends upon the partition coefficient (k) defined by Scheil-Gulliver equation and the weight percentage [176]. Here the partition coefficient (k) is defined as the ratio between the equilibrium concentrations of solute in solid and liquid phases at the solidification front during solidification process. The partition coefficients of the main alloying elements are given in the **Table 2.3** [177,178]. The lower the value of the partition coefficient the higher the chance of segregation. It can be seen that the manganese has relatively higher partitioning coefficient. However, the presence of high concentration of manganese in multiphase steels (here DP steels) enable it to segregate significantly higher when compared to other elements. From **Table 2.3**, it can also be seen that carbon also has very high tendency of segregation. To decrease segregation, steel industries generally employ processes such as dynamic soft reduction and/or electromagnetic stirring processes [179–181]. In laboratories, the solidified cast is soaked at high temperatures (1200 ^{0}C) such that solute diffusion happens [182]. But, due to the presence of high concentration of Mn in the present day AHSS steels and its very low diffusion coefficient (10^{-26} m^2/s), the centreline segregation exists throughout the downstream processes [183]. Moreover, to eliminate macro segregation, the solute atoms need to move over very large distances, and therefore is impossible to completely eliminate it in industrial production. Therefore, this micro-segregation from casting influences the microstructure of the steels throughout the downstream processes. **Figure 2.32 (a, b)** shows the inter-dendritic micro-segregation distribution of manganese after casting and the corresponding segregation bands after hot rolling process [184].

Table 2.3: Partition coefficients of common alloying elements in DP steels [177,178].

S. No.	Alloying element	Partition coefficient (k)	Weight % range
1	Silicon	0.63	0.2 % - 0.5 %
2	Manganese	0.71	1 % – 3 %
3	Chromium	0.33	0.5 % - 1 %
4	Carbon	0.26	0.06 % - 0.15 %
5	Niobium	0.05	PPM level
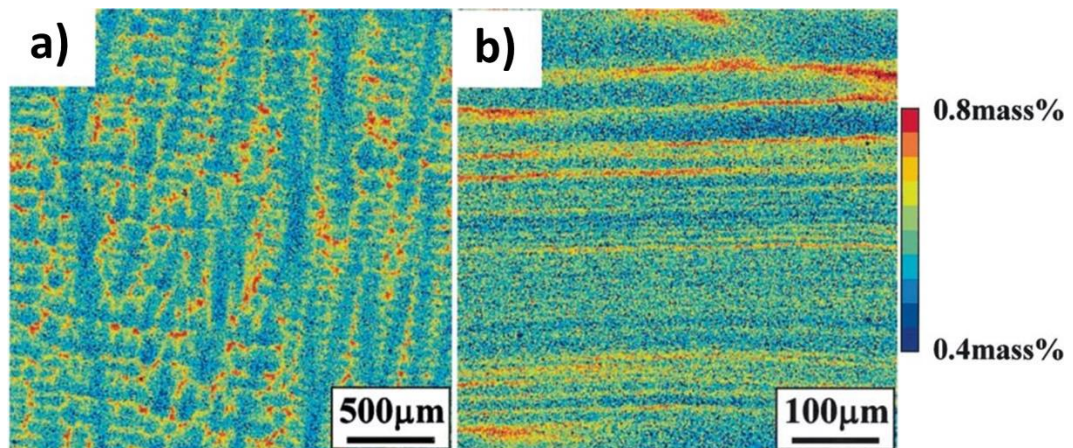
Figure 2. 32: Distribution of manganese segregation: a) Before rolling b) After rolling [184]**.**

Many researchers have reported that the presence of these manganese segregation bands leads to the formation of martensite bands in the final microstructure of DP steels. Ennis et al., reported that the martensite bands produced after inter-critical annealing showed positive overlap with manganese bands and a negative overlap with

aluminium bands. **Figure 2.33** shows the DP steel microstructure with corresponding EDX line graphs for manganese and aluminium[68]. It is also reported in this study that the cooling rate during the coiling process of hot rolling significantly effects the subsequent martensitic banding. It was found that the sample with slower cooling rate (0.2 ^{0}C/s) during coiling process generated significantly higher banding than the sample produced with higher cooling rate (100 ^{0}C/s). This is due to the influence of manganese on the ferrite-austenite equilibrium temperature (A_{e3}). During cooling, ferrite preferentially forms in the manganese depleted region thereby rejecting the carbon atoms into the manganese rich regions. This enriched carbon and manganese region will generate the formation of pearlite bands on further cooling. Caballero et al., also reported that increase in cooling rate decreases the degree of banding. However it was found that the banding reappears for higher martensite fraction microstructures or higher inter-critical annealing temperatures [185].
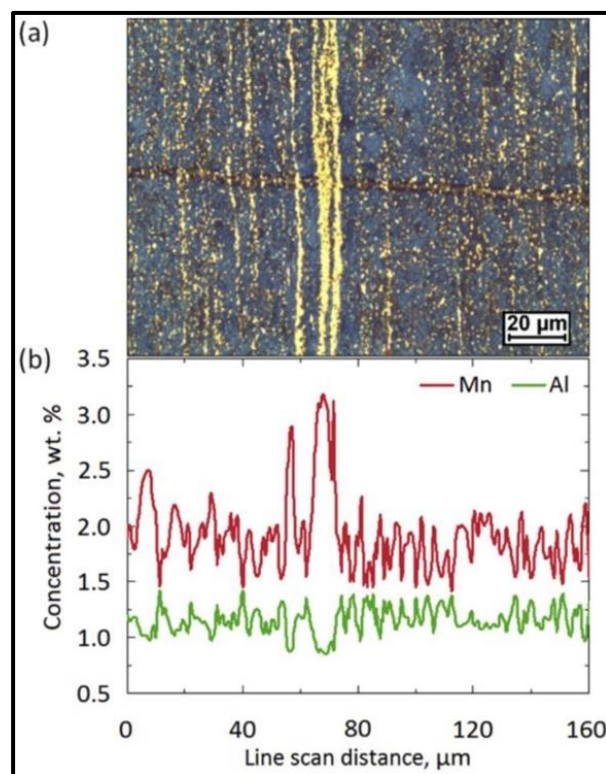
Figure 2. **33**: a) Dual phase steel microstructure showing martensite with banded morphology, and b) EDX line scan showing the presence of Mn and Al segregation [68].

In addition to the effect on the formation of martensite bands, manganese segregation bands also have significant effect on austenite and ferrite deformation and

recrystallization processes. Yamashita et al., studied the effect of manganese segregation on prior austenite grain size and the subsequent ferrite grain size during hot rolling process [184]. It was found out that the presence of manganese bands increased the prior austenite grain size, however, decreased the ferrite grain size after hot rolling. **Figure 2.34** shows the SEM microstructural images of the samples with and without manganese segregation representing prior austenite grain size and ferrite grain size. It was proposed that the sample with manganese segregation will have higher percentages of ferrite nucleating sites in the manganese depleted regions. The higher percentage of ferrite grains enable mutual impingement and therefore reduces the grain growth. Moreover, the manganese bands along the rolling direction also act as the obstacles for ferrite grain growth in the segregated sample. Vitesh et al., studied the effect of heating rate on the solute drag of manganese and silicon atoms on the ferrite recrystallization process in DP steel manufacture [149]. It was found that with the increase in heating rate the sensitivity of solute drag effect on the solute concentration decreases. In other words, the kinetics of recrystallization process is significantly affected by the increase in heating rate than the increase in manganese concentration. Similarly, San et al., studied the effect of heating rate (0.05 ^{0}C/s to 20 ^{0}C/s) on low carbon-manganese steel with increasing aluminium content. It was found that the faster dissolution of cementite lamella in the pearlite colonies during the slow heating rate condition is more pronounced in the samples with higher aluminium content [186].Chbihi et al., studied the effect of heating rate (1 and 100 °C/s) on the austenite formation process with special emphasis on the effect of austenite nucleating site with respect to the position of manganese bands [159]. It was found that the preferential austenite nucleating sites in the deformed matrix coincides with Mn bands especially in the high heating rate sample (100 °C/s). **Figure 2.35 (a, b)** shows the microstructure and the corresponding EDX map of DP steel produced by inter-critically annealing the manganese segregated steel at 740 ^{0}C at a heating rate of 100 °C/s. It can be clearly seen that austenite (now martensite) bands overlap the manganese segregation bands. Moreover, it was found that the areas with manganese bands contained less equiaxed ferrite grains than that of manganese depleted regions. Therefore, it was proposed that the solute drag effect caused by Mn retarded the recrystallization process. Moreover, the presence of Mn promoted the nucleation of austenite in the deformed matrix. This in turn hindered the progress of recrystallization and therefore promoted martensite banding [159]. On the other hand, Bos et al.,

systematically studied the effect of heating rate (2, 10, 20, 40, and 80 °C/s) on reducing the martensitic banding [187]. In this study martensite banding was observed in the final microstructure irrespective of the heating rates employed during the manufacturing process This was attributed to the Mn segregation and pearlitic banding in the hot rolled microstructure. This martensite banding is generally considered to deteriorate the mechanical properties as it enhances the strain incompatibilities between ferrite-martensite phases leading to interphase cracking and therefore decreases the formability of these steels [168]. One of the most effective ways to decrease the banding, as reported by Schemmann et al., is to produce bainite-martensite initial microstructure during hot rolling process instead of typical ferrite-pearlite microstructure [188]. This is generally feasible on laboratory scale but will be extremely difficult to employ in the industries due to the requirement of complex time-consuming processes involved during coiling and the requirement of huge loads during the subsequent cold rolling process. There is lot of research work being done to decrease the Mn bands and its harmful effects [189,190]. However, there is limited research on the effect of Mn bands on the microstructural evolution with respect to various process parameters in CAL especially with the increasing heating rate [68]. Therefore, in this PhD work one of the prime focuses is to study the microstructural evolution in Mn segregated low carbon steel with respect to CAL parameters.
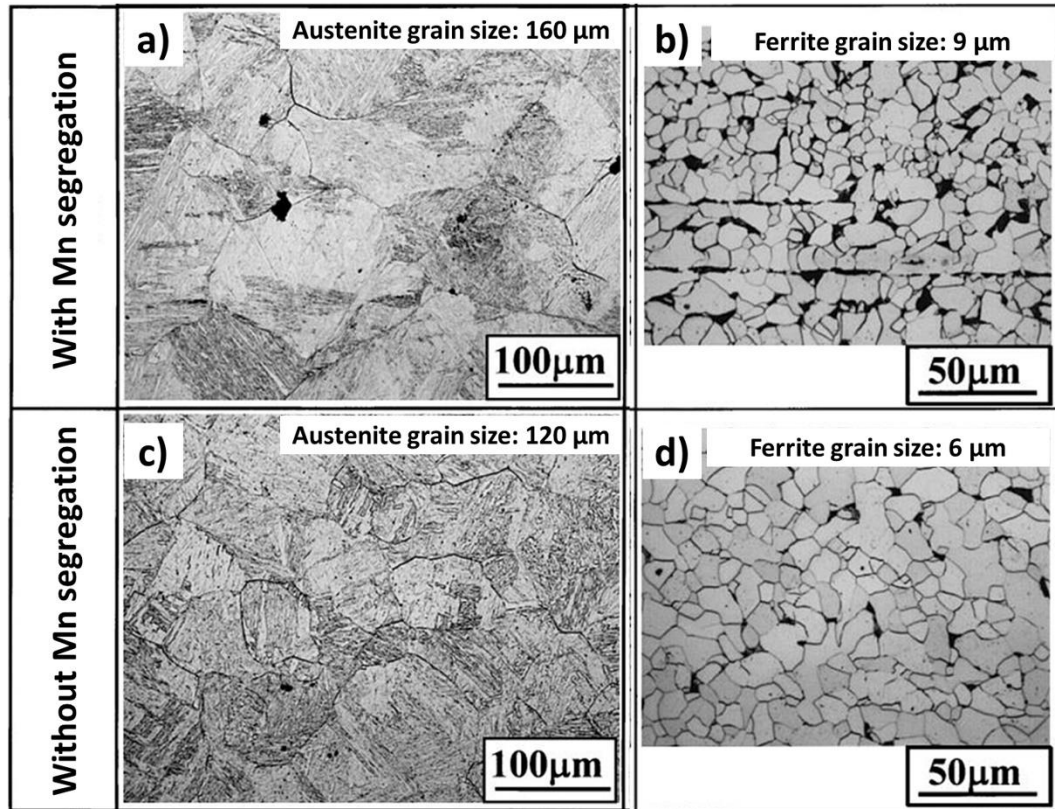
Figure 2. 34: SEM microstructural images of samples (a, b) with manganese segregation and (c, d) without manganese segregation showing (a, c) prior austenite grain size and (b, d) ferrite grain size after hot rolling process.
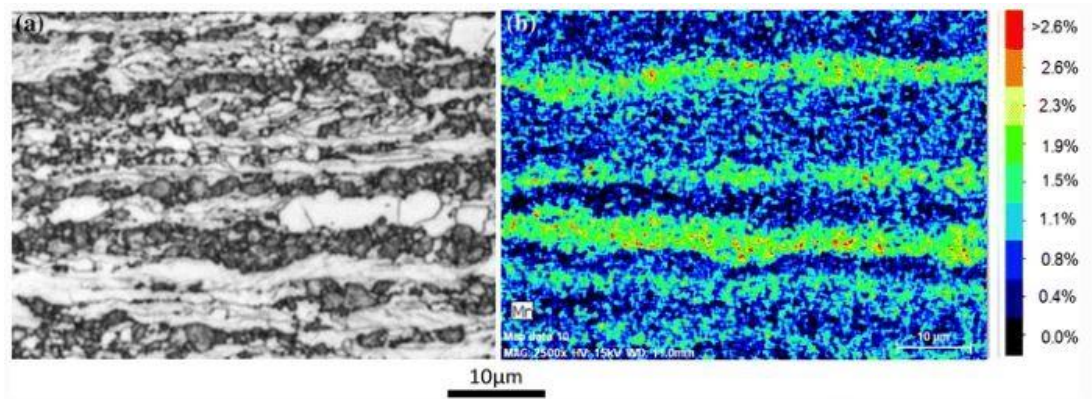
Figure 2. 35: a) DP steel microstructure produced after intercritical annealing at 740 °C and **b)** Corresponding manganese EDX map [159].

From the above literature survey, it is evident that high heating rate studies obtained various contradictory results in terms of austenite nucleation density, nucleating sites, and overall microstructural evolution. Moreover, there are many different proposed

mechanisms explaining the kinetics and the microstructural evolution of DP steels at high heating rates. It should also be noted that a wide range of chemical compositions, initial microstructures and cold reductions were used to understand the effect of concurrent mechanisms on the austenite formation process. However, the chosen heating rates in these studies were mostly arbitrary and the percentage of overlap between ferrite recrystallization and austenite formation were different. Therefore, to systematically compare microstructural evolution for various steels, it is absolutely critical to choose heating rates in such a way that a predefined amount of overlap is obtained. Moreover, to clear the ambiguity in the research studies, it is necessary to understand the austenite formation mechanisms for the various percentages of overlaps and inter-critical temperatures. Additionally, it is also necessary to understand the influence of Mn segregation on the final microstructures of DP steels.

Chapter 3 - Aim of the project

During the seemingly simple heating and cooling cycles of DP steel manufacture, there exists a series of overlapped processes happening both consequently and concurrently. With the introduction of strict emission laws and with the increasing demand for safe vehicles, automotive manufacturers are striving to produce steels with strengths as high as Giga-Pascal (GPa) levels [3,36,191]. To fulfil these demands, automotive-steel industries add higher quantities of alloying elements (Cr, B, Ti, V and Mn) into the steel composition [31,36,103,192]. However, as discussed in the literature review section, these alloying elements are known to retard the recrystallization process and thereby can significantly enhance its overlap with austenite formation, even at lower heating rates [132,162,193,194].

Based on the knowledge gained from the literature, a chart is prepared to emphasise the overlap between these various processes happening during the heating step of CAL, at an approximately defined temperature range. This schematic is shown in **Figure 3.1**. It should be noted that the heating rate assumed for this chart is relatively slow. Firstly, at very low temperatures below 400 ^{0}C, ferrite recovery (annihilation of point defects and alignment of dislocations) starts to progress. At a slightly above temperature range (400 ^{0}C to 600 ^{0}C), an overlap between ferrite recovery and recrystallization (new strain free grains) can take place. However, ferrite recovery is expected to be the dominating process because a higher temperature is generally required for the recrystallization process. Along with this, cementite spheroidization takes place at a slower pace even in the cold rolled material. At slightly higher temperatures (600 ^{0}C to 700 ^{0}C), ferrite recrystallization and cementite spheroidization will progress at a higher pace. Moreover, the coarsening of precipitate particles (Orowan mechanism) also starts at this temperature range and continues to very high temperature range until the complete dissolution takes place. In this chart vanadium, titanium and boron precipitated are considered. At lower inter-critical temperature range, austenite formation and rapid recrystallization of remaining deformed ferrite grains takes place. At the same time precipitate particles like vanadium carbides etc are expected to be completely dissolved into the microstructure. At higher and above

inter-critical temperature range, rapid austenite formation takes place and the remaining precipitates dissolve into the solid solution.
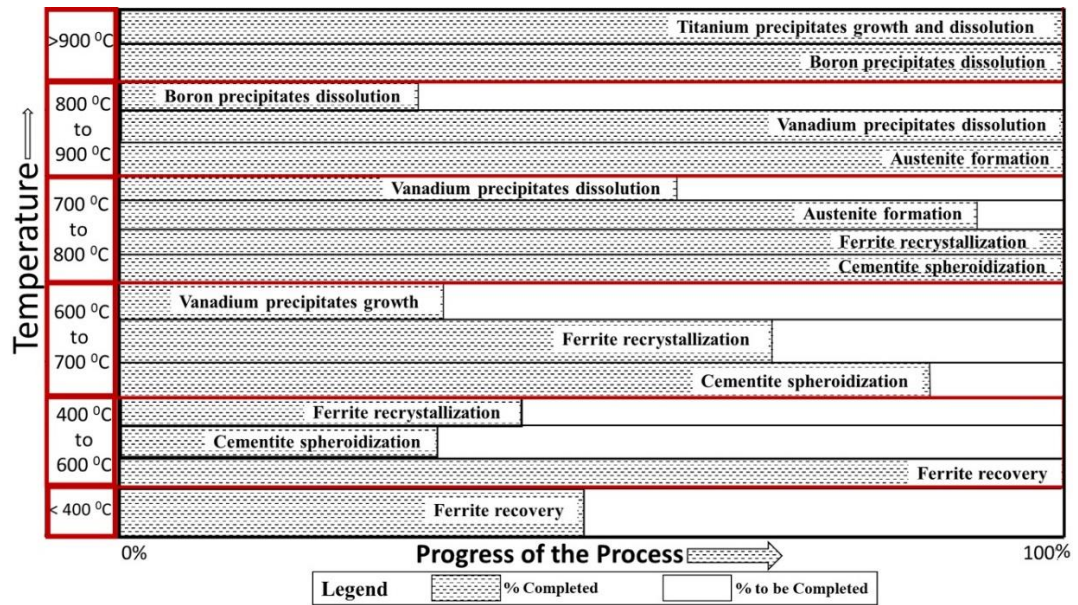
Figure 3. 1: A brief pictorial representation of the progress of various processes going on during heating step in DP steel manufacture.

The above chart represents the progress of various high temperature processes during the heating step of CAL at relatively normal heating rates. With the increase in heating rates, the amount of overlap between these high temperature processes increases, especially between ferrite recrystallization, cementite spheroidization and austenite formation. Therefore, the main aim of this PhD work is to understand the effect of complex interplay of these process on the microstructure evolution of DP steels at various percentages of overlaps and inter-critical temperatures.

3.1. Research objectives

The main objectives of this work are as follows:

➤ To understand the effect of common industrial cold reduction percentages (50, 60 and 75%) on the recrystallization kinetics of low carbon ferrite-pearlite steels.

➤ To calculate Johnson-Mehl-Avrami-Kolmogorov (JMAK) constants and critical temperatures for the three different cold reductions (50, 60 and 75%) and to develop a model that predicts the heating rates required for obtaining a pre-

defined amount of overlap between ferrite recrystallization and austenite formation.

➢ To study the effect of progress of high temperature mechanisms (with and without overlap) and inter-critical processing parameters on the austenite formation kinetics and the subsequent microstructural evolution of cold rolled manganese segregated DP steels . To briefly study the effect of inter-critical annealing parameter on vanadium precipitation.

➢ To propose mechanisms explaining the various differences in the characteristics of the microstructures with respect to the progress of high temperature mechanisms and process parameters.

➢ To study the effect of high heating rate on microstructural evolution of hot rolled DP steels and to study the effect of hot rolled texture anisotropy on the final DP steel texture.

Chapter 4 - Experimental Procedure

4.1. Research outline

This research work aims to study the microstructural evolution of manganese segregated DP steels by systematically understanding the austenite formation mechanism during the heating step of DP steel manufacture. The heating rates in inter-critical annealing were employed in such a way that a predefined amount of overlap is obtained between ferrite recrystallization and austenite formation. For this purpose, a model has been developed based upon the JMAK equation which predicts the heating rate required for a specific amount of overlap to happen. The heating rates obtained by the model were used to conduct heat treatment experiments at various inter-critical annealing parameters. Various characterizing techniques were used to study and understand the microstructural evolution in both cold rolled and hot rolled steels. Finally, based upon the results obtained, this study explains the mechanisms of austenite formation with respect to the heat treatment parameters.

4.2. Materials

In this thesis work, low carbon micro-alloyed steels with minute additions of boron and vanadium (BV) is used to study the effect of overlap on the microstructural evolution of DP steels. Boron is added to increase the hardenability, whereas, Vanadium is added to slow down the recrystallization process and also to impart precipitate hardening into the final microstructure. The initial industrial cast material was hot rolled and pickled to 2 mm thickness at Tata steel, Netherlands. In order to understand the effect of cold reduction percentage on recrystallization kinetics and overlap, the hot rolled steel is further cold rolled into three different reductions of 50%, 60%, and 75 % using a laboratory cold rolling mill (Hille-Müller). It should be noted that all the sheets are produced from the same cast. The final thicknesses of the 50%, 60% and 75% cold rolled sheets were 1 mm, 0.8 mm and 0.5 mm respectively. Hot rolled and cold rolled steels (50%, 60%, and 75 %) micro-alloyed with Boron and Titanium (BT) were also developed at Tata steel, Netherlands to compare the initial microstructures and hardness values with BV steels. Optical Emission Spectroscopy (Hitachi-OE750) was used to measure the elemental composition of all the steels.

Table 4.1 shows the composition of BV and BT steels. ThermoCalc 2019b(Sweden) analysis was done to understand the various critical temperatures such as equilibrium austenite start and finish temperatures and as well as various equilibrium precipitate dissolution temperatures. To understand the effect of chemical composition on the various critical temperatures, a comparative ThermoCalc analysis was also done on BV and BT steels. The software version used was 2019b and the databases used for the thermodynamic and kinetic simulations were TCFE9 (v9.2) and MOBFE3 (v3.0) respectively. One axis equilibrium mode was used for calculating the equilibrium austenite start and finish temperatures and precipitate formation/dissolution temperatures. Precipitate simulation mode was used to understand the vanadium carbide precipitate characteristics during the inter-critical annealing in the ferrite matrix phase. In the initial work of this study, hot rolled and cold rolled microstructures and hardness measurements of BV and BT steels were compared. BV steel was used for the bulk work of understanding the complex interplay between high temperature processes during DP steel manufacturing process. The reason behind this is because of the presence of large titanium precipitates (2-4 μm) in the hot rolled microstructure and their high dissolution temperatures (> 1200 °C). Due to this, the effect of titanium addition on the overlap during inter-critical annealing should be negligible. BV steel was used due to the absence of any vanadium precipitates and their corresponding low dissolution temperature (650-800 °C).

Table 4. 1: Compositions of BV and BT steels by wt%.

Alloy	Fe	C	Mn	Si	V	Ti	B	Al	Cr	N	S
BV Steel	96.8	0.14	2.1	0.37	0.06	-	0.002	0.3	0.2	0.002	0.002
BT Steel	96.8	0.13	1.9	0.3	-	0.03	0.002	0.5	0.3	0.002	0.002

4.3. Heat Treatments

Heat treatments were conducted on hot rolled and cold rolled low carbon Boron-Vanadium steels. Bähr dilatometer was used to perform all the heat treatments. The heat treatments conducted in this PhD work can be categorized into three different

types based upon the purpose of the experiments: 1). Ramp and hold type of heat treatments for understanding the recrystallization kinetics. 2). Continuous type of heat treatments for evaluating various critical temperatures with respect to the heating rates employed. 3). Ramp and hold type of heat treatments for producing DP steels with respect to various inter-critical annealing parameters.

To conduct the heat treatments, the through thickness samples were cut into 10x4 mm^2 dimensions using an Electron Discharge Machining equipment (EXCETEK V650G). The samples were cut in such a way that the transverse direction aligns with the length dimension (10 mm) and the rolling direction aligns with width dimension (4 mm). **Figure 4.1** shows the schematic representation of steel sheet and the dilatometry samples with corresponding thermocouple location. For evaluation of recrystallization kinetics and calculation of the Johnson–Mehl–Avrami–Kolmogorov (JMAK) constants, various sub-critical (below A_{c1}) heat treatments were conducted on all the three cold reductions. **Figure 4.2** shows a pictorial representation of recrystallization kinetics heat treatments. **Table 4.2** shows the various heat treatment parameters used to evaluate the recrystallization kinetics for the three cold reductions. For 50% and 60% cold reductions, the samples were heated to two holding temperatures of 650 ^{0}C and 675 ^{0}C. The 75% cold reduction sample was held at 625 ^{0}C and 650 ^{0}C. The lower temperatures for 75% reduction were chosen because of its higher recrystallization kinetics. For all the recrystallization experiments, a heating rate of 50 ^{0}C/s was used. The soaking times before quenching varied from 1 second to 900 seconds. **Figure 4.2** shows a pictorial representation of recrystallization kinetics heat treatments. The continuous type of heat treatments were done on all the three cold reductions to calculate the recrystallization start and austenite start temperatures with respect to the heating rates employed. The samples were heated at four different heating rates of 1, 10, 100, and ~500 ^{0}C/s to temperature above A_{c3} followed by quenching. The dilation data was simultaneously measured along the length dimension (transverse direction), and the corresponding critical temperatures were found. For inter-critical annealing heat treatments, the 50 % cold reduced samples were heated at various heating rates corresponding to different overlaps of ferrite recrystallization and austenite formation. **Table 4.3** shows the various heat treatment parameters used to produce DP steel microstructures. **Figure 4.3** shows a pictorial representation of inter-critical annealing heat treatments. The soaking times at each inter-critical temperature varied from 0

seconds to 900 seconds. After heating and soaking step, the samples were quenched using Helium gas quenching where a cooling rate of -150 ^{0}C/s is produced. This was sufficient enough to transform all the austenite at inter-critical region to martensite in the final microstructure.
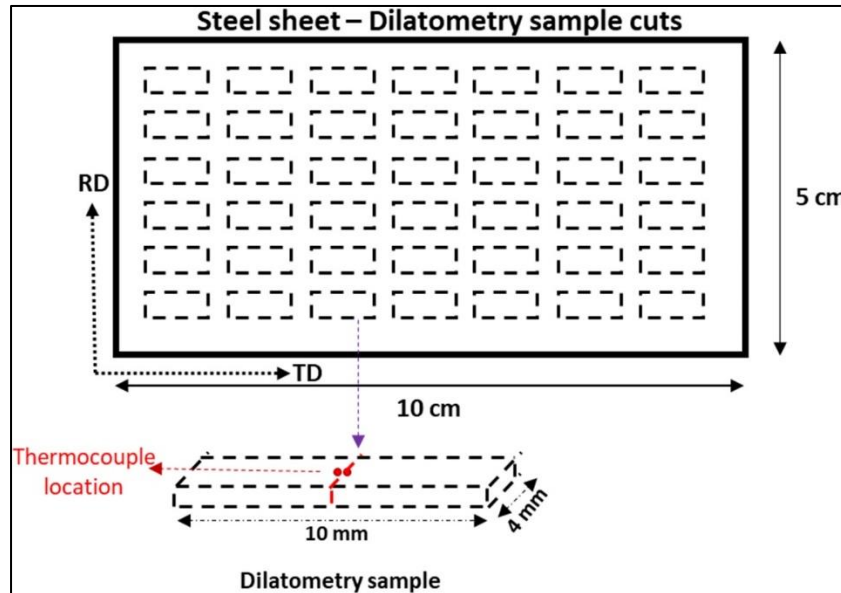
Figure 4. 1: Schematic representation of steel sheet and the dilatometry samples with corresponding thermocouple location.
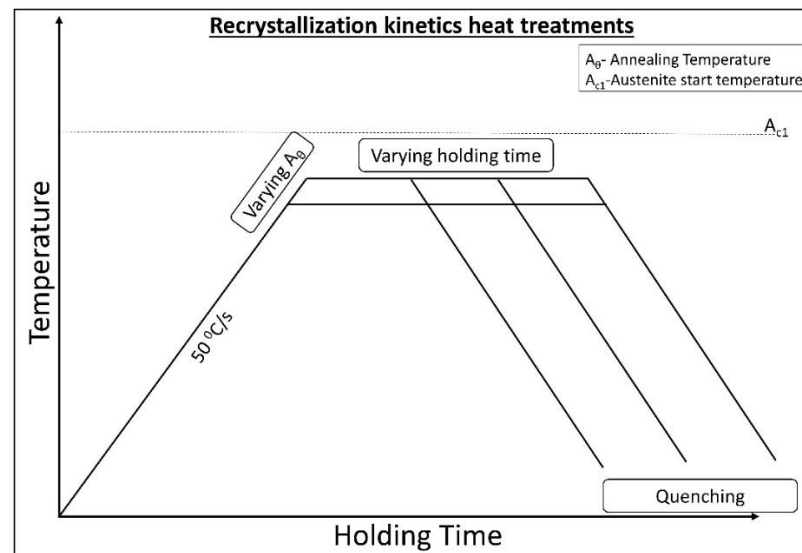
Figure 4. 2: A pictorial representation of recrystallization kinetics heat treatments.
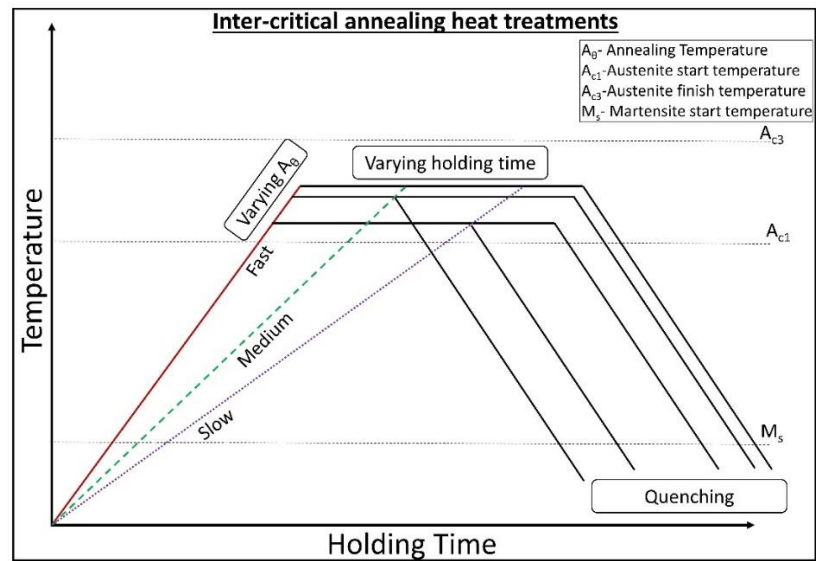
Figure 4. 3: A pictorial representation of inter-critical annealing heat treatments.

Table 4. 2: Typical heat treatment parameters used to study the ferrite recrystallization process.

S. No.	Material	Heating rate (^{0}C/s)	Soaking Temperature (^{0}C)	Time (s)
1	Cold rolled 50% and 60%	50 ^{0}C/s	650 ^{0}C and 675 ^{0}C	**Range:** 0-900 s
2	Cold rolled 75%	50 ^{0}C/s	625 ^{0}C and 650 ^{0}C	**Range:** 0-900 s

Table 4. 3: Typical heat treatment parameters used to study the austinite formation and the subsequent final microstructure.

S. No.	Material	Heating rate (^{0}C/s)	Soaking Temperature (^{0}C)	Time (s)
1	Cold rolled steel	0.2, 7, 50.5, and 511 ^{0}C/s	715 ^{0}C to 780 ^{0}C	**Range:** 0 to 900 s
2	Hot rolled steel	0.2, 7, 50.5, and 511 ^{0}C/s	715 ^{0}C to 780 ^{0}C	**Range:** 0 to 900 s

4.4. Characterization

4.4.1. Sample preparation for metallographic analysis

For characterization purpose, all the samples were cut into the transverse plane near the thermocouple (**Figure 4.1**) using 11-2700 IsoMet High Speed Pro Precision Cutter. The samples were hot mounted on the RD⊥ND plane using Kundoctomet resin with a SimpliMet 4000 Mounting Press machine. Depending upon the characterization techniques, the samples were polished according to the standard metallographic procedures using the AutoMet 300 Pro automatic polishing machine. **Table 4.4** shows the stepwise polishing procedure used in this study. Step 1 to 4 were commonly used for the sample preparation for all the characterization techniques. The final ultrafine polishing step on Vibromet (step 5) was only done for sample preparation of Electron Dispersive X-ray Spectroscopy analysis (EDX), Electron Back Scattered Diffraction analysis (EBSD) and Nano-indentation measurements. For microstructural analysis samples were etched for 10 seconding using 2% Nital solution.

Table 4. 4: Standard metallographic polishing procedure.

S. No.	Type	Cloth	Suspension	Direction	Force (N)	Time	Speed (rpm)
1	Grinding	P400	Water	Same	30	Until flat (25 s)	300
2	Polishing	Ultrapad	9 μm silica aqua solution	Opposite	27	5 minutes	150
3	Polishing	Trident	3 μm silica aqua solution	Same	25	4 minutes	150
4	Polishing	Chemomet	0.05 μm alumina aqua solution	Opposite	25	4 minutes	150
5	Ultrafine Polishing	Vibromet	0.01 μm alumina aqua solution	-	-	3-4 hours	-

4.4.2. Optical Microscopy

The etched samples of the initial hot rolled and cold reduced samples were analysed using Nikon Eclipse LV150N equipment. The microstructural images were taken on the RD⊥ND plane near the thermocouple as shown in **Figure 4.1**. ImageJ software

was used to measure the various microstructural features (aspect ratios and volume fractions) from the optical images.

4.4.3 Scanning Electron Microscopy analysis

Scanning Electron Microscopy analysis was done using a FEG JEOL 7800F-SEM equipped with a secondary electron detector, an EDX detector and an EBSD detector. The SEM images of rolled and heat treated samples were taken on secondary electron mode (SE) at high magnifications. The volume fraction of ferrite and martensite phases in the heat treated samples were calculated using point counting method in accordance with ASTM E562-11 [195]. In this technique, a representative number of points are laid over the SEM image using ImageJ software and the number of points falling on the particular phase are counted. According to the standard, if the point completely falls on the phase than it must be counted as 1, if the point falls on two phases than it must be counted as 0.5 and if a point falls on the other phase than it must be counted as 0. The sum of this count divided by total number of points give volume fraction of that phase. The grain size and aspect ratio measurements were done using line intercept method in accordance with ASTM E112-12 [196]. In this method representative lines of known length are drawn on the microstructures using Image J software. The total length of the lines divided by number of intercepts intersecting the grain boundaries gives the average grain size. EDX mapping was used to identify the type of inclusions present in the initial microstructure. Moreover, the Mn segregation in both the initial and heat treated steels was analysed using EDX line scans on Aztec software (Oxford instruments UK). For EDX analysis a voltage of 10 kV, a probe current of 3 µA and a working distance of 10 mm was used. EBSD analysis using Aztec and HKL Channel 5 softwares (Oxford instruments, UK) was done on the heat treated samples to measure the misorientation profile in the ferrite grains. A voltage of 20 kV, a probe current of 21 µA and a working distance of 10 mm was used for EBSD analysis.

4.4.4 Micro-hardness tests

Micro-Vickers hardness measurements were carried out in both recrystallization annealed samples and inter-critical annealed samples to understand the progress of recrystallization and austenite formation processes. Samples were first polished until

step 4 in **Table 4.4,** and then the hardness measurements were taken with a Wilson®
UH4750 Universal Hardness Tester. For inter-critically annealed samples the load
employed was 2 kg and the dwell time used was 10 s. For both rolled samples and
recrystallization heat treated samples, a load of 500 g and a dwell time of 10 s was
used for hardness measurements. The amount of recrystallization completed was
calculated on the basis of softening of ferrite grains with the progress of
recrystallization process. This was measured based upon the following formula shown
in Equation 1. The calculation of recrystallization fraction using the hardness
measurements showed good agreement with the metallographic measurements in
published literature [132]. Moreover, the calculation of recrystallization fraction using
hardness measurements is less time consuming compared to that of metallographic
measurements.

$$Recrystallization\ Fracation\ (X)\ =\ \frac{H_0 - H}{H_0 - H_c} \cdots\cdots\cdots\cdots\cdots\cdots Eq.1$$

Where H_0 is the hardness of the initial cold rolled material, H_c is the hardness of the
fully recrystallized material and H is the hardness value of the recrystallization
annealed material. The hardness value for each sample was calculated by taking
average of 10 indents.

4.4.5 Nano-Indentation tests

Nano-indentation experiments were conducted on different inter-critical annealed
samples with variations in heating rates, inter-critical temperatures and soaking times.
The purpose of these experiments was to understand the strength differences between
ferrite and martensite phases with respect to the annealing parameters. The
measurements were carried out on ultra-fine polished samples on a Nano-Indentation
machine (Micro Materials) equipped with a standard Berkovich indenter (included
angle, 142.3°). The measurements were taken under depth controlled mode of 200 nm
with loading and unloading rate of 10nm/s, and a dwell time of 10 seconds. The
measurements were taken in such a way that an array of indents (10x10) were carried
out on the polished sample. The force-displacement curves were analysed and saved
according to the number in the array (1 to 100). After this, SEM images were taken on
the array of indents before and after etching in such a way that the indents falling

exactly inside the ferrite and martensite phase were properly identified. Then, the Nano-hardness measurements of the indents falling exactly inside the phases were systematically calculated and compared.

4.4.6. Transmission Electron Microscopy analysis

Transmission Electron Microscopy analysis (TEM) was done to understand the effect of heating rate on the number and size distribution of the vanadium carbide nanoparticles. Precipitate analysis was done on two samples annealed at heating rates of 0.2 ^{0}C/s and 50.5 ^{0}C at 750 ^{0}C for 60 seconds. After polishing, ultrathin Focused Ion Beam (FIB) samples were prepared using FEI Scios Dual-Beam instrument. TEM analysis was done using Talos F200X microscope (FEI) equipped with an EDX detector, operated at an accelerating voltage of 200 kV. ImageJ software was used to measure the number and size distribution of the vanadium carbide nanoparticles.

Chapter 5 - Effect of chemical composition and cold reduction

The microstructure evolution of DP steels is highly influenced by the various alloying elements present in the steel composition. The percentage of cold reduction also effects the final DP steel microstructure by the addition of other high temperature mechanisms during the heating step of CAL. Therefore, this chapter discusses about the effect of alloying elements, especially Mn, on the critical equilibrium temperatures of the phase transformations using ThermoCalc simulations. ThermoCalc precipitation simulation analysis is also used to understand the precipitate characteristics of vanadium carbo nitrides in the inter-critical temperature region (750 ^{0}C). This chapter also studies the effect of percentage of cold reduction on the initial microstructure and the hardness measurements.

5.1. ThermoCalc analysis

5.1.1. Austenite formation

In this PhD work, the study of overlap between high temperature processes was conducted on low carbon steel micro-alloyed with Boron and Vanadium (BV). The composition of this steel is given in **Table 4.1**. **Figure 5.1** represents the ThermoCalc one axis equilibrium simulation of BV steel, which shows the relative volume fractions of various equilibrium phases with respect to the corresponding temperatures. The major phases include BCC_A2, FCC_A1 and Cementite_D011 which correspond to ferrite, austenite and cementite (Fe$_3$C) phases respectively. The precipitate phase in this steel is vanadium carbo-nitride and is represented by FCC_A1#2. It should be noted that Cementite_D011 phase also includes other stochiometrical carbides such as (Fe,Mn)$_7$C$_3$ [70]. However, these additional iron manganese carbides are not easily distinguishable from the Fe$_3$C carbides in the conventional microstructure and therefore are together termed as the cementite phase.
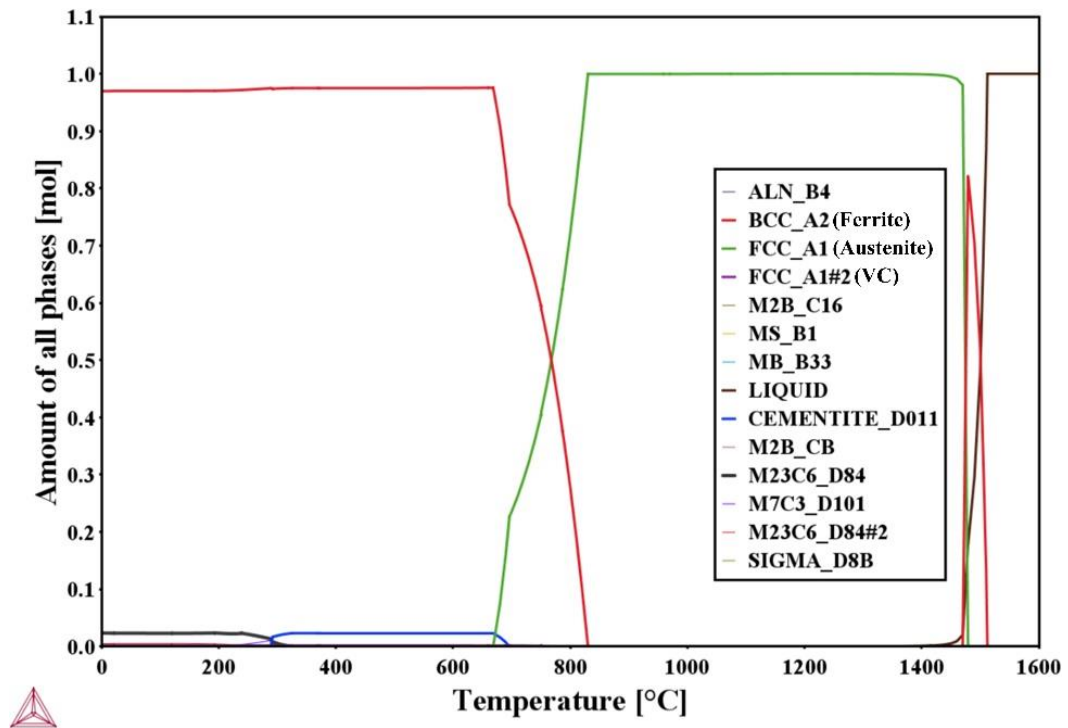
Figure 5. 1: ThermoCalc simulation showing the volume fractions of various equilibrium phases present in BV steel (Fe-0.14C-2.1Mn-0.37Si-0.06V-0.002B).

Figure 5.2 shows the equilibrium volume fractions of ferrite, cementite and austenite phases present in the inter-critical temperature region. The equilibrium austenite start (A_{e1}) and finish (A_{e3}) temperatures are found to be 668 ^{0}C and 830 ^{0}C respectively. However, it should be noted that the actual A_{c1} and A_{c3} temperatures during continuous heating will be much higher than these equilibrium critical temperatures. Moreover, it can be seen from the **Figure 5.2** that the austenite volume fraction increases rapidly with temperature until the complete dissolution of cementite at 696 ^{0}C. After complete dissolution of cementite, the austenite volume fraction initially increases relatively slower. However, with increase in driving force at higher temperature the austenite volume fraction increases rapidly towards the A_{e3} temperature. It is also critical to find out the martensite start temperature for the given alloy, as the critical cooling rate required to completely transform austenite to martensite depends both on the pearlitic nose and the martensitic start temperature. The martensitic start temperature is directly influenced by the type and the amount of

alloying elements present in the steel composition and is approximately calculated using **Equation 5.1** [31,197]**,** and was found to be 438 ^{0}C.

$$Ms(°C) = 571 - 474.4C - 33Mn - 17Ni - 17Cr - 21Mo \dots\dots\dots\dots\text{.Eq. 5.1}$$
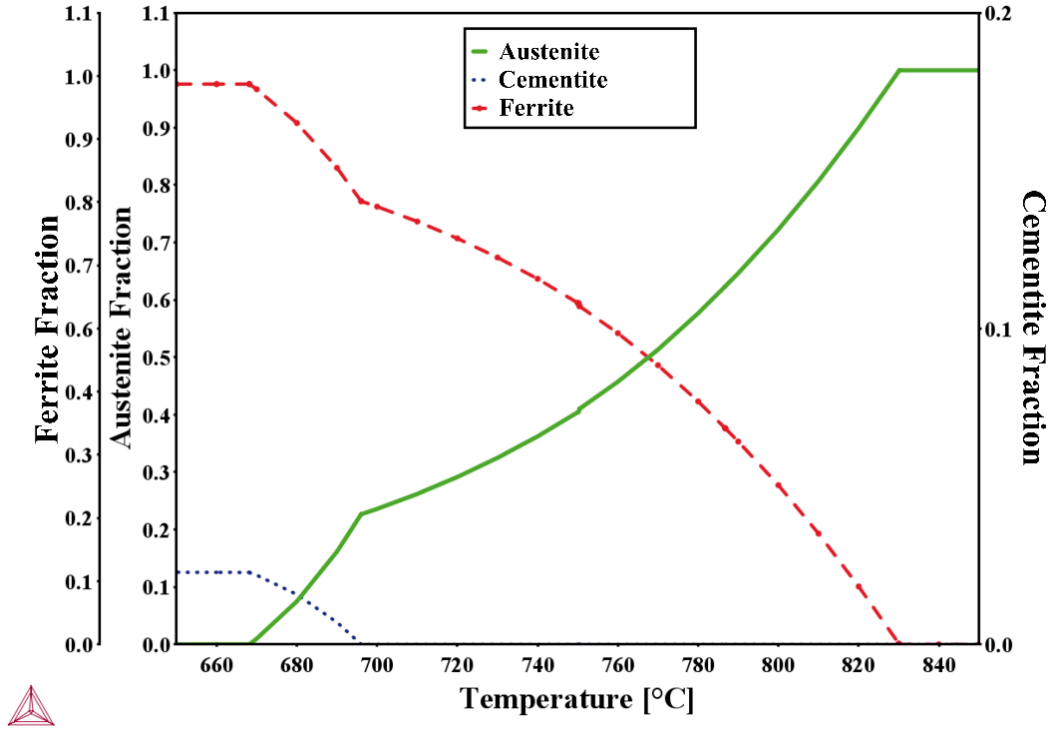
Figure 5. 2: ThermoCalc simulation showing the equilibrium fractions of Austenite, Cementite and Ferrite phases in the inter-critical region for BV Steel (Fe-0.14C-2.1Mn-0.37Si-0.06V-0.002B).

To understand the effect of vanadium in the BV steel, another low carbon steel micro-alloyed with Boron and Titanium (BT) was developed. The composition of this BT steel in wt% is shown in **Table 4.1**. **Figure 5.3** shows the comparison of equilibrium austenite fractions for BV and BT steels in the inter-critical region. It can be clearly seen that the temperature range at which the austenite is stable is smaller in the BT steel when compared to the BV steel. This can be attributed to the higher percentage of titanium and it's relatively higher ferrite stabilizing effect. **Figure 5.4 (a, b)** shows the comparison of equilibrium vanadium carbo-nitride (V(C,N)) and titanium carbo-nitride (Ti(C,N)) phase fractions in BV and BT steels respectively. The equilibrium precipitate formation/dissolution temperatures for V(C,N) and Ti(C,N) was found to be 786 ^{0}C and 1481 ^{0}C respectively. It should be noted that V(C,N) precipitate formation temperature is in the inter-critical region and the Ti(C,N) precipitation

formation temperature is near the solidification region. The sharp decrease in the equilibrium V (C,N) fraction corresponds to the decrease in the carbon content due to the pearlite formation at the eutectoid temperature.
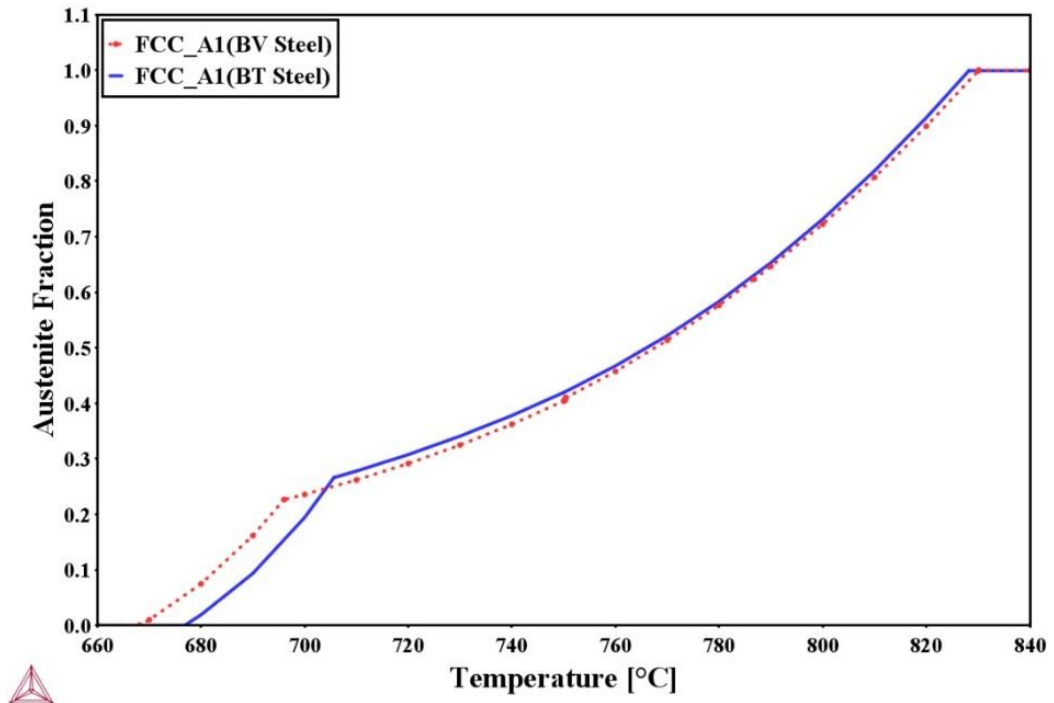
Figure 5. 3: Comparison of equilibrium volume fractions of Austenite phase for the BV (Fe-0.14C-2.1Mn-0.37Si-0.06V-0.002B) and BT (Fe-0.13C-1.9Mn-0.3Si-0.03Ti-0.002B) steels.
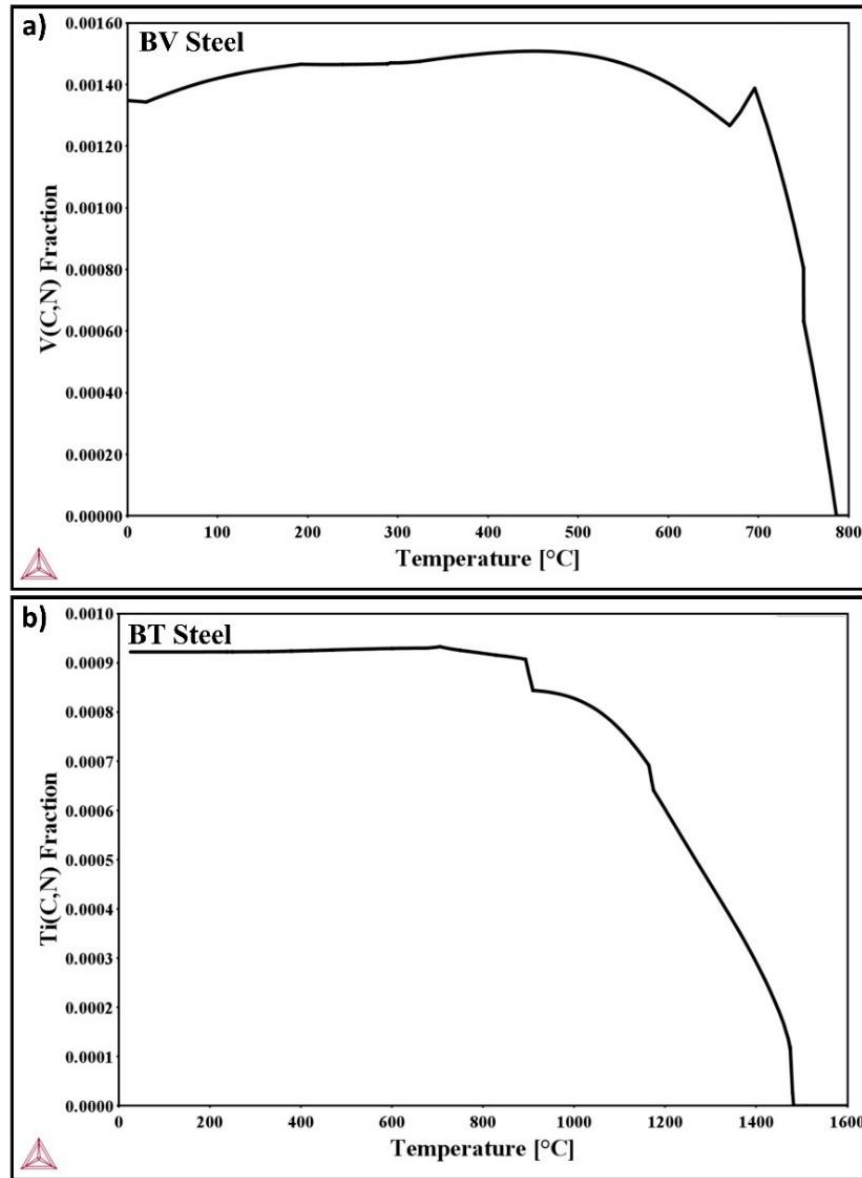
Figure 5. 4: a) Equilibrium Vanadium carbo-nitride volume fraction in BV steel (Fe-0.14C-2.1Mn-0.37Si-0.06V-0.002B), and b) Equilibrium Titanium carbo-nitride volume fraction in BT steel (Fe-0.13C-1.9Mn-0.3Si-0.03Ti-0.002B).

To understand the effect of manganese on austenite formation, a comparative ThermoCalc one axis equilibrium simulation was done on two steel compositions with 1% and 1.5% higher manganese than the original BV steel composition (Base). **Figure 5.5** shows the comparison of equilibrium volume fraction of all the three steel alloys. The A_{e1}-A_{e3} temperature ranges for Base alloy, Base + 1% Mn alloy, and Base + 1.5% Mn alloy were found to be 934-1082 K, 887-1053 K, and 858-1040 K respectively. Moreover, the martensite start temperatures for Base + 1% Mn alloy, and Base + 1.5% Mn alloy were found to be decreased by 36 K and 50 K respectively. This decrease in

critical temperatures is attributed to the increase in austenite stability with the increase in manganese concentration. Moreover, manganese widens α + γ + cementite temperature region, thereby enabling higher percentage of austenite formation in this three phase region. Additionally, formation of martensite at low temperatures in high Mn alloys increases the dislocation content in the ferrite phase adjacent to martensite islands [31].
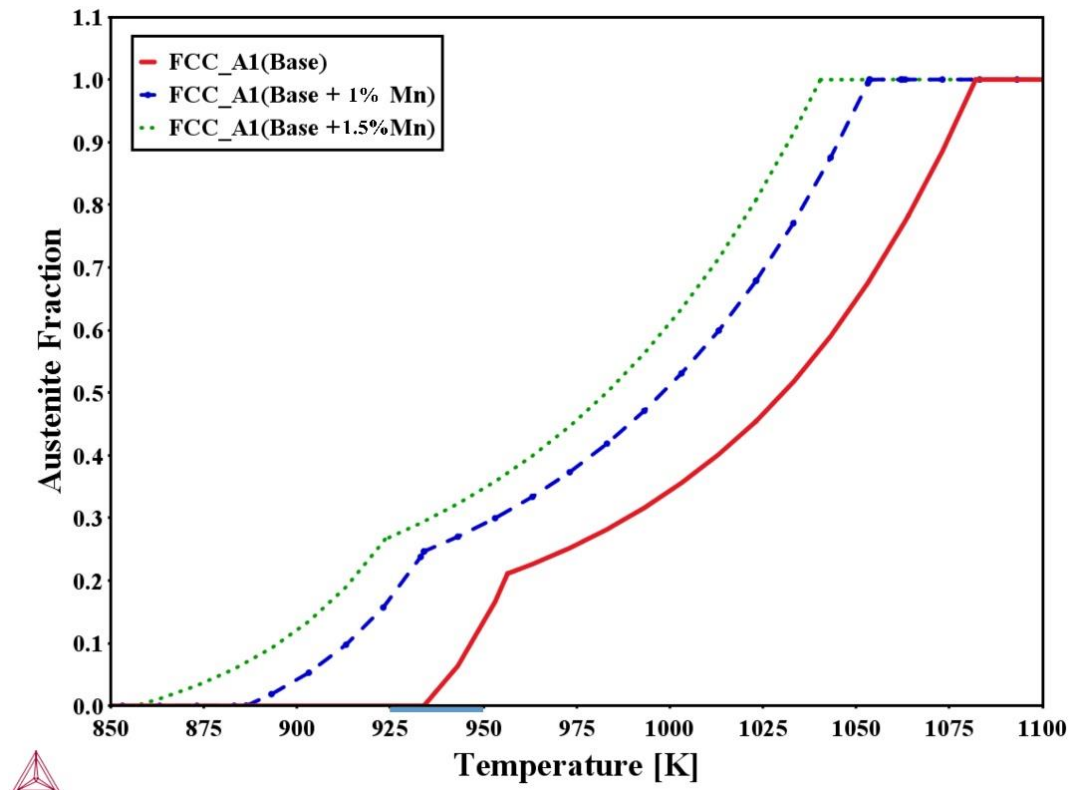
Figure 5. 5: Comparison of equilibrium austenite fraction of the BV steel composition with steels with higher manganese concentration (1% Mn and 1.5% Mn).

5.1.2. Precipitate analysis

To understand the formation of vanadium nano-carbides in a Fe-C(0.12-0.14)-V(0.05-0.1) system, an isothermal precipitate analysis at 750 ^{0}C (inter-critical temperature) was done using Prisma precipitation simulation mode in the ThermoCalc software. Ferrite was chosen as the matrix phase and the vanadium carbides as the precipitate phase. All the remaining settings such as nucleation sites and the interfacial energy are accepted from the default settings. **Figure 5.6** shows the variation in number density, mean radius and homogenous nucleation rate as a function of time at 750 ^{0}C in the ferrite matrix. It can be seen that the mean radius of the precipitates are very small and

grow very slow during the initial holding times. However, with the increase in holding time, the mean radius significantly increased. Moreover, the number density initially increased rapidly until a very short holding time and then gradually decreased with time. This is because the homogenous nucleation rate is initially very high during the short holding times and thereby increases the number density of the precipitates (**Figure 5.6**). However, at longer holding times the homogenous nucleation rate decreases and the growth of precipitates occurs by consumption of tiny precipitates. Therefore, this decreases the overall number density and also increases the overall mean radius of the precipitates. **Figure 5.7** shows the variation in size distribution at 750 ^{0}C for 0s, 10s, 60s and 900s in the ferrite matrix. It can be seen that the peak of the size distribution decreases and moves towards higher mean radius with increase in soaking time from 0 seconds to 900 seconds.
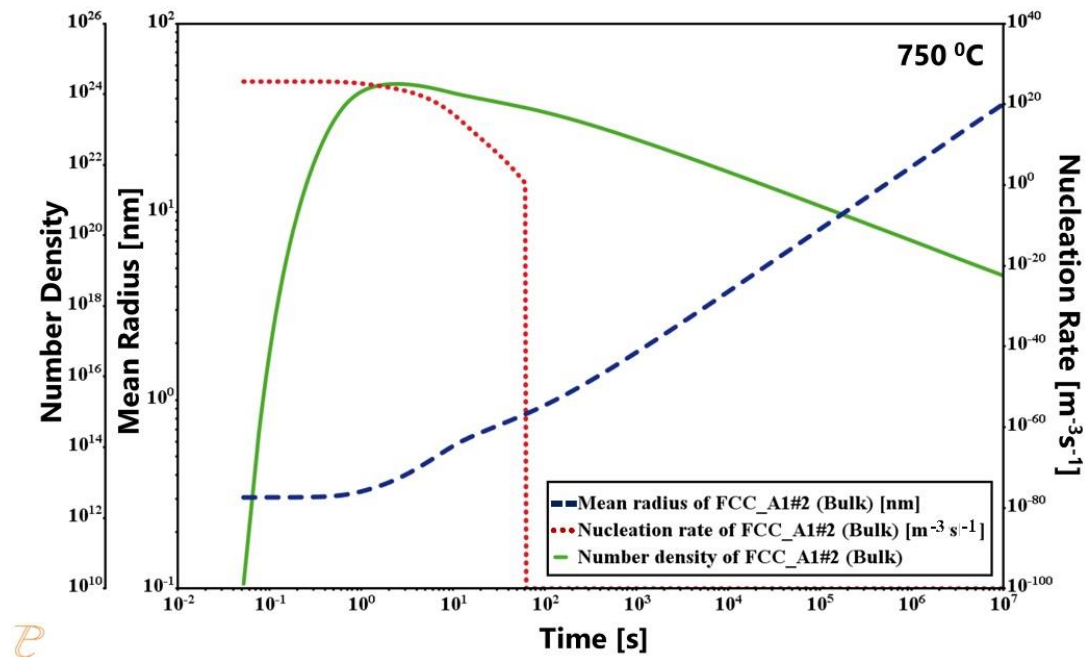
Figure 5. 6: ThermoCalc precipitate simulation showing number density, mean radius and nucleation rate of vanadium carbide precipitates at 750 ^{0}C as a function of time.
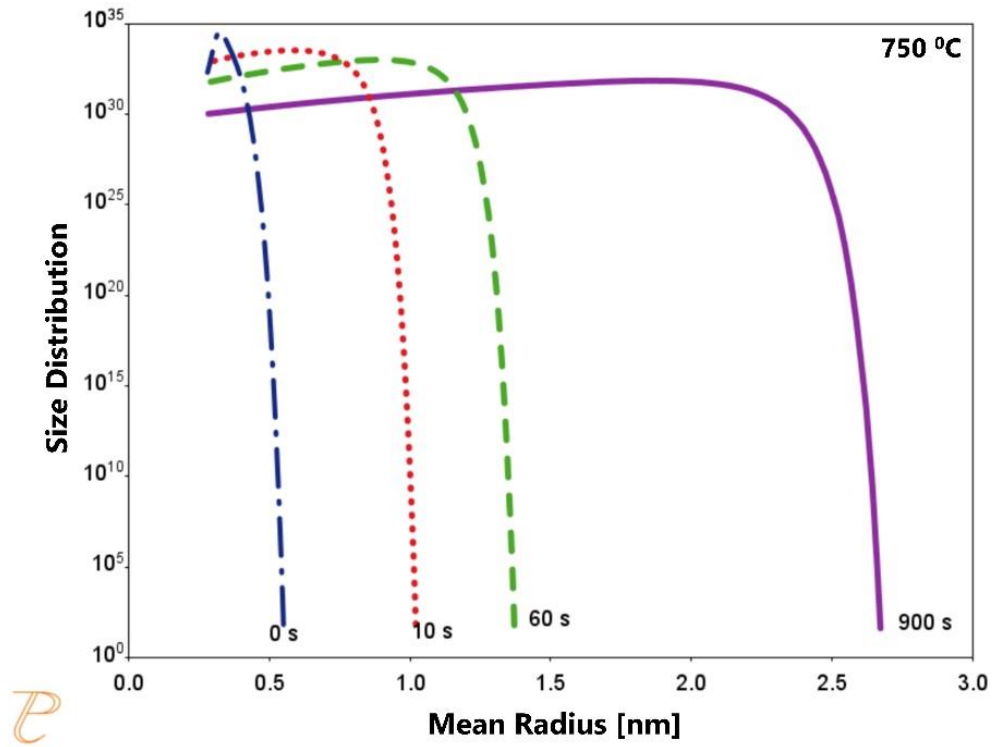
Figure 5. 7: ThermoCalc simulation of size distribution of Vanadium carbides at 750 ^{0}C held for 0, 10, 60 and 900 seconds.

5.2. Microstructure analysis and Hardness Measurements

Figure 5.8 (a-d) shows the microstructural images of hot rolled (HR) and cold rolled (CR) microstructures (50%, 60% and 75%) of the BV steel. **Figure 5.8 e)** shows the corresponding micro-hardness (HV 0.5) values. The ferrite grain size in the HR steel was calculated using line-intercept method and was found to be 7 μm. The pearlite volume fraction was calculated using point counting method and was found to be 21 ± 2 %. It can be seen that with the increase in cold reduction percentage, the deformation of both the ferrite grains and the pearlite colonies increases. However, ferrite grains deform to a higher aspect ratio when compared to pearlite colonies, due to its higher ductility and softness. **Figure 5.9** shows the high magnification microstructural image of BVCR 50% steel. It can be seen that the fragmented cementite particles are generally aligned along the rolling direction. Moreover, it can also be seen that some percentage of cementite particles are present at the ferrite grain boundaries and ferrite grain interiors. The increase in hardness values with the increase in cold reduction percentage is due to the increase in stored deformation energy

83

through higher dislocation density and higher residual stresses. **Figure 5.10 (a-d)** shows the microstructural images and hardness measurements of HR and CR (50%, 60% and 75%) BT steels. The ferrite grain size was found to be 9 μm and the pearlite volume fraction was found to be 31 ± 2 %. As expected the hardness values increased with the increase in the cold reduction percentage.
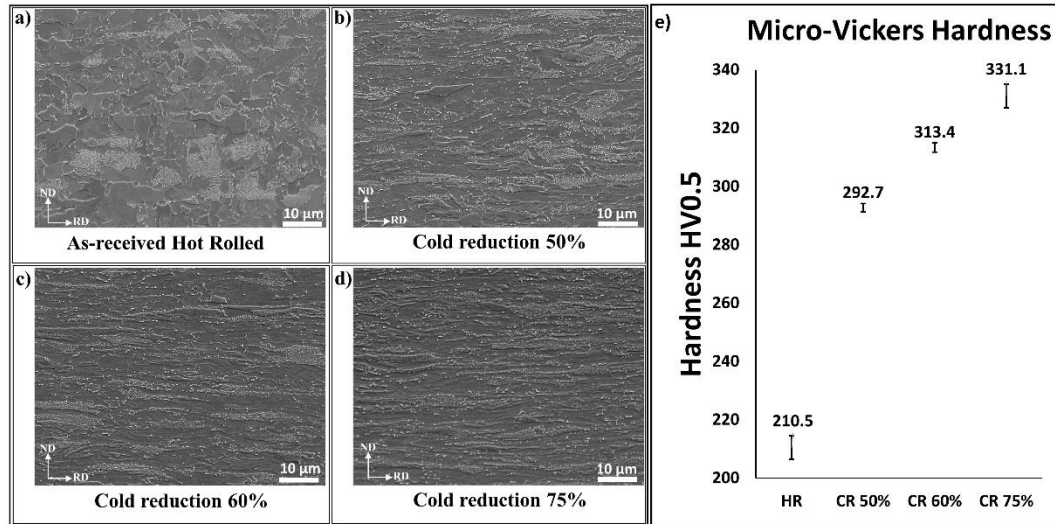
Figure 5. 8: Microstructural images of a) BV HR steel, b) BV CR50% steel c) BV CR60% steel, and d) BV CR75% steel with the e) Corresponding micro-hardness measurements [198]. BV steel composition - (Fe-0.14C-2.1Mn-0.37Si-0.06V-0.002B)
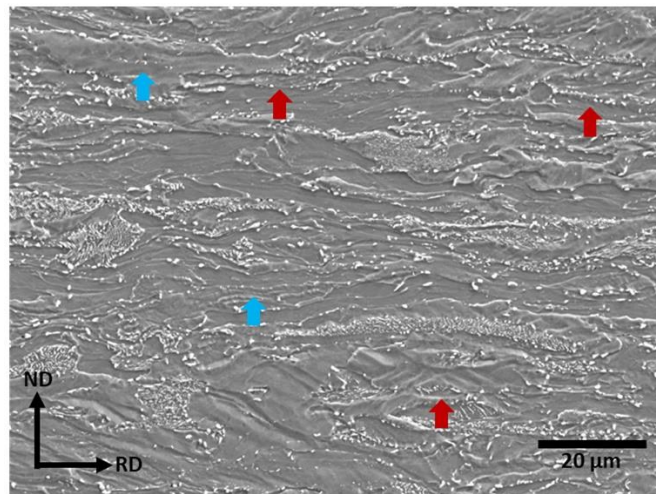
Figure 5. 9: SEM microstructural image of BVCR 50% steel with fragmented cementite particles at ferrite grain boundaries (red arrow) and ferrite grain interiors (blue arrow). BV steel composition - (Fe-0.14C-2.1Mn-0.37Si-0.06V-0.002B).
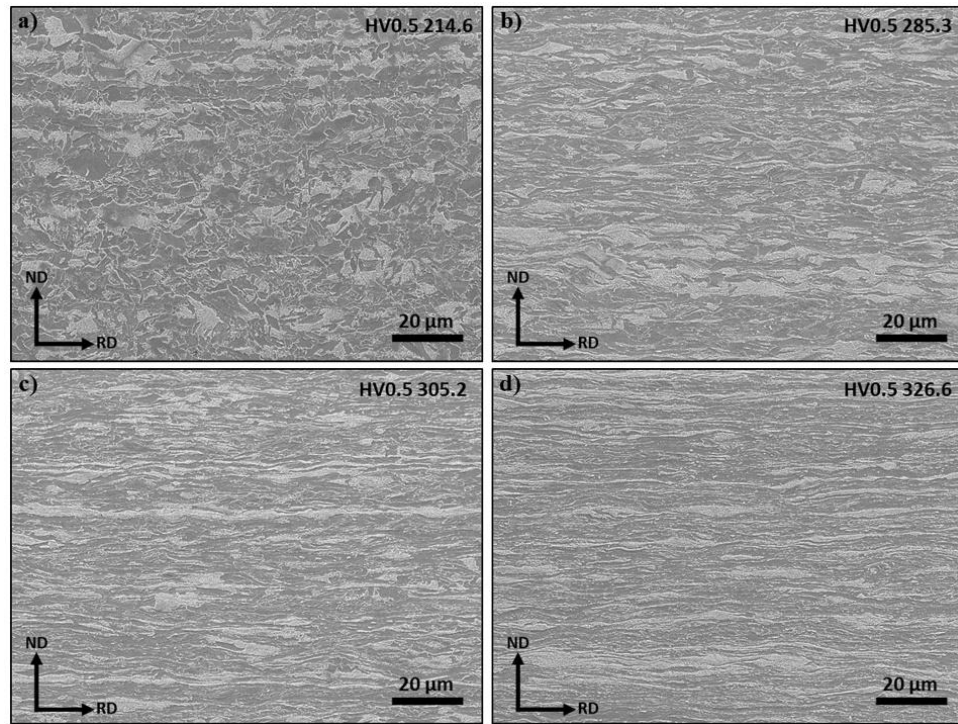
Figure 5. 10: SEM microstructural images and hardness values of a) BTHR steel, b) BTCR 50% steel, c) BTCR 60% steel, and d) BTCR 75% steel. BT steel composition - ((Fe-0.13C-1.9Mn-0.3Si-0.03Ti-0.002B)).

5.3. Inclusion analysis.

Figure 5.11 shows the SEM EDX map of the BVHR steel with the presence of alumina (Al_2O_3) inclusions. It was observed that the alumina inclusions are generally spherical in shape with an average size of 6 ± 3 µm. Aluminium is generally added to deoxidize the steel which leads to the formation of alumina inclusions. Moreover, complex inclusions such as CaS-Al_2O_3 inclusions were also observed. The spherical nature of Al_2O_3 inclusions can be attributed to the presence of small amount Ca in the steel composition. **Figure 5.12** shows the SEM EDX map of the BTHR steel. It can be seen that along with alumina inclusions, cuboidal titanium nitride inclusions (TiN) are also present in this steel. **Figure 5.13** shows the SEM EDX map of BVCR 50% steel. It was observed that the alumina inclusions in cold reduced samples are deformed and are elongated along the rolling direction. The presence of TiN inclusions can be attributed to its formation temperature (1481 ^{0}C) being near to the steel solidification temperature (see **Figure 5.4 b**)). This indicates that the majority of

titanium in this study won't be in the solid solution and therefore wouldn't have influence in retarding the recrystallization process. Therefore, in this study, vanadium micro-alloyed steel (BV steel) was used for the study of effect of overlap of high temperature mechanisms during inter-critical annealing process.
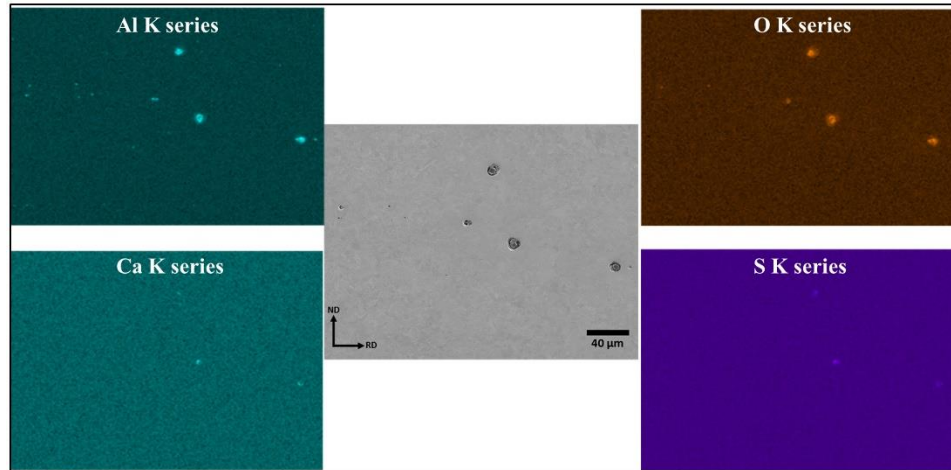
Figure 5. 11: SEM EDX map of BVHR steel (Fe-0.14C-2.1Mn-0.37Si-0.06V-0.002B).
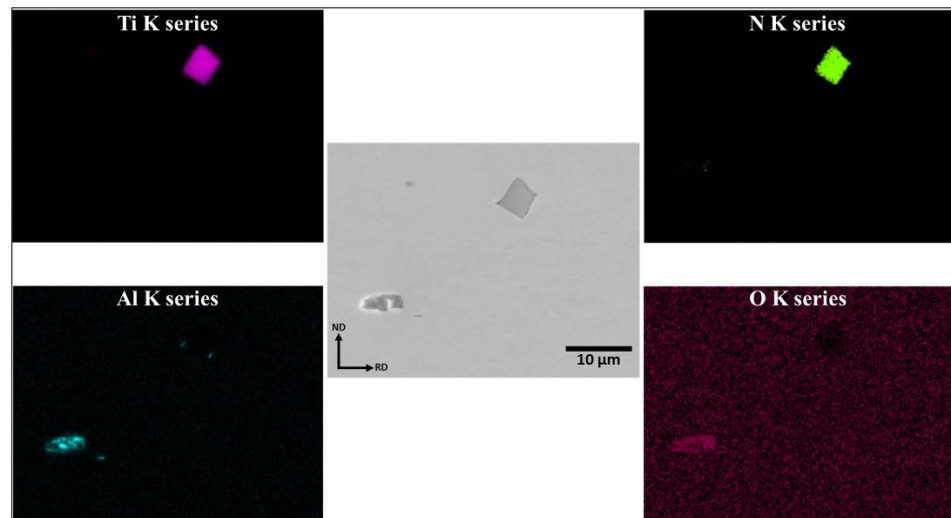
Figure 5. 12: SEM EDX map of BTHR steel (Fe-0.13C-1.9Mn-0.3Si-0.03Ti-0.002B).
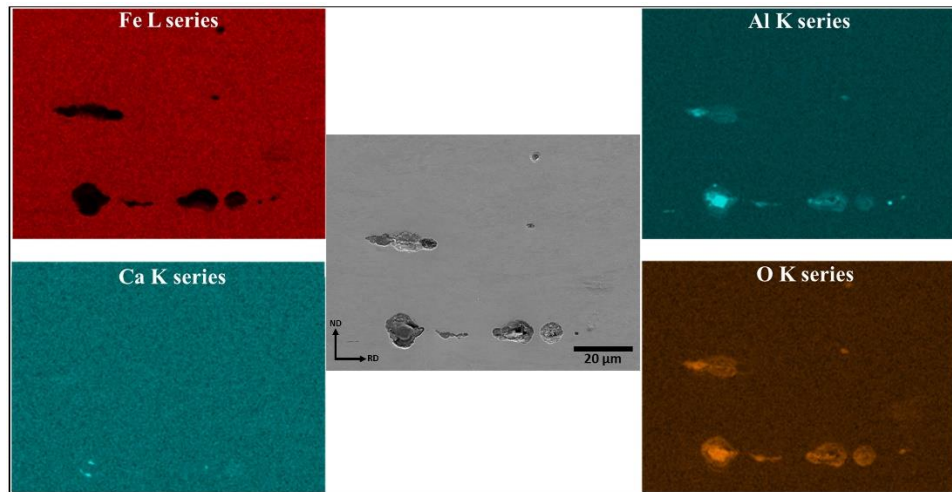
Figure 5. 13: SEM EDX map of BVCR 50% steel (Fe-0.14C-2.1Mn-0.37Si-0.06V-0.002B).

Chapter 6 - Effect of heating rate and cold reduction on the recrystallization process

In the heating step of DP steel manufacture, processes such as ferrite recrystallization, and cementite spheroidization happen consecutively and/or concurrently with the austenite formation process. The amount of overlap between these processes depends upon the chemical composition, initial microstructures, cold reduction percentage and the heating rate employed during the CAL process. In order to systematically understand the effect of the concurrent mechanisms on the microstructural evolution it is critical to establish the heating rates required to obtain a predefined amount of overlap, especially between ferrite recrystallization and austenite formation processes. This chapter discusses the effect of percentage of cold reduction on the recrystallization kinetics of the BVCR steels. Additionally, the effect of heating rate on the recrystallization process is also discussed for all the cold reductions (50%, 60% and 75%). Most importantly, a continuous heating rate model based upon the Johnson-Mehl-Avrami-Kolmogorov (JMAK) equation is developed to get the heating rates required for a predefined amount of overlap to happen between ferrite recrystallization and austenite formation processes.

6.1 Recrystallization kinetics in BVCR 50% steel

Figure 6.1 (a, b, c, and d) shows the microstructural images of BVCR 50% samples heat treated at 650 ^{0}C for a holding time of 3 s, 30 s, 100 s, and 300 s respectively. The black arrows in the 3 s, 30 s and 100 s samples indicate the formation of tiny equi-axed recrystallized grains along the ferrite grain boundaries. It can be seen that for the heat treated for 3 s, a very tiny fraction of recrystallization happened and the majority of the microstructure is still in the deformed condition. With the increase in time, the amount of recrystallized grains was found to be increased (**Figure a-d**) and visually just a tiny fraction of un-recrystallized grain were remaining in the sample annealed for 300 s (indicated by red arrow).
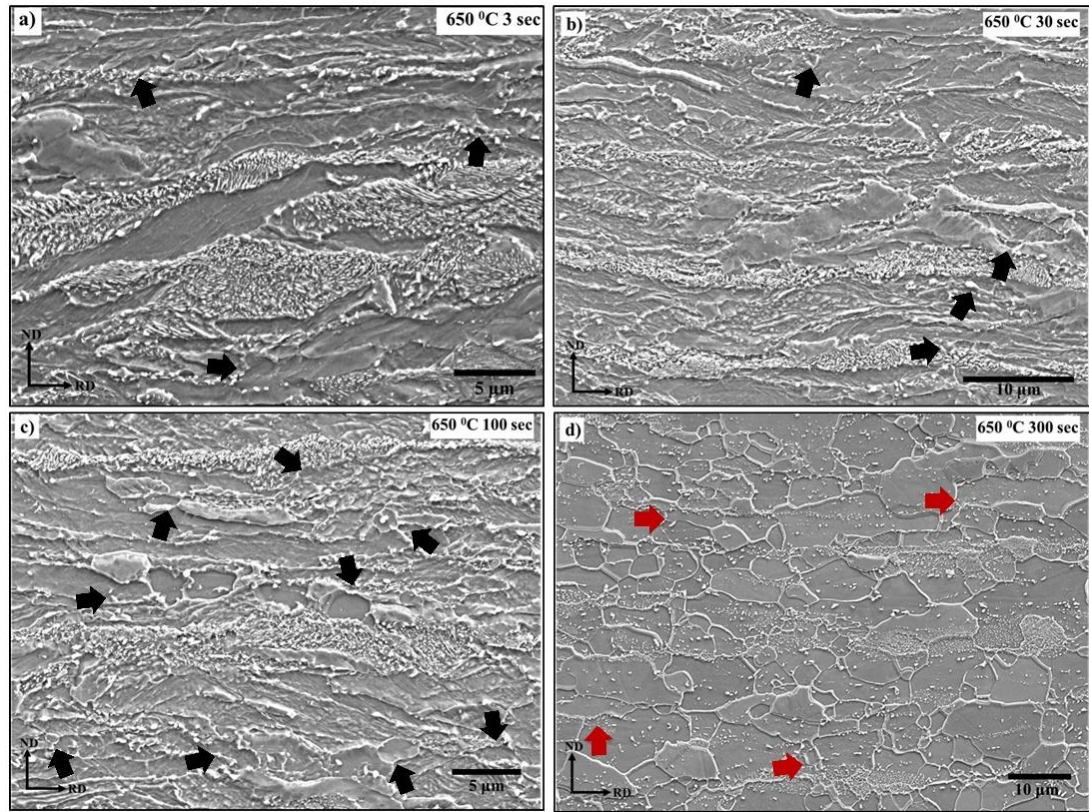
Figure 6. 1: SEM microstructural images of BVCR 50% steel heat treated at 650 ^{0}C for a soaking time of a) 0 s, b) 30 s, c) 100 s, and d) 300 s. Black arrow indicate recrystallized grains and red arrow indicate un-recrystallized grains. BV steel composition - (Fe-0.14C-2.1Mn-0.37Si-0.06V-0.002B).

The progress of recrystallization was calculated by the accompanied softening of the ferrite grains, by using the **Eq. 4.1** (**Chapter 4**). It should be noted that the increase in hardness due to carbon dissolution and decrease in hardness due to grain growth at high temperatures are negligible when compared to the decrease in hardness due to the progress of recrystallization process. **Figure 6.2** shows the progress of the recrystallization as a function of soaking time for the samples heat treated at 650 ^{0}C and 675 ^{0}C. As expected the recrystallization fraction increased with the increase in soaking time for both the temperatures. Moreover, with the increase in temperature, the degree of recrystallization has increased for all the soaking times. This is because the recrystallization process is a diffusion driven process and therefore the increase in temperature increases its kinetics. **Figure 6.3 (a, b)** shows the microstructural images of BVCR 50% steel heat treated for a soaking time of 300 s at 650 ^{0}C and 675 ^{0}C respectively. It can be seen that the sample heat treated at 650 ^{0}C still consists of a tiny

fraction of unspheroidized fragmented cementite lamella structure. However, at the higher temperature of 675 ^{0}C there are very limited amount of fragmented cementite particles present in the microstructure. Both samples contain spheroidized carbides which are present at not only grain boundaries but also at grain interiors. The intra-granular spheroidized carbides could be formed by the growth of the recrystallization front into the lamella structure and thereby leaving a trail of spheroidized carbides [49]. It can also be noticed that the spheroidized cementite particles are generally aligned along the rolling direction for both the samples.
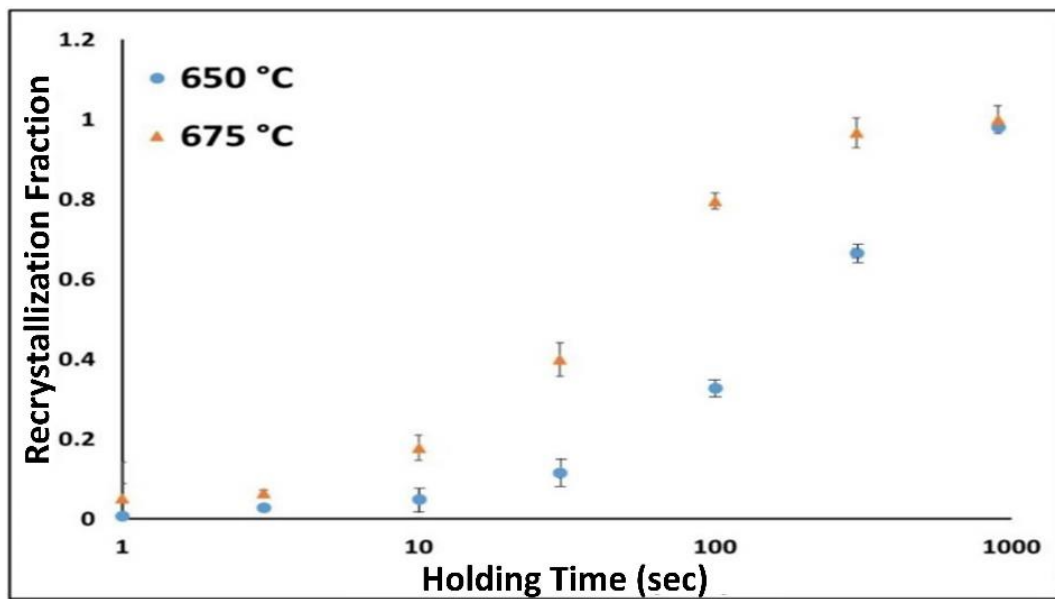
Figure 6. 2: Recrystallization kinetics determined through hardness measurements for BVCR 50% steel heat treated at 650 ^{0}C and 675 ^{0}C. BV steel composition - (Fe-0.14C-2.1Mn-0.37Si-0.06V-0.002B).
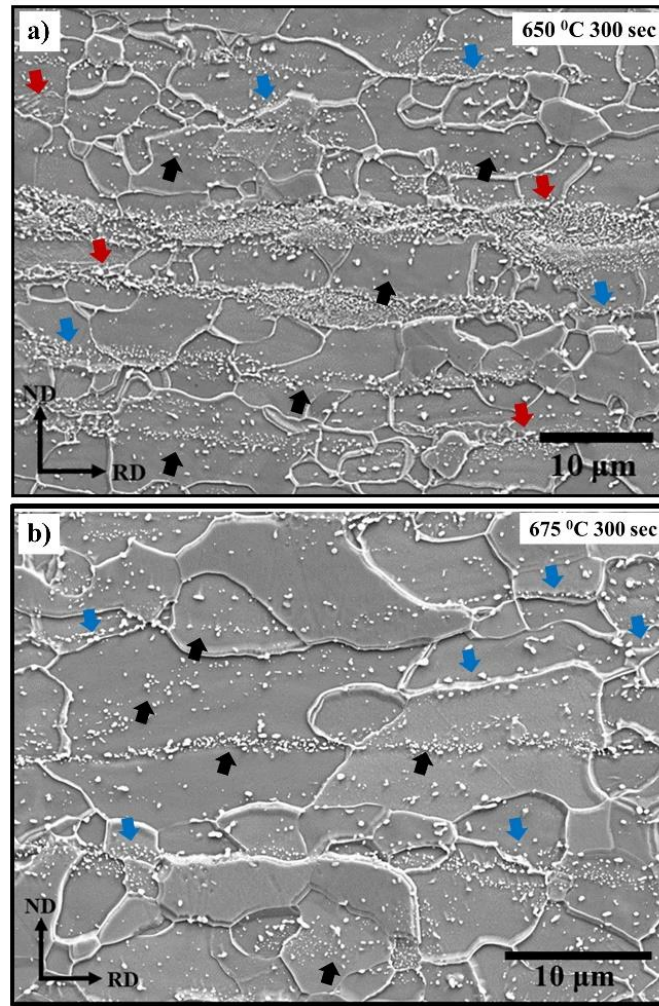
Figure 6. 3: SEM microstructural images of BVCR 50% steel heat treated at a) 650 ^{0}C and b) 675 ^{0}C for 300 s. Red arrow indicates fragmented cementite particles. Blue and black arrow indicates spheroidized cementite particles at grain boundaries and grain interiors respectively. BV steel composition - (Fe-0.14C-2.1Mn-0.37Si-0.06V-0.002B).

6.2 Effect of cold reduction on recrystallization kinetics

Figure 6.4 a) compares the recrystallization kinetics at 650 ^{0}C for BVCR steels with the cold reductions of 50 %, 60 %, and 75 %. It is evident that with the increase in cold reduction the fraction of recrystallization completed has increased for all the soaking times. **Figure 6.4 (b, c)** shows the microstructural images of BVCR 50% and BVCR 75% samples heat treated at 650 ^{0}C for 900 s and 300 s respectively. It can be seen that even though there is a huge difference in the soaking times, the type/shape

of recrystallization grains look almost similar. This is due to the fact that with the cold reduction the amount of stored deformation increases and therefore the driving force for the recrystallization process also increases. Moreover, with the increase in deformation the amount of ferrite grain boundary area increases and therefore the potential nucleating sites for the recrystallized grains also increases. These two factors contribute to the increase in recrystallization kinetics for higher cold reductions. **Figure 6.5 (a, b)** shows the microstructural images of BVCR 60% and BVCR 75% steels heat treated at 650 ^{0}C for 10 seconds. It can be seen that a significant amount of cementite spheroidization (black arrow) had already completed in the sample with higher cold reduction (CR 75%). Whereas significant amount of fragmented cementite lamella (red arrow) is still preserved in the sample with lower cold reduction of 60%. This rapid spheroidization at higher cold reductions can be attributed to the increase in fragmentation and increase in dislocation density in the deformed microstructure. These two factors contribute to the increase in carbon diffusion and therefore enhance rapid progress in spheroidization process. It can also be seen from **Figure 6.5** that the ferrite recrystallization is preferentially happening along the deformed ferrite grain boundaries and the ferrite in the prior pearlitic colonies undergo sluggish recrystallization. This sluggish recrystallization of ferrite in prior pearlitic colonies can be attribute to the pinning action induced by the cementite particles. This pinning action decreases the grain boundary mobility of ferrite grains and therefore causes delay in the progress of recrystallization process.
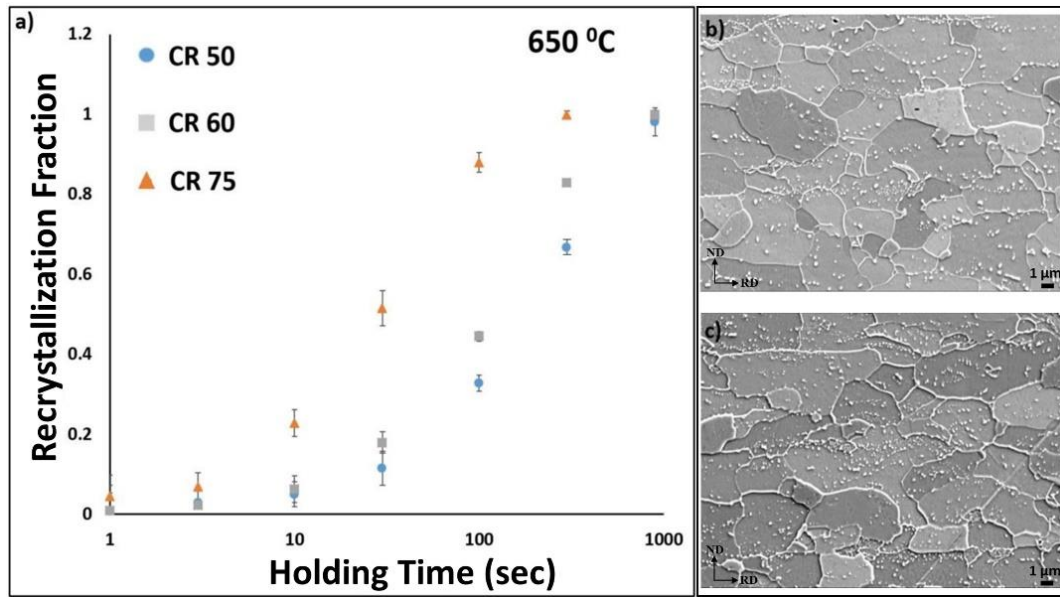
Figure 6. 4: a) Recrystallization kinetics determined through hardness measurements for BVCR 50%, 60% and 75% steels heat treated at 650 ^{0}C, (b, and c) SEM microstructural images of BVCR 50%, and 75% samples heat treated at 650 ^{0}C for soaking times of 900 s and 300 s respectively. BV steel composition - (Fe-0.14C-2.1Mn-0.37Si-0.06V-0.002B).
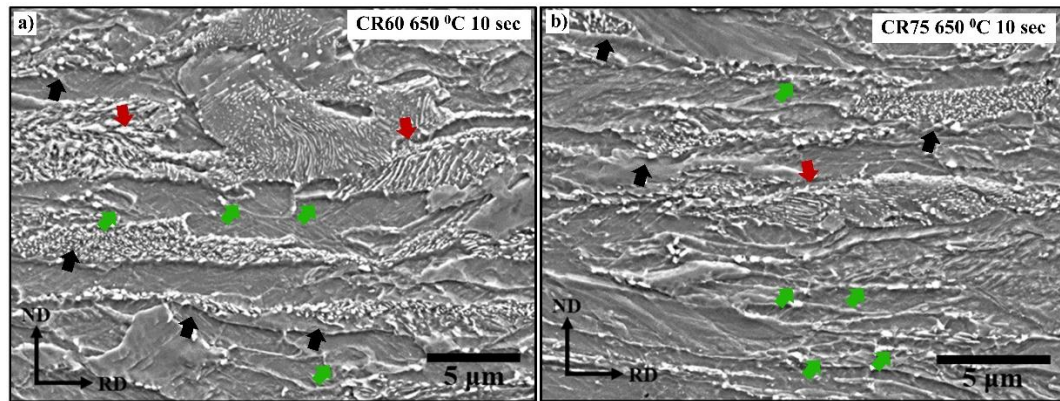
Figure 6. 5: SEM microstructural images of a) BVCR 60% and b) BVCR 75% steels heat treated at 650 ^{0}C and 10 s. Red and black arrow indicate fragmented and spheroidized cementite particles. Green arrow indicates recrystallized grains. BV steel composition - (Fe-0.14C-2.1Mn-0.37Si-0.06V-0.002B).

6.3 Determination of Johnson-Mehl-Avrami-Kolmogorov parameters

The experimentally obtained recrystallization kinetics can be suitably fit into the JMAK equation shown in the **Eq. 6.1** below. The JMAK equation represents the isothermal kinetics of recrystallization process as a function of soaking time (t) [132]. For JMAK model to be applicable, the transformation should progressively happen with continuous substitution of product phase on the parent phase where the volume of the formed grain is much smaller than the volume of the whole system [199]. The JMAK model assumes that the nucleation occurs randomly throughout the material. It also assumes that the growth rate is uniform in all directions and is unaffected by the extent of transformation. These assumptions are mostly applicable throughout the progress of recrystallisation process in metal alloys and is extensively used in the literature for evaluating the recrystallisation kinetics of low carbon steels [132,166,200]

$$X = 1 - exp^{-bt^n} \dots\dots\dots\dots\dots\dots\dots\dots\dots\dots\dots\dots\dots\dots\dots\dots\dots\dots\dots\text{...}\textbf{Eq. 6.1}$$

Where b is defined as **Eq. 6.2** below:

$$b = b_0 exp^{-Q}/_{RT} \dots\dots\dots\dots\dots\dots\dots\dots\dots\dots\dots\dots\dots\dots\dots\dots\dots\dots\dots\textbf{Eq. 6.2}$$

In this equation, X represents the fraction of recrystallization already competed (0 to 1), t represents the soaking time of the heat treatment, n represents the Avrami exponent, b_0 represent the JMAK constant, Q represents the activation energy required for the recrystallization process, T represent the absolute annealing temperature, and R represents the universal gas constant. The activation energy Q, the JMAK constant b_0, and the Avrami exponent n are calculated by rearranging the **Eq. 6.1** and applying a logarithm on both the sides of the equation. The modified equation is in the form of a straight line and is shown in the **Eq. 6.3** below. It should be noted that the double log function $(\ln(-\ln(1-X)))$, will significantly decrease the difference between the recrystallization fraction (X) and therefore can potentially lead to errors.

$$\ln(-\ln(1-X)) = n \ln t + \ln b \dots\dots\dots\dots\dots\dots\dots\dots\dots\dots\dots\dots\dots\dots.\textbf{Eq. 6.3}$$

$$y \qquad = mx \quad + \quad c \dots\dots\dots\dots\dots\dots\dots\dots\dots\dots\dots\dots\dots\text{..}\dots\text{..}\textbf{Eq. 6.4}$$

Eq. 6.4 represents the equation for the general form of a straight line. Therefore, the Avrami constant n is directly evaluated from the slope of **Eq. 6.3** and the activation energy Q and JMAK constant b_0 is calculated using the **Eq. 6.2** and the intercept of the **Eq. 6.3**. **Figure 6.6 a)** shows the straight line graphs of **Eq. 6.3** for the BVCR 50% samples heat treated at 650 ^{0}C and 675 ^{0}C. The n value is calculated by averaging the slopes of the two graphs and was found to be 0.87. Similarly, b_0 value was found to be 1.3 x 10^{17}/s. The activation energy (Q) required for the recrystallization process was found 339 kJ/mole. It should be noted that this value is peculiarly very high when compared to the activation energy for the self-diffusion of α-iron (251 kJ/mole) [201]. This increase in activation energy can be attributed to the effect of alloying additions on the progress of recrystallization process. The presence of high concentration of Mn (1.8-2.2 wt%), and the precipitate forming V (0.05-0.1 wt%) elements induce solute drag effect and grain boundary pinning action [193,200]. This increases the activation energy required for the progress of recrystallization process. **Figure 6.6 b)** shows the experimentally evaluated recrystallization fractions fitted with the obtained JMAK equation. It can be seen that the model fits with the actual recrystallization fractions with slight deviations. This deviations from the model is generally seen with the continuously heated material [132].
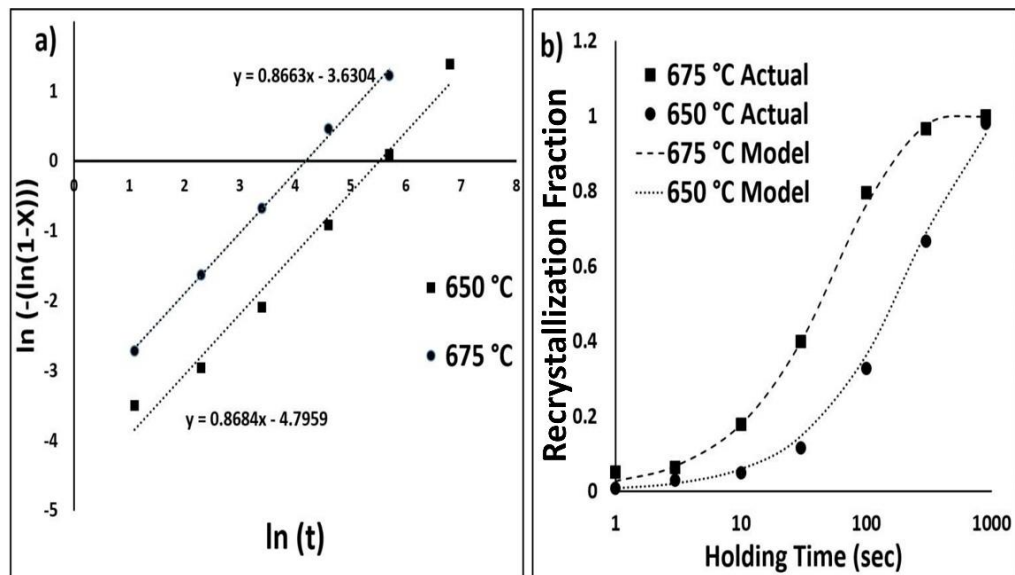
Figure 6. 6: a) JMAK straight line graphs for BVCR 50% steel heat treated at 650 ^{0}C, and 675 ^{0}C, and b) JMAK plot fit with the experimentally obtained recrystallization fractions for BVCR 50% steel heat treated at 650 ^{0}C, and 675 ^{0}C. BV steel composition - (Fe-0.14C-2.1Mn-0.37Si-0.06V-0.002B).

Similarly, using the experimentally obtained recrystallization fractions all the JMAK constants are evaluated for the BVCR 60% and BVCR 75% steels. **Figure 6.7 a)** compares the linearized JMAK plots for the three cold reduction (50 %, 60 %, and 75 %) with the corresponding slope values. **Figure 6.7 b)** shows the various JMAK constants obtained for all the cold reductions. It should be noted that with the increase in cold reduction the linearized plot moved towards the left side. This type of behaviour is well reported in the literature [117]. Using the calculated JMAK constants, the experimentally obtained recrystallization fractions for all the three cold reductions are fitted with the JMAK equation. **Figure 6.7 c)** shows the JMAK fitted plots for the three cold reductions at 650 ^{0}C.

Material	Activation energy, Q (kJ/mol)	Avrami exponent n	JMAK constant b_0 (/s)
BV 50% CR	339	0.87	1.3×10^{17}
BV 60% CR	329	0.94	3.73×10^{16}
BV 75% CR	326	0.98	7.42×10^{16}
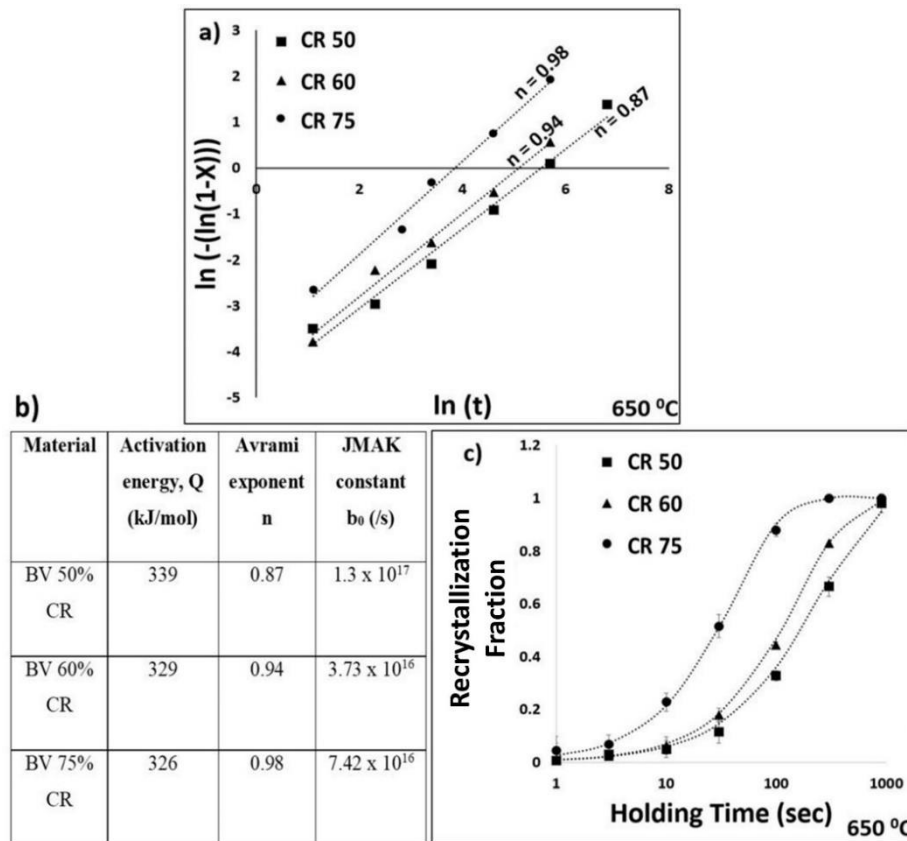
Figure 6. 7: a) JMAK straight line graphs for the three cold reductions heat treated at 650 ^{0}C, b) Calculated JMAK constants for all the cold reductions, and c) JMAK plot fit with the experimentally obtained recrystallization fractions for the three cold reductions heat treated at 650 ^{0}C. BV steel composition - (Fe-0.14C-2.1Mn-0.37Si-0.06V-0.002B).

6.4 Determination of critical temperatures

In order to evaluate the percentage of recrystallization completed before the onset of austenite formation, it is necessary to identify the ferrite recrystallization start temperature and the austenite start temperature for a given heating rate. For this purpose, heat treatments in the dilatometer furnace was used to track the change in the length accompanied with the phase transformations. **Figure 6.8 a)** shows the dilation curve for the BVCR 50% steel heat treated at a heating rate of 10 ^{0}C/s to the fully austenitic temperature. As expected with the increase in temperature, the length of the sample initially increased. However, there are three distinct temperatures at which the dilation response changes. Firstly, the deviation in linearity of the dilating curve at 625 ^{0}C. This is considered to be the recrystallization start temperature (RxT). This was determined by drawing a tangent to the dilation curve below 500 ^{0}C and the point where the tangent stops overlapping the dilation curve was considered as RxT temperature. Secondly, the sharp decrease in the length at 722 ^{0}C. This indicates to the onset of austenite formation. Ferrite has a BCC crystal structure and austenite has a close-packed FCC crystal structure. Therefore, the transformation from ferrite to austenite at A_{c1} temperature causes a decrease in the overall volume of the sample and therefore decreases the length in the dilation curve. The third distinct temperature is the A_{c3} temperature where a fully austenitic microstructure is formed and the increase in temperature continuously increases the length of the sample. The deviation in the linearity at the ferrite recrystallization start temperature can be attributed to the anisotropy induced by the newly formed recrystallized grains. This anisotropy is reported to be caused due to the change in texture of ferrite grains on the onset of ferrite recrystallization [202]. Moreover, it is also reported in the literature that the stress applied on the sample in the push rod type of dilatometer causes a recrystallization induced plasticity [166]. This causes directional movement of atoms or defects during recrystallization and therefore causes deviation in linearity at the onset of the process. Moreover, to confirm that this deviation in linearity corresponds to the onset of ferrite recrystallization process, samples were heated up to RxT and RxT + 5 ^{0}C temperatures followed by quenching. **Figure 6.8 (e, f, and g)** shows the microstructural images of BVCR 50%, 60% and 75% samples heated at 10 ^{0}C/s up to RxT and RxT + 5 ^{0}C temperatures followed by quenching. It can be seen that tiny recrystallized grains started to nucleate at the ferrite grain boundaries. Moreover, the

clear decrease in the hardness values also indicate the onset of ferrite recrystallization at the first deviation from the linearity in the dilation curves. Similarly, the RxT and A_{c1} temperatures were evaluated for the BVCR 50% steels heated at different heating rates of 1 ^{0}C/s, 10 ^{0}C/s, 100 ^{0}C/s, and 500 ^{0}C/s. **Figures 6.8 b), and c)** show the change in RxT and A_{c1} temperatures respectively with respect to heating rate employed. It can be seen that both the recrystallization and austenite formation processes being thermally activated processes, increase in heating rate caused increase in both the temperatures. This type of behaviour is well reported in the literature [166]. However, the increase in RxT temperature is significantly higher than the increase in A_{c1} temperatures. In the similar way, the RxT and the A_{c1} temperatures are evaluated for BVCR 60% and BVCR 75% steels and are shown in **Figure 6.8 d)**. For the same heating rate, increase in cold reduction percentage decreased the recrystallization start temperature. This is because of the fact that the increase in cold reduction increases the stored deformation energy and the ferrite grain boundary area and therefore causes the increase in driving force for the recrystallization. It should be noted that for the same heating rate, increase in cold reduction didn't cause much effect on the A_{c1} temperature.
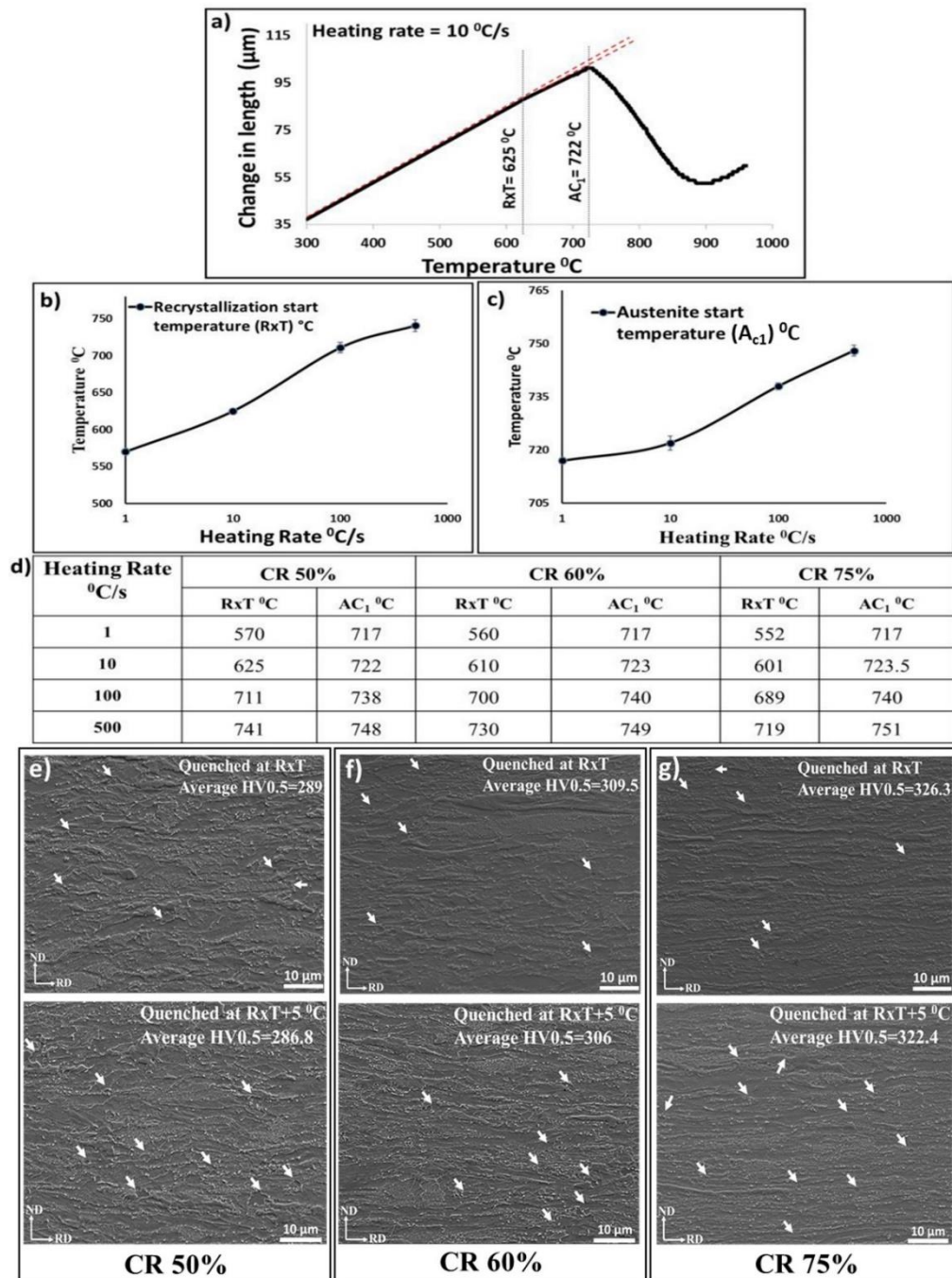
Figure 6. 8: a) Dilation curve for the BVCR 50% steel heated at a heating rate of 10 ^{0}C/s, (b, and c) Variation in b) RxT and c) A_{c1} temperatures with respect to the applied heating rate, d) RxT and Ac1 temperature values for all the three cold reductions with respect to the heating rate employed, and (e, f, and g) SEM microstructural images of e) BVCR 50%, e) BVCR 60%, and e) BVCR 75% steels heat treated to RxT and RxT + 5 ^{0}C at a heating rate of 10 ^{0}C/s. White arrow indicate the presence of tiny recrystallized grains. BV steel composition - (Fe-0.14C-2.1Mn-0.37Si-0.06V-0.002B).

6.5 Continuous heating rate model

A continuous heating rate model has been developed using the JMAK equation (**Eq 6.1**), to calculate the fraction of ferrite recrystallization completed before the start of austenite formation. The JMAK equation is differentiated with respect to time and rearranged to obtain a first order differential equation as shown in the equations **Eq. 6.5 and Eq. 6.6** below.

$$\frac{dX}{dt} = bn\,exp^{-bt^n}\,t^{n-1} \quad \dotfill Eq.\,6.5$$

$$\frac{dX}{dt} = bn(1-X)t^{n-1} \quad \dotfill Eq.\,6.6$$

The **Eq. 6.6** is further integrated with respect to time to obtain an integration function of recrystallization fraction (X), time and JMAK constants as shown below in the equation **Eq. 6.7**. It should be noted from equation 6.2 that b is a function of time (t).

$$\ln(1-X) = -n\int_0^t bt^{n-1}\,dt \quad \dotfill Eq.\,6.7$$

The additive principle of continuous heating is applied, where the increase in temperature at a particular heating rate (H.R) is subdivided into a series of infinitesimally small isothermal soaking times. This is represented in equation **Eq. 6.8** where the heating rate is defined as the rate of change in temperature from the recrystallization start temperature. This equation (**Eq. 6.8**) is further simplified by differentiating on both sides as shown in **Eq. 6.9**.

$$H.R. = \frac{T - RxT}{t} \quad \dotfill Eq.\,6.8$$

$$\Rightarrow dt = \frac{dT}{H.R.} \quad \dotfill Eq.\,6.9$$

Further rearrangement of integrated JMAK equation (**Eq. 6.7**), and the substitution of **Eq. 6.9** into it gives a relation shown below as **Eq. 6.10**.

$$X = 1 - exp^{-n\int_{RxT}^T b\frac{(T-RxT)^{n-1}}{H.R.^{n-1}}\frac{dT}{H.R.}} \quad \dotfill Eq.\,6.10$$

Finally, the b value from the equation **Eq. 6.2** is substituted into the equation **Eq. 6.10** and was further rearranged to obtain the equation **Eq. 6.11** as shown below.

$$X = 1 - exp^{\left\{-\frac{b_0 n}{H.R.^n}\int_{RxT}^{T} exp\left(\frac{-Q}{RT}\right)[(T-RxT)^{n-1}]dT\right\}} \quad\dots\dots\dots\dots\dots\dots\dots Eq.\,6.\,11$$

For a given heating rate, the modified JMAK equation **Eq. 6.11**, gives the fraction of ferrite recrystallization completed before the onset of austenite formation. Using the RxT and A_{c1} temperatures from **Figure 6.8 d)**, the fraction of ferrite recrystallization completed before the onset of austenite formation is calculated for the three cold reductions. **Table 6.1** shows the fraction of ferrite recrystallization completed for the three cold reductions and four heating rates (1 ^{0}C/s, 10 ^{0}C/s, 100 ^{0}C/s, and 500 ^{0}C/s). For all the cold reductions, the increase in heating rate caused the decrease in the fraction of ferrite recrystallization before the austenite formation. This is because of the fact that the increase in heating rate will significantly decrease the amount of time available for the recrystallized grains to nucleate and grow. Additionally, at higher rates the mobility of iron atoms will be sluggish as the time available for the progress of diffusion process will be limited. Moreover, for a given heating rate, it was found that as the percentage of cold reduction increased the fraction of ferrite recrystallization before the onset austenite formation also increased significantly. For instance, from **Table 6.1**, 26 % of recrystallization is completed for BVCR 50% steel heated at 10 ^{0}C/s, whereas 73% of recrystallization is already completed for BVCR 75% steel. This implies that extremely high heating rates are required for higher cold reductions (60 % and 75 %) to produce high amount of overlap between ferrite recrystallization and austenite formation processes. For instance, Azizi-Alizamini et al., used heating rates as high as 900 C/s to achieve overlap in 80% cold reduced ferrite pearlite steels [49]. Similarly, Massardier et al., and Petrov et al., required heating rates higher than 1000 ^{0}C/s to achieve complete overlap in 75% and 95% cold reduced steels respectively [157,203]. Therefore, the amount of ferrite recrystallization to be completed after the start of austenite formation will be significantly less in higher cold reductions. In this regard, among the cold reductions in this work, the BVCR 50% steels will produce maximum amount overlap for a given heating rate.

Table 6. 1: Fraction of **ferrite** recrystallization completed before the start of austenite formation for BVCR 50%, 60% and 75% steels. BV steel composition - (Fe-0.14C-2.1Mn-0.37Si-0.06V-0.002B)

Heating Rate	Ferrite recrystallization fraction before austenite formation		
	BVCR 50%	BVCR 60%	BVCR 75%
1 ^{0}C/s	0.82	0.92	1.00
10 ^{0}C/s	0.265	0.316	0.73
100 ^{0}C/s	0.07	0.075	0.22
500 ^{0}C/s	0.012	0.017	0.06

6.6 Determination of heating rates for a predefined amount of overlap

To predict the heating rates required to obtain a predefined amount of overlap between ferrite recrystallization and austenite formation, the equation **Eq. 6.11** is rearranged as shown below as the equation **Eq. 6.12**.

$$\% \, Overlap = \, exp\left\{-\frac{b_0 n}{H.R.^n}\int_{RxT}^{T} exp\left(\frac{-Q}{RT}\right)[(T-RxT)^{n-1}]dT\right\} \quad\text{............................} \quad Eq. 6.12$$

The above equation was used to predict the heating rates required to obtain a specific amount of overlap in the BVCR 50% steel. The various JMAK constants and the critical temperatures required for the calculations were taken from **Figures 6.7 b) and 6.8 d)** respectively. The heating rates required to obtain overlaps of 1%, 15%, 34%, 67%, 88%, and 99% were calculated to be 0.2 ^{0}C/s, 0.9 ^{0}C/s, 1.8 ^{0}C/s, 7 ^{0}C/s, 50.5 ^{0}C/s, and 511^{0}C/s respectively. Therefore, heating rates higher than 511 ^{0}C/s are required to obtain complete overlap between ferrite recrystallization and austenite

formation processes in BVCR 50% steel. However, it should be noted that these heating rates are not yet economically feasible in the present day industrial practice. Conventionally, industries use radiant tube furnaces for heating the material, which can achieve heating rates up to 10 ^{0}C/s. However, direct flame furnaces are also used in the present industries which can produce heating rates higher than 50 ^{0}C/s. To validate the heating rates obtained for the predefined amount of overlap, interrupted quench tests were done at the A_{c1} temperatures. **Figure 6.9 (a, b, c, and d)** shows the EBSD IPF maps of BVCR 50% samples heat treated at the heating rates of 0.2 ^{0}C/s, 0.9 ^{0}C/s, 7 ^{0}C/s, and 50.5 ^{0}C/s respectively. It can be seen that at 0.2 ^{0}C/s, a fully recrystallized microstructure is produced indicating completion of ferrite recrystallization process. With the increase in heating rate the amount of ferrite recrystallization clearly decreased and texture from the cold reduction is still retained. **Figure 6.9 e)** compares the experimentally obtained overlap values with the model values at the predicted heating rates. It can be seen that at lower percentage overlaps, the model perfectly matches with the experimentally obtained heating rate values. However, at higher percentages of overlap, the model slightly underpredicts the heating rates required for the overlap. Therefore, this model can be used to predict the heating rates required to obtain same amount of overlap for various initial microstructures, compositions and cold reductions. This will not enable a systematic comparison of microstructural evolution of various material but also helps to understand the austenite formation mechanism at various percentages of overlap.
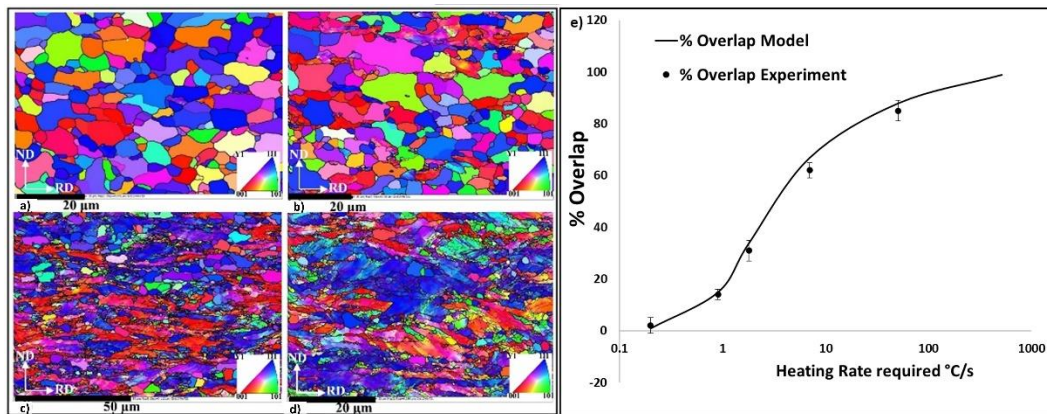
Figure 6. 9: **(a-d)** EBSD IPF maps of BVCR 50% samples heated at heating rates of a) 0.2 ^{0}C/s, b) 0.9 ^{0}C/s c) 7 ^{0}C/s, and d) 50.5 ^{0}C/s to the A_{c1} temperatures, and e) Comparison of experimentally obtained overlap values with the model values at the predicted heating rates. BV steel composition - (Fe-0.14C-2.1Mn-0.37Si-0.06V-0.002B).

Chapter 7 - Effect of overlap on the mechanism of austenite formation in cold rolled DP steels

To understand the mechanism of austenite formation at high heating rates, it is crucial to systematically evaluate the final DP steel microstructure at the various percentages of interactions between high temperature processes. This chapter systematically evaluates the microstructural evolution of DP steels at various percentages of overlap for the BVCR 50% steel. The microstructure evolution is studied at various model predicted heating rates (0.2, 7, 50.5, 511 ^{0}C/s), inter-critical annealing temperatures (Range 730 – 750 ^{0}C) and soaking times (Range 0 - 900 s). SEM microstructural images, EDX line scans, EBSD images and micro-hardness measurements were used to track the progress of the ferrite recrystallization and austenite formation processes. With a systematic comparison of microstructural characteristics, various mechanisms for austenite formation were proposed for different percentages of overlaps and inter-critical temperatures.

7.1. Initial microstructure of BVCR 50% steel

Figure 7.1 (a, b) shows the initial microstructure of the BVCR 50% steel in the RD⊥ND plane along with its corresponding EDX map of manganese. Both ferrite grains and pearlite colonies were found to be deformed along the rolling direction with some pearlite colonies elongated around the ferrite grains. This is due to the higher strength of pearlite relative to ferrite. The volume fraction of pearlite was found to be 21±2% with some parts of fragmented cementite distributed along the ferrite grain boundaries and grain interiors. The manganese EDX map reveals that the majority of the pearlite colonies overlap with the manganese bands. **Figure 7.1 c)** represents EDX line graph of manganese, which shows that the majority of pearlite colonies have at least 2 times higher Mn concentration than the ferrite grains. The large solubility differences between liquid and solid steel is responsible for this kind of solute segregation. During the continuous casting process, the solid continuously rejects the solute into remaining liquid leading to a through thickness concentration gradient. The amount of solute rejection depends on the partition coefficient and the concentration

of the solute in the steel composition [204]. The severity of solute segregation increases with a decrease in partition coefficient and an increase in the concentration. Even though the partition coefficient of Mn (0.71) is high when compared to other solute elements, its high concentration (2.1 wt%) and low diffusivity (10^{-26} m^2/s) is responsible for the existence of its segregation throughout the downstream processes [159].
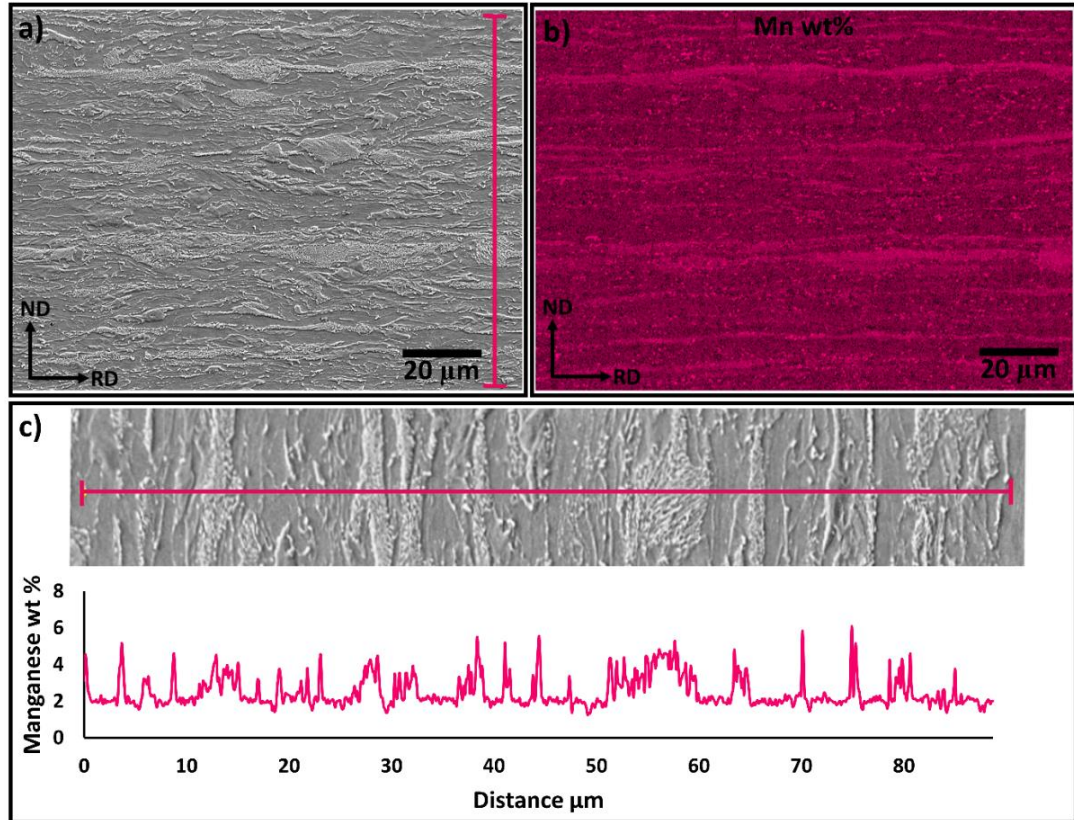
Figure 7. 1 (a, b and c): a) SEM microstructural image of BVCR 50% steel, b) Overlapped manganese EDX map and c) corresponding manganese concentration profile (wt%). BV steel composition - (Fe-0.14C-2.1Mn-0.37Si-0.06V-0.002B).

7.2. Effect of heating rate at low inter-critical annealing temperature

Figure 7.2 a) shows the effect of soaking times and heating rates on the martensite volume percentage of the samples annealed at 730 ^{0}C. Similarly, **Figure 7.2 b)** shows the effect of heating rate on the martensite volume percentage of the samples quenched immediately after reaching 730 ^{0}C (soaking time 0 s). It can be seen that the increase in heating rate decreased the amount of martensite in the final microstructure for short

soaking times. However, with the increase in soaking time, an opposite phenomenon is seen, where increase in the heating rate significantly increased the martensite percentage. This can be explained by the fact that the austenite transformation kinetics is slow at the low inter-critical temperatures, and a higher amount of incubation time is required for its progress [144]. Therefore, the higher amount of time available at a slow heating rate condition gives additional time for the formation of austenite even for shorter soaking times. The local segregation can lead to deviation of the actual austenite fractions from the equilibrium values. **Figure 7.2 c)** represents the variation in the aspect ratio of ferrite grains with respect to increasing soaking times and heating rates for the samples annealed at 730 ^{0}C. **Figure 7.2 d)** shows the effect of soaking times and heating rates on the micro-hardness values. Both aspect ratio and micro-hardness values indicate the progress of ferrite recrystallization process. Moreover, the hardness values also indicate the progress of austenite formation. As the ferrite recrystallization progresses, the aspect ratio of the ferrite grains decreases [132]. The progress of ferrite recrystallization also decreases the micro-hardness values. However, austenite formation (final martensite) increases the micro-hardness values. Therefore, hardness indicates a relative progress of ferrite recrystallization and austenite formation processes [118]. It can be seen from **Figure 7.2 c)** shows that the aspect ratio of slow heating condition samples remained constant between 1 and 2 for all the holding times. This can be attributed to the completion of the ferrite recrystallization process before the inter-critical temperature. However, the aspect ratio values were to be higher for higher heating rate conditions for all holding times. Moreover, during the initial holding times a significant decrease in aspect ratio values was observed for high heating rate conditions. This indicates the presence of deformed ferrite grains before the inter-critical temperature. Moreover, the decrease in aspect ratio indicates a rapid progress of ferrite recrystallization process at low inter-critical temperature during the initial holding times. With the increase in soaking time, a continuous increase in hardness values was observed for slow heating rate condition. This indicates the continuous formation of austenite with the increase in soaking times. However, for high heating rate conditions the hardness values initially decreased for initial holding times, and then increased with the increase in soaking time. This clearly indicates that the ferrite recrystallization process dominates the austenite formation process for the initial holding times at low inter-critical annealing temperature for high

heating rate conditions. After sufficient holding times, austenite formation increases and therefore the hardness values also increases.

Figure 7.2 (e, f) shows the SEM microstructural images of the BVCR 50% steel annealing at an inter-critical temperature of 730 ^{0}C for 0 s with a heating rate of 0.2 ^{0}C/s and 50.5 ^{0}C/s. The microstructure of the slower heating rate condition shows a fully recrystallized microstructure indicated by the equiaxed polygonal ferrite grains. The higher magnification image reveals that the nucleation of austenite (now martensite) occurred at the recrystallized ferrite grain boundaries more preferentially at the triple points. Additionally, a solid martensite band was also observed at the centre of the sample. This could be from the presence of prior pearlitic band region. Moreover, fully spheroidized cementite particles were observed to be uniformly distributed throughout the microstructure. The microstructure of the sample heated at 50.5 ^{0}C/s consists of deformed ferrite (blue arrow) and unspheroidized cementite. A very small quantity of fine spheroidized cementite was observed in the microstructure. Moreover, a very tiny quantity of martensite islands were present at this condition with majority of them in the prior pearlitic region (black arrow).
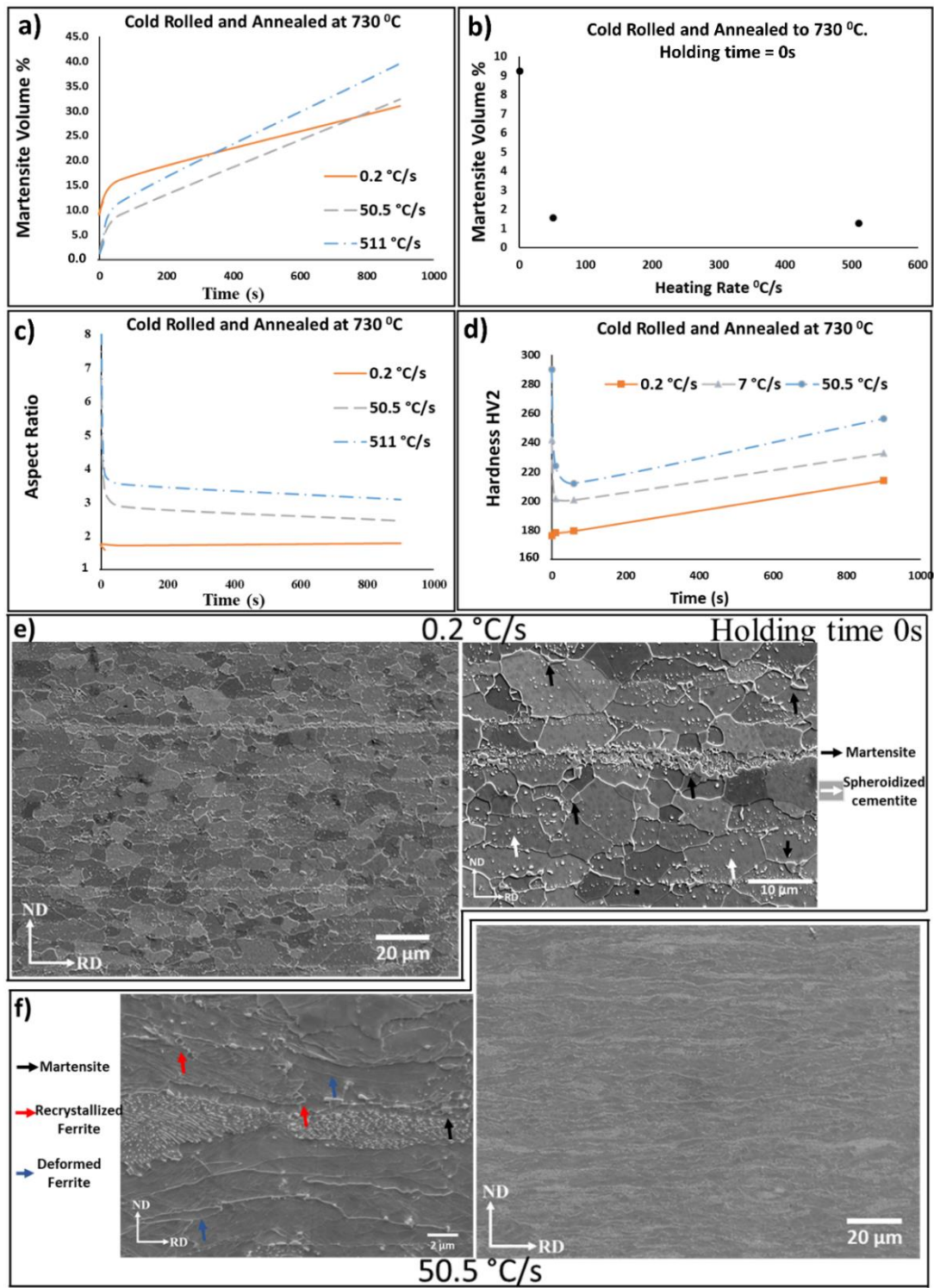
Figure 7. 2: (a-d): Effect of heating rate on (a, b) Martensite volume percentage, c) Ferrite grain aspect ratio and d) Micro-Vicker's hardness at 730 ^{0}C; (e, f): SEM microstructural images of the BVCR 50% samples annealed at 730 ^{0}C (0 s) at heating rates of e) 0.2 ^{0}C/s and f) 50.5 ^{0}C/s respectively. BV steel composition - (Fe-0.14C-2.1Mn-0.37Si-0.06V-0.002B).

Figure 7.3 (a, b) shows the microstructure of the samples annealed at inter-critical temperature of 730 ^{0}C for a soaking time of 900 s with heating rates of 0.2 ^{0}C/s and 511 ^{0}C/s respectively. Even though the samples were annealed at same temperature and same holding times, the difference in heating rates produced very different morphologies of martensite in final microstructures. The sample annealed at slower heating rate condition produced a fully necklace morphology of martensite on fully recrystallized ferrite grains. This can be attributed to the preferential formation of austenite on the ferrite grain boundaries (black arrow). Additionally, one or two solid martensite bands were present at the centre of the sample. The sample annealed at higher heating rate (**Figure 7.3 b**), produced martensite with banded morphology (violet arrow). Moreover, the high magnification image reveals the presence of polygonal ferrite grains even at high heating rate condition of the sample annealed at low inter-critical temperature. This supports the decrease in aspect ratio and hardness values for the initial soaking times of high heating rate condition, and therefore indicates that ferrite recrystallization dominates for the initial soaking times. It can also be noticed that a tiny fraction of spheroidized cementite is aligned along the rolling direction (white arrow). **Figure 7.3 (c, d)** shows the EBSD band contrast images of the BVCR 50% steel annealed at inter-critical temperature of 730 ^{0}C and soaking time of 900 s with heating rates of 0.2 ^{0}C/s and 50.5 ^{0}C/s respectively. It can be seen that the martensite islands in the slow heating rate condition are randomly distributed on the ferrite grain boundaries. In contrast to this, the martensite islands are preferentially located at the pearlite colonies and the deformed ferrite structure. The martensite islands in slow heating rate condition are distant from each other, whereas, in the higher heating rate condition the martensite islands are very close to each other and seem to be connected.
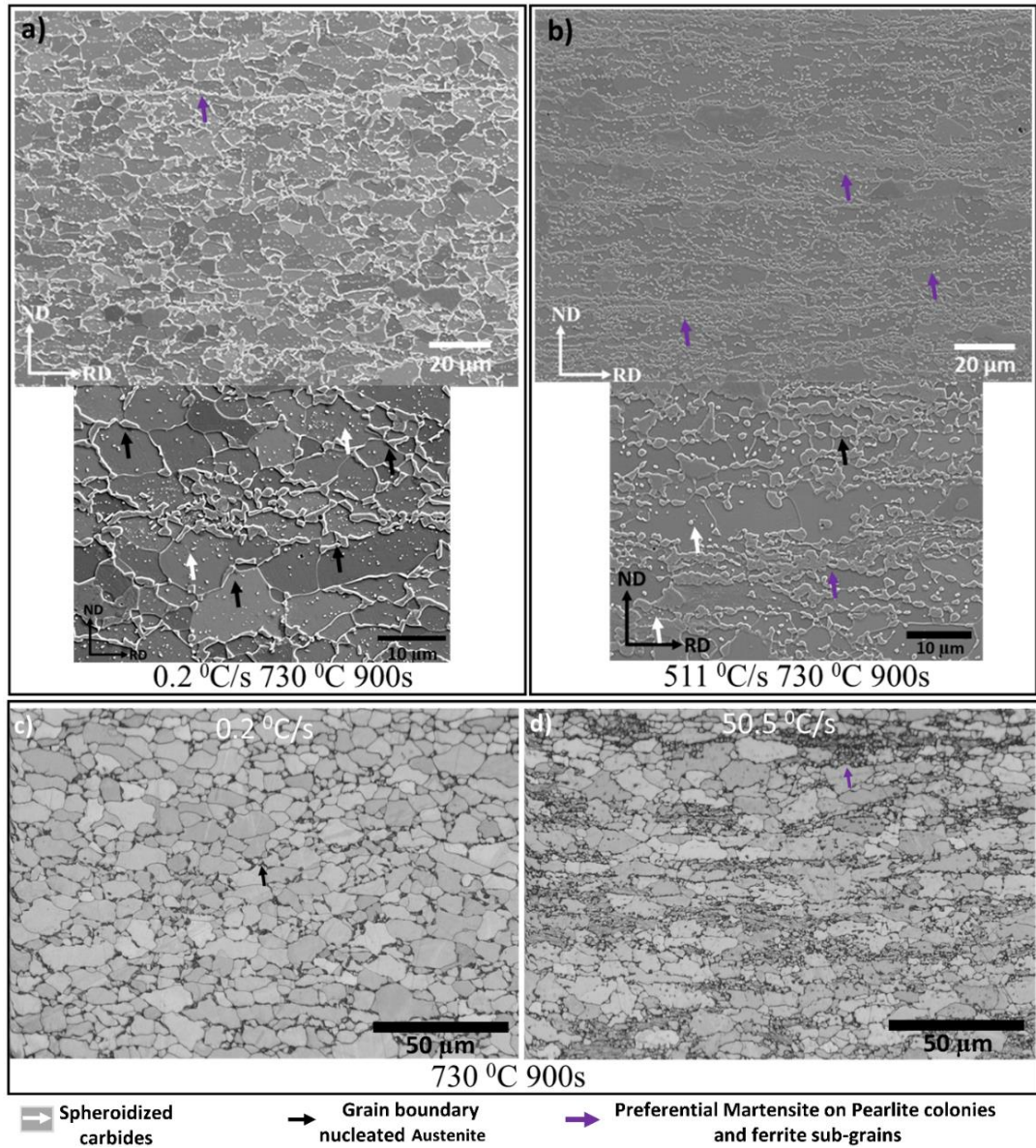
Figure 7. 3: (a, b): Microstructure of the samples annealed at 730 ^{0}C for 900 seconds with heating rates of a) 0.2 ^{0}C/s and b) 511 ^{0}C/s; (c, d): EBSD band contrast images of BVCR 50% samples annealed at 730 ^{0}C for 900 seconds with heating rates of c) 0.2 ^{0}C/s and d) 50.5 ^{0}C/s respectively. BV steel composition - (Fe-0.14C-2.1Mn-0.37Si-0.06V-0.002B)

Figure 7.4 a) shows the variation in martensite volume percentage as a function of varying heating rates and soaking times for BVCR 50% samples annealed at 750 ^{0}C. F**igure 7.b)** shows the effect of heating rate on the martensite volume percentage of the samples heat treated at 750 ^{0}C an no soaking time (0 s). As expected, for shorter holding time increase in heating rate caused decrease in the martensite volume percentage (same as in 730 ^{0}C). However, for 750 ^{0}C, after very short soaking time

the martensite volume percentage increased rapidly. This can be attribute to the increase in austenite kinetics at higher temperature. Moreover, increase in heating rate caused significant increase in martensite percentage for longer holding times. However, as the soaking time increased the difference in martensite volume percentage for different heating rates seems to be decreased. **Figure 7.4 c)** shows the variation in aspect ratio as a function of soaking times and heating rates for the samples heat treated at 750 ^{0}C. Similarly, **Figure 7.4 d)** shows the variation in hardness measurements. The variation in aspect ratio and hardness values for slower heating rate condition were found to be following similar behaviour as in 730 ^{0}C. However, for higher heating rates at 750 ^{0}C, the hardness values started to increase after very short holding times. This indicates that as the temperature increases the domination of ferrite recrystallization process decreases to shorter holding times. **Figure 7.4 (e, f)** shows the SEM microstructural images of samples heat treated at 7 ^{0}C/s at 750 ^{0}C for 0 s and 10 s respectively. Similarly, **Figure 7.4 (g, h)** shows the microstructural images of samples heat treated at 50.5 ^{0}C/s at 750 ^{0}C for 10 s and 60 s. The ferrite recrystallization process completed by almost 10 s in the sample heat treated at 7 ^{0}C/s. whereas, it took more than 60 s for recrystallization process to complete in the sample heat treated at 50.5 ^{0}C/s.
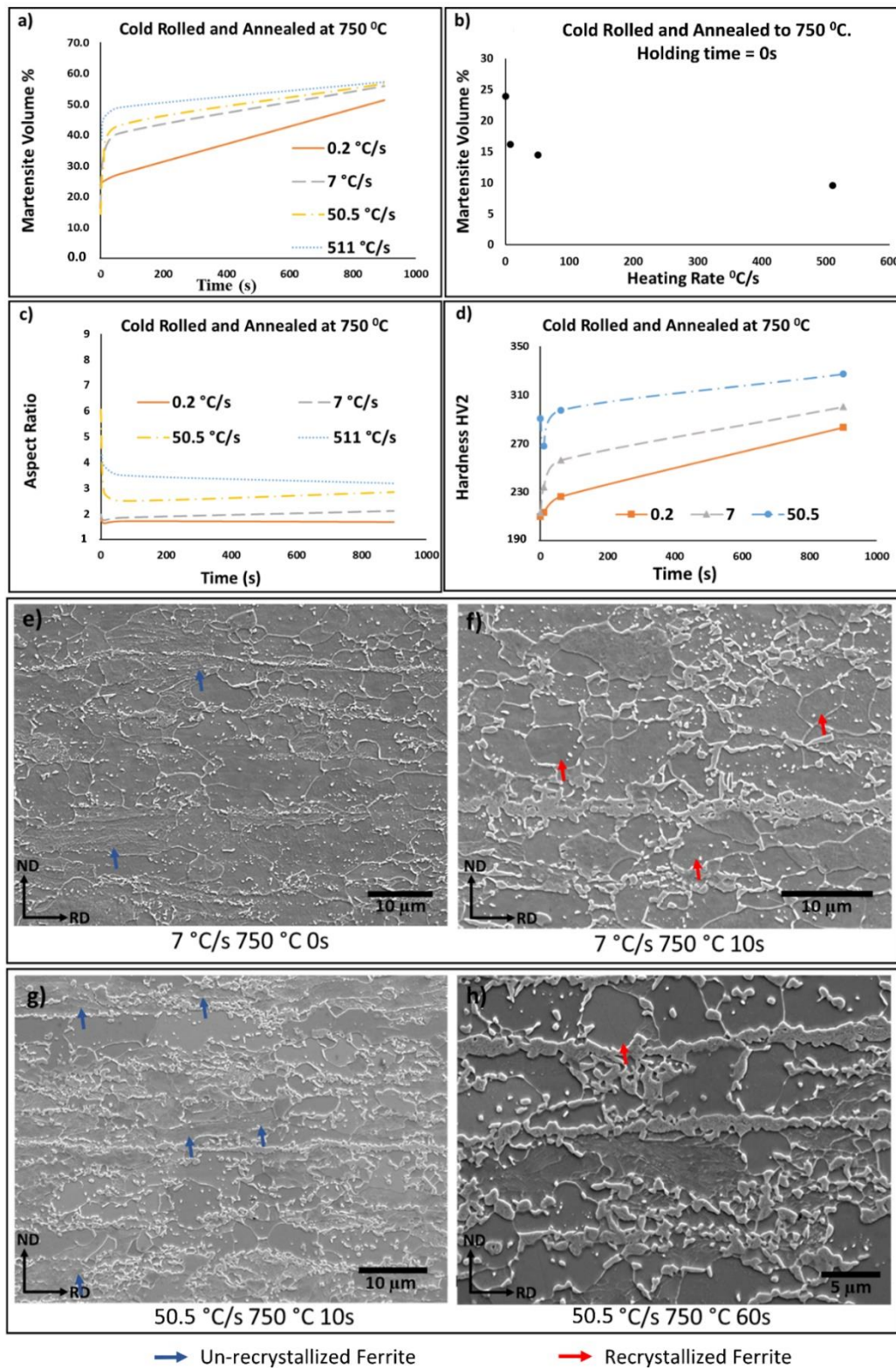
Figure 7. 4: (a-d): Effect of heating rate on (a, b) Martensite percentage, c) Ferrite grain aspect ratio and d) Micro-Vicker's hardness at 750 ^{0}C; (e-h): SEM microstructural images of the samples annealed at 750 ^{0}C at heating rates of (e, f) 7 ^{0}C/s for e) 0s and f) 10, and (g, h) 50.5 ^{0}C/s for g) 10s and h) 60s. BV steel composition - (Fe-0.14C-2.1Mn-0.37Si-0.06V-0.002B).

Figure 7.5 (a, b, c, and d) shows the SEM microstructural images of the BVCR 50% samples heat treated at 750 ^{0}C and 900 s at heating rates of 0.2 ^{0}C/s, 7 ^{0}C/s, 50.5 ^{0}C/s and 511 ^{0}C/s respectively. The martensite in the slow heating rate condition completely enveloped the ferrite grain boundaries, and therefore developed a necklace morphology (black arrow). Additionally, one or two solid martensite bands (violet) were observed at the centre of the thickness. In contrast to this, the samples annealed at higher heating rates produced martensite with banded morphology. As shown in **Figure 7.5**, increase in heating rate caused an increase in the amount of banded martensite in the microstructure. The high magnification images in **Figure 7.5 (c, d)** reveals the presence of martensite in the recovery bands as well (green arrow). Moreover, samples heat treated at medium heating rates produced thin martensite bands, whereas the higher heating rate samples produced thicker bands. Very tiny fraction of undissolved spheroidized cementite was observed even after annealing at 750 ^{0}C for 900 s.
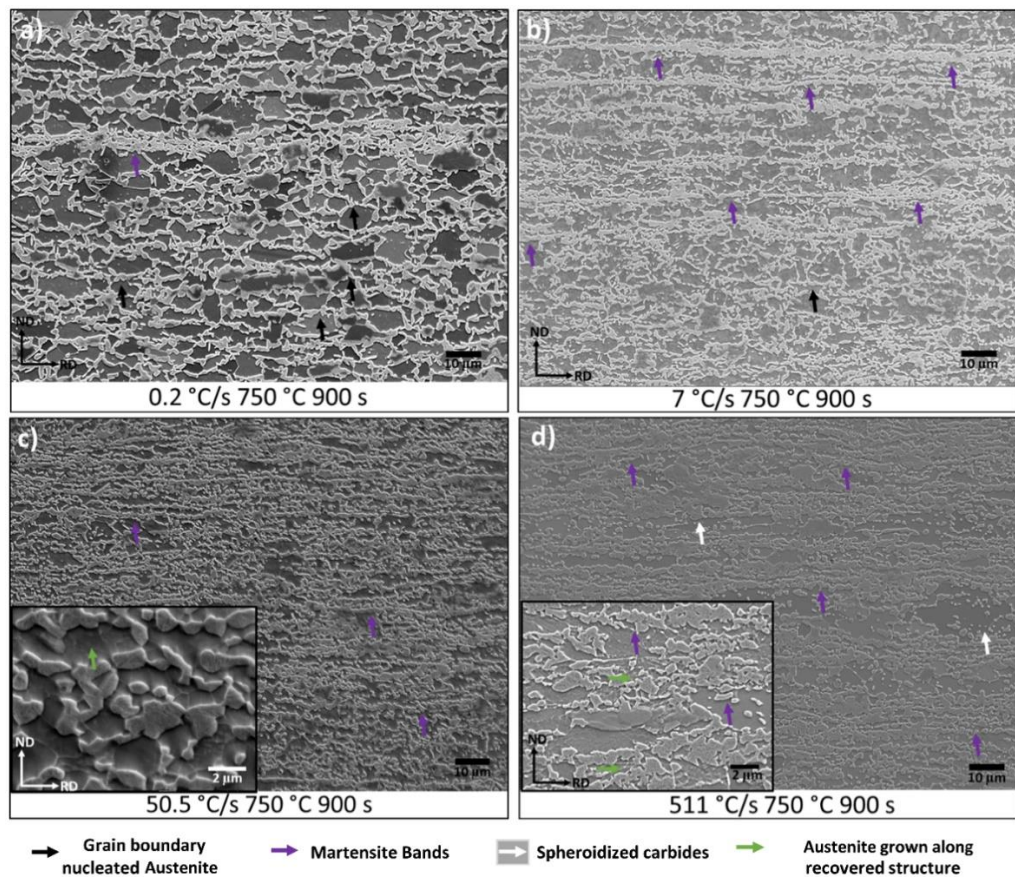
Figure 7. 5: SEM images of the samples annealed at 750 ^{0}C for 900 seconds at heating rates of a) 0.2 ^{0}C/s, b) 7 ^{0}C/s, c) 50.5 ^{0}C/s and d) 511 ^{0}C/s. BV steel composition - (Fe-0.14C-2.1Mn-0.37Si-0.06V-0.002B).

To understand the effect of manganese segregation on the morphological variation of martensite in final microstructure, EDX line scans were done for various heating rates and annealing temperatures. Such EDX manganese concentration profiles overlapped on the corresponding microstructures is shown in the **Figure 7.6 (a, b)** for the BVCR 50% steel samples annealed at 750 ^{0}C and 100 s with heating rates of 0.2 ^{0}C/s and 50.5 ^{0}C/s respectively. The manganese concentration profiles in both the samples (0.2 ^{0}C/s and 50.5 ^{0}C/s) were found to be having segregated and depleted regions. However, it can be seen that in 0.2 ^{0}C/s sample that the austenite nucleated at the grain boundaries are not always the regions with high manganese concentration. However, the martensite bands at the centre of the thickness (one or two) were found to have very high manganese concentration in it. Moreover, the grain size near the bands were found to be smaller than the overall microstructure. In case of sample heat treated at 50.5 (^{0}C/s), it was found that the Mn concentration profile was not only uniform along the thickness of the microstructure (**Figure 7.6 b**) but also majority of martensite bands were found to overlap with high manganese concentration regions. Only a tiny fraction of martensite bands were found to possess normal manganese concentration. The ferrite grain interiors were generally found to have average manganese concentration. This phenomenon can be explained by the change in preferential nucleation sites of austenite and the effect of deformed matrix on the microstructure evolution. The comparison of mechanisms involved are more detailly discussed in section **7.4**.
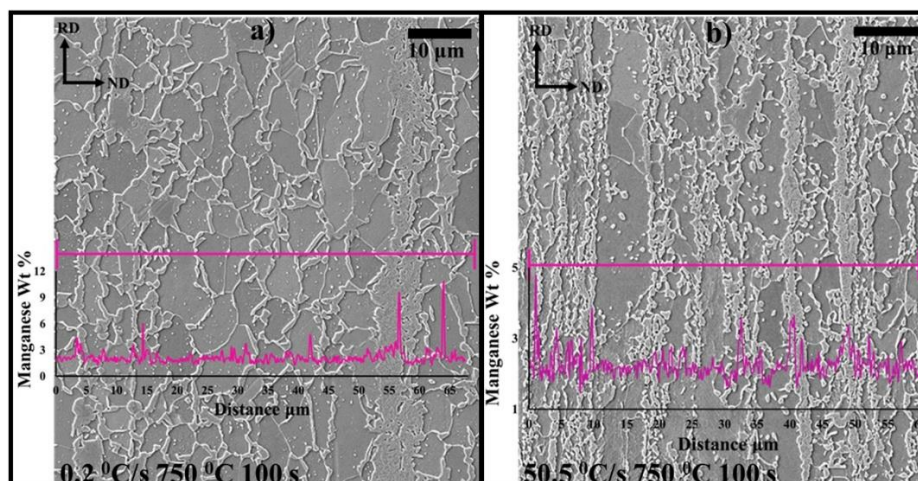
Figure 7. 6: SEM microstructural images overlapped with corresponding manganese EDX line graphs for the samples annealed at 750 ^{0}C for a soaking time of 100 s with heating rates of a) 0.2 ^{0}C/s, and b) 50.5 ^{0}C/s. BV steel composition - (Fe-0.14C-2.1Mn-0.37Si-0.06V-0.002B).

114

## 7.3. Effect of heating rate at high inter-critical annealing temperature

Figure 7.7 a) shows the effect of soaking times and heating rates on the martensite volume percentage of the samples annealed at high inter-critical temperature of 780 ^{0}C. **Figure 7.7 b)** shows the variation in micro-hardness value with respect to soaking time for samples annealed with high heating rate of 50.5 ^{0}C/s. Similar to lower temperatures, the martensite volume percentage increased with increase in heating rate. With the increase in soaking time the difference in martensite volume percentage for different heating rates decreased. In other words, the effect of heating rate decreased with the increase in temperature and soaking time. Moreover, **Figure 7.7 b)** shows that the micro-hardness values continuously increased with increase in soaking time without any initial dip in the values. This indicates a complete domination of austenite formation over ferrite recrystallization process for all the soaking times, including the initial soaking times unlike for lower inter-critical temperature annealing. **Figure 7.7 (c, d)** shows the microstructure of samples annealed at 780 ^{0}C for 900 s with high heating rates of 50.5 ^{0}C/s and 511 ^{0}C/s respectively. As expected the high heating rate produced a complete banded martensite morphology in the final microstructure. Medium heating rates produced thinner bands which were large in number and very high heating rates produced thicker bands which are fewer in number. Moreover, the ferrite grains are relatively elongated when compared to lower inter-critical temperature annealed samples. This indicates incomplete progress of ferrite recrystallization process. This is also evidenced by lack of any decrease in micro-hardness values for the initial holding times (**Figure 7.7 b**). When compared to Huang et al., study [132], the present work showed the presence of martensite central bands even at slow heating rate condition owing to the presence of industrially relevant manganese segregation. Moreover, unlike other major studies relevant to the overlap of high temperature mechanisms [49,158,159], this study shows the difference in the number of bands and the thickness of bands with respect to the percentage overlap and the corresponding predicted employed heating rate. This is very important in industrial production as most of the high heating rates employed in the literature are not feasible to producing on the continuous annealing lines. The heating rates employed in the industry majorly depends on the furnace length, strip thickness and the line speed. For instance, in Tata steel, UK, the DP steel production is generally done with heating rates ranging from 1.2 ^{0}C/s to 35 ^{0}C/s. The present study also shows that at the

prolonged soaking times and high inter-critical temperatures, the martensite fraction tends to stabilize to slower heating rate samples.
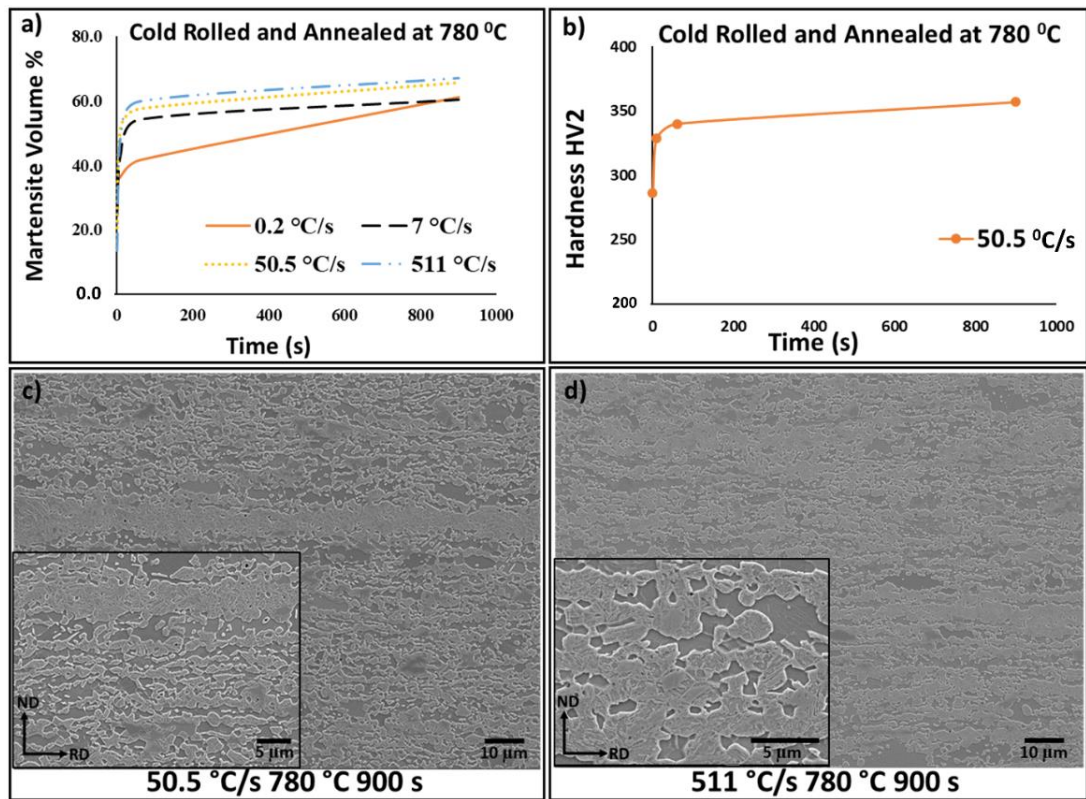
Figure 7. 7: (a, b): Effect of heating rate on (a, b) Martensite percentage, and b) Micro-Vicker's hardness at 780 ^{0}C; (c, d): SEM microstructural images of the samples annealed at 780 ^{0}C and 900 s at heating rates of c) 50.5 ^{0}C/s and d) 511 ^{0}C/s respectively. BV steel composition - (Fe-0.14C-2.1Mn-0.37Si-0.06V-0.002B).

7.4. Mechanisms of austenite formation

7.4.1. Microstructure before austenite formation

To understand the variation in the final DP steel microstructure, it is critical to understand the formation mechanism of austenite during the inter-critical annealing step. However, with the variation in heating rate different microstructures are developed prior to the onset of austenite formation i.e., at the A_{c1} temperature. In other words, change in the kinetics of ferrite recrystallization and cementite spheroidization with respect to different heating rates, changes the initial microstructure on which the austenite forms. Therefore, before understanding the microstructure evolution during

the inter-critical annealing step it is crucial to establish the microstructure developed prior the A_{c1} temperature. **Figure 7.8** shows the schematic representation of the microstructure developed prior to A_{c1} temperature with respect to slow, medium and fast heating rates. The cold rolled ferrite-pearlite microstructure is illustrated by elongated grains where the deformed ferrite is represented as elongated plain grains and deformed pearlite is represented as patterned grains. The slow heating rate condition is where a fully recrystallized microstructure is developed prior to the start of austenite formation. The ferrite grains present in the pearlite colonies also get recrystallized during this condition. However, the recrystallized ferrite grains in prior pearlitic region possesses finer grain size when compared to the recrystallized ferrite grains produced at the prior deformed ferritic region. The presence of high amount of manganese in the prior pearlitic region causes severe solute drag effect and therefore is responsible for such grain size differences [193]. This difference in grain size is represented in the **Figure 7.8**, and it can be clearly seen in the **Figures 7.2 e) and 7.3 a)**. Moreover, the fragmented cementite particles in the initial cold deformed material gets enough time to fully spheroidize and distribute throughout the microstructure. Dissolution of carbon and simultaneous grain boundary enrichment also takes place during the spheroidization process. In contrast to this, only partial spheroidization of cementite is expected in the medium heating rate condition before A_{c1} temperature. Additionally, the ferrite recrystallization process will be incomplete with presence of remaining recovered ferrite in the microstructure. Therefore, a combination of partially recovered, partially recrystallized and partially spheroidized microstructure is expected in the medium heating rate condition. For the very high heating rate condition, there is no progress in both the spheroidization and recrystallization processes prior to the austenite formation step. Therefore, the only difference between the initial cold deformed microstructure to that of the microstructure before Ac1 temperature will be the presence of recovered ferrite.
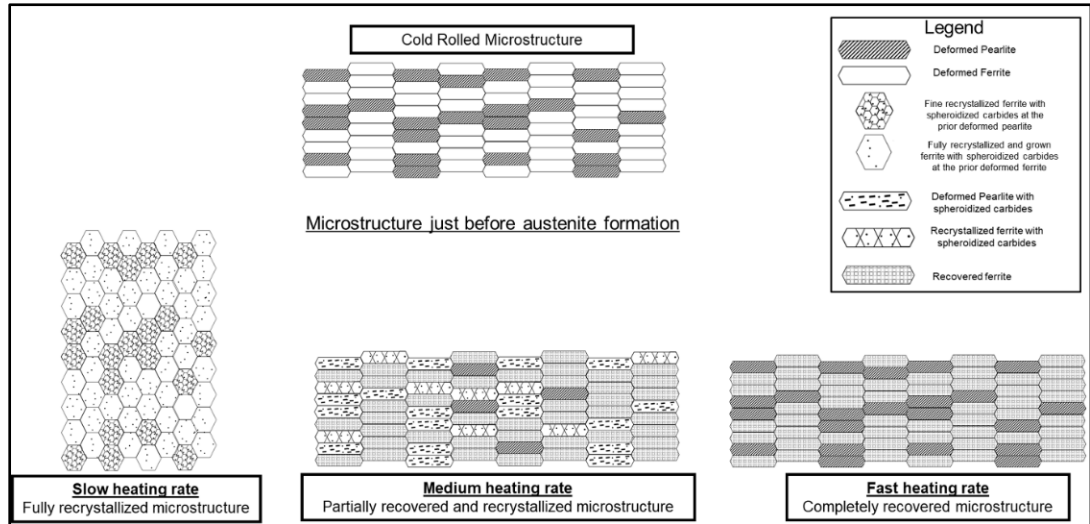
Figure 7. 8: Schematic representation of cold rolled microstructure along with the microstructure present just before the start of austenite formation.

7.4.2. Microstructure evolution at slow heating rate

Figure 7.9 a) shows the schematic representation of the mechanism involved in the formation of austenite in slow heating rate condition. There is no interaction between ferrite recrystallization and austenite formation in this condition, as a fully recrystallized microstructure is already produced before A_{c1} temperature as discussed in **Figure 7.8**. As discussed above, majority of cementite spheroidization is expected to be completed before the onset of austenite formation. Granbom et al., reported that in cold reduced steels, spheroidization occurs by simultaneous dissolution and diffusion of carbon atoms towards the ferrite grain boundaries. This enriches the ferrite grain boundaries with high carbon concentration. With the absence of any deformed structure and the presence of carbon rich ferrite grain boundaries in the microstructure, the potential nucleating sites will be the recrystallized ferrite grain boundaries, more specifically the triple points. **Figure 7.9 b)** shows the EBSD band contrast image with the corresponding recrystallization map for the sample annealed at slow heating rate of 0.2 ^{0}C/s at 745 ^{0}C and 10 s. It is clear that all austenite nucleated (martensite islands) on the ferrite grain boundaries, more specifically on the triple points. The presence of tiny fraction of recovered ferrite can be attributed to the deformation induced by the martensite formation at the grain boundaries. With the increase in inter-critical temperature and soaking time the austenite grows along the preferential diffusion paths of solute atoms. In this slow heating rate condition, the preferential growth will

be grain boundaries because of higher concentration of carbon and grain boundary energy. This growth of austenite along the ferrite grain boundaries leads to the necklace morphology, as shown in **Figure 7.5 a)**. Moreover, the growth of austenite in slow heating rate condition will be relatively slow because of large grain boundaries and long distances between austenite nuclei. The austenite nucleated at the ferrite grain boundaries of prior pearlitic region grows relatively fast. This is because of higher carbon and manganese concentration and finer grain sizes, therefore shorter diffusion paths [132,159]. Therefore, rapid growth of austenite at these prior pearlitic regions produce one or two solid bands at the centre of the thickness. However, under close observation at high magnifications these bands can still be depicted as necklace morphology as these are also present on the recrystallized grain boundaries. This can be seen in **Figure 7.3 a)**.
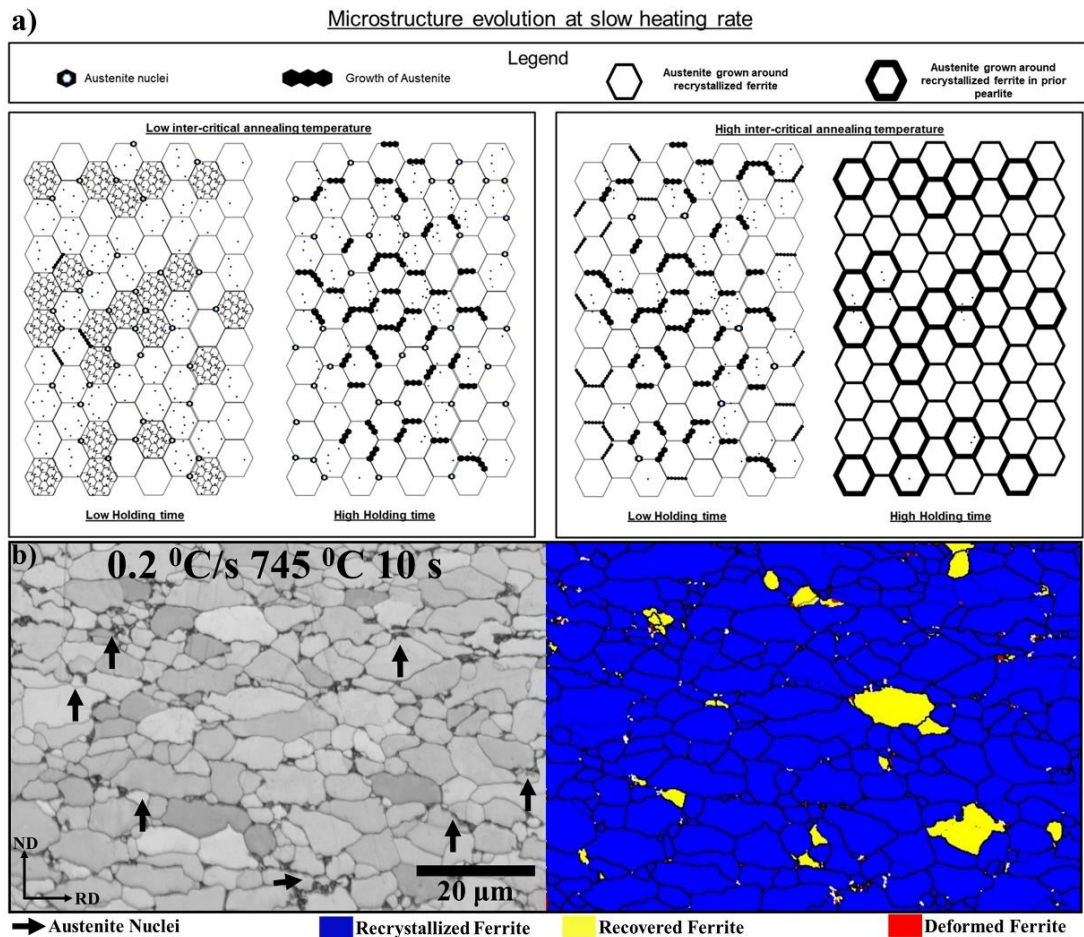
Figure 7. 9: a) Schematic representation of microstructure evolution at low heating rate, b) EBSD band contrast image and recrystallization fraction map of the BVCR

50% steel sample annealed at 745 ^{0}C and 10 s with a slow heating rate of 0.2 ^{0}C/s. BV steel composition - (Fe-0.14C-2.1Mn-0.37Si-0.06V-0.002B).

7.4.3. Microstructure evolution at medium heating rate

Figure 7.10 a) shows the schematic representation of the mechanism involved in the formation of austenite under the medium heating rate condition. A weak interaction between the various high temperature mechanisms is expected due to the presence of partially recrystallized and partially spheroidized cementite in the microstructure. **Figure 7.10 b)** shows the EBSD band contrast image with the corresponding recrystallization map for the sample annealed at heating rate of 50.5 ^{0}C/s at 745 ^{0}C and 10 s. The microstructure consists of partially recovered ferrite (yellow), partially recrystallized ferrite (blue) and partially deformed ferrite (red) in it. Due to the presence of high concentration of carbon and manganese, preferential nucleation of austenite takes place at the fragmented cementite region and recovered ferrite grain boundaries. When compared to the slow heating rate condition, the number of potential austenite nucleating sites will be higher in the form of fragmented cementite interfaces and recovered ferrite grain boundaries. Unlike slow heating rate condition, the austenite nuclei are close to each other and generally aligned along the rolling direction (**Figure 7. 10 b**). The growth of the closely nucleated austenite occurs rapidly along the dislocation rich recovered ferrite grains and the carbon rich fragmented cementite. This preferential growth along the rolling direction leads to the banded morphology. It should also be noted that the fragmented cementite particles are thermodynamically less stable and degenerate faster than the spheroidized carbides in slow heating rate condition, therefore enable faster growth of austenite Therefore, the presence of dislocation rich recovery bands and carbon rich fragmented cementite particles leads to faster austenite formation kinetics in this condition. However, the presence of partially recrystallized ferrite in the microstructure restricts the growth in the normal direction. **Figure 7.11** shows the EBSD band contrast image of the sample annealed at 50.5 ^{0}C/s at 750 ^{0}C for 60 s. Misorientation profile are calculated along the recovered (green line) and recrystallized ferrite (red line). Due to the presence of high dislocation density in the recovered ferrite, the cumulative misorientation profile along it was found to be higher when compared to the recrystallized ferrite. Moreover, from the **Figure 7.11**, it can be seen that the austenite phase (now martensite) is pinned

by the grain boundaries of the recrystallized ferrite. Only after complete consumption of recovered ferrite at very high inter-critical temperatures and/or very long holding times, the austenite starts to grow into the recrystallized grains. Therefore, medium heating rate produces large number of thin bands due to the combination of restricted growth along the normal direction due to the presence of partially recrystallized grains and preferential growth along the rolling direction due to the presence of partially fragmented cementite and partially recovered ferrite.
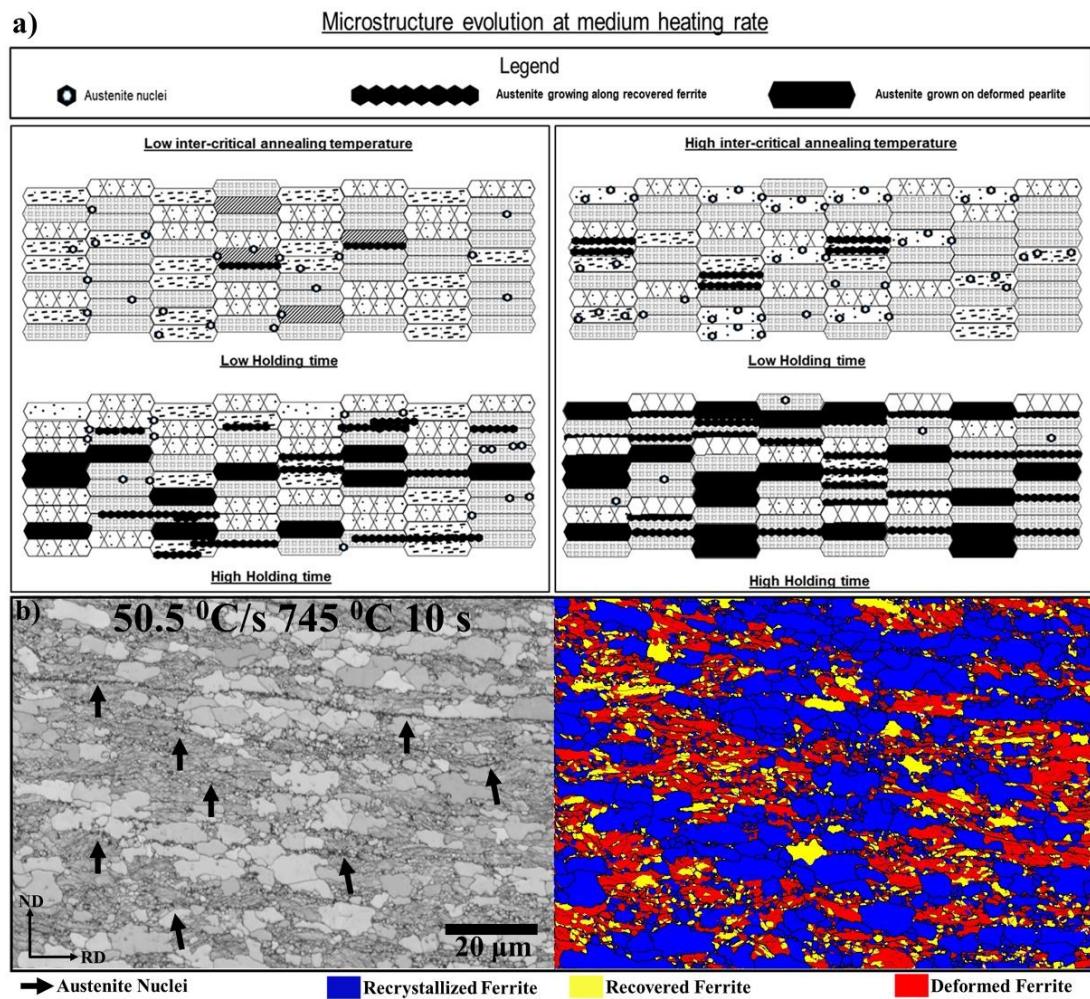
Figure 7. 10: a) Schematic representation of microstructure evolution at medium heating rate, b) EBSD band contrast image and recrystallization fraction map of the BVCR 50% steel sample annealed at 745 ^{0}C and 10 s with a slow heating rate of 50.5 ^{0}C/s. BV steel composition - (Fe-0.14C-2.1Mn-0.37Si-0.06V-0.002B).
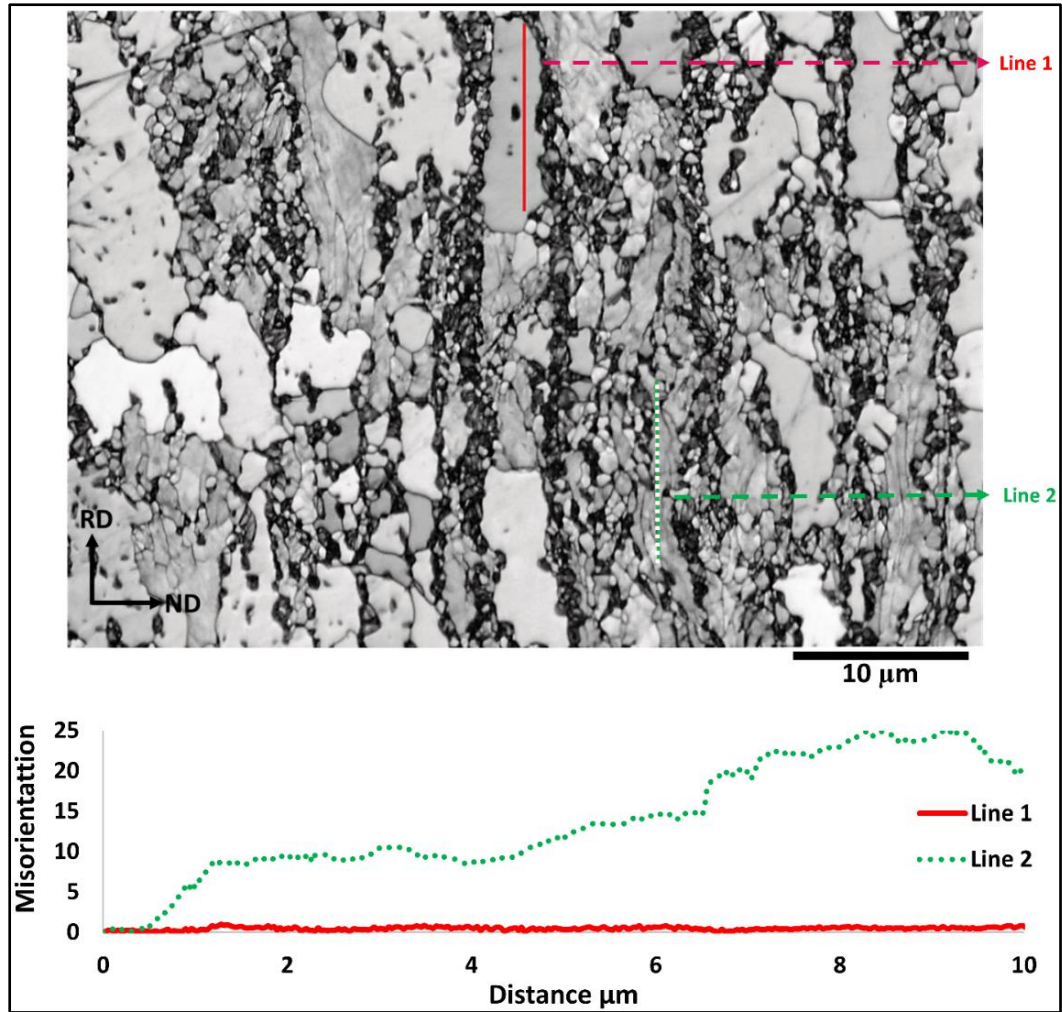
Figure 7. 11: EBSD band contrast image depicting the misorientation profiles (relative to first point) along the recrystallized and the recovered ferrite for the sample annealed at 750 ^{0}C for 60 seconds using heating rate of 50.5 ^{0}C/s. BV steel composition - (Fe-0.14C-2.1Mn-0.37Si-0.06V-0.002B).

7.4.4. Microstructure evolution at fast heating rate

Figure 7.12 shows the schematic representation of the mechanism involved in the formation of austenite under the high heating rate condition. A strong overlap between ferrite recrystallization and austenite formation happens in this condition. The large superheat produced by the fast heating rate increases the potential nucleating sites. The presence of fully recovered/deformed structure enables rapid growth of austenite as the presence of dislocations act as excellent diffusion paths for carbon and manganese solute atoms. When compared to medium heating rate condition, the complete lack of recrystallized grains before A_{c1} temperature enables growth in the normal direction as

122

well. However, due to the alignment of recovered ferrite bands and the fragmented cementite particles along the rolling direction, the preferential austenite growth direction will also be the rolling direction. This enables faster austenite kinetics and thicker martensite bands in the final microstructure when compared to the medium heating rate condition. The driving force for the austenite formation is relatively low at the low inter-critical temperature. It is due to the fact that austenite phase is thermodynamically not stable at lower inter-critical temperatures, as its growth mechanism is dependent on the sluggish diffusion of manganese and chromium solute atoms [205]. This enables rapid progress of recrystallization process during the initial soaking times of lower inter-critical temperature annealing. This domination of ferrite recrystallization over austenite formation is indicated by the sharp dip in the micro-hardness values for the initial soaking times of lower inter-critical temperature annealing, as shown in **Figure 7.2 d**). However, with the increase in soaking time, the driving force for austenite formation increases and the formation of austenite occurs along the degenerate cementite particles and the left over recovery bands. For high inter-critical annealing, the driving force for austenite formation is given by the decrease in the free enthalpy [118]. Moreover, the decrease in stored deformation energy by the transformation of deformed ferrite to austenite phase will also act as the additional driving force at this stage. This enables complete domination of austenite formation process over ferrite recrystallization process at high inter-critical temperature annealing. The formation of austenite in the deformed ferrite decreases the stored deformation energy and therefore further decreases the progress of ferrite recrystallization process. Moreover, the austenite nuclei on the deformed ferrite grain boundaries induce pinning action and decrease its mobility which leads to further decrease in the progress of recrystallization process. The elongated ferrite grains and the absence of dip in the micro-hardness values at the high inter-critical temperature annealing (**Figure 7.7**) can be explained by this phenomenon of domination of austenite formation process over austenite formation process.
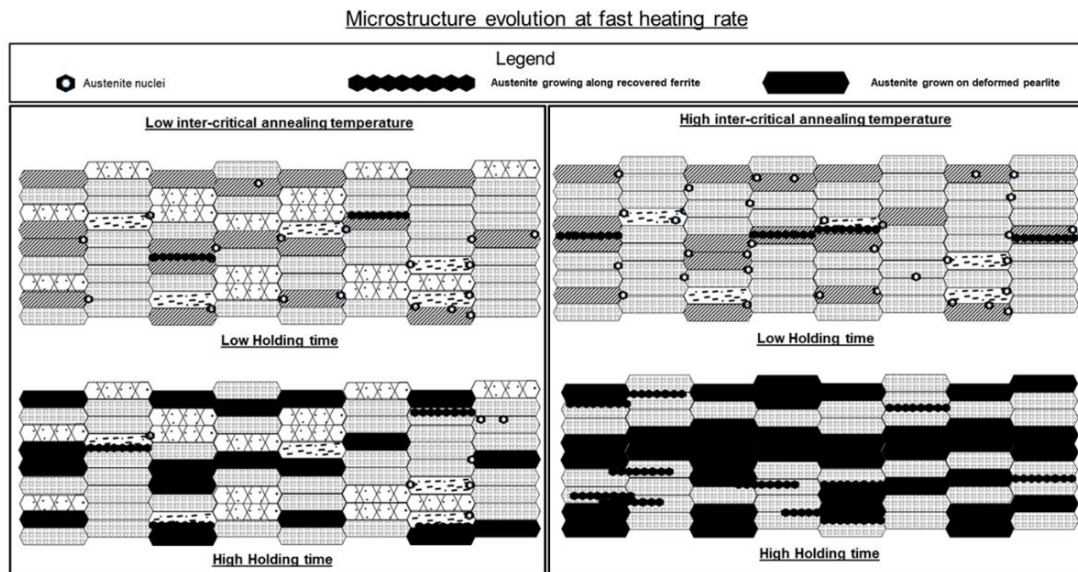
Figure 7. 12: Schematic representation of microstructure evolution at fast heating rate.

In this chapter, it was found that increase in heating rate increases the austenite formation kinetics and therefore leads to higher martensite volume fraction in the final microstructure. The relatively large ferrite grain size and the stability of spheroidized cementite particles caused the sluggish austenite formation during slow heating rate condition. The presence of dislocation structure and fragmented cementite particles enhanced the kinetics of austenite formation during fast heating rate condition. Increase in heating rate transformed martensite from a necklace morphology to banded morphology. This is due to the fact that austenite preferentially formed on ferrite grain boundaries in slow heating rate condition, whereas in faster heating rate condition austenite preferentially formed along dislocation structure and fragmented cementite particles which are aligned along the rolling direction. In the medium heating rate condition, the presence of recrystallized ferrite grains restricted the growth along the normal directions leading to thin martensite bands when compared to thick bands in fast heating rate condition. From the aspect ratio and hardness measurements, it was found that for fast heating rate condition, recrystallization process dominates at low inter-critical temperature whereas austenite process dominates at high inter-critical temperature.

Chapter 8 - Effect of heating rate on the microstructural evolution in hot rolled DP steels

This chapter discusses the effect of heating rate on the microstructural evolution of the BV steel with an initial hot rolled (HR) microstructure. In order to maintain consistency, the BVHR steels were also annealed at the same heating rates employed to the BVCR 50% steels. A systematic comparison is done with the cold rolled DP steels to understand the changes in the final microstructure with respect to the applied heating rate and annealing temperature. This chapter also discusses the morphological anisotropy developed in the hot rolled samples. Through thickness texture analysis is discussed with respect to the annealing parameters. Comparison of strengths between ferrite and martensite has been evaluated using nano-indentation measurements for various annealing parameters.

8.1. Effect of heating rate on hot rolled initial microstructure

Figure 8.1 a) shows the change in martensite volume % with respect to heating rate employed for the BVHR samples annealed at 730 ^{0}C for 900 s. Similar to the BVCR samples, an increase in heating rate in the BVHR samples caused a significant increase in the martensite fraction in the final microstructure. **Figure 8.1 b)** shows the effect of heating rate and soaking time for the samples heat treated at 750 ^{0}C. As expected, the volume fraction of austenite (now martensite) increased with increase in soaking time for all heating rates and temperatures. However, without the role of ferrite recovery and recrystallization process, the final martensite volume fraction increased with increase in heating rate. **Figure 8.1 (c, d)** shows the high magnification SEM microstructural images of the BVHR steel annealed at 730 ^{0}C for 900 s at heating rates of 0.2 ^{0}C/s and 511 ^{0}C/s respectively. It can be seen that the lower heating rate condition produced microstructure with lower amount of martensite islands which are evenly distributed on the grain boundaries. However, at high heating rates the microstructure clearly indicates higher austenite kinetics, and the produced martensite is mostly in banded morphology. **Figure 8.2 (a, b, and c)** shows the SEM microstructural images (low magnification) of the samples annealed at 750 ^{0}C for 900

s at heating rates of 0.2 ^{0}C/s, 7 ^{0}C/s, and 511 ^{0}C/s respectively. It can be clearly seen that with the increase in heating the martensite transformed from randomly distributed islands to more of a banded morphology.
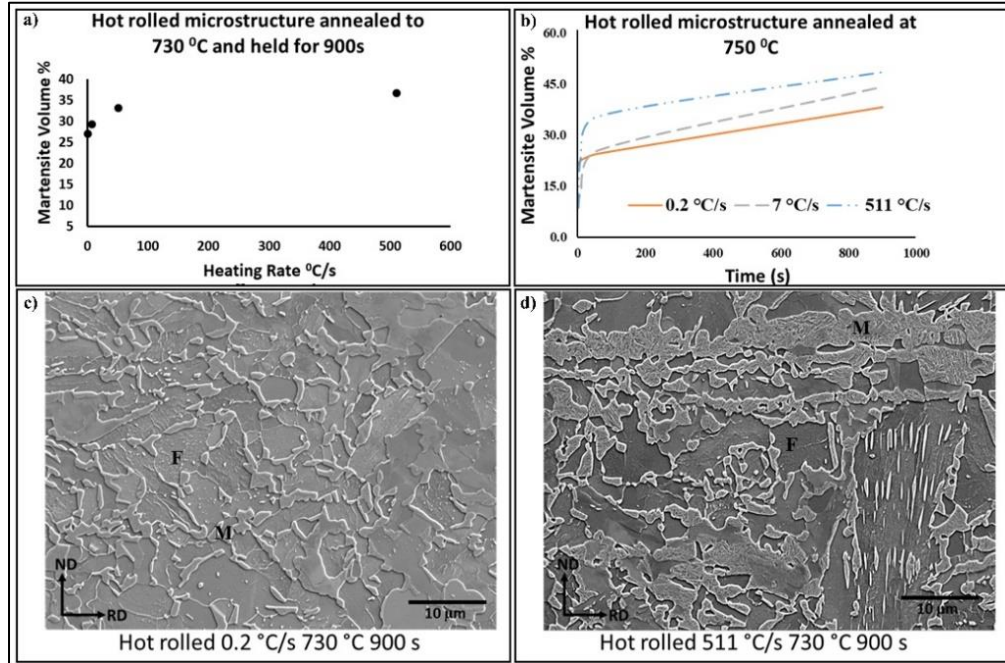
Figure 8. 1: a) Effect of heating rate on martensite volume percentage of BVHR steel annealed at 730 ^{0}C for 900 s, b) Effect of heating rate and soaking time on martensite volume percentage of samples annealed isothermally at 750 ^{0}C; (c, d): SEM microstructural images of samples annealed at 730 ^{0}C for 900 s at heating rates of c) 0.2 ^{0}C/s and d) 50.5 ^{0}C/s respectively. BV steel composition - (Fe-0.14C-2.1Mn-0.37Si-0.06V-0.002B).
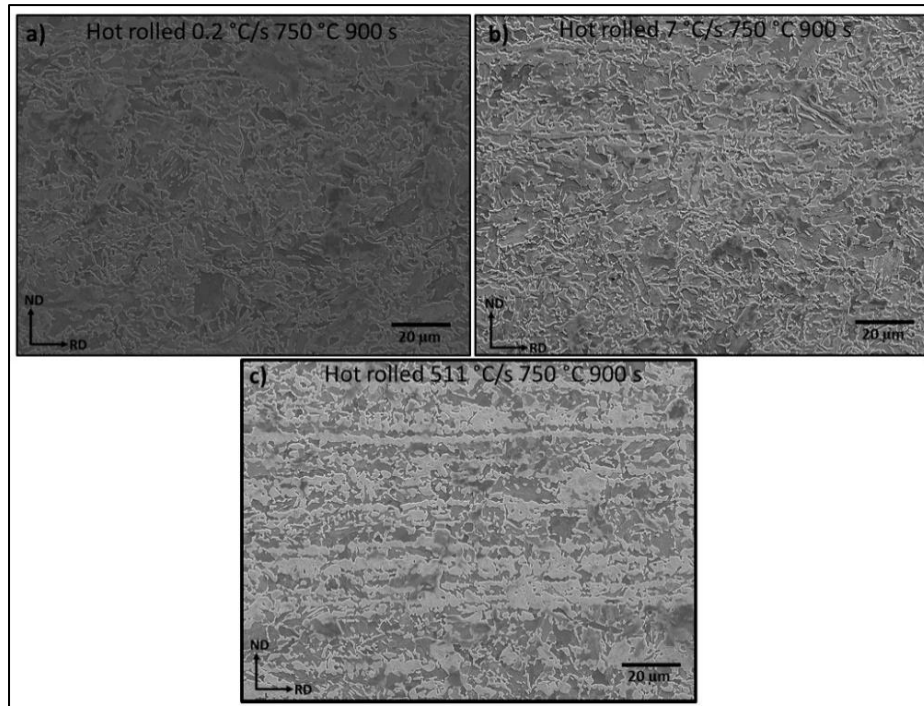
Figure 8. 2: SEM microstructural images of hot rolled samples annealed at 750 ^{0}C for 900 seconds at heating rates of a) 0.2 ^{0}C/s, b) 7 ^{0}C/s, and c) 511 ^{0}C/s. BV steel composition - (Fe-0.14C-2.1Mn-0.37Si-0.06V-0.002B).

8.2. Comparison of microstructural evolution in hot rolled and cold rolled steels

To have a better understanding of the microstructural evolution in hot rolled steels, a systematic comparison is done with respect to cold rolled steels in terms of martensite volume fractions, phase morphologies, and hardness values. **Figure 8.3 a)** shows the comparison of micro-hardness values of BVHR and BVCR 50% steels annealed at 715 ^{0}C at a heating rate of 0.2 ^{0}C/s. For all the soaking times, the hardness values for hot rolled samples were found to be higher than the cold rolled samples. Moreover, for both the samples increase in soaking time decreased the hardness values. It should be noted that ferrite recrystallization is already completed in the BVCR steel and there is no possibility of ferrite recrystallization in the BVHR steel because of the absence of stored deformed energy. Therefore, the decrease in hardness with increase in soaking time in both the samples can be attribute to the grain growth. Similarly **Figure 8.3 b)** shows the variation in hardness values for the hot rolled and cold rolled samples isothermally annealed at 730 ^{0}C and 750 ^{0}C at slow heating rate of 0.2 ^{0}C/s. For this

127

slow heating rate condition, the cold rolled samples have lower hardness values when compared to hot rolled samples for both annealing temperatures (730 ^{0}C and 750 ^{0}C). Unlike 715 ^{0}C, the hardness values increased with increase in soaking time indicating the increase in the austenite content (now martensite). **Figure 8.3 c)** shows the comparison of hardness variation for the hot rolled and cold rolled samples isothermally annealed at 750 ^{0}C and 780 ^{0}C at faster heating rates of 50.5 ^{0}C/s. Unlike in slow heating rate condition (0.2 ^{0}C/s), the hardness values for both the temperatures (750 ^{0}C and 780 ^{0}C) are found to be higher in cold rolled steel when compared to the hot rolled steel. As discussed in **Chapter 7**, the hardness values decreased for the initial soaking times for the BVCR samples annealed at 750 ^{0}C due to the progress in the recrystallization process. As expected, the hardness values continuously increased for the hot rolled samples indicating the progress in austenite formation without any ferrite recrystallization process taking place. **Figure 8.3 d)** shows the comparison of martensite volume percentages of BVCR and BVHR steels annealed at 750 ^{0}C at a heating rate of 7 ^{0}C/s. Similarly **Figure 8.3 (e, f)** shows the comparison of martensite volume percentages of BVCR and BVHR steels annealed at heating rate of 511 ^{0}C/s at annealing temperatures of 750 ^{0}C and 780 ^{0}C respectively. It can be seen that the martensite content is higher for the BVCR steel when compared to the BVHR steel for the majority of the soaking times. This indicates that when compared to hot rolled steels, the austenite kinetics is higher in the cold rolled steels for higher heating rate condition. This higher austenite kinetics can be attributed to the presence of deformed structure in the cold rolled condition enabling faster growth of austenite and thereby higher martensite content in the final microstructure. However, it can be seen from the slope of **Figure 8.3 f)** that after enough soaking time the differences in the austenite content will disappear, and the only parameter which dictates the austenite content will be the annealing temperature. **Figure 8.4 (a, b)** and **(c, d)** shows the comparison of microstructures developed in BVCR 50% and BVHR steels heat treated at 7 ^{0}C/s at 750 ^{0}C for 900 s and 511 ^{0}C/s at 780 ^{0}C for 60 s. It can be seen that increase in heating rate produced a banded martensite morphology even in the hot rolled steels. However, in the published literature, it is reported that increase in heating rate in the hot rolled steels produced a randomly distributed martensite islands along the grain boundaries [132]. This difference in results can be attributed to the presence of strong manganese segregation bands in the initial microstructure. Slower austenite kinetics for slower heating rate can be attributed to the growth competition between the distantly

nucleated austenite islands. Moreover, during slow heating rate condition the cementite particles have enough time to spheroidize before austenite formation when compared to the faster heating rate condition (**Figure 8.1 c**). This will further diminish the austenite formation rate due to the higher stability of spheroidized cementite particles. The martensite banded morphology produced in the final microstructure can be attributed to the presence of manganese segregation bands in the initial microstructure. This will be discussed further in the following sections with concentration on the through thickness anisotropy developed in the final microstructure.
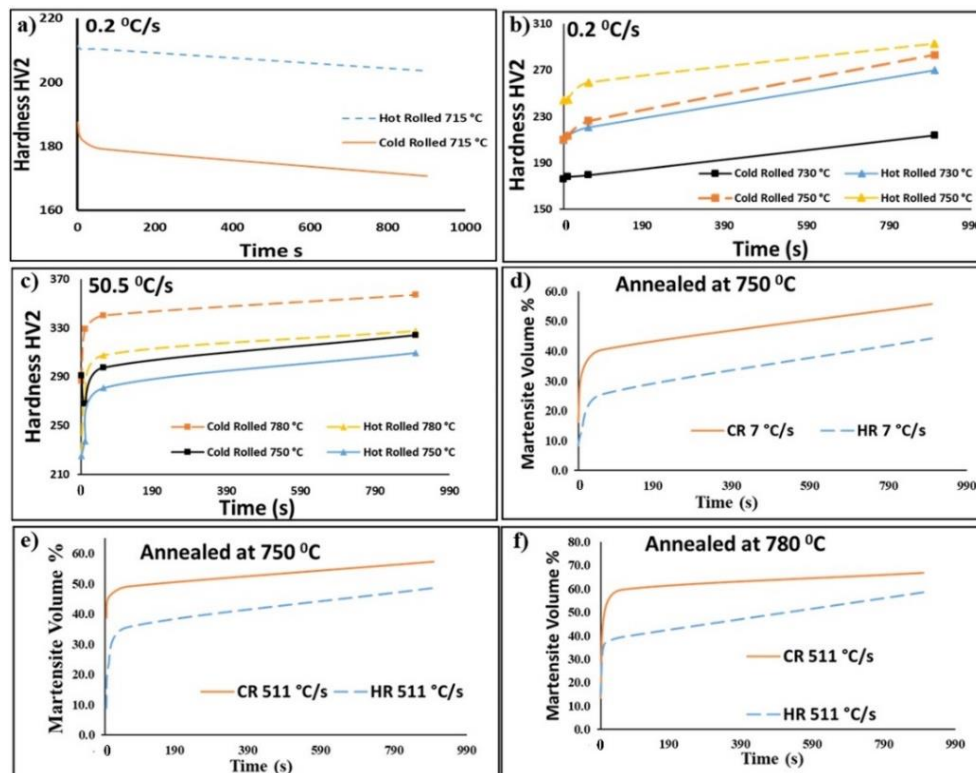
Figure 8. 3: (a, b, and c) Hardness comparison of BVHR and BVCR 50% steels heat treated at a) Heating rate of 0.2 ^{0}C/s and 715 ^{0}C, b) Heating rate of 0.2 ^{0}C/s at 730 ^{0}C and 750 ^{0}C, and c) Heating rate of 50.5 ^{0}C/s at 750 ^{0}C and 780 ^{0}C; (d, e, and f) Martensite volume percentage comparison of BVHR and BVCR 50% steels heat treated at d) Heating rate of 7 ^{0}C/s and 750 ^{0}C, e) Heating rate of 511 ^{0}C/s at 750 ^{0}C, and f) Heating rate of 50.5 ^{0}C/s at 780 ^{0}C. BV steel composition - (Fe-0.14C-2.1Mn-0.37Si-0.06V-0.002B).
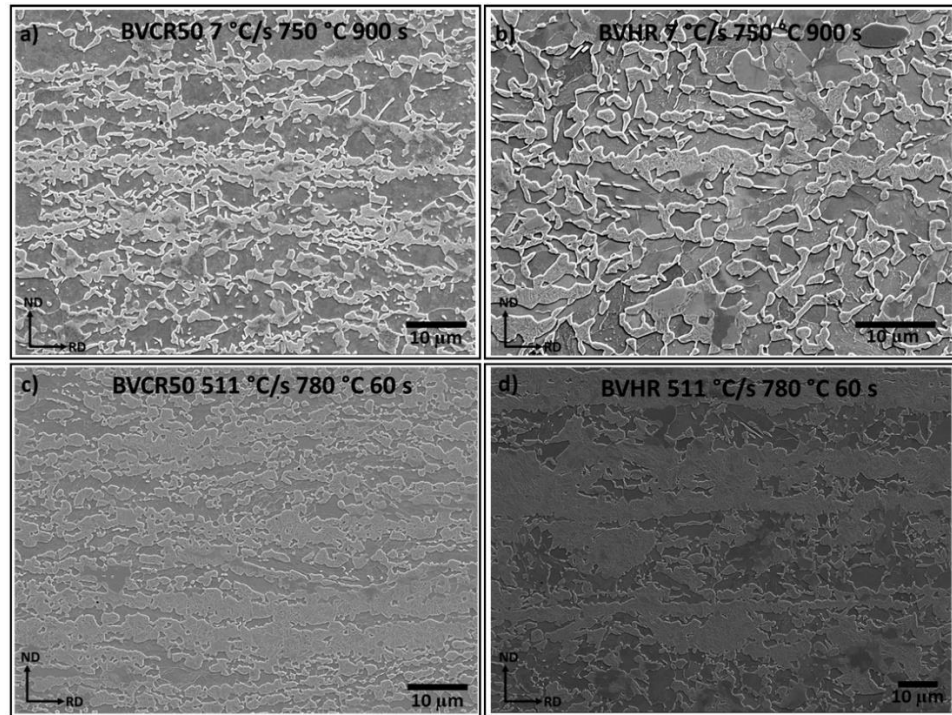
Figure 8. 4 (a, b, c, and d): SEM microstructural images of the BVCR 50 % steel (a, c) and the BVHR steel (b, d) samples annealed at 7 ^{0}C/s at 750 ^{0}C for 900 s (a, b) and at 511 ^{0}C/s at 780 ^{0}C for 60 s (c, d). BV steel composition - (Fe-0.14C-2.1Mn-0.37Si-0.06V-0.002B).

8.3. Through thickness anisotropy in hot rolled microstructure

Figure 8.5 shows the through thickness SEM microstructural images of the BVHR steel annealed at heating rate of 511 ^{0}C/s at temperature of 750 ^{0}C for 100 s. It can be seen that the spatial distribution of martensite phase at center is relatively more banded than that of the surface morphology. To understand this anisotropy behaviour EDX line scans are done on the center region of the initial hot rolled steel and the final heat treated steels. **Figure 8.6 a)** shows the SEM microstructural image of the BVHR steel with EDX Mn line scan overlapped on it. It can be seen that the pearlite bands present it center overlap with the Mn segregation bands. The EDX line scans reveal that the Mn concentration is at least 3 times higher in the banded region when compared to the non-banded region. Even though the solute partition coefficient of Mn is reported to be 0.71 (Scheil-Gulliver equation), the higher concentration (2.1 wt%) of it enables continuous rejection during solidification. This leads to the center line segregation and will remain throughout the downstream process. It can also be seen from **Figure 8.6 a)**, that beside the Mn enriched regions, there exists a slightly Mn depleted region.

Thus, a three different Mn compositions were developed in the initial BVHR microstructure. To understand the effect of this compositional variation, ThermoCalc analysis has been done to evaluate the equilibrium austenite formation. **Figure 8.6 b)** shows the comparative equilibrium austenite fraction of the compositions with three different Mn concentrations. It can be seen that the locally enriched Mn region has at least 70 ^{0}C lower A_{e1} temperature. This will enable preferential austenite formation on the pearlite bands with high Mn concentration. This can be seen from **Figure 8.6 c)**, where Mn high concentration peaks exactly match with martensite bands in the sample annealed at 7 ^{0}C/s at 750 ^{0}C for 60 s. At high heating rate conditions, the carbon in the pearlite colonies diffuse less extensively due to limited time available and therefore enhance even higher rate of banded martensite formation.
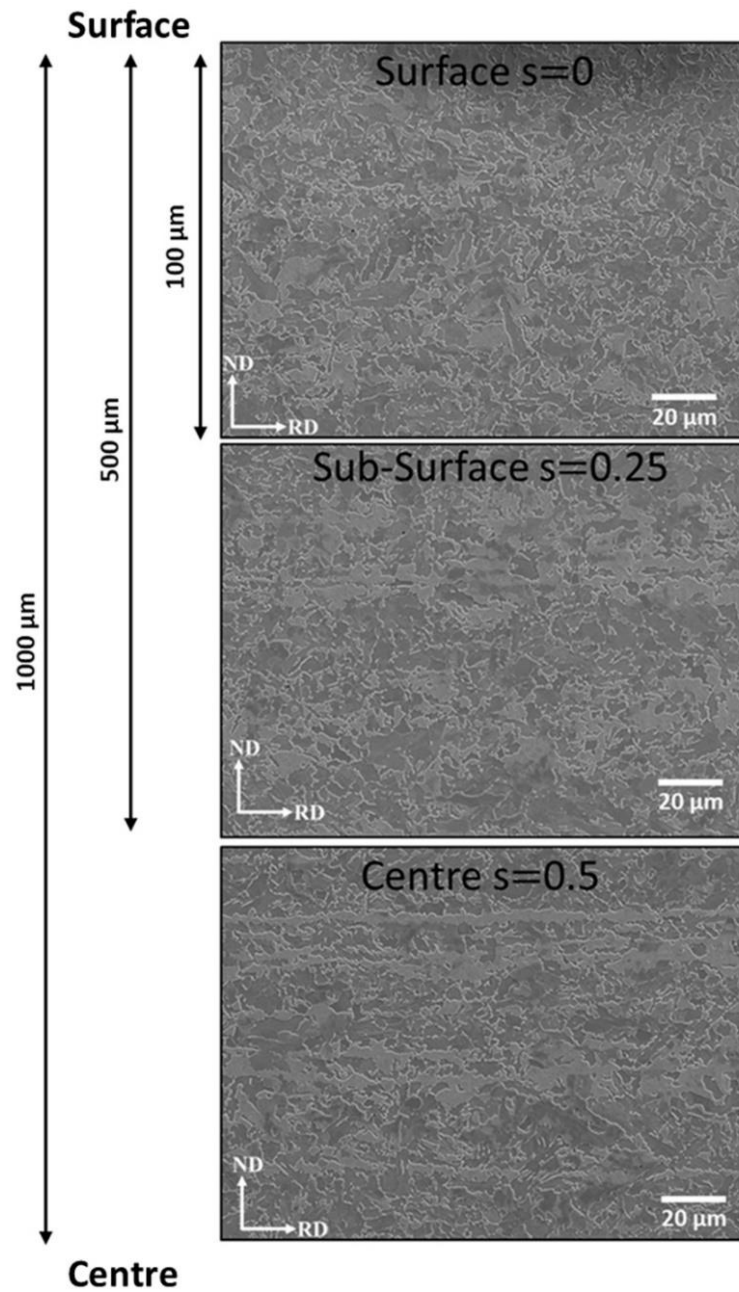
Figure 8. 5: Through thickness SEM microstructural images of the BVHR steel annealed at 511 ^{0}C/s at 750 ^{0}C for 100 s. BV steel composition - (Fe-0.14C-2.1Mn-0.37Si-0.06V-0.002B).
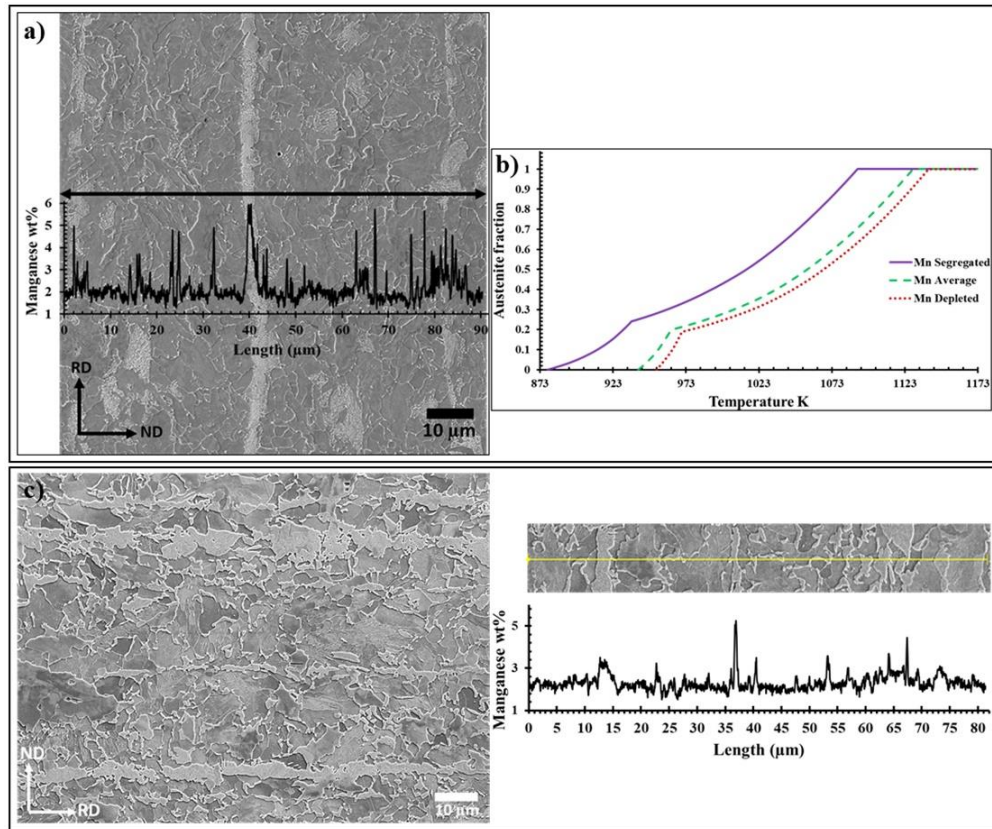
Figure 8. 6: a) SEM microstructural image of BVHR steel (center) with its corresponding EDX Mn line graph, b) Comparative ThermoCalc simulation showing equilibrium austenite fraction for compositions with three different Mn concentrations, and c) SEM microstructural image and its corresponding EDX Mn line graph of BVHR steel (center) annealed at 7 ^{0}C/s at 750 ^{0}C for 60 s. BV steel composition - (Fe-0.14C-2.1Mn-0.37Si-0.06V-0.002B).

The hot rolled steels not only developed through thickness morphological anisotropy, but also exhibited through thickness texture anisotropy. **Figure 8.7 and 8.8** shows ODF sections at Euler angles of $\varphi_2 = 0°$ and $\varphi_2 = 45°$ at the surface and centre through thickness positions for BVHR sample and the sample annealed at 511 ^{0}C/s at 750 ^{0}C for 60 s. **Figure 8.9** compares the quantified texture fibers such as α, γ, ε, θ, η, and ζ in the reduced Euler space for BVHR sample, sample annealed at 0.2 ^{0}C/s at 750 ^{0}C for 60 s and 511 ^{0}C/s at 750 ^{0}C for 60 s. It can be seen that the as received BVHR steel possessed through thickness texture inhomogeneity. The BVHR sample produced strong α fiber at the center ({112}<110> component) location when compared to the surface of the sample. Heat treated samples also showed similar strong plain-strain texture at the center of the thickness. It can be seen that γ Fiber ({111}<112>

133

component)is strong at center and weak at the surface for all the three samples. The surface of the three samples produced strong ζ fiber when compared to the center, especially {011}<211> component. In summary the center of the three samples produced plain strain texture and the surface produced shear texture.
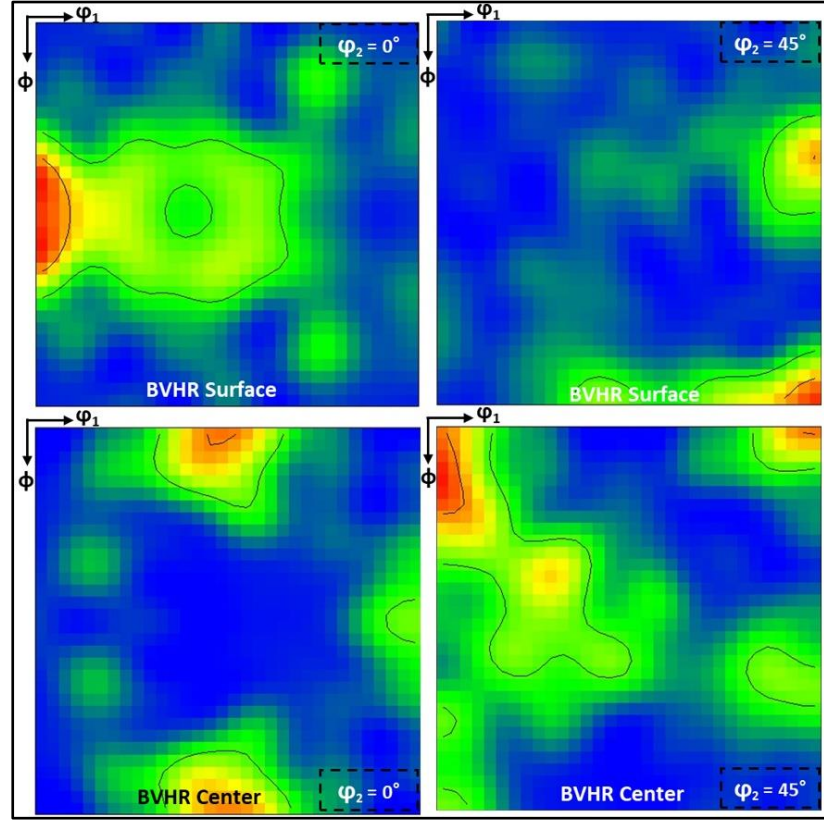
Figure 8. 7: ODF maps at $\varphi_2 = 0°$ and $\varphi_2 = 45°$ at surface and center for BVHR steel. BV steel composition - (Fe-0.14C-2.1Mn-0.37Si-0.06V-0.002B).
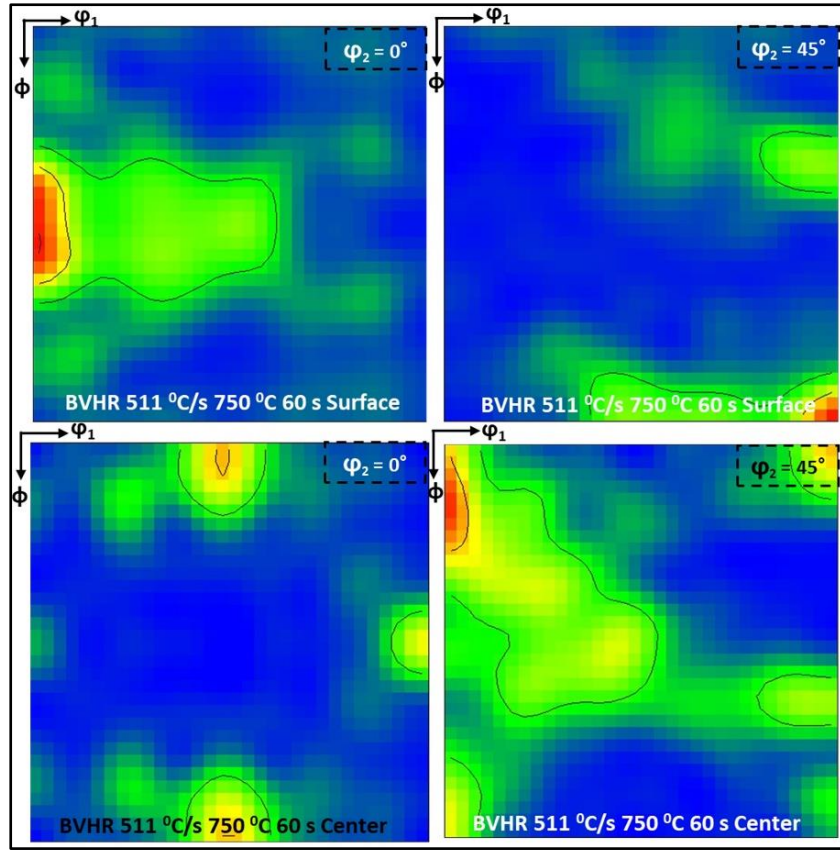
Figure 8. 8: ODF maps at $\varphi_2 = 0°$ and $\varphi_2 = 45°$ at surface and center for BVHR steel. BV steel composition - (Fe-0.14C-2.1Mn-0.37Si-0.06V-0.002B).
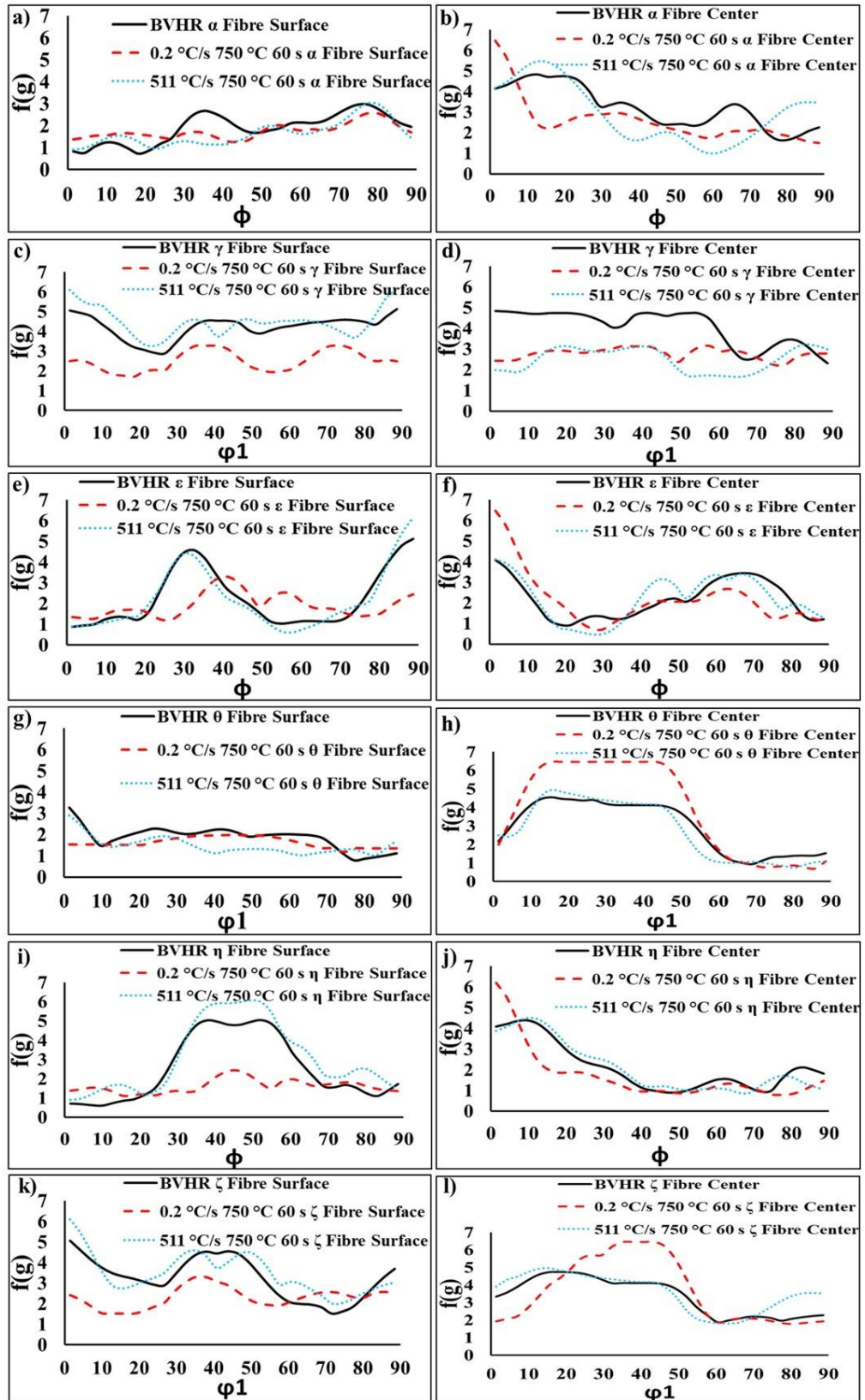
Figure 8. 9: Quantified texture fibers of α, γ, ε, θ, η, and ζ in the reduced Euler space for BVHR sample, sample annealed at 0.2 ^{0}C/s at 750 ^{0}C for 60 s (left) and 511 ^{0}C/s at 750 ^{0}C for 60 s (right). BV steel composition - (Fe-0.14C-2.1Mn-0.37Si-0.06V-0.002B).

8.4. Vanadium carbide precipitation study

Figure 8.10 (a, b) shows the vanadium carbide precipitate characteristics of the BVCR 50 % steels annealed at 750 ^{0}C for 60 s at heating rates of 0.2 ^{0}C/s and 50.5 ^{0}C/s respectively. The number density of precipitates in both the samples were found to be similar at 1.9 x 10^{13} /m^2 and 7.7 x 10^{12} /m^2 for 0.2 ^{0}C/s and 50.5 ^{0}C/s respectively. However, the average size of the precipitates was found to be higher for the slow heating rate condition. The slow heating rate condition (0.2 ^{0}C/s) sample contained precipitates with an average size of 20 nm and the fast heating rate condition (50.5 ^{0}C/s) sample contained precipitates with an average size of 14.9 nm. The reason for this higher average size precipitates in slower heating rate condition can be attributed to higher time available for the coarsening of the precipitates to happen. This brief precipitation study is done to emphasis the fact that the vanadium precipitation also happens during the inter-critical annealing process. This simultaneous happening of vanadium precipitation should not have any influence on the microstructural characteristics such as volume fractions, grain sizes, morphologies and distributions of ferrite and martensite phases. But the presence of these fine vanadium precipitates enhances the mechanical properties of these steels.
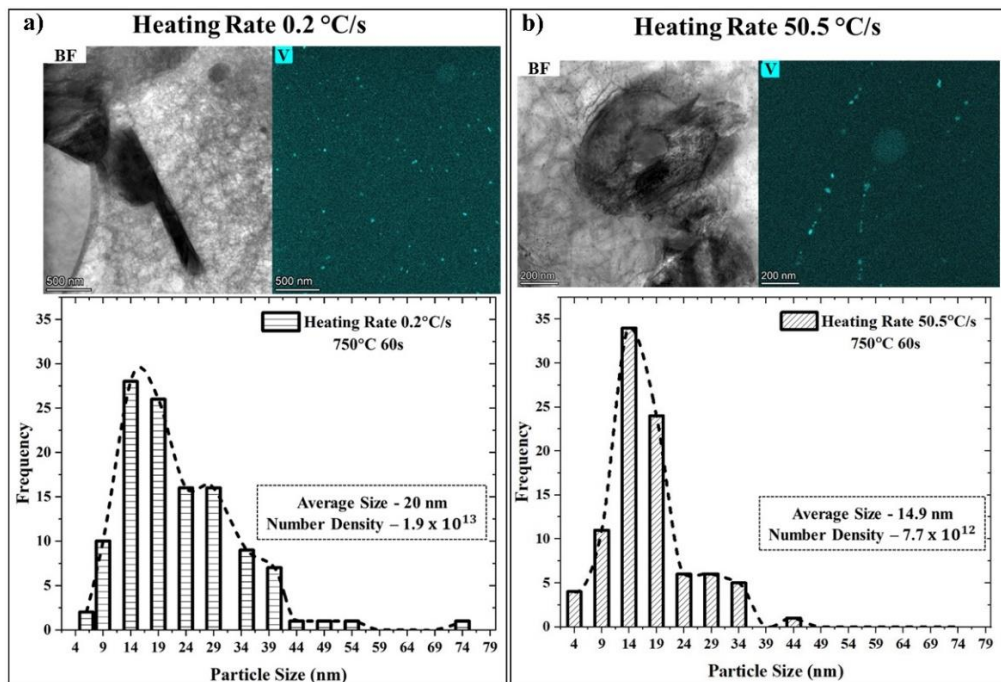
Figure 8. 10: Comparison of vanadium precipitate characteristics in BVCR 50% steels annealed at heating rates of a) 0.2 ^{0}C/s and b) 50.5 ^{0}C/s at inter-critical temperature of

750 ^{0}C and soaking time of 60 seconds with total number of particles of 121 and 98 respectively. BV steel composition - (Fe-0.14C-2.1Mn-0.37Si-0.06V-0.002B).

8.5. Nano-indentation measurements

Figure 8.11 a) shows the SEM image of BVCR 50% steel annealed at 0.2 ^{0}C/s at 750 ^{0}C for 60 s with the 10 x 10 matrix of nano-indents. **Figure 8.11 (b and c)** shows the representative indents for ferrite and martensite phases which are used for the measurement of the corresponding hardness values. Such indents in the various heat treated samples were located in the matrix of indents after etching and the corresponding nano-hardness values are measured. **Figure 8.11 (d and e)** shows the comparison of the nano-hardness values of the ferrite and martensite phases with respect to the martensite volume fractions for hot rolled and cold rolled samples. As expected, the nano-hardness values of martensite phase was found to be very high when compared to the ferrite phase for all the volume fractions. It can also be seen that increase in the volume fraction in both BVHR and BVCR 50% samples caused a slight but noticeable decrease in the decreased the martensite nano-hardness values. Moreover, the martensite nano-hardness values for the BVCR 50% samples are slight lower than the BVHR values. This is because as the volume fraction of the martensite increases in the inter-critical annealing, its average carbon content decreases [206]. This in turn decreases the strength of the martensite phase as evidenced by the nano-hardness values. Moreover, the ferrite individual strength is found to be increased with the increase in martensite volume fraction for both the samples. This can be attributed to the increase in the dislocation density in the ferrite grains due to the increase in the formation of martensite phase and decrease in the ferrite fraction.
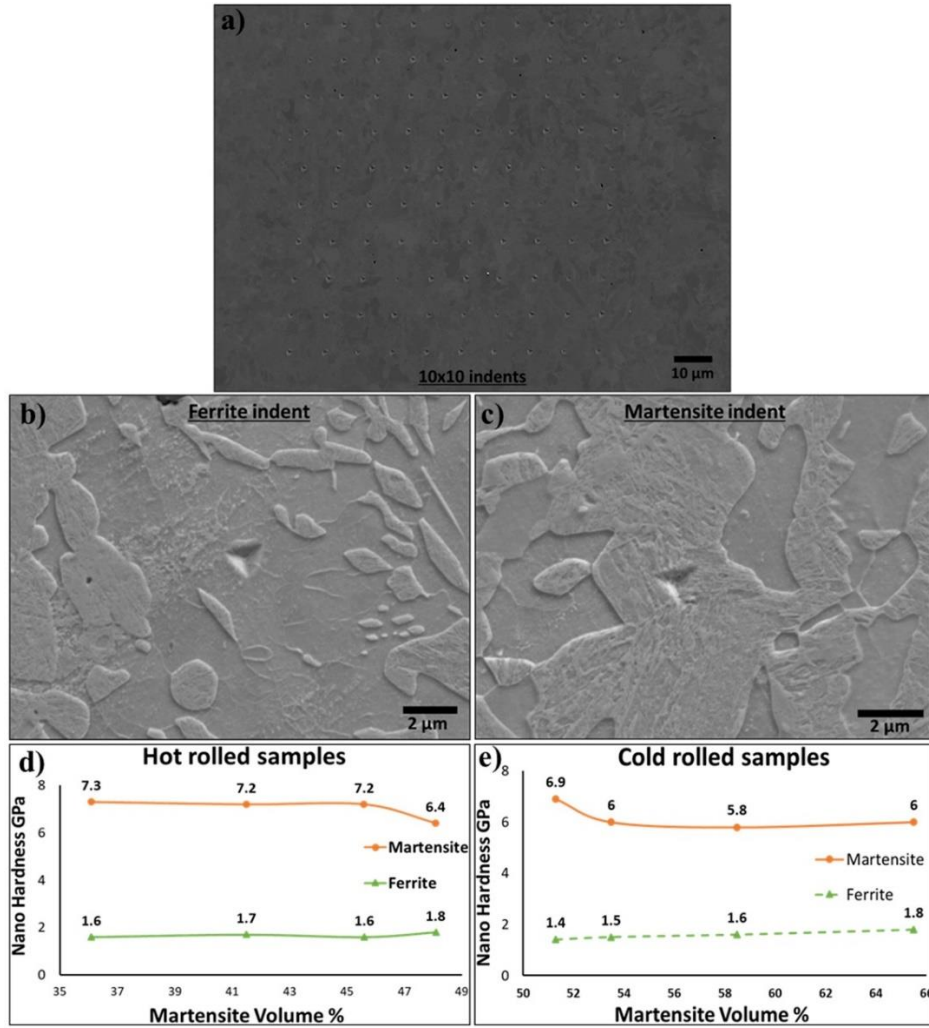
Figure 8. 11: **a)** SEM image of BVCR 50% steel annealed at 0.2 ^{0}C/s at 750 ^{0}C for 60 s with matrix of 10 x 10 nano-indents (without etching), **(b and c)** Representative nano-indents in the ferrite and martensite phases respectively (after etching), **(d and e)** Comparison of nano-hardness measurements of ferrite and martensite phases with respect to martensite volume fraction for BVHR and BVCR 50% steels respectively. BV steel composition - (Fe-0.14C-2.1Mn-0.37Si-0.06V-0.002B).

In this chapter, it was found that for hot rolled initial microstructure, increase in heating rate increased the martensite volume fraction and transformed martensite to banded morphology. When compared to cold rolled initial microstructure, the austenite formation kinetics was found to be low in hot rolled initial microstructure. The presence of manganese bands, especially at the centre of the thickness, caused a through thickness gradient for martensite morphology (Centre–Banded, Surface-Random). A through thickness texture gradient was observed for both hot rolled and annealed microstructures.

Chapter 9 - Conclusions and Future work

9.1 Summary

The microstructural features of DP steels consist of various important characteristics such as volume fractions of the phases, corresponding grain sizes, aspect ratios and morphologies, through thickness texture anisotropy (Hot rolled steels), compositional segregation and texture etc. These microstructural features are greatly influenced by the heating and the soaking steps of the inter-critical annealing step of DP steel manufacture. This project systematically evaluates the microstructural evolution of both hot rolled and cold rolled steels during the heating and soaking step of the inter-critical annealing. The primary focus of this project was to understand the effect of simultaneous happening of high temperature processes such as ferrite recovery, ferrite recrystallization and grain growth and austenite formation processes on the final DP steel microstructure. Moreover, the influence of manganese segregation on the microstructure evolution with respect to austenite formation was also studied in this research work.

In this research work it was found that with the increase in the cold reduction the amount of overlap between ferrite recrystallization and austenite formation decreases (Chapter 6). This is a key aspect to evaluate as it ultimately changes the final microstructure of different cold reductions annealed at same annealing parameters. Most importantly, this research work proves that with the increase in overlap of ferrite recrystallization and austenite formation, the volume fraction of austenite forming in the annealing step increases for cold rolled steels (Chapter 7). Moreover, with the increase in heating rate, the morphology of the martensite was found to be transformed from necklace morphology to banded morphology. Increase in heating rate in hot rolled steels also increased the austenite kinetics and produced a banded martensite in the following microstructure (Chapter 8).

This research work systematically understands the mechanism of austenite formation at various heat treatment parameters. This is not only critical for DP steel microstructure but also is applicable to other steels such as Quench partitioned steels, TRIP steels, carbide free bainite steels and medium Mn steels. This research work

helps to understand the consequences of employing high heating rate in the industrial process. Firstly, increase in heating rate during the heating step of annealing process can potentially decrease the furnace length and therefore increase the energy efficiency of the process. Moreover, higher austenite kinetics during the high heating rate condition decreases the amount of soaking time required to obtain a specific amount of austenite. This also decreases the overall time required for the annealing process and thereby increases the energy efficiency of the continuous annealing line.

9.1.1 Conclusions

The main conclusions obtained from this study are summarized as follows:

- ➢ Increase in temperature (625 ℃, 650 ℃, and 675 ℃) increased the recrystallization kinetics because recrystallization is a diffusion driven thermally activated process.

- ➢ Increase in the percentage of cold reduction (50%, 60% and 75 %) increased the recrystallization kinetics because of the increased stored deformation energy and the associated driving force for the progress of recrystallization process.

- ➢ The JMAK model with the calculated constants was found to be in good agreement with the experimentally found recrystallization fraction. The activation energy for the recrystallization process (339 kJ/mole) was found to be very high when compared to the self-diffusion activation energy of the BCC iron (251 kJ/mole). This can be understood by the retarding effect induced by the solute elements such as manganese and vanadium either solute drag effect or precipitate pinning fraction.

- ➢ It was found that with the increase in heating rate, the recrystallisation start temperature and the austenite start temperature increases because both processes follow diffusion driven nucleation and growth mechanism and therefore require incubation time for the progress to happen.

- ➢ A modified JMAK model was developed which predicts the heating rates required to obtain specific amount of overlaps between ferrite recrystallization and austenite formation processes. For the BV steel, the modified JMAK model predicted the heating rates required to obtain specific amount of

overlaps of 1%, 15%, 34%, 67%, 88% and 99% to be 0.2 ^{0}C/s, 0.9 ^{0}C/s, 1.8 ^{0}C/s, 7 ^{0}C/s, 50.5 ^{0}C/s, and 511 ^{0}C/s respectively.

➢ After inter-critical annealing, it was found that the austenite formation kinetics is lowest for the slow heating rate condition. This was due to the presence of fully recrystallized structure and the spheroidized cementite particles in the microstructure prior to the austenite formation step.

➢ The sluggish growth of the austenite along the distantly located austenite nuclei and the higher stability of spheroidized cementite retards the austenite formation kinetics in slow heating rate condition. The preferential nucleation and growth of austenite along the recrystallized ferrite grain boundaries produce martensite with necklace morphology in the final microstructure.

➢ Increase in heating rate during inter-critical annealing increased the amount of martensite in the final microstructure. The martensite was found to be in banded morphology for higher heating rate conditions.

➢ The presence of directionally aligned recovered ferrite and fragmented cementite prior to austenite formation step was the main reason for higher austenite kinetics and banded martensite morphology in the high heating rate condition,

➢ When compared to fast heating rate condition, the medium heating rate condition produced thin martensite bands due the presence of recrystallized ferrite grains and the consequent restricted austenite growth along the normal directions.

➢ It was found that for fast heating rate condition, recrystallization process dominates at low inter-critical temperature whereas austenite process dominates at high inter-critical temperature.

➢ Increase in heating rate also caused significant increase in austenite kinetics in the hot rolled steels. Through thickness martensite morphological anisotropy and texture inhomogeneity was found in the hot rolled steels. ThermoCalc analysis coupled with EDX scans proved that the presence of manganese segregated bands contributed to the banding of martensite in the final microstructure.

➢ Nano-indentation measurements showed that increase in martensite volume fraction decreases the strength of martensite phase in both hot rolled and cold rolled steels because of the decrease in carbon content in it.

9.2 Suggestions for future work

The knowledge generated in this research work about the microstructural evolution of DP steels can be useful in developing steels with better mechanical properties. As this research work is completely based on manganese segregated steels, it will be interesting to evaluate the austenite formation mechanism for steels with completely lean composition in which segregation won't have a major influence on the microstructure evolution. In terms of initial microstructure, research work on the microstructural evolution from a fully bainitic or a fully martensitic microstructure can be very interesting as these microstructures have relatively uniform carbon distribution. On the other hand, it will also be very interesting to evaluate the austenite formation mechanism in high Mn steels such as TRIP steels where segregation plays a huge role in the final microstructure. Moreover, it will also be interesting to use the continuous heating rate model from this research work to generate heating rates required for overlap of other compositions and cold reductions used for commercial DP steels. Even though the high martensite at high heating rate condition will contribute to increase in strength, the banding phenomenon will increase the chance of de-cohesion between ferrite and martensite during loading and therefore can lead to reduced ductility. In this regard, research work to decrease the strain compatibilities between ferrite and martensite phases will be very critical to produce high strength DP steels with acceptable levels of ductility.

Chapter 10: References

[1]   J. Fallows, The 50 Greatest Breakthroughs Since The Wheel, Atl. (2013) 9. http://www.theatlantic.com/magazine/archive/2013/11/innovations-list/309536/ (accessed March 30, 2020).

[2]   G. Davies, Design and material utilization, in: Mater. Automob. Bodies, 2003: pp. 10–60. doi:10.1016/b978-075065692-4/50019-4.

[3]   J.R. Fekete, J.N. Hall, Design of auto body: Materials perspective, in: Automot. Steels Des. Metall. Process. Appl., 2017: pp. 1–18. doi:10.1016/B978-0-08-100638-2.00001-8.

[4]   C. Reid, C. Reid, How the Dutch Really Got Their Cycleways, in: Bike Boom, 2017: pp. 179–210. doi:10.5822/978-1-61091-817-6_9.

[5]   SMOV, Road Deaths in the Netherlands. AMOV Fact Sheet, SWOV Fact Sheet. (2017). https://www.swov.nl/en/facts-figures/factsheet/road-deaths-netherlands.

[6]   M. Moguen-Toursel, Emergence and transfer of vehicle safety standards: why we still do not have global standards, Entrep. Hist. 51 (2008) 88. doi:10.3917/eh.051.0088.

[7]   R.L. Huston, A Review of the effectiveness of seat belt systems: Design and safety considerations, Int. J. Crashworthiness. 6 (2001) 243–252. doi:10.1533/cras.2001.0175.

[8]   Global Carbon Project. (December 4, 2019). Historical carbon dioxide emissions from global fossil fuel combustion and industrial processes from 1758 to 2018 (in million metric tons)* [Graph]. In Statista., (n.d.). https://www.statista.com/statistics/264699/worldwide-co2-emissions/ (accessed May 27, 2020).

[9]   M. L, Ross, How the 1973 Oil Embargo Saved the Planet, Counc. Foreign Relations. (2013). https://www.foreignaffairs.com/articles/north-america/2013-10-15/how-1973-oil-embargo-saved-planet (accessed June 26, 2020).

[10] J.D. Hamilton, Historical oil shocks, in: Routledge Handb. Major Events Econ. Hist., 2015. doi:10.4324/9780203067871.ch21.

[11] J.D. Hamilton, What is an oil shock?, J. Econom. 113 (2003) 363–398. doi:10.1016/S0304-4076(02)00207-5.

[12] J.D. Hamilton, Causes and consequences of the oil shock of 2007-08, Brookings Pap. Econ. Act. (2009) 215–261. doi:10.2139/ssrn.2583456.

[13] UK Department for Business, Energy and Industrial Strategy. (February 4, 2020). Greenhouse gas emissions in the United Kingdom (UK) in 2018, by gas and sector (in million metric tons of carbon dioxide equivalent) [Graph]. In Statista., (n.d.). https://www.statista.com/statistics/780263/greenhouse-gas-emissions-by-gas-united-kingdom-uk/ (accessed May 27, 2020).

[14] T.B. Hilditch, T. de Souza, P.D. Hodgson, Properties and automotive applications of advanced high-strength steels (AHSS), in: Weld. Join. Adv. High Strength Steels, 2015: pp. 9–28. doi:10.1016/B978-0-85709-436-0.00002-3.

[15] N. Lutsey, Review of technical literature and trends related to automobile mass-reduction technology, Inst. Transp. Stud. 1 (2010) 1–40. https://escholarship.org/uc/item/9t04t94w.

[16] R.A. Schultz, A.K. Abraham, Metallic Material Trends For North American Light Vehicles, Ducker Worldw. (2009). https://www.buildusingsteel.org/~/media/Files/Autosteel/Great Designs in Steel/GDIS 2009/06 - Metallic Material Trends For North American Light Vehicles.pdf.

[17] R.L. Pastorek, A.B. Sipler, Strain aging properties of high-strength hot-rolled steels, in: SAE Tech. Pap., 1977. doi:10.4271/770165.

[18] P.B. Lake, J.J. Grenawalt, Partially annealed high strength cold rolled steels, in: SAE Tech. Pap., 1977. doi:10.4271/770163.

[19] D.G. Adams, S. Dinda, R.A. George, R.W. Karry, A.S. Kasper, J. Pogorel, W.E. Swenson, W.L. Weeks, Charger XL: A lightweight materials development vehicle, in: SAE Tech. Pap., 1976. doi:10.4271/760203.

[20] C.L. Bambenek, S. Mocarski, J.W. Mitchell, M.K. Bidol, J.A. Lumm, 1983

Ford ranger truck HSLA steel wheel, in: SAE Tech. Pap., 1982. doi:10.4271/820019.

[21]   R.P. Krupitzer, R.E. Miner, P.J. Vander Arend, F. Reis, J.A. Slane, J.K. Abraham, S.J. Matas, Progress in HSLA steels in automotive applications, in: SAE Tech. Pap., 1977. doi:10.4271/770162.

[22]   G. Davies, Future trends in automotive body materials, in: Mater. Automob. Bodies, 2003. doi:10.1016/b978-075065692-4/50026-1.

[23]   M. Shome, M. Tumuluru, Introduction to welding and joining of advanced high-strength steels (AHSS), in: Weld. Join. Adv. High Strength Steels, 2015: pp. 1–8. doi:10.1016/B978-0-85709-436-0.00001-1.

[24]   A. Abraham, Metallic material trends in the North American light vehicle., in: . . Gt. Des. Steel Semin. Livonia M, 2015.

[25]   L.F. Romano-Acosta, O. García-Rincon, J. p. Pedraza, E.J. Palmiere, Influence of thermomechanical processing parameters on critical temperatures to develop an Advanced High-Strength Steel microstructure, J. Mater. Sci. (2021).

[26]   A. Grajcar, Segregation Behaviour of Third Generation Advanced High-Strength Mn-Al Steels, Arch. Foundry Eng. 12 (2012) 123–128. doi:10.2478/v10266-012-0049-2.

[27]   P.D. Bois, C.C. Chou, B.B. Fileta, A.I. King, H.F. Mahmood, Vehicle crashworthiness and occupant protection, Am. Iron Steel Inst. (2004). doi:10.1121/1.2783205.

[28]   S. Keeler, M. Kimchi, Advanced High-Strength Steels Application Guidelines Version 5.0, World AutoSteel.Org. (2014). doi:10.1016/S1644-9665(12)60197-6.

[29]   J. Reed, Advanced High-Strength Steel Technologies in the 2015 Ford Edge., Gt. Des. Steel. (2015).

[30]   S.A. Golovanenko, N.M. Fonstein, Dual-phase low alloyed steels., M. Met. (1986).

[31]   N. Fonstein, Dual-phase steels, in: Automot. Steels Des. Metall. Process. Appl., 2016: pp. 169–216. doi:10.1016/B978-0-08-100638-2.00007-9.

[32]   Chevy Malibu: Larger, Lighter, More Efficient with HSS, (2018). https://www.worldautosteel.org/why-steel/steel-muscle-in-new-vehicles/2016-chevy-malibu-larger-lighter-more-efficient-with-hss/.

[33]   Dual Phase Steels, (2018). https://www.worldautosteel.org/steel-basics/steel-types/dual-phase-dp-steels/.

[34]   M.. Rashid, Dual phase steels., Annu. Rev. Mater. Sci. 11 (1981) 245–266. doi:10.1146/annurev.ms.11.080181.001333.

[35]   M. Delincé, P.J. Jacques, T. Pardoen, Separation of size-dependent strengthening contributions in fine-grained Dual Phase steels by nanoindentation, Acta Mater. 54 (2006) 3395–3404. doi:10.1016/j.actamat.2006.03.031.

[36]   C.C. Tasan, M. Diehl, D. Yan, M. Bechtold, F. Roters, L. Schemmann, C. Zheng, N. Peranio, D. Ponge, M. Koyama, K. Tsuzaki, D. Raabe, An Overview of Dual-Phase Steels: Advances in Microstructure-Oriented Processing and Micromechanically Guided Design, Annu. Rev. Mater. Res. 45 (2015) 391–431. doi:10.1146/annurev-matsci-070214-021103.

[37]   M. Mazinani, W.J. Poole, Effect of martensite plasticity on the deformation behavior of a low-carbon dual-phase steel, Metall. Mater. Trans. A Phys. Metall. Mater. Sci. 38 (2007) 328–339. doi:10.1007/s11661-006-9023-3.

[38]   D.A. Korzekwa, D.K. Matlock, G. Krauss, Dislocation substructure as a function of strain in a dual-phase steel, Metall. Trans. A. 15 (1984) 1221–1228. doi:10.1007/BF02644716.

[39]   L.F. Ramos, D.K. Matlock, G. Krauss, On the deformation behavior of dual-phase steels, Metall. Trans. A. 10 (1979) 259–261. doi:10.1007/BF02817636.

[40]   G.R. Speich, R.L. Miller, Mechanical properties of ferrite-martensite steels., IEEE Conf. Rec. Annu. Pulp Pap. Ind. Tech. Conf. (1979) 145–182.

[41]   A. Bag, K.K. Ray, E.S. Dwarakadasa, Influence of martensite content and morphology on tensile and impact properties of high-martensite dual-phase steels, Metall. Mater. Trans. A Phys. Metall. Mater. Sci. 30 (1999) 1193–1202. doi:10.1007/s11661-999-0269-4.

[42]   Y. Granbom, Structure and mechanical properties of dual phase steels– An

experimental and theoretical analysis, 2010.

[43]   R.K. Ray, J.J. Jonas, Transformation textures in steels, Int. Mater. Rev. 35 (1990) 1–36. doi:10.1179/095066090790324046.

[44]   A. Chattopadhyay, V. Subramanya Sarma, B.S. Murty, A. Haldar, D. Bhattacharjee, Studies on hot rolled galvanized steel sheets: Effect of reheating on galvanizing, Surf. Coatings Technol. 203 (2009) 3465–3471. doi:10.1016/j.surfcoat.2009.05.005.

[45]   P. Jacques, X. Cornet, P. Harlet, J. Ladriere, F. Delannay, Enhancement of the mechanical properties of a low-carbon, low-silicon steel by formation of a multiphased microstructure containing retained austenite, Metall. Mater. Trans. A Phys. Metall. Mater. Sci. 29 (1998) 2383–2393. doi:10.1007/s11661-998-0114-1.

[46]   R.. Mehl, The Decomposition of Austenite by Nucleation and Growth Process., J. I. S. I. 159 (1948) 113.

[47]   S. Serajzadeh, A. Karimi Taheri, A study on austenite decomposition during continuous cooling of a low carbon steel, Mater. Des. 25 (2004) 673–679. doi:10.1016/j.matdes.2004.03.006.

[48]   R.T. Van Tol, L. Zhao, J. Sietsma, Kinetics of austenite decomposition in manganese-based steel, Acta Mater. 64 (2014) 33–40. doi:10.1016/j.actamat.2013.10.037.

[49]   H. Azizi-Alizamini, M. Militzer, W.J. Poole, Austenite formation in plain low-carbon steels, in: Metall. Mater. Trans. A Phys. Metall. Mater. Sci., 2011: pp. 1544–1557. doi:10.1007/s11661-010-0551-5.

[50]   F. Liu, G. Xu, Y.L. Zhang, H.J. Hu, L.X. Zhou, Z.L. Xue, In situ observations of austenite grain growth in Fe-C-Mn-Si super bainitic steel, Int. J. Miner. Metall. Mater. 20 (2013) 1060–1066. doi:10.1007/s12613-013-0834-0.

[51]   M. Calcagnotto, D. Ponge, D. Raabe, Ultrafine grained ferrite/martensite dual phase steel fabricated by large strain warm deformation and subsequent intercritical annealing, in: ISIJ Int., 2008: pp. 1096–1101. doi:10.2355/isijinternational.48.1096.

[52]   J.O. Arnold and A. McWilliams: J. Iron Steel Inst., (1905) 352.

[53] G.A. Roberts, R.. Mehl, The mechanism and the rate of formation of austenite from ferrite-cementite aggregates, Trans. ASM. 31 (1943) 613–650.

[54] G.R. Speich, V.A. Demarest, R.L. Miller, Formation of Austenite During Intercritical Annealing of Dual-Phase Steels., Metall. Trans. A, Phys. Metall. Mater. Sci. 12 A (1981) 1419–1428. doi:10.1007/BF02643686.

[55] G.R. Speich, A. Szirmae, M.J. Richards, Formation of Austenite From Ferrite and Ferrite-Carbide Aggregates, Met Soc AIME-Trans. 245 (1969) 1063–1074.

[56] M. Hillert, K. Nilsson, L.E. ToerndahlL, Effect of alloying elements on the formation of austenite and dissolution of cementite, J Iron Steel Inst. 209 (1971) 49–66.

[57] R.D. Lawson, D.K. Matlock, and G. Krauss: Fundamentals of Dual-Phase Steels, R.A. Kot and B.L. Bramfitt, eds., TMS-AIME, Warrendale, PA, (1981) 347–81.

[58] Garcia, C.I. and. DeArdo, A.J, Metall. Mater. Trans. A. 12A (1981) 521–30.

[59] G. Krauss, D.K. Matlock, E.A. Cornford, HSLA Steels Technology and Applications, ASM, Met. Park. OH. (1984) 297-328.

[60] C.I. Garcia, A.J. Deardo, Formation of austenite in 1.5 pct Mn steels, Metall. Trans. A, Phys. Metall. Mater. Sci. 12 A (1981) 521–530. doi:10.1007/BF02648551.

[61] V.L. de la Concepción, H.N. Lorusso, H.G. Svoboda, Effect of Carbon Content on Microstructure and Mechanical Properties of Dual Phase Steels, Procedia Mater. Sci. 8 (2015) 1047–1056. doi:10.1016/j.mspro.2015.04.167.

[62] S. Hironaka, H. Tanaka, T. Matsumoto, Effect of Si on mechanical property of galvannealed dual phase steel, in: Mater. Sci. Forum, 2010: pp. 3260–3265. doi:10.4028/www.scientific.net/MSF.638-642.3260.

[63] N. Fonstein, H.J. Jun, O. Yakubovsky, R. Song, N. Pottore, Evolution of Advanced High Strength Steels (AHSS) to Meet Automotive Challenges, Aist. (2013) 1–13.

[64] S.J. Kim, C.G. Lee, T.H. Lee, C.S. Oh, Effect of Cu, Cr and Ni on mechanical properties of 0.15 wt.% C TRIP-aided cold rolled steels, Scr. Mater. 48 (2003)

539–544. doi:10.1016/S1359-6462(02)00477-3.

[65]   S. Oliver, T.B. Jones, G. Fourlaris, Dual phase versus TRIP strip steels: Microstructural changes as a consequence of quasi-static and dynamic tensile testing, Mater. Charact. 58 (2007) 390–400. doi:10.1016/j.matchar.2006.07.004.

[66]   O.A. Girina, N.M. Fonstein, Influence of Al additions on austenite decomposition in continuously annealed dual-phase steels, in: Mater. Sci. Technol., 2005: pp. 65–76.

[67]   J.Y. Kang, H.C. Lee, S.H. Han, Effect of Al and Mo on the textures and microstructures of dual phase steels, Mater. Sci. Eng. A. 530 (2011) 183–190. doi:10.1016/j.msea.2011.09.071.

[68]   B.L. Ennis, E. Jimenez-Melero, R. Mostert, B. Santillana, P.D. Lee, The role of aluminium in chemical and phase segregation in a TRIP-assisted dual phase steel, Acta Mater. 115 (2016) 132–142. doi:10.1016/j.actamat.2016.05.046.

[69]   F.B. Pickering, Physical Metallurgy and the Design of Steels: Austenitic Stainless Steels, 1978. doi:10.1002/9780470872864.

[70]   M. Calcagnotto, D. Ponge, D. Raabe, On the effect of manganese on grain size stability and hardenability in ultrafine-grained ferrite/martensite dual-phase steels, Metall. Mater. Trans. A Phys. Metall. Mater. Sci. 43 (2012) 37–46. doi:10.1007/s11661-011-0828-3.

[71]   N. Fonstein, M. Kapustin, N. Pottore, I. Gupta, O. Yakubovsky, Factors that determine the level of the yield strength and the return of the yield-point elongation in low-alloy ferrite-martensite steels, Phys. Met. Metallogr. 104 (2007) 315–323. doi:10.1134/S0031918X07090153.

[72]   J.W. Spretnak, R. Speiser, A Critical Evaluation of the Boron Hardenability Effect in Steel., OHIO STATE UNIV COLUMBUS. (1952).

[73]   C.R. Simcoe, A.R. Elsea, G.K. Manning, Further Work on the Boron-Hardenability Mechanism, Jom. 8 (1956) 984–988. doi:10.1007/bf03377806.

[74]   Y. Imai, H. Imai, An Investigation on Boron-Treated Steels. I: On the Hardenability of Boron-Treated Medium-Carbon Steels, especially the Effect of Nitrogen-Content in Steels. Science reports of the Research Institutes,

Tohoku University. Ser. A, Physics, chemistry and met, 2 (1950) 260–269.

[75]   K. Ishikawa, H. Nakamura, R. Homma, M. Fujioka, M. Hoshino, Effect of Molybdenum Content on Hardenability of Boron and Molybdenum Combined Added Steels, in: 2018: pp. 25–28. doi:10.1007/978-3-319-76968-4_4.

[76]   S. Kawasaki, A. Hishinuma, R. Nagasaki, Behaviour of boron in stainless steel detected by fission track etching method and effect of radiation on tensile properties, J. Nucl. Mater. 39 (1971) 166–174. doi:10.1016/0022-3115(71)90021-3.

[77]   B. Hwang, D.W. Suh, S.J. Kim, Austenitizing temperature and hardenability of low-carbon boron steels, Scr. Mater. 64 (2011) 1118–1120. doi:10.1016/j.scriptamat.2011.03.003.

[78]   P. Maitrepierre, D. Thivellier, R. Tricot, Influence of boron on the decomposition of austenite in low carbon alloyed steels, Metall. Trans. A. 6 (1975) 287–301. doi:10.1007/BF02667283.

[79]   X.M. Wang, X.L. He, Effect of boron addition on structure and properties of low carbon bainitic steels, ISIJ Int. 42 (2002). doi:10.2355/isijinternational.42.suppl_s38.

[80]   P. Chokshi, R. Dashwood, D.J. Hughes, Artificial Neural Network (ANN) based microstructural prediction model for 22MnB5 boron steel during tailored hot stamping, Comput. Struct. 190 (2017) 162–172. doi:10.1016/j.compstruc.2017.05.015.

[81]   N.D. Raath, D. Norman, I. McGregor, S. Hepple, R. Dashwood, D.J. Hughes, Characterization of Loading Responses and Failure Loci of a Boron Steel Spot Weld, Metall. Mater. Trans. A Phys. Metall. Mater. Sci. 49 (2018) 1536–1551. doi:10.1007/s11661-018-4502-x.

[82]   N.D. Raath, D. Norman, I. McGregor, R. Dashwood, D.J. Hughes, Effect of Weld Schedule on the Residual Stress Distribution of Boron Steel Spot Welds, Metall. Mater. Trans. A Phys. Metall. Mater. Sci. 48 (2017) 2900–2914. doi:10.1007/s11661-017-4079-9.

[83]   R. Priestner, M. Ajmal, Effect of carbon content and microalloying on martensitic hardenability of austenite of dual-phase steel, Mater. Sci. Technol.

(United Kingdom). 3 (1987) 360–364. doi:10.1179/mst.1987.3.5.360.

[84]   R.A. Grange, Estimating the hardenability of carbon steels, Metall. Trans. 4 (1973) 2231–2244. doi:10.1007/BF02669363.

[85]   X.P. Shen, R. Priestner, Effect of boron on the microstructure and tensile properties of dual-phase steel, Metall. Trans. A. 21 (1990) 2547–2553. doi:10.1007/BF02647000.

[86]   S. Qiu, L. Xiao, J. Liu, Y. Gan, Softening mechanism of boron-bearing low-carbon hot strips produced by TSCR route, Jinshu Xuebao/Acta Metall. Sin. 42 (2006) 1202–1206.

[87]   C.F. Jatczak, Hardenability in high carbon steels, Metall. Trans. 4 (1973) 2267–2277. doi:10.1007/BF02669366.

[88]   N.J. Kim, Y.G. Kim, Effect of boron on the structure and mechanical properties of intercritically annealed Fe-1.5Mn-0.06C steels, Mater. Sci. Eng. A. 129 (1990) 35–44. doi:10.1016/0921-5093(90)90342-Z.

[89]   H. Tamehiro, M. Murata, R. Habu, M. Nagumo, Optimum Microalloying of Niobium and Boron in Hsla Steel for Thermomechanical Processing., Trans. Iron Steel Inst. Japan. 27 (1987) 120–129. doi:10.2355/isijinternational1966.27.120.

[90]   F.G. Wilson, T. Gladman, Aluminium nitride in steel, Int. Mater. Rev. 33 (1988) 221–286. doi:10.1179/imr.1988.33.1.221.

[91]   S. Zhang, N. Hattori, M. Enomoto, T. Tarui, Ferrite nucleation at ceramic/austenite interfaces, ISIJ Int. 36 (1996) 1301–1309. doi:10.2355/isijinternational.36.1301.

[92]   F. Ishikawa, T. Takahashi, T. Ochi, Intragranular ferrite nucleation in medium-carbon vanadium steels, Metall. Mater. Trans. A. 25 (1994) 929–936. doi:10.1007/BF02652268.

[93]   F. Alizon, S.B. Shooter, T.W. Simpson, Henry Ford and the Model T: lessons for product platforming and mass customization, Des. Stud. 30 (2009) 588–605. doi:10.1016/j.destud.2009.03.003.

[94]   J.S. Gau, J.Y. Koo, A. Nakagawa, G. Thomas, Microstructure and properties of

dual-phase steels containing fine precipitates (No. LBL-12177)., 1981.

[95] S.G. Hong, H.J. Jun, K.B. Kang, C.G. Park, Evolution of precipitates in the Nb-Ti-V microalloyed HSLA steels during reheating, Scr. Mater. 48 (2003) 1201–1206. doi:10.1016/S1359-6462(02)00567-5.

[96] R. Lagneborg, T. Siwecki, S. Zajac, B. Hutchinson, Role of vanadium in microalloyed steels, Scand. J. Metall. 28 (1999) 186–241.

[97] T. Gladman, The physical metallurgy of microalloyed steels, 1997. doi:10.5860/choice.35-2725.

[98] F.A. Khalid, D. V. Edmonds, Interphase precipitation in microalloyed engineering steels and model alloy, Mater. Sci. Technol. (United Kingdom). 9 (1993) 384–396. doi:10.1179/mst.1993.9.5.384.

[99] T.N. Baker, Processes, microstructure and properties of vanadium microalloyed steels, Mater. Sci. Technol. 25 (2009) 1083–1107. doi:10.1179/174328409X453253.

[100] T. Senuma, Physical metallurgy of modern high strength steel sheets, ISIJ Int. 41 (2001) 520–532. doi:10.2355/isijinternational.41.520.

[101] G. Avramovic-Cingara, C.A.R. Saleh, M.K. Jain, D.S. Wilkinson, Void nucleation and growth in dual-phase steel 600 during uniaxial tensile testing, Metall. Mater. Trans. A Phys. Metall. Mater. Sci. 40 (2009) 3117–3127. doi:10.1007/s11661-009-0030-z.

[102] K. Hasegawa, K. Kawamura, T. Urabe, Y. Hosoya, Effects of microstructure on stretch-flange-formability of 980 MPa grade cold-rolled ultra high strength steel sheets, ISIJ Int. 44 (2004) 603–609. doi:10.2355/isijinternational.44.603.

[103] C.P. Scott, F. Fazeli, B. Shalchi Amirkhiz, I. Pushkareva, S.Y.P. Allain, Structure-properties relationship of ultra-fine grained V-microalloyed dual phase steels, Mater. Sci. Eng. A. 703 (2017) 293–303. doi:10.1016/j.msea.2017.07.051.

[104] N. Fonstein, Advanced high strength sheet steels: Physical metallurgy, design, processing, and properties, 2015. doi:10.1007/978-3-319-19165-2.

[105] F.L.G. Oliveira, M.S. Andrade, A.B. Cota, Kinetics of austenite formation

during continuous heating in a low carbon steel, Mater. Charact. 58 (2007) 256–261. doi:10.1016/j.matchar.2006.04.027.

[106] M.D. Geib, D.K. Matlock, G. Krauss, The effect of intercritical annealing temperature on the structure of niobium microalloyed dualphase steel, Metall. Trans. A. 11 (1980) 1683–1689. doi:10.1007/BF02660523.

[107] R. G.Davies, The deformation behavior of a vanadium-strengthened dual phase steel, Metall. Trans. A. 9 (1978) 41–52. doi:10.1007/BF02647169.

[108] Q. Lai, L. Brassart, O. Bouaziz, M. Gouné, M. Verdier, G. Parry, A. Perlade, Y. Bréchet, T. Pardoen, Influence of martensite volume fraction and hardness on the plastic behavior of dual-phase steels: Experiments and micromechanical modeling, Int. J. Plast. 80 (2016) 187–203. doi:10.1016/j.ijplas.2015.09.006.

[109] E.N. Birgani, M. Pouranvari, Effect of Martensite Volume Fraction on the Work Hardening Behavior of Dual Phase Steels, Met. 2009. (2009).

[110] Y. Mazaheri, A. Kermanpur, A. Najafizadeh, Nanoindentation study of ferrite-martensite dual phase steels developed by a new thermomechanical processing, Mater. Sci. Eng. A. 639 (2015) 8–14. doi:10.1016/j.msea.2015.04.098.

[111] V.H. Baltazar Hernandez, S.K. Panda, M.L. Kuntz, Y. Zhou, Nanoindentation and microstructure analysis of resistance spot welded dual phase steel, Mater. Lett. 64 (2010) 207–210. doi:10.1016/j.matlet.2009.10.040.

[112] G. Cheng, F. Zhang, A. Ruimi, D.P. Field, X. Sun, Quantifying the effects of tempering on individual phase properties of DP980 steel with nanoindentation, Mater. Sci. Eng. A. 667 (2016) 240–249. doi:10.1016/j.msea.2016.05.011.

[113] R.R. Mohanty, O.A. Girina, Effect of Coiling Temperature on Kinetics of Austenite Formation in Cold Rolled Advanced High Strength Steels, Mater. Sci. Forum. 706 (2012) 2112–2117. doi:https://doi.org/10.4028/www.scientific.net/MSF.706-709.2112.

[114] N.C. Law, D. V. Edmonds, The formation of austenite in a low-alloy steel, Metall. Mater. Trans. A. 11 (1980) 33–46. doi:10.1007/BF02700436.

[115] Y. Granbom, Effects of Process Parameters prior to Annealing on the Formability of Two Cold Rolled Dual Phase Steels, Steel Res. Int. 79 (2008) 297–305. doi:10.1002/srin.200806354.

154

[116] F.J. Humphreys, M. Hatherly, The Deformed State, in: Recryst. Relat. Annealing Phenom., 2004: pp. 11–II. doi:10.1016/b978-008044164-1/50006-2.

[117] D.Z. Yang, E.L. Brown, D.K. Matlock, G. Krauss, Ferrite recrystallization and austenite formation in cold-rolled intercritically annealed steel, Metall. Trans. A. 16 (1985) 1385–1392. doi:10.1007/BF02658671.

[118] N. Peranio, Y.J. Li, F. Roters, D. Raabe, Microstructure and texture evolution in dual-phase steels: Competition between recovery, recrystallization, and phase transformation, Mater. Sci. Eng. A. 527 (2010) 4161–4168. doi:10.1016/j.msea.2010.03.028.

[119] I. Nikitin, M. Besel, Residual stress relaxation of deep-rolled austenitic steel, Scr. Mater. 58 (2008) 239–242. doi:10.1016/j.scriptamat.2007.09.045.

[120] A. Rollett, F. Humphreys, G.S. Rohrer, M. Hatherly, Recrystallization and Related Annealing Phenomena: Second Edition, 2004. doi:10.1016/B978-0-08-044164-1.X5000-2.

[121] R.E. Smallman, Plasticity of crystals with special reference to metals by E. Schmid and W. Boas, 1969. doi:10.1107/s0021889869006819.

[122] T.W. Clyne, J.E. Campbell, Mechanisms of Plastic Deformation in Metals, in: Test. Plast. Deform. Met., 2021: pp. 43–80. doi:10.1017/9781108943369.005.

[123] P.G. Heighway, J.S. Wark, Kinematics of slip-induced rotation for uniaxial shock or ramp compression, J. Appl. Phys. 129 (2021). doi:10.1063/5.0038557.

[124] Y. Perlovich, M. Isaenkova, P. Dobrokhotov, D. Zhuk, A. Rubanov, Modeling of Crystallographic Texture Formation in Hot-rolled Sheets of Ferritic Steel, KnE Mater. Sci. 4 (2018) 199. doi:10.18502/kms.v4i1.2144.

[125] Y.B. Park, D.N. Lee, G. Gottstein, Development of texture inhomogeneity during hot rolling in interstitial free steel, Acta Mater. 44 (1996) 3421–3427. doi:10.1016/1359-6454(95)00414-9.

[126] D. Raabe, Overview on Basic Types of Hot Rolling Textures of Steels, Steel Res. Int. 74 (2003) 327–337. doi:10.1002/srin.200300194.

[127] D. Raabe, Inhomogeneity of the crystallographic texture in a hot-rolled

austenitic stainless steel, J. Mater. Sci. 30 (1995) 47–52. doi:10.1007/BF00352130.

[128] S. Narayanswamy, S.R. Reddy, R. Saha, P.P. Bhattacharjee, Texture homogeneity and stability in severely warm-rolled and annealed ultrafine pearlite, Mater. Sci. Technol. (United Kingdom). 35 (2019) 437–447. doi:10.1080/02670836.2019.1569746.

[129] K. Muszka, M. Sitko, P. Lisiecka-Graca, T. Simm, E. Palmiere, M. Schmidtchen, G. Korpala, J. Wang, L. Madej, Experimental and numerical study of the effects of the reversal hot rolling conditions on the recrystallization behavior of austenite model alloys, Metals (Basel). 11 (2021) 1–17. doi:10.3390/met11010026.

[130] Y. Perlovich, M. Isaenkova, Effects of dynamical deformation ageing on structure and texture of hot-rolled sheets from alloyed BCC metals, Int. J. Mater. Form. 3 (2010) 1143–1146. doi:10.1007/s12289-010-0974-y.

[131] D. Raabe, Z. Zhao, S.J. Park, F. Roters, Theory of orientation gradients in plastically strained crystals, Acta Mater. 50 (2002) 421–440. doi:10.1016/S1359-6454(01)00323-8.

[132] J. Huang, W.J. Poole, M. Militzer, Austenite formation during intercritical annealing, Metall. Mater. Trans. A Phys. Metall. Mater. Sci. 35 A (2004) 3363–3375. doi:10.1007/s11661-004-0173-x.

[133] F.J. Humphreys, M. Hatherly, Recovery After Deformation, in: Recryst. Relat. Annealing Phenom., 2004: pp. 169–213. doi:10.1016/b978-008044164-1/50010-4.

[134] R. Abbaschian, L. Abbaschian, R. Reed-Hill, Chapter 8. Annealing, 2009.

[135] F.J. Humphreys, M. Hatherly, Recrystallization of Single-Phase Alloys, in: Recryst. Relat. Annealing Phenom., 2nd ed., 2004: pp. 215–266. doi:10.1016/B978-008044164-1/50011-6.

[136] E.J. Palmiere, P.W. Bradley, Recrystallization and Grain Growth IV, Mater. Sci. Forum. (2012) 715–716. https://www.scientific.net/book/recrystallization-and-grain-growth-iv/978-3-03813-675-0.

[137] Y. Lü, D.A. Molodov, G. Gottstein, Recrystallization kinetics and

microstructure evolution during annealing of a cold-rolled Fe-Mn-C alloy, Acta Mater. 59 (2011) 3229–3243. doi:10.1016/j.actamat.2011.01.063.

[138] M. Fanfoni, M. Tomellini, The Johnson-Mehl-Avrami-Kolmogorov model: A brief review, Nuovo Cim. Della Soc. Ital. Di Fis. D - Condens. Matter, At. Mol. Chem. Physics, Biophys. 20 (1998) 1171–1182. doi:10.1007/BF03185527.

[139] A.N. Kolmogorov, On the statistical theory of the crystallization of metals, Bull. Acad. Sci. USSR, Math. Ser. (1937).

[140] M. Avrami, Kinetics of phase change. I: General theory, J. Chem. Phys. 7 (1939) 1103–1112. doi:10.1063/1.1750380.

[141] W.A. Johnson, R.F. Mehl, Reaction Kinetics in Processes of Nucleation and Growth, Trans. Am. Inst. Minning Metall. Eng. 135 (1939) 416–458.

[142] S. Chattopadhyay, C.M. Sellars, Quantitative Measurements of Pearlite Spheroidization, Metallography. 10 (1977) 89–105.

[143] J. Teixeira, M. Moreno, S.Y.P. Allain, C. Oberbillig, G. Geandier, F. Bonnet, Intercritical annealing of cold-rolled ferrite-pearlite steel: Microstructure evolutions and phase transformation kinetics, Acta Mater. 212 (2021). doi:10.1016/j.actamat.2021.116920.

[144] N. Peranio, F. Roters, D. Raabe, Microstructure evolution during recrystallization in dual-phase steels, in: Mater. Sci. Forum, 2012: pp. 13–22. doi:10.4028/www.scientific.net/MSF.715-716.13.

[145] M. Bellavoine, M. Dumont, J. Drillet, V. Hébert, P. Maugis, Combined Effect of Heating Rate and Microalloying Elements on Recrystallization During Annealing of Dual-Phase Steels, Metall. Mater. Trans. A Phys. Metall. Mater. Sci. 49 (2018) 2865–2875. doi:10.1007/s11661-018-4642-z.

[146] F. Perrard, C. Scott, Vanadium precipitation during intercritical annealing in cold rolled TRIP steels, ISIJ Int. 47 (2007) 1168–1177. doi:10.2355/isijinternational.47.1168.

[147] G.H. Zhu, X.H. Zhang, W.M. Mao, Development in high-grade dual phase steels with low C and Si design, Front. Mater. Sci. China. (2009). doi:10.1007/s11706-009-0059-3.

[148] P. Gong, E.J. Palmiere, W.M. Rainforth, Thermomechanical processing route to achieve ultrafine grains in low carbon microalloyed steels, Acta Mater. 119 (2016) 43–54. doi:10.1016/j.actamat.2016.08.010.

[149] V. Shah, M. Krugla, S.E. Offerman, J. Sietsma, D.N. Hanlon, Effect of Silicon, Manganese and Heating Rate on the Ferrite Recrystallization Kinetics, ISIJ Int. 60 (2020) 1312–1323. doi:10.2355/isijinternational.isijint-2019-475.

[150] Y. Granbom, Influence of niobium and coiling temperature on the mechanical properties of a cold rolled dual phase steel, Rev. Metall. Cah. D'Informations Tech. 104 (2007) 191–197. doi:10.1051/metal:2007147.

[151] W. Callister, Fundamentals of materials science and engineering, Vol. 47166, London: Wiley, 2000.

[152] P. Li, J. Li, Q. Meng, W. Hu, D. Xu, Effect of heating rate on ferrite recrystallization and austenite formation of cold-roll dual phase steel, J. Alloys Compd. 578 (2013) 320–327. doi:10.1016/j.jallcom.2013.05.226.

[153] L. Kestens, A.C.C. Reis, W.J. Kaluba, Y. Houbaert, Grain refinement and texture change in interstitial free steels after severe rolling and ultra-short annealing, in: Mater. Sci. Forum, 2004: pp. 287–292. doi:10.4028/www.scientific.net/msf.467-470.287.

[154] T. Lolla, G. Cola, B. Narayanan, B. Alexandrov, S.S. Babu, Development of rapid heating and cooling (flash processing) process to produce advanced high strength steel microstructures, Mater. Sci. Technol. 27 (2011) 863–875. doi:10.1179/174328409X433813.

[155] H. Azizi-Alizamini, M. Militzer, W.J. Poole, Formation of ultrafine grained dual phase steels through rapid heating, ISIJ Int. 51 (2011) 958–964. doi:10.2355/isijinternational.51.958.

[156] V. Massardier, A. Ngansop, D. Fabrègue, J. Merlin, Microstructure and mechanical properties of low carbon Al-killed steels after ultra-rapid annealing cycles, in: Mater. Sci. Forum, 2010: pp. 3368–3373. doi:10.4028/www.scientific.net/MSF.638-642.3368.

[157] V. Massardier, A. Ngansop, D. Fabregue, S. Cazottes, J. Merlin, Ultra-rapid intercritical annealing to improve deep drawability of low-carbon, al-killed

steels, Metall. Mater. Trans. A Phys. Metall. Mater. Sci. 43 (2012) 2225–2236. doi:10.1007/s11661-012-1096-6.

[158] M. Kulakov, W.J. Poole, M. Militzer, The effect of the initial microstructure on recrystallization and austenite formation in a DP600 steel, Metall. Mater. Trans. A Phys. Metall. Mater. Sci. 44 (2013) 3564–3576. doi:10.1007/s11661-013-1721-z.

[159] A. Chbihi, D. Barbier, L. Germain, A. Hazotte, M. Gouné, Interactions between ferrite recrystallization and austenite formation in high-strength steels, J. Mater. Sci. 49 (2014) 3608–3621. doi:10.1007/s10853-014-8029-2.

[160] D. De Knijf, A. Puype, C. Föjer, R. Petrov, The influence of ultra-fast annealing prior to quenching and partitioning on the microstructure and mechanical properties, Mater. Sci. Eng. A. 627 (2015) 182–190. doi:10.1016/j.msea.2014.12.118.

[161] C. Philippot, M. Bellavoine, M. Dumont, K. Hoummada, J. Drillet, V. Hebert, P. Maugis, Influence of Heating Rate on Ferrite Recrystallization and Austenite Formation in Cold-Rolled Microalloyed Dual-Phase Steels, Metall. Mater. Trans. A Phys. Metall. Mater. Sci. 49 (2018) 66–77. doi:10.1007/s11661-017-4407-0.

[162] E.A. Simielli, S. Yue, J.J. Jonas, Recrystallization kinetics of microalloyed steels deformed in the intercritical region, Metall. Trans. A. 23 (1992) 597–608. doi:10.1007/BF02801177.

[163] R. Petrov, F. Hajyakbari, F.R. Saz, J. Sidor, M.J. Santofimia, J. Sietsma, L. Kestens, Microstructure and properties of ultrafast annealed high strength steel, in: Mater. Sci. Forum, 2013: pp. 554–558. doi:10.4028/www.scientific.net/MSF.753.554.

[164] C. Zheng, D. Raabe, Interaction between recrystallization and phase transformation during intercritical annealing in a cold-rolled dual-phase steel: A cellular automaton model, Acta Mater. 61 (2013) 5504–5517. doi:10.1016/j.actamat.2013.05.040.

[165] B. Zhu, M. Militzer, Phase-Field Modeling for Intercritical Annealing of a Dual-Phase Steel, Metall. Mater. Trans. A Phys. Metall. Mater. Sci. 46 (2015)

1073–1084. doi:10.1007/s11661-014-2698-y.

[166] L.S. Thomas, D.K. Matlock, Formation of Banded Microstructures with Rapid Intercritical Annealing of Cold-Rolled Sheet Steel, Metall. Mater. Trans. A Phys. Metall. Mater. Sci. 49 (2018) 4456–4473. doi:10.1007/s11661-018-4742-9.

[167] V. Andrade-Carozzo, P.J. Jacques, Interactions between Recrystallisation and Phase Transformations during Annealing of Cold Rolled Nb-Added TRIP-Aided Steels, Mater. Sci. Forum. 539–543 (2007) 4649–4654. doi:10.4028/www.scientific.net/msf.539-543.4649.

[168] R.R. Mohanty, O.A. Girina, N.M. Fonstein, Effect of heating rate on the austenite formation in low-carbon high-strength steels annealed in the intercritical region, in: Metall. Mater. Trans. A Phys. Metall. Mater. Sci., 2011: pp. 3680–3690. doi:10.1007/s11661-011-0753-5.

[169] D. Das, P.P. Chattopadhyay, Influence of martensite morphology on the work-hardening behavior of high strength ferrite-martensite dual-phase steel, J. Mater. Sci. 44 (2009) 2957–2965. doi:10.1007/s10853-009-3392-0.

[170] D. San Martín, T. De Cock, A. García-Junceda, F.G. Caballero, C. Capdevila, C. García De Andrés, Effect of heating rate on reaustenitisation of low carbon niobium microalloyed steel, Mater. Sci. Technol. 24 (2008) 266–272. doi:10.1179/174328408X265640.

[171] V.I. Savran, Y. Leeuwen, D.N. Hanlon, C. Kwakernaak, W.G. Sloof, J. Sietsma, Microstructural features of austenite formation in C35 and C45 alloys, Metall. Mater. Trans. A Phys. Metall. Mater. Sci. 38 (2007) 946–955. doi:10.1007/s11661-007-9128-3.

[172] T. Ogawa, N. Maruyama, N. Sugiura, N. Yoshinaga, Incomplete recrystallization and subsequent microstructural evolution during Lntercritical annealing in cold-rolled low carbon steels, ISIJ Int. 50 (2010) 469–475. doi:10.2355/isijinternational.50.469.

[173] D. Mumford, G. Fourlaris, A. Smith, N. Silk, The Interaction of Recrystallization and Transformation during the Reheating of Multiphase Steels, in: AISTech Conf. Proc., 2008.

[174] C. Slater, A. Mandal, C. Davis, The Influence of Segregation of Mn on the Recrystallization Behavior of C-Mn Steels, Metall. Mater. Trans. B Process Metall. Mater. Process. Sci. 50 (2019) 1627–1636. doi:10.1007/s11663-019-01603-2.

[175] W. Wang, P.D. Lee, M. McLean, A model of solidification microstructures in nickel-based superalloys: Predicting primary dendrite spacing selection, Acta Mater. 51 (2003) 2971–2987. doi:10.1016/S1359-6454(03)00110-1.

[176] M.E. Glicksman, Principles of solidification: An introduction to modern casting and crystal growth concepts, 2011. doi:10.1007/978-1-4419-7344-3.

[177] D. Chakrabarti, C. Davis, M. Strangwood, Development of bimodal grain structures in Nb-containing high-strength low-alloy steels during slab reheating, in: Metall. Mater. Trans. A Phys. Metall. Mater. Sci., 2008: pp. 1963–1977. doi:10.1007/s11661-008-9535-0.

[178] R.. Fisher, G.. Speich, L.. Cuddy, H. Hu, Phase transformations during steel production, in: Proc. Darken Conf. "Physical Chem. Metall., Monroeville, PA, USA, 1976.

[179] Y. Chen, G.J. Li, S.B. Yang, M.Y. Zhu, Dynamic Soft Reduction for Continuously Cast Rail Bloom, J. Iron Steel Res. Int. 14 (2007). doi:10.1016/S1006-706X(07)60066-1.

[180] T.I. Malinovskaya, A.H. Kurasov, G. V. Glaskova, Y.I. Spektor, Effect of homogenization of dendritic segregation of chromium and manganese in steel ShKh15, Met. Sci. Heat Treat. 17 (1975) 609–610. doi:10.1007/BF00680413.

[181] O. Haida, H. Kitaoka, Y. Habu, S. Kakihara, H. Bada, S. Shiraishi, Macro- and Semi-Macroscopic Features of the Centerline Segregation in Cc Slabs and Their Effect on Product Quality., Trans. Iron Steel Inst. Japan. 24 (1984) 891–898. doi:10.2355/isijinternational1966.24.891.

[182] G. Krauss, Solidification, Segregation, and Banding in Carbon and Alloy Steels, Metall. Mater. Trans. B Process Metall. Mater. Process. Sci. 34 (2003) 781–792. doi:10.1007/s11663-003-0084-z.

[183] T.F. Majka, D.K. Matlock, G. Krauss, Development of microstructural banding in low-alloy steel with simulated Mn segregation, Metall. Mater. Trans. A Phys.

Metall. Mater. Sci. 33 (2002) 1627–1637. doi:10.1007/s11661-002-0172-8.

[184] T. Yamashita, S. Torizuka, K. Nagai, Effect of manganese segregation on fine-grained ferrite structure in low-carbon steel slabs, ISIJ Int. 43 (2003) 1833–1841. doi:10.2355/isijinternational.43.1833.

[185] F.G. Caballero, A. García-Junceda, C. Capdevila, C.G. De Andrés, Evolution of microstructural banding during the manufacturing process of dual phase steels, in: Mater. Trans., 2006: pp. 2269–2276. doi:10.2320/matertrans.47.2269.

[186] D.S. Martín, Y. Palizdar, C. García-Mateo, R.C. Cochrane, R. Brydson, A.J. Scott, Influence of aluminum alloying and heating rate on austenite formation in low carbon-manganese steels, Metall. Mater. Trans. A Phys. Metall. Mater. Sci. 42 (2011) 2591–2608. doi:10.1007/s11661-011-0692-1.

[187] C. Bos, M.G. Mecozzi, D.N. Hanlon, M.P. Aarnts, J. Sietsma, Application of a three-dimensional microstructure evolution model to identify key process settings for the production of dual-phase steels, in: Metall. Mater. Trans. A Phys. Metall. Mater. Sci., 2011: pp. 3602–3610. doi:10.1007/s11661-011-0696-x.

[188] L. Schemmann, S. Zaefferer, D. Raabe, F. Friedel, D. Mattissen, Alloying effects on microstructure formation of dual phase steels, Acta Mater. 95 (2015) 386–398. doi:10.1016/j.actamat.2015.05.005.

[189] S.W. Thompson, P.R. Howell, Factors influencing ferrite/pearlite banding and origin of large pearlite nodules in a hypoeutectoid plate steel, Mater. Sci. Technol. 8 (2012) 777–784. doi:10.1179/026708392790171332.

[190] W.J. Boettinger, S.R. Coriell, A.L. Greer, A. Karma, W. Kurz, M. Rappaz, R. Trivedi, Solidification microstructures: recent developments, future directions, Acta Mater. 48 (2000) 43–70. doi:10.1016/S1359-6454(99)00287-6.

[191] UNFCC, Adoption of the Paris Agreement, Conf. Parties Its Twenty-First Sess. (2015) 32. doi:FCCC/CP/2015/L.9.

[192] S. Ohkita, The effect of oxide inclusion on microstructure of Ti-B containing weld metal., Aust. Weld. J. 29 (1984) 29.

[193] H. Hu, S.R. Goodman, Effect of manganese on the annealing texture and strain

ratio of low-carbon steels, Metall. Trans. 1 (1970) 3057–3064. doi:10.1007/BF03038419.

[194] V. Raghavan, Physical metallurgy: principles and practice, II, PHI Learning Pvt. Ltd., 2015.

[195] ASTM, Standard Test Method for Determining Volume Fraction by Systematic Manual Point Count, Practice. (2011) 1–7. doi:10.1520/E0562-11.2.

[196] ASTM Standard, E112-12:Standard Test Methods for Determining Average Grain Size, ASTM Int. E112-12 (2012) 1–27. doi:10.1520/E0112-12.1.4.

[197] N. Imai, N. Komatsubara, K. Kunishige, Effect of alloying element and microstructure on mechanical properties of low-alloy TRIP-steels, CAMP-ISIJ. 8 (1995) 572–575. doi:doi.org/10.5026/jgeography.104.4_572.

[198] B. Bandi, J. van Krevel, N. Aslam, P. Srirangam, A Model and Experimental Validation to Predict Heating Rates for Overlap Between Ferrite Recrystallization and Austenite Transformation in Dual Phase Steel Manufacture, JOM. 71 (2019) 1386–1395. doi:10.1007/s11837-019-03358-2.

[199] A.A. Burbelko, E. Fraś, W. Kapturkiewicz, About Kolmogorov's statistical theory of phase transformation, Mater. Sci. Eng. A. 413–414 (2005) 429–434. doi:10.1016/j.msea.2005.08.161.

[200] A. Rollett, F. Humphreys, G.S. Rohrer, M. Hatherly, Recrystallization and Related Annealing Phenomena: Second Edition, Pergamon, 2004. doi:10.1016/B978-0-08-044164-1.X5000-2.

[201] R.A. Oriani, Ostwald ripening of precipitates in solid matrices, Acta Metall. 12 (1964) 1399–1409. doi:10.1016/0001-6160(64)90128-2.

[202] T. De Cock, C. Capdevila, F.G. Caballero, C.G. De Andrés, Interpretation of a dilatometric anomaly previous to the ferrite-to-austenite transformation in a low carbon steel, Scr. Mater. 54 (2006) 949–954. doi:10.1016/j.scriptamat.2005.10.052.

[203] R.H. Petrov, J. Sidor, L.A.I. Kestens, Texture formation in high strength low alloy steel reheated with ultrafast heating rates, in: Mater. Sci. Forum, 2012: pp. 798–801. doi:10.4028/www.scientific.net/MSF.702-703.798.

[204] A. Ghosh, Segregation in cast products, in: Sadhana - Acad. Proc. Eng. Sci., 2001: pp. 5–24. doi:10.1007/BF02728476.

[205] E. Navara, R. Harrysson, On the mechanism of austenite formation during inter- and subcritical annealing of a CMn steel, Scr. Metall. 18 (1984) 605–610. doi:10.1016/0036-9748(84)90350-8.

[206] A. Ebrahimian, S.S. Ghasemi Banadkouki, Mutual mechanical effects of ferrite and martensite in a low alloy ferrite-martensite dual phase steel, J. Alloys Compd. 708 (2017) 43–54. doi:10.1016/j.jallcom.2017.02.287.